UNIVERSITY OF CALIFORNIA
RIVERSIDE

Probing the Gluon Contribution to the Proton Spin with Charged Pion Production

A Dissertation submitted in partial satisfaction
of the requirements for the degree of

Doctor of Philosophy

in

Physics

by

Astrid Morreale

August 2009

Dissertation Committee:

Dr. Kenneth N. Barish, Chairperson
Dr. Richard Seto
Dr. Robert Clare

The Dissertation of Astrid Morreale is approved:

_____

_____

_____

Committee Chairperson

University of California, Riverside

Acknowledgements

The study presented in this thesis has been carried out under the academic support of my adviser professor Kenneth Barish. I would like to acknoledge the helpful editing comments of the manuscript from my dissertation committe: Dr. Kenneth Barish, Dr. Robert Clare and Dr. Richard Seto. I want to thank the extraordinary guidance, mentoring and scientific advices from both Aneta Iordadova and Richard Hollis who have helped me work out countless details in my analysis and thesis. Since their arrival at UCR, they have shared their deep scientific knowledge with anyone in our group, with humility and patience.

I thank Ondřej Chvála, Kieran Boyle, Robert Bennett, Baldo Sahlmüller, Shin-Chuan Kao and Olive. Ondřej allowed me to succesfully finish my research by sharing with me GB of his own allocated space when It become difficult to find space to finish my analysis. Kieran for the hours spent past midnight at the Physics building trying to fit functions and calculate backgrounds in the early stage of the assymetry measurements. Robert and Baldo for always being available when I needed clear explanations. Shih-Chuan and Olive for always helping me when I was stranded during/after conference or research trips. I am very happy for having worked with all of you and the privilege of having earned your friendship.

The road to this thesis has not been an easy one. But I have been surrounded by encouraging folks who believed in my work and oftentimes offered a helping hand when I

faced adversities. I will always remember Professor George Igo and Dr. Vahe Ghazikhanian. They saw my potential and encouraged my determination. During my times as an enlisted Marine and as a part time student, I always encountered encouragement in my studies. I thank *Gunny* Alan Proctor in particular who have always been a supportive adviser and friend - even if the advise was given during a ten mile run in the desert. I will not forget the early academic influence of professor Benjamin Crowell, for his great skateboarding skills in the classroom, who swore I was the first Marine that had passed his class (I think he meant the first Marine to attend his class).

While being a graduate student can be at times an isolating experience at BNL, I am grateful for having met some great people through the Association of Students and Postdocs at BNL. All these individual scientific experiences I have heard through ASAP presented me the big picture shared by all scientists from all fields and countries. I thank, Nathalie Bouet for her constant positivity on the things of science and life in general, Mirko Milas and Guillaume Robert-Demolaize for the countless laughs (quelle rigolade avec ces deux-là !), also Boaz Nash for his philosophy and my partner in crime Christine Nattrass, who tought me that a mere student has the power to make a difference in the lives of those we represent. I thank my friend Marco Giovanni Pruna, who explained to me so many physics principles and was always available to help me -con estrema pazienza ha sopportato i miei sbalzi di umore e le mie paranoie quando, sotto stress, mi sfogavo in modo particolare con lui.

Finally, I save my biggest grattitude to those closest to me: my family. Sebastien Parmentier, my husband and friend since 2004 has been more than a shoulder I could lean on. I can only hope to support him through your journey the same way he has supported mine. Through his kindness and trust in human beings I have become a better human and have learned how to be proud of my own life experiences. *"Le véritable voyage de découverte ne consiste pas à chercher de nouveaux paysages, mais à avoir de nouveaux yeux."*[1] I thank my younger brothers: Günther, who shared many difficult times with me, specially after our father left this world. I am certain you will acomplish anything you set your mind to. I will always believe in you, just as you have always believed in me. Little William, how can I not mention you, you made me forget the stress of the Ph.D comprehensive exams by making your funny monkey dances in the kitchen (cést vrai !). My mother Rosa, I only wish we could had spend more time together. I finally reserve the last lines to the most influential person in my life. My Father Edwin Morreale, to whom I owe my passion for physics, my determination and my confidence. You did not have many material things to leave us, but you left us with your lessons. There are more important things in this world to pursue than material wealth: knowledge about us, our place in a universe governed by physics laws. You tought us that race, gender, or country of origin were not obstacles, but rather, intellect and compasion were the true global parameters for judgement. Because of this, my confidence on my capabilities never faltered me. I never once doubted my role in science, nor forgotten that science's

[1]The only real voyage consists not in seeking new landscapes, but in having new eyes

goal is to help humanity, not destroy it. I hope that wherever you are, I have made you proud of the life I have led after your departure.

Infine, non posso che esprimere la mia più grande gratitudine nei confronti di chi mi è vicino: la mia famiglia.

Ringrazio Sebastien Parmentier, mio marito e amico dal 2004, che dai momenti più stressanti e sfiancanti fino ai più felici di questo viaggio è stato molto più di un sostegno su cui ho potuto poggiare, e a cui spero di poter offrire, in futuro, lo stesso supporto. Attraverso la sua gentilezza e fede negli esseri umani e la sua salda fede nell'umanità, sono diventata migliore, e ho imparato ad essere orgogliosa delle esperienze della mia vita. *"Le véritable voyage de découverte ne consiste pas à chercher de nouveaux paysages, mais à avoir de nouveaux yeux."*[2]

Ringrazio il mio fratello minore, Günther, con cui ho condiviso tante difficoltà, specialmente dopo che nostro padre se n'è andato. Sono certa che raggiungerà tutti gli obiettivi, una volta che si convincerà di poterlo fare. Crederò sempre in lui, così come lui ha sempre creduto in me, e spero che non abbandoni mai i suoi sogni.

E il piccolo William, come non ringraziarlo… mi ha fatto dimenticare lo stress degli esami del PhD con quelle sue strane danze da scimmietta in cucina (cést vrai!).

E mia madre Rosa con mio padre Edwin. Sarebbe stato bello se avessi potuto passare più tempo con loro…

Infine serbo queste ultime righe per la persona che più ha influenzato la mia vita:

[2] L'unico vero viaggio consiste non nello scoprire nuove terre, ma nell'avere nuovi occhi.

mio padre Edwin Morreale, a cui devo la passione per la fisica, la mia determinazione e sicurezza. Non aveva molte cose materiali da lasciarci, ma ci ha lasciato i suoi insegnamenti. Ci sono obiettivi in questo mondo da raggiungere ben più importanti dei beni materiali: conoscere noi stessi e il luogo in cui viviamo, in un Mondo governato dalle leggi della fisica. Ci ha insegnato che le ”razze” sono una falsa costruzione, e che il genere e il paese di origine non sono ostacoli, ma piuttosto l’intelletto e la compassione sono i veri parametri universali di giudizio. Grazie a ciò, la sicurezza nelle mie capacità non ha mai vacillato. Neanche una volta ho dubitato del mio ruolo nella scienza, nè dimenticato che l’obiettivo finale è quello di aiutare l’umanità e non di distruggerla.

In memoria di mio padre Edwin Morreale.

ABSTRACT OF THE DISSERTATION

Probing the Gluon Contribution to the Proton Spin with Charged Pion Production

by

Astrid Morreale

Doctor of Philosophy, Graduate Program in Physics
University of California, Riverside, August 2009
Dr. Kenneth N. Barish, Chairperson

Spin has been compared to the way the Earth rotates about its axis as it travels around the Sun. While quantum spin is indeed a fundamental property of matter, when it is applied to particles such as protons this does not imply that these particles do rotate about their central axis. The proton is made of quarks and gluons which are themselves spin-1/2$\hbar$ and $\hbar$. Experimental data may not have revealed quarks and gluons directly, yet it is understood that the behavior of gluons, quarks and their orbital angular momentum dictate the gross properties of a proton. Protons as spin-1/2 particles can exist in one of two quantum spin states ($\pm\hbar/2$). Furthermore, the spin 1/2 nature of the proton itself can help explain the structure of matter.

Double-helicity asymmetry (A_{LL}) measurements yield valuable information on gluon contribution in the total spin of the proton:$1/2 = 1/2\Delta\Sigma+\Delta G+L$, where $\Delta\Sigma$ is the con-

tribution due to all quarks and anti-quarks within the proton and L is the orbital angular momentum of the quarks and gluons. At large transverse momenta and at midrapidity, quark-gluon scattering dominates pion production at RHIC energies. $\pi^{\pm}$ then provide a special opportunity for studying processes sensitive to ΔG: the gluon contribution to the proton spin. Preferentially, up quarks fragment into π^{+} and down quarks to π^{-}. This preference leads to the dominance of up-quark gluon, and down-quark gluon contributions in the sum over flavors in a factorized pQCD calculation of pion production.

The work presented here details a study which measures A_{LL} of final state $\pi^{\pm}$ proceeding from polarized proton proton collisions at $\sqrt{s} = 200$GeV at RHIC. Measurement of charged separated differential cross sections proceeding from such collisions is also presented. As will be demonstrated, the measurements are compatible with the underlying theoretical framework (pQCD), and have directly ruled out maximum ΔG scenarios. The measurements presented form part of an international effort to understand how gluons influence and participate in the spin of the proton.

SOMMARIO DELLA TESI

Studio sul Contributo del Gluone allo Spin del Protone Attraverso la Produzione di Pioni Carichi in Collisioni di Protoni Polarizzate.

per

Astrid Morreale

Doctor of Philosophy, Graduate Program in Physics
University of California, Riverside, August 2009
Dr. Kenneth N. Barish, Chairperson

Lo spin è stato messo in relazione al modo in cui la Terra ruota attorno al proprio asse mentre orbita attorno al Sole. Sebbene lo spin quantistico sia in tutto e per tutto una proprietà fondamentale della materia, quando ne applichiamo il concetto a particelle come protoni, ciò non implica una reale rotazione di questi attorno al proprio asse. Il protone è costituito da quark e gluoni, rispettivamente particelle di spin-$1/2$ e 1 in unità di $\hbar$. I dati sperimentali non hanno mai confermato direttamente l'esistenza di quark e gluoni, sebbene sia ormai compreso e accettato che tali costituenti, ed il loro momento angolare orbitale, diano luogo alla quasi totalità delle proprietà manifeste del protone. Il protone, come particella di spin-$1/2$, può esistere solamente in uno dei due stati quan-

tistici di spin ($\pm\hbar/2$). Inoltre, la natura fermionica della particella stessa contribuisce a spiegare la struttura della materia.

Le misure di asimmetria di "doppia elicità" (double-elicity asymmetry, A_{LL}) forniscono importanti informazioni sul contributo dei gluoni allo spin totale del protone: $1/2 = 1/2\Delta\Sigma + \Delta G + L$, dove $\Delta\Sigma$ è il contributo legato alla presenza di tutte le coppie quark-antiquark (quark del mare) contenute nel protone ed L è il momento angolare orbitale dei quark e dei gluoni. Per grandi momenti trasversi e rapidità intermedie, il canale diffusivo quark-gluoni è predominante nella produzione di pioni alle energie di RHIC ($\sqrt{s} = 200$ GeV). La produzione di pioni $\pi^{\pm}$, quindi, diventa importante come studio di un canale preferenziale per l'analisi di ΔG, ovvero il contributo gluonico allo spin del protone. Preferenzialmente, i quark di tipo "up" frammentano in mesoni π^{+}, mentre i quark di tipo "down" in mesoni π^{-}. Questo fatto porta, a livello partonico, ad una dominanza del canale di diffusione quark "up" o "down" su gluoni, in uno schema di calcolo perturbativo.

In questo lavoro viene presentato uno studio dettagliato della misura di A_{LL} in stati finali di mesoni $\pi^{\pm}$, in una configurazione sperimentale di collisioni fra fasci polarizzati di protoni con energia di $\sqrt{s} = 200$ GeV nel centro di massa adronico, a RHIC. Inoltre, la stessa analisi viene presentata a livello di sezione d'urto differenziale per ambedue i tipi di mesone carico. Come verrà dimostrato, le misure sono compatibili con l'apparato teorico noto come QuantoCromoDinamica perturbativa (pQCD), ed escludono per os-

servazione diretta degli scenari fisici in cui ΔG è massimizzato. I risultati di questo lavoro fanno parte di un quadro di lavoro internazionale che ha come obiettivo quello di capire il ruolo ed il contributo dei gluoni in relazione allo spin del protone.

RESÚMEN DE LA DISERTACIÓN

Investigando el Papel que Empeña la Polarización de el Gluón en el Espín Total de el Protón Via la Producción de Piones Cargagos.

por

Astrid Morreale

Doctor of Philosophy, Graduate Program in Physics
University of California, Riverside, August 2009
Dr. Kenneth N. Barish, Chairperson

El espín se ha comparado en ocasiónes con la manera que el planeta gira sobre su propio eje al mismo tiempo que gira alrededor del sol. El espín es una propiedad mecanocuántica fundamental de la materia, pero quando esta propiedad es ejercitada a particulás como el protón o neutrón, no significa que las particulas estan girando sobre un eje. Los protónes son partículas con espín 1/2 que pueded existir en uno de dos posibles estados cuánticos ($\pm\hbar/2$.) El protón está compuesto de quarks y gluónes: particulás sub-atómicas que tambien contienen espín -1/2$\hbar$ y $\hbar$. Experimentalmente no es posible observar directamente los quarks y gluónes, pero se conoce que su comportamiento dentro de el protón incluyendo su momento angular-orbital dicta las propiedades observadas en el proton. Las mediciones experimentales de asimétrias de polarizacion longitudinal

doble (A_{LL}) proporcionan información sobre el papel que los gluones desempeñan en el espín total de el protón: $1/2 = 1/2\Delta\Sigma + \Delta G + L$, donde $\Delta\Sigma$ es la contribución de todos los quarks y anti-quarks y L es el momento orbital angular de los gluónes y los quarks. Para alto momento transverso y pseudo-rapidez central, la dispersión entre quarks y gluons domina la producción de piones a energias de RHIC (colisiónes de iones pesados y relativísticos). En estas condiciones, los piones cargados - $\pi^{\pm}$ ofrecen una oportunidad especial para estudiar processos con sensitividad a ΔG: la contribución gluonica al espín total de el proton. Preferencialmente los quarks-arriba fragmentan a mesones π^{+} y quarks-abajo a mesones π^{-}, fenómeno que conduce a la dominación de las contribuciones de quarks "arriba" o "abajo" y gluones en la producción de piones, según se calcula sobre la suma de sabores en la teoría factorizada perturbativa de QCD (CuántoCromoDinámica).

En el presente trabajo se detalla un estudo de medidas A_{LL} de $\pi^{\pm}$, provenientes directamente de collisiones entre protones polarizados a $\sqrt{s} = 200$GeV en el RHIC. También se presentan medidas de secciónes eficaces diferenciales de piones cargados procedientes de estas colisiones. El análisis demostrará que las medidas son compatibles con la teoriá pQCD, obteniéndose la discriminación directa de valores máximos de ΔG. Las medidas presentadas en esta disertación forman parte de un esfuerzo internacional en entender cómo los gluónes influyen y participan en el espín total de el protón.

RÉSUMÉ DE LA THÈSE

Etude sur Le Rôle de la Polarisation des Gluons dans le Spin Total du Proton Par la Production de Pions Chargés.

par

Astrid Morreale

Doctor of Philosophy, Graduate Program in Physics
University of California, Riverside, August 2009
Dr. Kenneth N. Barish, Chairperson

Spin est souvent comparé avec la maniére dont nôtre planéte tourne sur elle-même, lorsque cette propriété est exercé à par des particules comme le proton ou le neutron. Celà ne signifie pas en aucune façon que les particules tournent sur un elle-mêmes. Les protons sont des partcules dotées d'une propriété spin 1/2, qui peuvent cependant exister dans deux formes d' éats quantiques ($\pm\hbar/2$.). Le proton est composé de quarks et gluons. Ces derniers sont des particules sub-atomiques qui contiennent aussi des spins -1/2$\hbar$ et $\hbar$. Expérimentalement, il n'est pas possible d'observer directement ces particules. Pourtant nous savons fort aujourd'hui que le comportement de ces particules au sein même du proton, en incluant son impulsion angulaire orbitale, dicte les propriétés observées dans le proton.

Les mesurements des asymétries d'hélicité á double longitudinalité offrent beaucoup d'informations de trè hautes valeurs sur le rôle joué par les gluons dans le spin du proton: $1/2 = 1/2\Delta\Sigma + \Delta G + L$, où $\Delta\Sigma$ dénote la contribution de tous les quarks et les anti-quarks. L dénote l'impulsion orbitale angulaire des gluons et des quarks. Au sein d'une grande impulsion transversale et d'une pseudo-rapiditié centrale, la production de pions sous les énergies employé à RHIC (collisions d'ions lourds et relativistic) est fortement dominée par une dispersion entre les quarks et les gluons. Cette dispersion permet alors d'étudier de près les réactions en oeuvre au coeur des pions avec une sensitivité á ΔG: ou la contribution gluonic dans le spin total du proton.

Une fragmentation préférentielle vers quarks-up á π^+ ainsi que quarks-down á π^- conduit à une domination des quarks (up, down) et des gluons dans la production de pions. Cette domination est ainsi calculée simplement par l'obtention d'une somme des saveurs, suivant la teorié factorizée de pQCD.

Ce travail présente les mesurements obtenus des A_{LL} de $\pi^{\pm}$ détectés sous leur état final et des piones provenant de collisions entre les protons polarisés á $\sqrt{s} = 200$GeV en RHIC. Les mesurements de sections efficaces des pions chargés issus de ces collisiones sont aussi présentés. L'analyse démontre que les résultats de ces mesurements sont tout à fait compatibles avec les calculs theoriques de pQCD. De plus, ces résultats permettent l' éliminé des valeurs maximales en ΔG. Les mesures présentées dans cette dissertation font parties d'un effort international de recherche sur l'influence que pourraient avoir les

gluons dans le spin total du proton.

Contents

List of Tables

List of Figures

Chapter 1

Introduction

Our curiosity and desire to predict natural phenomena to benefit us, both physically and intellectually, has led us to investigate what are the fundamental physics laws that govern our surroundings — including the matter we ourselves are made of. It appears that human curiosity has thankfully persisted since the first humans began using scientific methods to explain the natural phenomena surrounding them. As a child my father used to tell me that the first scientists must have been the first hominids who studied the cause and effect of rubbing two stones. We have come a long way since domesticating fire through our understanding of friction however; we are merely continuing the work of our scientific predecessors. Spin physics research may seem just a pure intellectual quest to satisfy answers to the proton's spin puzzle. Spin measurements, however, have laid the groundwork to a plethora of scientific advancements, from the medical field, to astronomy research, which have brought impact to the link between science and

technology. The 3-dimensional imaging of the human's interior-for identification and treatment of malignous tumors - for example - is a now a robust field that has directly benefited from quantum spin physics research. Other examples where quantum spin has contributed, are dark matter searches in astronomy, as well as the blooming field of semi conductor spintronics, where electronics are taken down to the quantum level for development of new technologies for data storing at ultra high densities. Investing in the theoretical work and experiments which aim at probing matter at the femto-scale, is thus a worthwhile endevour which society as a whole can benefit from for years to come.

Chapter 2

Probing Inside Matter

There exists today more than one hundred chemical elements in nature, all neatly classified in Mendeleev's table of elements. Mendeleev's original table was created before the discovery of subatomic structure of matter. Yet before the formulation of quantum mechanics elements were already listed in order of increasing atomic number. Experiments in 1918 done by Ernest Rutherford had determined that when α particles were shot into nitrogen gas, signatures of hydrogen nuclei could be observed. Rutherford proposed that the hydrogen nuclei were elementary particles. This led to the discovery of the proton. The discovery of the neutron followed that of the proton some decades later when James Chadwick made several experiments trying to understand[1] the gamma theory of the strong radiation which was observed by Bothe and Becker[2] (when very energetic al-

[1] or rather disprove.

[2] and detailed later by I. Joliot-Curie and her husband F.Joliot-Curie.

pha particles emitted from polonium fell on certain light elements). Nowadays, it is well established that an atom is made up of protons and neutrons. Nucleons (the collective name for protons and neutrons) also have structure. They are composed of quarks and gluons whose interactions, as well the interactions of other fundamental particles, have helped us understand matter at its most fundamental level. There are four types of forces distinguishable in nature: **gravitation** (which becomes relevant in densely aggregated matter), **electromagnetism**, the **weak** force, and the **strong** force. The strong interaction will be the main focus in this work. The strong force has charge– the strong color charge, with 3 charges and eight carriers.

2.1 Strong Interactions

In nature, the strong force holds atomic nuclei together despite strong electrostatic repulsion. It is a force that dominates the nucleons, and one that is responsible for strong binding of the quarks and gluons (called **partons** collectively) in order to form the proton and the neutron. However, as experiments in the late 1960s have shown, the distance at which this force is exerted is quite small – about one Fermi (10^{-15} meters). Data from deep inelastic scattering (DIS) of electrons on protons have indicated that, after being hit by an energetic electron, one of the quarks from the proton propagates freely appearing to barely interact with the other quarks[34]. One can probe QFT at short distances by changing the wavelength or the momentum of the probe used. As the probe being used

becomes shorter and shorter, one can observe virtual particles taking part in the reaction, thus violating conservation of energy. Heinsenberg's uncertainty relation, at the heart of quantum mechanics ($\Delta E \Delta t \geq \hbar$), allows for this apparent violation of conservation of energy. These apparent violations can be described by virtual particles going off the mass shell. This process renormalizes the coupling constant *g* (the strength of the interaction) and makes the coupling depend on the energy scale, μ. The dependence of a coupling g(μ) on the energy-scale is known as the running of the coupling. One can typically replace the strong coupling given by:

$$\alpha_s \equiv \frac{g^2}{a\pi} \tag{2.1}$$

by the effective, *running coupling*: $\alpha_s(Q^2)$, where Q^2 is the momentum transfer. The renormalization equation which describes the running of the coupling constant (the β function) is given by:

$$\beta(g) = \mu \frac{\partial g}{\partial \mu} = \frac{\partial g}{\partial \ln \mu} \tag{2.2}$$

One can then try to increase the energy scale μ in order to probe and observe the way the coupling constant flows. If this relation is negative, as it is the case in quantum chromodynamics (QCD), it implies that the coupling is running towards zero. Once the coupling reaches this point, it stays in equilibrium. Within the data observed in the DIS experiments, this means that the QCD coupling decreased at high energies as

the strength of the interaction became increasingly weaker toward higher energy scales. QCD is the theory used to describe the strong interactions: the interaction of mass-less spin - $\frac{1}{2}$ objects which possess color as an internal degree of freedom. The set of mass-less gauge bosons called gluons mediate the force between the quarks in a similar way in which photons mediate the force in quantum electro dynamics (QED). Gluons, unlike photons however, also carry strong color charge (Figure 2.1).

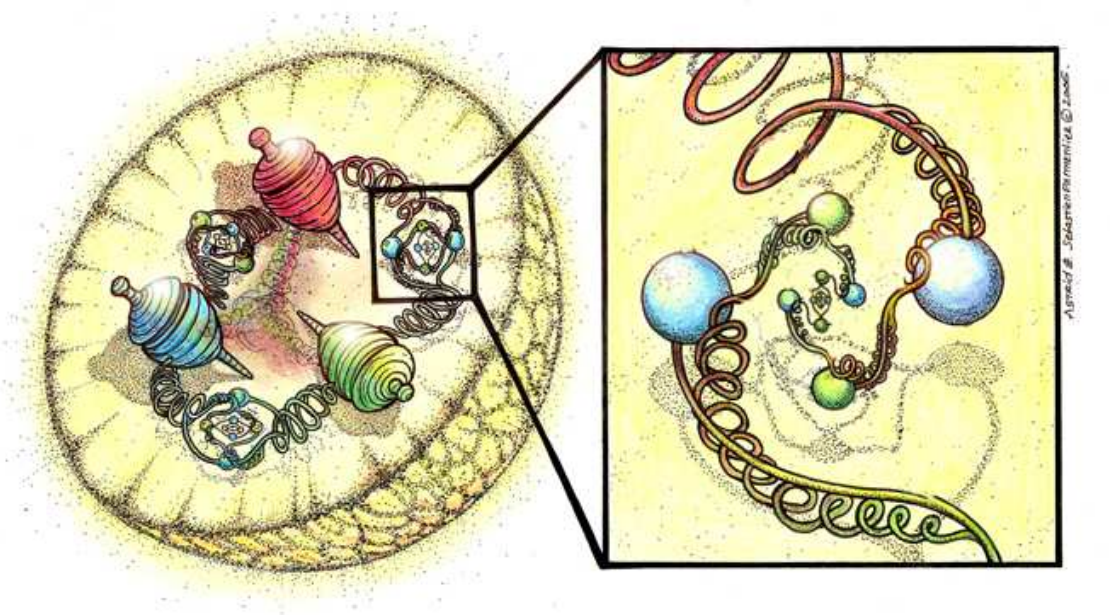

Figure 2.1: An artistic depiction of the QCD picture of the proton's structure.

2.1.1 Asymptotic Freedom and Confinement

When partons undergo hard collisions[3], the coupling - the strength of the interaction - becomes weak, and partons appear to be free. This property is called *asymptotic freedom*.

[3]Direct scattering.

Asymptotic freedom is a property sprung from the coupling constant running towards zero in the large momentum limit (known also as the "ultraviolet" limit). A consequence of asymptotic freedom is that in a short distance, a hard (large momentum transfer) interaction may be calculated in terms of a series expansion in powers of the coupling (α_s). In other words, perturbative methods can be used to tackle certain problems. It is assumed that the QCD Lagrangian has no quark masses. This would make QCD symmetric both in flavor and chirality. Quarks are not allowed to exist as free particles; their masses are simply another parameter in the Lagrangian which can be determined by experiment. When one uses perturbative methods, the quark propagator has a pole at $m^2 = p^2$. This pole is assumed not to exist in an *exact theory*. Perturbative methods are only considered reliable where momentum transfers are large in comparison with m. For the work presented here, it will be shown that a large momentum transfer reaction ($pp \longrightarrow \pi^{\pm} X$), which can be described by perturbative QCD, has been observed. However, if on the other hand, the interaction occurs at a long distance, then the coupling constant will be too strong and perturbative methods cannot be used to account for the quark and gluon interactions of the QCD Lagrangian. Instead, theories such as lattice gauge must be employed[28][25] . Gauge invariant interactions can be described by the following Lagrangian:

$$\mathcal{L} \;=\; -\frac{1}{4} G^{a}_{\mu\nu} G^{a\mu\nu} + i\bar{\psi}_{i\gamma\mu}(D^{\mu})_{ij}\psi_{j}$$

$$(D^{\mu})_{ij} \quad = \quad \partial_{\mu}\delta_{bc} - gA^{a}_{\mu}f_{abc} \tag{2.3}$$

where $G^{a}_{\mu\nu}$ is the generalized field tensor. The co-variant derivative operator D^{μ}_{ij} acts on the quark fields, where A^{a}_{μ} are eight vector fields (gluons). The co-variant operator also holds the bare coupling constant g, where f_{abc} are the structure constants and a, b and c are the color indices. ψ and $\bar{\psi}$ are the quark spinor fields indexed by quark color. The second term in Equation 2.3 represents a sum, where mass-less quarks are assumed to be of identical terms, one for each flavor and are summed over [4]. A contradictory behavior of partons is that, while they may act "free" when they are hit hard, quarks cannot be produced as free particles under ordinary conditions. Rather, they seem to exist as bound combinations of three quarks and three anti-quarks – also called *quark-antiquark pairs*. Quarks are elementary particles, but they can only be studied within the confinement of composite particles. Confinement of partons indicates that it would take an infinite amount of energy to separate two quarks[5]. In the early stages of hadron structure studies, quarks seemed to defy Pauli's exclusion principle as their wave function did not come to be anti-symmetric under the interchange of a quark. This apparent contradiction was solved when it was postulated and later verified experimentally that quarks carry color. Color is a quantum number that couples to a vector field whose quanta are the field of gluons which also carry color. For any quark flavor (up, down, strange, charm, bottom

[4]To determine current quark masses then one must resort to perturbative methods such as QCD sum rules etc

[5]Confinement is also referred to as *infrared slavery*.

and top), a quark can exist as any of three colors (red, green and blue) and gluons can exist in eight. Quarks behave like confined point-like objects: asymptotic freedom fits perfectly with the result that partons[6] carry color. The increase of the coupling at large distance and the direct color coupling to which this is related confine the chromo field. The color field will freely penetrate the vacuum only up to a distance of about one femtometer from a color source. When two color quarks are pulled apart, the color field between the two charges does not spread through space the way an electric field between two charges would. In nature, real physical objects are colorless – a consequence of asymptotic freedom and confinement. Given a collision where a quark or a gluon undergoes hard (elastic) collisions where one of the partons shoots out sideways, as the color charges separate, the flux tube will stretch and the energy stored in the field will increase at the expense of the kinetic energy of the parton. This flux tube will stretch even more, until its energy will exceed the mass of the lightest hadrons. The energy then materializes (or $hadronize$) and one will obtain a copious number of pions and other hadrons with each hadron carrying a fraction of the original momentum of the quark or gluon. In the present work, it is hoped that each produced pion carries information about the polarized gluon which took part in the initial hard scattering.

[6]Partons being quarks and gluons.

2.2 Polarized Deep Inelastic Scattering

One cannot begin a discussion about nucleon structure studies - using proton-proton collisions - without reviewing the work, variables (Table 2.1) and definitions inherited from *Deep inelastic scattering experiments* (DIS). These experiments have played a crucial role in our understanding of nucleon structure. They mark the birth of modern high energy physics. The present work utilizes some of the variables and measurements inherited from these experiments. It was their early results in the 1960's and the discovery of Björken scaling that led to the parton model. They determined the sub-atomic structure found within nucleons. DIS experiments led to the idea of quarks being a fundamental point like particles into which currents couple. For example, let us consider the reaction $l + N \longrightarrow l^{'} + X$, where $l(l^{'})$ would be an incoming (outgoing) lepton, and N would be a target nucleon. This reaction is illustrated by the Figure 2.2 showing the exchange of a virtual photon (γ) between the lepton and the target. A solid red circle represents the internal structure of the proton - which can be expressed in terms of *structure functions* (Equation 2.3.) In inclusive DIS processes (semi-inclusive processes)[7], the outgoing lepton with momentum *k* is identified, while all over possible final state hadrons X are integrated over. Unpolarized DIS probed the number density of partons (Section 2.1) with a fraction x of the momentum of the parent nucleon.

[7] A semi-inclusive process is one where the hadron is detected in coincidence with the outgoing lepton.

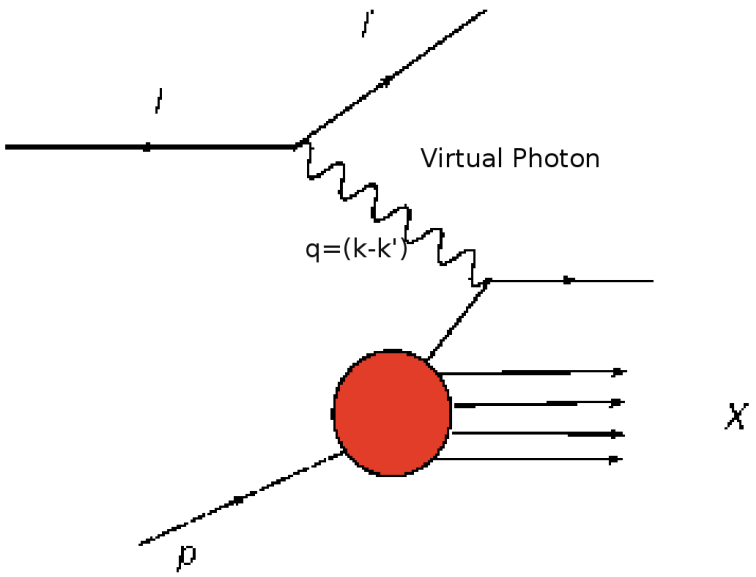

Figure 2.2: Kinematic quantities for Deep Inelastic Scattering where an electron and a parton constituent of the nucleon exchange a γ, $W^{\pm}$ or Z. l and l' are the four momentum of the incoming and outgoing leptons, *p* is the four-momentum of a nucleon and *X* is the recoiling system; the exchanged particle transfers four-momentum *q* to the nucleon.

Polarized deep inelastic scattering involves the collision of a polarized lepton beam on a transversely or longitudinally polarized target. Complementary to the unpolarized case, it has given information about the number density of partons (Section 2.1) with a given momentum fraction x and given spin polarization in a nucleon of a known polarization.

2.3 pQCD-Form Factors and Structure Functions

Before the proton spin structure is discussed, there are several elements within the nucleon structure that paved the preliminary insights of strongly interacting matter. Form factors (FF) are fundamental dynamical quantities that describe the inner properties of a composite particle. They can provide detailed information about the spatial distribu-

$Q^2 \equiv -q^2 = 2(EE' - k \cdot k' - m_l^2 - m_{l'}^2)$	Momentum transfer of lepton or hardness, $m_l^2(m_{l'}^2)$ is the initial(final) lepton mass.
$\simeq 4EE' sin^2 \frac{\theta^2}{2}$	If $EE' sin^2(\theta/2 >> m_l^2, m_{l'}^2$, then: θ is the lepton scattering angle w.r.t. the lepton beam direction.
$\nu = \frac{p \cdot q}{M}; \nu = (E - E')$	Lepton's energy losses in the nucleon rest frame.
$x = \frac{Q^2}{2M\nu}$	Björken scaling variable, x gives the fraction of the nucleon's momentum, carried by the struck quark.
$p_T = \frac{\|\vec{p_h} \times \vec{q}\|}{\|\vec{q}\|}$	Transverse momentum of hadron-h.
$p_\parallel = \frac{\|p_h \times \vec{q}\|}{\|q\|}$	longitudinal momentum of hadron-h.
μ	Energy scale of the reaction.
$y = \frac{1}{2}(\frac{E+p_L}{E-p_L})$	Rapidity. p_L is the component of the momentum along the beam direction.
$s = (k+p) = \frac{Q^2}{xy} + M^2 + m_l^2$	center of mass (cms) energy of the lepton-N system.

Table 2.1: Invariant quantities in deep inelastic variables and definitions, these variables will also be relevant to proton proton collisions.

tion of charges and currents within the proton (and neutron). They can be illustrated by Fourier transforms emerging naturally from the scattering of a charge distribution which undergoes a magnetic interaction with the nucleon due to its magnetic moment. For spin - $\frac{1}{2}$ particles with no inner structure, also coined *Dirac particles*, the magnetic moment is expected to be: $\mu_{moment} = \frac{g}{2}\frac{e}{2m_i}$, where g = 2 from the Dirac Equation and m_i is the mass of particle i. However, due to the inner structure of the proton, the magnetic moment was found to be anomalous: $g \neq 2$. FF are directly accessible from experiment through the measurement of differential cross-section and polarization ob-

servables. Additionally, they emerge naturally in nucleon models as they enter explicitly in to expression of the hadronic current. Considering the nucleon to consist entirely of its valence quarks confined independently in a scalar-vector harmonic potential, the unpolarized structure functions $F_1(x, \mu^2)$ and $F_2(x, \mu^2)$ were derived in the Björken limit (in which $Q^2 \longrightarrow \infty$ and the momentum fraction x is a fixed constant between 0 and 1) under certain simplifying assumptions generalizing the framework of pQCD.

2.3.1 Factorization

While QCD is a well established theory of strong interactions, it is not exactly solvable. This implies that there are components that cannot be calculated by perturbative methods. As a result, the theory relies on experimental data in order to make predictions in the likelihood of a given process occurring in a collision. For example, the polarized and unpolarized likelihood for pions to be produced in proton proton collisions has three components in its calculation – from which, only one component is fully calculable:

- The partonic cross-section (calculable).
- Quark and gluon distribution functions (which have to be extracted from deep inelastic scattering).
- Fragmentation functions (which are extracted from from e^+e^- collisions, Semi Inclusive DIS processes and (proton - proton) p+p collisions).

This splitting of an unsolvable problem into a tractable part and a part which cannot be calculable in theory is referred to as *factorization*. Mathematically, for π production in $p+p$, factorization can be written as,

$$\begin{aligned} d\Delta\sigma &= \sum_{a,b,c} \int dx_a \int dx_b \int dz_c \; \Delta f_a(x_a, \mu_F)\, \Delta f_b(x_b, \mu_F) D_c^{\pi}(z_c, \mu'_F) \\ &\quad \times d\Delta\hat{\sigma}_{ab}^{c}(x_a P_A, x_b P_B, P_\pi/z_c, \mu_R, \mu_F, \mu'_F). \end{aligned} \tag{2.4}$$

The term which precedes $\times$ denotes the incalculable objects that must be measured: $f_{a,b}$ refers to the parton density functions (PDFs). D_c^{π} refers to the probability of finding a parton (c) that will fragment into a π. The term following $\times$ represents the fully calculable part: $\hat{\sigma}_{ab}^{c}$, or the hard scattering cross-section or the process likelihood of the partonic channel $a+b \rightarrow c+X$. (The Δ in front of $f_{a,b}$ and $\hat{\sigma}_{ab}^{c}$ refers to the difference in parton helicity and Σ is the sum over all possible quarks and gluons.) One key factor of the factorization conjecture is that the parton distribution functions and fragmentation functions are treated as universal. Tests of this universality are fundamental for validating the QCD framework.

2.3.2 Universality

QCD's asymptotic and confinement features make it attractive in the understanding of strong interactions. QCD also has another relevant feature, universality. Universality denotes the observation that there are properties for a large class of systems that are independent of the dynamical details of the system. This means that within QCD calculations, PDFs (parton density functions) are independent of the hard scattering process, allowing the transition from hadronic to partonic beams and targets (DIS to p+p). Once parton distributions are determined from DIS, they yield a large set of predictions.

2.3.3 QCD Evolution

QCD evolution is essential in order to switch the measured parton densities from one momentum transfer scale Q to a different one. NLO calculations (perturbative expansions in terms of the coupling constant) of partonic cross-sections are needed in order to correctly specify the scale – and in general the definition – of the parton densities, as well as the running coupling in the leading term. When one computes corrections at the large Q^2 limit, collinear divergences appear through $\log(Q^2/\mu^2)$ corrections[31]. These logarithmic divergences are known as scaling violations. Such violations imply that PDFs within the proton can become Q^2 dependent. Re-summation in the pQCD framework of these divergences leads to PDF Q^2 evolution Equations. These Equations are called DGLAP[6][23][12] after their founders: Grivov-Lipatove, Altarelli-Parisi, and

Dokshitzer. Observation of scaling violations in experimental data is considered to be a precision test of pQCD.

2.4 Spin and Helicity States

Spin is an intrinsic property of all particles and nuclei. This occurs only within multiples of a basic quantum mechanical unit. In classical mechanics, a rigid object can have two kinds of angular momentum; both of which are associated with motion:

1. Orbital angular momentum, associated with the motion about the center **of** mass ($L = r \times p$).

2. Spin associated with the angular momentum of an object **about** its center of mass.

The motion of the Earth is a classical illustration of this phenomena. One full rotation of the Earth around the sun gives rise to its orbital angular momentum L, while its daily rotation would give rise to its spin (S) angular momentum. However classically this definition of S is in fact a mere matter of convenience. Classical spin in this example is nothing more than the sum of the orbital angular momenta of all the matter that makes up our planet as they circle around the Earth's axis [24]. In quantum mechanics, something analogous occurs where orbital angular momentum arises from the motion of the electron around the hydrogen atom. However, another form of angular momentum also exists. Nevertheless the name (**spin**) is highly misleading. This quantum mechanical

property coined as such has nothing to do with the motion of particles in space about some axis. Spin is indeed an angular momentum with direction and magnitude. However, unlike the classical angular momentum, only one of the vector components can be specified with arbitrary accuracy at any single time. Particles can only be in a state of "up-ness" or "down-ness". This derives from the Heisenberg uncertainty principle. The basic spin operator vector: $\hat{S} = (\hat{S}_x, \hat{S}_y, \hat{S}_z)$, has as its components the spin projector operators. These do not commute:

$$\begin{aligned} [\hat{S}_x, \hat{S}_y] &= i\hbar\hat{S}_z, [\hat{S}_y, \hat{S}_z] = i\hbar\hat{S}_x \\ [\hat{S}_z, \hat{S}_x] &= i\hbar\hat{S}_y \end{aligned} \tag{2.5}$$

Because of these properties, they cannot have common eigenstates and thus one cannot exactly specify the spin angular momentum vector of a particle at any time. The squared spin operator $\hat{S^2}$ does commute with any of the projection operators we are interested in; for example, $\hat{S}_z$, where z is defined along a magnetic field direction, a particularly important direction in space. Nevertheless, modeling an electron as a spinning classic sphere can help remove the analogy of quantum spin with moving bodies:

A calculation can thus be made to estimate how fast would the equator of the spinning electron sphere would have to move, assuming it has the known electron half integer spin $\frac{1}{2}\hbar$ obtained in a Stern-Gerlach type experiment. Assuming the classical electron

radius of *r*, relating $L = I\omega$ and angular velocity ω to linear velocity (*v*) and *c* the speed of light one can trivially find the following:

$$\begin{aligned} r &= \frac{e^2}{4\pi\epsilon_o mc^2} \\ \omega &= \frac{L}{I} \\ \omega &= \frac{\frac{\hbar}{2}}{\frac{2}{5}mr^2} \\ &= 1.8 * 10^{25} s^{-1} \\ &= \frac{v}{r} \\ v &= (1.8x10^{25} s^{-1})(2.8x10^{-15} m) = 171 * c \end{aligned} \tag{2.6}$$

It is evident from the non-sensible solution of an sphere spinning at a velocity of 170 times the speed of light, that spin cannot be decomposed in terms of orbital motion of constituent parts, nor can it be described as a function of position variables. Quantum spin is thus an inherent property of particles that cannot be altered; a property as fundamental as mass or electric charge. The difference between Fermions - particles that, like the electron, have half-integer spins $\frac{1}{2}\hbar$ – and Bosons – particles with integer spins – has particular significance. Fermions obey the Pauli exclusion principle, which states that two identical fermions cannot exist in the same state. We are now aware that without the Pauli exclusion principle, chemistry would have no periodic table. Bosons on the other hand, tend to congregate in the same state, leading to the phenomena such as

superconductivity and Bose-Einstein condensation. Spin $\frac{1}{2}$ is one of the most important concepts in explaining the electronic structure of atoms and nuclear matter interactions. We would probably not exist if electrons and protons were to have different spin quantum number. Spin does serve as a model for other notions that do not have simple classical analogies, even the more abstract ones. For instance, isotopic spin is employed to illustrate the two states of a 'nucleon': the proton and neutron. Similarly, quarks are paired as isospin 'up' and 'down', which are the names given to the two quarks that make up ordinary matter[8]. The rotational symmetry of space and time is generalized to include symmetries in more abstract 'inner' dimensions, with the result that much of the complex structure of the micro-world can be seen as resulting from symmetry breaking. This connects profoundly with the ideas describing the spontaneous formation of structure in the macro-world.

2.5 Spin in Quantum Chromodynamics

QCD has a well defined spin structure. Therefore, the studies of spin-dependent reactions provide excellent ways to probe the aspects of the theory not yet understood. In large momentum transfers, a proton is visualized as a composite of point like particles - quarks and gluons. Quarks have the same quantum numbers as the quarks in the

[8]Pions also compose an isospin triplet, which accounts for the 3 types of pions found in nature π^+, π^0, π^-.

constituent quarks model.[9], however their masses can be quite different. Gluons (the mediators of the strong force) are mass-less. In the original parton model which has been compared to the experimental data that led to the proton spin crisis[1], the unpolarized structure functions F_1 and F_2 were written as in Equation 2.7, while the polarized structure functions were defined as $g_1(x)$ and $g_2(x)$:

$$F_1 = \frac{1}{2x}F_2(x) = \frac{1}{2}\sum_q e_q^2(q(x) + \bar{q}(x)) \tag{2.7}$$

where *e* is the charge of the struck quark $q(x)$ carrying momentum fraction x from the proton. The polarized structure function $g_1(x)$ could then be defined as:

$$g_1(x) = \frac{4}{9}\Delta u + \frac{4}{9}\Delta\bar{u} + \frac{1}{9}\Delta d + \frac{1}{9}\Delta\bar{d} + \frac{1}{9}\Delta s + \frac{1}{9}\Delta\bar{s} \tag{2.8}$$

where Δu is the short hand notation for the difference between up quark distributions for quark spins with helicity aligned $(+)$ or anti aligned$(-)$ to that of the original proton. The other terms represent the down, anti down, strange and anti strange quarks which are also labeled collectively as $\Delta q(x)$ and $\Delta\bar{q}(x)$. The integral of $q(x) + \bar{q}(x)$ over all momentum fraction x is the fraction of the proton spin in the parton model. This led to the naive expectation that the spin-1/2 of the proton was to be equal to the sums of the

[9]Where the low energy properties of the proton are explained by three quarks sharing about $\frac{1}{3}$ each of the proton's mass. This corresponds to the ground state of a three particle system, into which the three quarks are in s-states with zero orbital angular momentum and gluonic degrees of freedom have no role.

spins of the valence quarks (q_i) or:

$$\int_0^1 g_1^p(x)dx = \frac{1}{2}(\frac{4}{9}\Delta u + \frac{1}{9}\Delta d + \frac{1}{9}\Delta s) \quad (2.9)$$

The first moment of $g_1^p(x)$ was then related to the quantity Γ_1^p, where:

$$\begin{aligned} \Gamma_1^p &= dx g_1^p(x, Q^2) \\ &= \frac{1}{2}_i e_i^2 \Delta q_i (Q^2(1 - \frac{\alpha_s(Q^2)}{\pi} + O(\alpha_s^2))) \end{aligned} \quad (2.10)$$

Two parameters became relevant for the studies of the proton spin, Γ_1^p and $\Delta\Sigma$ (Equation 2.11).

$$\begin{aligned} \Delta q_i(x) &= q_+(x) - q_-(x) \\ q_i(x) &= q_+(x) + q_-(x) \\ \Delta\Sigma &= (\Delta q_i(x) + \Delta\bar{q}_i(x)) \end{aligned} \quad (2.11)$$

These two parameters gave the following predictions for the $\Delta q_i(x)$, where Δu, Δd and Δs refer to the density of a parton q of type i (u, d, s) with helicity aligned or anti-aligned to the helicity of the proton.

$$\Delta u = \frac{4}{3}$$

$$\begin{aligned} \Delta d &= -\frac{1}{3} \\ \Delta s &= 0 \end{aligned} \tag{2.12}$$

These definitions lead to an asymmetry measurement (A^p) that related the expectation of valence quark contribution (Σ_1^p) to the proton spin (where a_o is the first moment):

$$\begin{aligned} \Sigma_1^p &= 0.28 \\ a_o &= \Delta\Sigma = 1(A^p(x, Q^2)) \end{aligned} \tag{2.13}$$

The actual measurements from EMC[10], and later confirmed by many other experiments, gave a different picture, provoking the "spin crisis".

$$\begin{aligned} \Delta u &= 0.782 \pm 0.032 \pm 0.046 \\ \Delta d &= -0.471 \pm 0.032 \pm 0.046 \\ \Delta s &= -0.190 \pm 0.032 \pm 0.046 \end{aligned} \tag{2.14}$$

These results led to a modification of the nucleon spin rule (central to this work), by incorporating the gluonic contribution to the first moment of g_1 ($a_0(Q^2)$). The gluonic

[10] European Muon Collaboration.

contribution: a_0^{g11} leads to a revised first moment : $a_o(Q^2) = \Delta\Sigma - \frac{3\alpha_s(Q^2)}{2\pi}\Delta G(Q^2)$. The term $\Delta G(Q^2) = \int \Delta G(x, Q^2)dx$ is the gluon analog of Δq_i and is also the motivation for the measurements presented in this work. The QCD picture of the nucleon spin can then be summarized with the longitudinal spin sum rule in the infinite momentum frame.

The proton spin-1/2 $\hbar$ is equal to the angular momentum L due to the quarks and gluons, to $\Delta\Sigma$ –the contribution due to quarks and anti quarks– and ΔG, the polarized gluon contribution:

$$\frac{1}{2} = \frac{1}{2}\Delta\Sigma + \Delta G + L \tag{2.15}$$

2.6 Unpolarized Cross Section

In the scattering of two point like particles, a differential cross-section is defined by the probability to observe a scattered particle in a given quantum state per solid angle unit - such as within a given cone of observation. Similarly, for an integrated cross-section, this scattering is proportional to the probability that an interaction will occur. Therefore, a cross-section can be defined as a measure of the effective surface area seen by interacting particles, and thus is naturally expressed in units of area, millibarn (mb). These are also the units used in the measurements of this work. In a factorized (Section 2.3.1) framework, a cross-section can be defined as:

[11] For an better explanation of how from the Equations of motion, gluons emerge coupling to the axial current see[28].

$$d\sigma = \sum_{a,b,c} \int dx_a \int dx_b \int dz_c \; f_a(x_a, \mu_F)\, f_b(x_b, \mu_F) D_c^{\pi}(z_c, \mu'_F) \qquad (2.16)$$

In a more practical way, a differential cross-section can be defined as well by its Lorentz invariant form, or its experimental form (Formula 5.3). The latter will be used and explained in more detailed in Section 5.1.

$$\begin{aligned} E\frac{d^3\sigma}{d\vec{p}^3} &= \frac{d^3\sigma}{p_T d\eta dp_T d\phi} = \frac{1}{2\pi p_T}\frac{d^2\sigma}{dp_T d\eta} \qquad \text{Lorentz invariant form} \\ E\frac{d^3\sigma}{dp^3} &= \frac{1}{2\pi p_T}\frac{N_{\pi^{\pm}}(p_T)}{\int L dt\, \epsilon_{reco}\epsilon_{geo}\epsilon_{bias}\Delta p_T \Delta\eta} \; \text{Experimental definition} \end{aligned} \qquad (2.17)$$

Unpolarized particle production measurements from RHIC are an important aspect of a high energy program. These measurements can add new significant results from other accelerators at different energies. The resulting data can help to verify applicable theoretical models. In addition, cross-sections can help constrain fragmentation functions (FF) which until now have been dominated by e^+e^- scattering data. The asymmetries in this work are compared to NLO pQCD models. Complementary cross-sections are measured and compared to unpolarized pQCD expectations using up to date charged separated charged pion fragmentation functions. The purpose of a cross-section is to verify that the unpolarized parton distributions functions, used in the measurements of

A_{LL}, as well as the fragmentation functions, can suitably explain the obtained data.

2.7 Longitudinal spin asymmetries

Measurements sensitive to the gluon's polarized density function ΔG can be performed by looking at cross-sections of final state inclusive identified particles. These, as mentioned in Section 2.3.1, contain three ingredients: the parton distribution functions $f_{q,g}(\Delta f_{q,g})$, the fragmentation functions (for charged pions in this case) $D_{\pi^{\pm}}$, and the hard scattering cross-section $\hat{\sigma}(\Delta\hat{\sigma})$. In practice, what is measured are asymmetries of identified particles (pions) in bins of measured transverse momentum p_T. Asymmetries are the ratio of the polarized to unpolarized cross-sections (Equation 6.2). Asymmetries offer an elegant way of accessing parton information by counting observed particle yields in different helicity states of incident protons ($++, --$ versus $+-, -+$). These are normalized by the polarization in each beam ($P_{B,Y}$), and also account for the relative luminosity (L)[12]

$$A_{LL} = \frac{\sum_{a,b,c=\mathrm{q},\bar{\mathrm{q}},\mathrm{g}} \Delta f_a \otimes \Delta f_b \otimes \Delta\hat{\sigma} \otimes D_{h/c}}{\sum_{a,b,c=\mathrm{q},\bar{\mathrm{q}},\mathrm{g}} f_a \otimes f_b \otimes \hat{\sigma} \otimes D_{h/c}} = \frac{\sigma_{++} - \sigma_{+-}}{\sigma_{++} + \sigma_{+-}},$$
$$A_{LL} = \frac{1}{P_B P_Y} \frac{N^{++} - RN^{+-}}{N^{++} + RN^{+-}}, \qquad R = \frac{L_{++}}{L_{+-}}. \tag{2.18}$$

[12]Luminosity is the number of particles per unit area per unit time times the opacity of the target, usually expressed in either the *cgs* units $cm^{-2}s^{-1}$ or $b^{-1}s^{-1}$. The integrated luminosity is computed by integrating the luminosity with respect to time. The luminosity is an important value to determine the performance of an accelerator. For an intersecting storage ring collider: $L = fn\frac{N_1 N_2}{A}$. Where f is the revolution frequency, n is the number of bunches in one beam in the storage ring, N is the number of particles in each beam and A is the cross-section of the beam.

Measuring A_{LL} in certain final states is a valuable tool to access polarized gluon distribution functions inside the proton. The most accurate way to proceed is to study those processes that can be calculated within the framework of pQCD.

2.8 Polarized Proton Proton Collisions

Polarized proton-proton collisions provide a unique environment for hard scattering between gluons and quarks, complementary to deep inelastic scattering. Polarized proton-proton collisions can directly probe the polarized gluon and anti-quark distributions as the collision couples the color charges of the participants. Polarized proton-proton collisions differ from DIS experiments as the momentum fraction *x* carried by a parton in a proton is not directly related to the hard scale in the interaction (p_T). Distributions of *x* that correspond to specific p_T bins are used instead in pQCD theoretical calculations. Therefore asymmetries are nominally measured with respect to the transverse momentum of the identified particle and used as input into global QCD analyses.

2.9 π Meson

The pion is the most commonly observed meson and hadron and can be found in any of the three – plus, minus, and neutral– charged states. Virtual pions also exist in nature

and are very important in understanding the nuclear structure. Pions have zero spin and are composed of first generation quarks. They are pseudo-scalars under a parity transformation. Pion currents couple to the axial vector current. Production of pions proceed from g-g and q-g initiated sub-processes in proton-proton collisions. Pions, as an isospin triplet, make asymmetry measurements from all three pion species particularly sensitive to the sign of ΔG in the transverse momentum range $5 < \mathrm{p}_T < 12$ GeV/c. It is expected that quark-gluon interactions dominate pion production in this p_T range (Figure 2.3). Pions are therefore sensitive to the sign of the contribution to the gluon parton density function through predominantly valence quark-gluon scattering - as charged pions enter linearly into the wave function (Figure 2.4). Neutral pions have already been measured (Figure 2.7) and mainly provide constrains to the magnitude of the gluon's polarization [5]. Charged pions, as a complementary probe, can help constrain both the sign and magnitude of ΔG: preferential fragmentation of up quarks (u) to π^+, and down quarks (d) to π^-, leads to the dominance of up-quark-gluon, and down-quark-gluon contributions. This dominance of u or d combined with the different signs of their polarized distributions translates into asymmetry differences for the different species π^+ , π^0 and π that depend on the sign of ΔG. For example, a positive ΔG could be indicated by an order of π asymmetries, i.e: $A_{LL}(\pi^+) > A_{LL}(\pi^0) > A_{LL}(\pi)$ - and vice-versa -, for a negative contribution. The focus of this work is charged pion asymmetries measured from longitudinally polarized proton+proton data collected in the years 2005 and 2006

at the relativistic heavy ion collider (RHIC). Asymmetries and cross-sections will be measured within a central pseudo-rapidity of $\eta < 0.35$, i.e. orthogonal to the beam axis. Pseudorapidity is a spatial coordinate that describes the angle of a particle relative to the beam axis. It is defined as $\eta = -\ln(\tan\frac{\theta}{2})$, where θ is the angle relative to the beam axis.

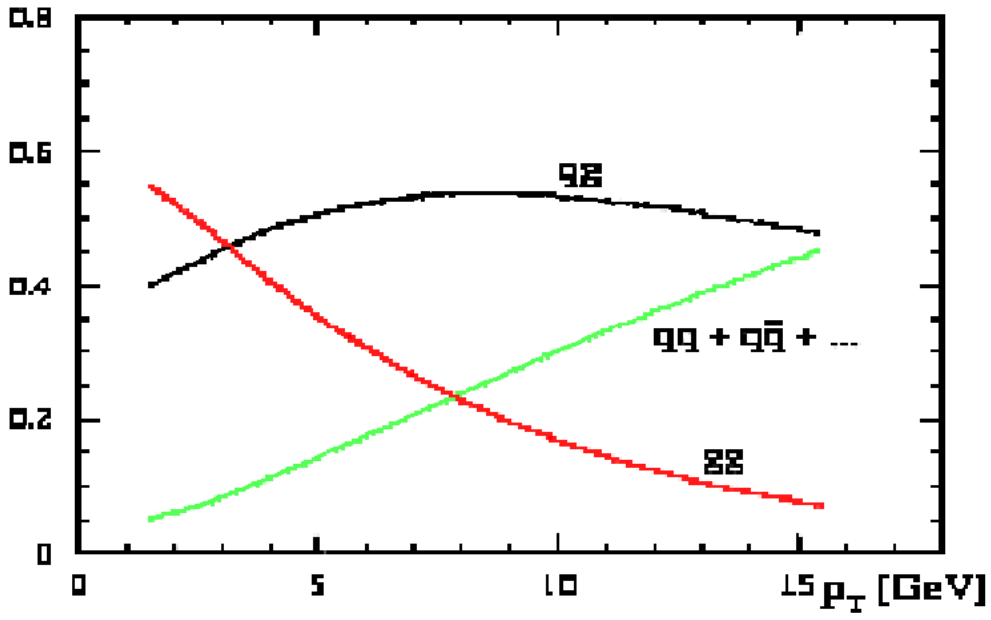

Figure 2.3: pp $\rightarrow \pi^{\pm}X$: partonic contributions as a function of pion's transverse momentum and detected at a central pseudo-rapidity. Partonic contributions calculated using NLO pQCD framework by Werner Vogelsang. The increasing curve labeled $qq+q\bar{q}+...$, represents the increasing order of partonic diagrams that enter the calculation with increasing momenta of charged pion production. The model is based on the GRSV[22] fits[33].

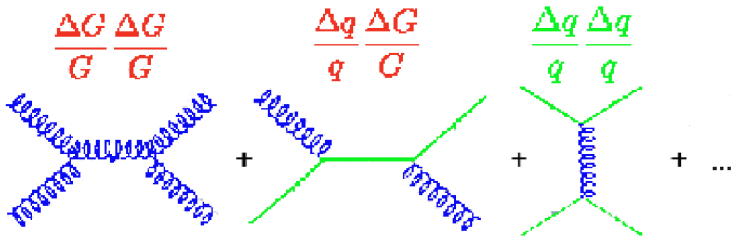

Figure 2.4: Feynman diagrams showing the valence quark and gluon sensitivities proceeding from pp $\rightarrow \pi^{\pm}$ X.

2.10 Discussion of DIS and RHIC Experiments

Much of our present knowledge about the spin structure of the proton comes from polarized deep inelastic scattering experiments. Polarized deep inelastic scattering (pDIS) experiments were performed by scattering a high-energy charged lepton beam from a nucleon target at large momentum transfer Q^2 (electrons at DESY, JLab and SLAC and muons at CERN). These experiments have found that the valence quarks carried only 25% of the nucleon spin. It is widely accepted that the picture of the nucleon extends past the valence quark picture. Nevertheless, there are still opened questions which continue to shake the field of spin physics. Experiments currently running and those that will be carried into the subsequent decade are designed to measure the different components to the nucleon spin with accuracy. The RHIC spin program was an early effort to directly map out ΔG using polarized proton beams. Experiments at RHIC have also played an important role in studying transverse spin effects. Figure 2.5 summarizes the

current knowledge of the polarized distribution functions from RHIC and DIS experiments. Figure 2.6 illustrates the most current knowledge to the unpolarized distribution functions. Figure 2.7 illustrates a χ^2 profile and partial contributions of RHIC and DIS data-sets for variations of ΔG in the limited x region. Illustrated in the figure are the constraints to the gluon polarizarion by individual data-sets. Negative values of ΔG are still poorly constrained by RHIC data. Data from the PHENIX detector particularly illustrates this lack of sensitivity (pink curve in the figure). Charged pions can make contributions by providing significant constraints to the negative values of ΔG in this region.

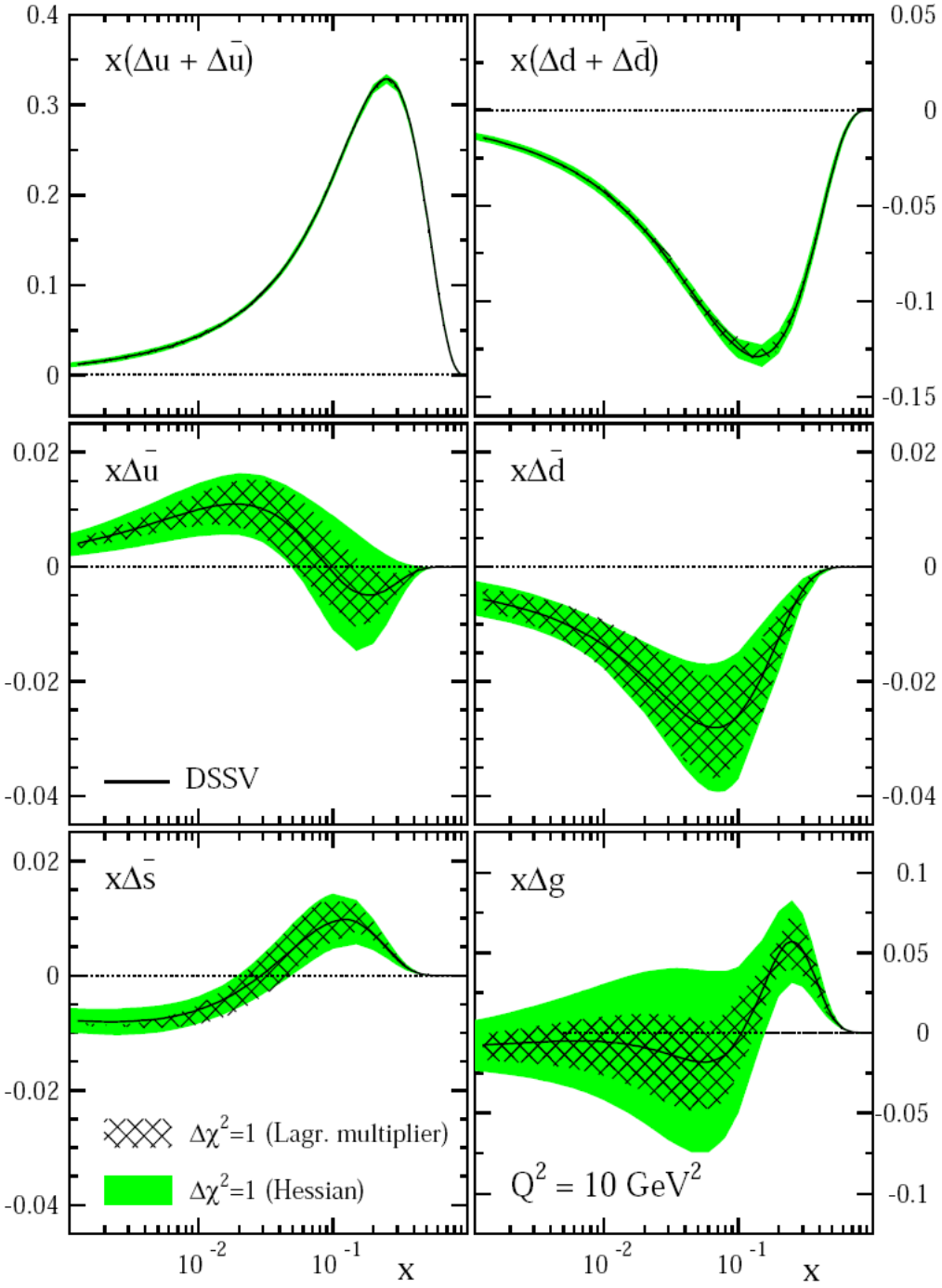

Figure 2.5: Current knowledge of polarized sea and gluon densities (Figure from[11]). Shaded bands represent uncertainties calculated with two different methods. The momentum fraction sampled by the charged pions of the present work is ∼0.02 to 0.1.

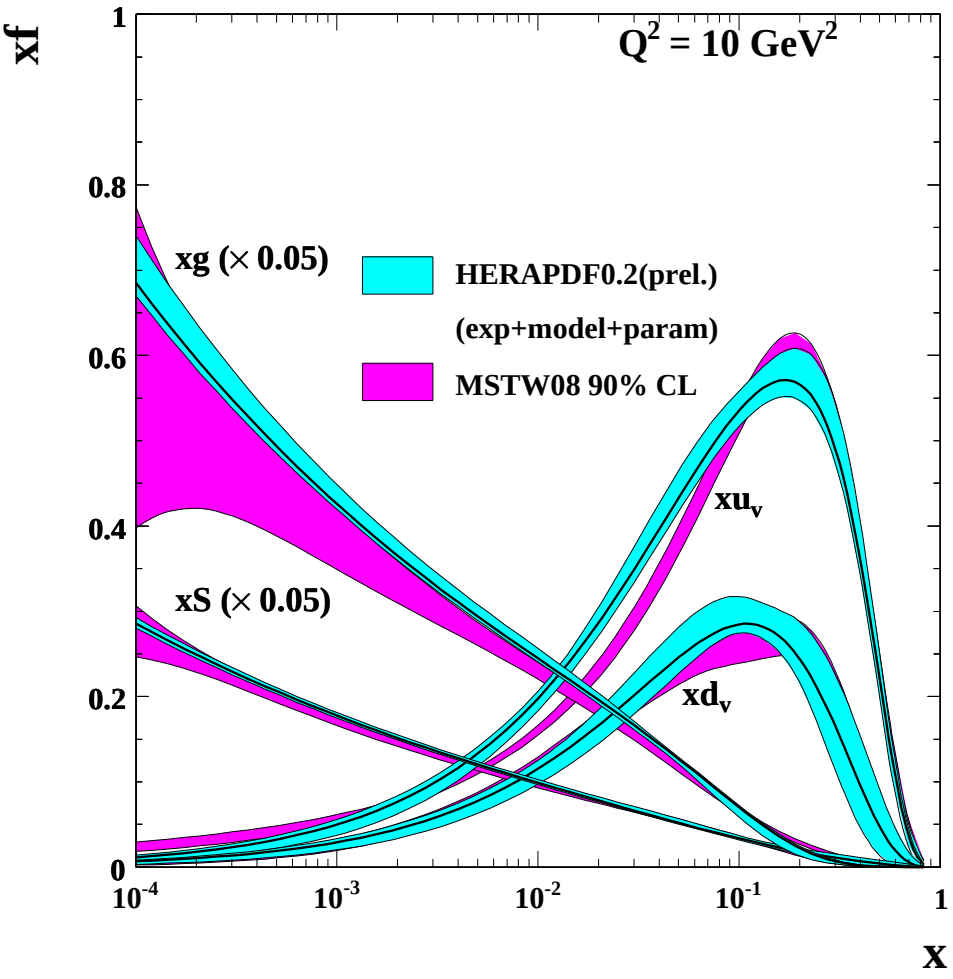

Figure 2.6: Summary of current knowledge of unpolarized parton densities functions. Where x is the momentum fraction carried by the parton. The shaded bands are uncertainties. Figure taken from[19].

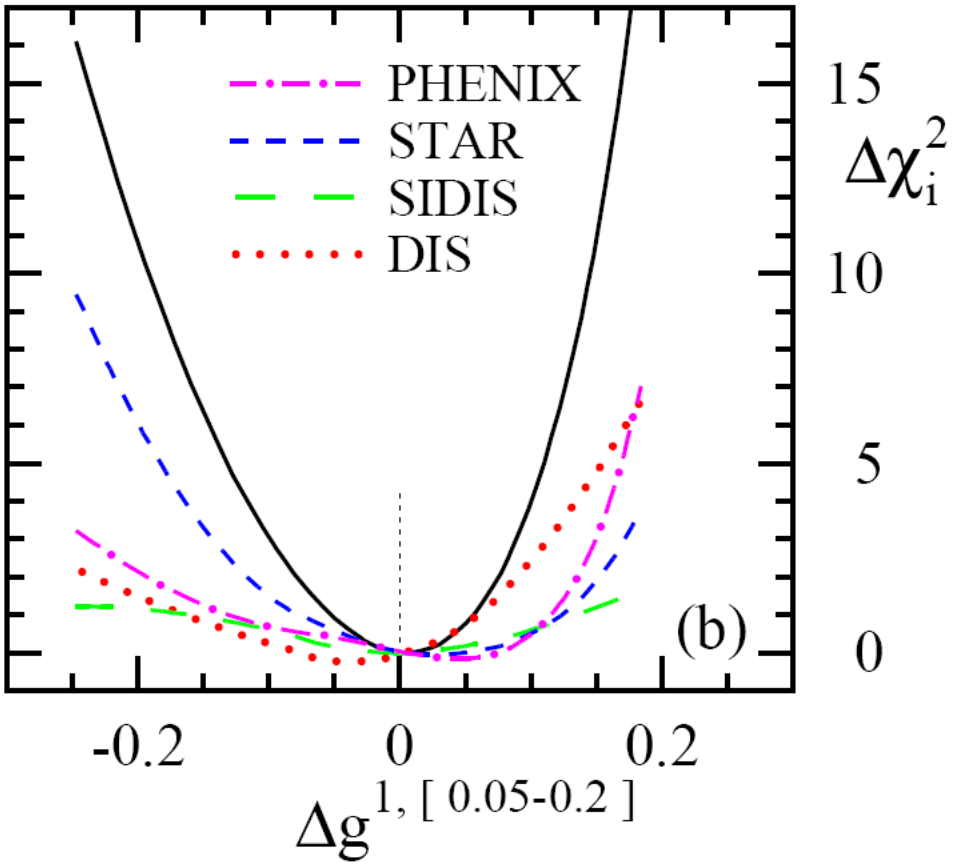

Figure 2.7: Figure taken from[11]. χ^2 distributions of individual RHIC and DIS datasets. The abscissa represents values of ΔG (Δg in figure) in the sampled x region. Negative values are poorly constrained by the RHIC data (pink and blue curves). Charged pions can contribute to the constraints of the left side of the plot.

2.11 Purpose Behind the Present Work

The purpose of this work is to further our understanding of the proton's intrinsic spin. Moreover, it is foreseen that this work will significantly advance the knowledge of the gluon's contribution to the proton's spin, ΔG, which is still relatively unknown. The measurements presented in this work comprise two pieces: a charged pion production cross-section measurement and a charged pion double asymmetry measurement, A_{LL}. Both measurements are performed at high enough momentum so they can be interpreted in the framework of pQCD. Through model fits, these measurements are expected to yield information on the sign and magnitude of ΔG. This expectation is born out of the dominance of up- and down-gluon scattering in charged pion production over the momentum range studied. The data presented here, alone, cannot be used to extract the gluon's spin contribution over the whole momentum fraction x. Instead, the results can be included in an a posteriori global analysis, which takes in appropriate data from across many analyses and from across the globe. Each individual analysis may be sensitive to different proton momentum fractions (x). Each measurement (and each p_T bin of each measurement) is integrated over a range of x. A global analysis is needed to unfold this and to optimize the incorporating multiple data sets that are sensitive not only to different x ranges, but different sub-process contributions. From these models, which currently are weakly constrained by data measurements, different parametrizations showed values which varied both in magnitude and the sign of ΔG. In order to add credance to

the asymmetry results, the measured unpolarized differential cross-sections of charged pions will be presented. These data provide a verification of the use of the pQCD framework with the comparison to next-to-leading order (NLO) pQCD predictions. The factorized pQCD framework, as previously defined, predicts that the unpolarized parton and polarized quark distribution functions, obtained from DIS, as well as the fragmentation functions, obtained from semi-inclusive DIS, can be used for the interpretation of A_{LL}. The measurements presented show that the measured differential cross-sections of charged pions agree with expectations. Thus, one can conclude that charged pions are well suited for proton spin studies in a NLO pQCD framework and can provide valuable information within the momentum fraction sampled of $\sim$0.02 to 0.1.

Chapter 3

Relativistic Polarized Proton Collisions at RHIC

Several experiments in the past have used polarized lepton probes (μ, e) scattering from polarized protons to study the parton spin contribution to the proton. However as mentioned in Section 2.2, these can only couple to the gluon indirectly as the probes used to couple to the parton are electromagnetic probes. RHIC (Figure 3.1) is the first hadron accelerator and collider consisting of two independent rings, which allow for separate beam steering and control. RHIC is also unique in its capability of accelerating polarized protons, with expected machine performance polarization values of up to 70%. Each experiment has the capability to choose between the stable transverse spin polarization or longitudinal beam polarizations with the use of spin rotators. For the measurements pre-

sented in this work, data taken with longitudinal polarized beams was relevant. RHIC its designed to operate at high collision luminosity over a wide range of beam energies with particle species ranging from polarized protons to heavy ions. Typical center-of-mass energies of 200 to the maximum 500 GeV, have been shown to be high enough for perturbative QCD methods to be applicable, and low enough for the typical momentum fraction of valence quarks to be about 0.1 or larger, guaranteeing significant levels of parton polarization [7].

3.1 Polarizing Protons

Stable polarization of RHIC is in the transverse direction. While transverse spin measurements are interesting in their own accord, for the measurements presented here it is the longitudinal polarization of the proton that is of interest. The longitudinal sum rule has an explicit term which relates the polarized gluon distribution (Equation 2.15) to the spin of the proton. Longitudinal polarization at RHIC is achieved through helical dipole magnets at each side of the interaction region. These magnets can thus rotate the spin vector from the vertical to the horizontal plane. Injecting protons into the RHIC rings begins with an optically pumped polarized hydrogen ion source. Polarization is transferred from the electrons in the source to the protons in a reversed magnetic field. The Hydrogen beam is stripped from its electrons and other charged particles through electrostatic deflection. The polarized protons are injected into a linear accelerator (LINAC)

and to a synchrotron booster. At the end of the booster cycle polarized protons are injected into the alternating gradient synchrotron which serves as a pre-accelerator to RHIC (Figure 3.1). Simplifying the details of proton beam polarization, four steps can be used to describe the polarization of protons at RHIC.

- Intense high quality beam from AGS[1].
- Polarize in a B-field by selecting the hyperfine states of one of the Zeeman levels.
- Polarization is achieved by inducing transitions from the occupied hyperfine states (undesired spin direction) to the unoccupied hyperfine states (correct spin).
- Finally, the beam is ionized in the presence of a B-field to preserve polarization.
- The stable spin polarization is in the transverse direction.

3.2 Mean Spin Vector

The evolution of the spin direction of an acceleration polarized proton in a collider can be described by the Thomas-BMT equation:

$$\frac{d\overrightarrow{P}}{dt} = -\frac{e}{\gamma m}(G\gamma \overrightarrow{B}_{\perp} + (1+G)\overrightarrow{B}_{\parallel})x\overrightarrow{P} \tag{3.1}$$

[1]The alternating gradient synchrotron (AGS) accelerates protons and heavy ions to high energies. The applications of the AGS are not limited to RHIC physics. NASA space science for example, uses the beams from AGS, to simulate cosmic rays radio-biological effects, to learn about the possible risks to human beings exposed to space radiation.

Where $\overrightarrow{P}$ is the polarization vector expressed in particle's frame, $\overrightarrow{B}_{\perp}(\overrightarrow{B}_{\parallel})$ are the perpendicular (parallel) external magnetic fields in the accelerator, G is the anomalous magnetic moment of the proton and γ is $\frac{E}{m}$. The Thomas-BMT can describe the precession of the particle, which can be compared to the evolution of a particle subject to the Lorentz force in an orbital motion in an external field:

$$\frac{d\overrightarrow{v}}{dt} = -\frac{e}{\gamma m}(\overrightarrow{B}_{\perp})x\overrightarrow{v} \tag{3.2}$$

In a pure perpendicular field to the direction of motion: the spin will rotate Gγ times faster than the orbital motion. It is Gγ that will then give the number of full spin precessions for every revolution. In a circular collider, numerous depolarizing resonances can exist making acceleration of protons a challenge, a resonance occurs every time the spin precession frequency equals the frequency on which the spin-perturbing fields are encountered. These spin-perturbations can be for example: machine imperfection resonances such as magnet error and misalignment and intrinsic resonances such as those driven by focusing fields. An imperfection resonance will arise when $G\gamma = n$, where n is some integer, intrinsic resonances will occur when $G\gamma = nP \pm \nu_y$ where n is an integer, P is the periodicity and ν_y is the transverse (vertical) betatron tune (betatron tune per period can be defined as $\nu_y = \frac{k_y L}{2\pi}$, where L is the Length of a period. Betatron resonances can occur when the condition $m\nu_x + n\nu_z = l$ where m, n and l are integers) [29]. During at typical acceleration cycle the stable spin direction (precession cycle) coincides

with the transverse magnetic field. Close to a perturbing resonance, the stable spin direction is deflected away from the transverse direction causing depolarization. A special set of magnets called *Siberian Snakes* were designed and built to cancel out these spin resonances.

3.3 Siberian Snakes and Spin Rotators

The acceleration of polarized protons in a circular collider is a challenge due to the proton's anomalous magnetic moment. Two Siberian Snakes are used at RHIC to maintain the polarization stable during the acceleration cycle. In addition to the Siberian Snakes, spin rotators are employed on each side of the two major interaction points which allow the spin orientation to be altered from the vertical plane to the longitudinal plane. Siberian Snakes generate a 180° spin rotation about a horizontal axis, the stable spin direction remains stable as long as the spin rotation by the snakes is much larger than the spin rotation of the depolarizing resonances. The snakes have a corkscrew like design, which causes the direction of the magnetic field to spiral along the direction of the beam. There are two snakes in each of RHICs two 2.4-mile-circumference rings located at opposite sides of each ring. As the beam moves through the snakes, the magnetic field flips the direction of spin and simultaneously averages out many smaller depolarizing resonances allowing to maintain a stable polarization of the beam. The polarization and luminosity achieved for the measurements presented in this work can be found in Table

3.1. Maximum average machine polarization is expected to be 70% (55% achieved for this work) with a peak luminosity of $1.5\times10^{31}\text{cm}^{-2}\text{s}^{-1}$. RHIC is capable of colliding protons at a maximum center of mass energy of 250 GeV. Luminosity at RHIC is typically limited by beam beam interactions with typical stable beam stores of $\sim$ 8 hours. The stable spin direction at RHIC is vertical. The PHENIX detector as well as STAR, have spin added capabilities which allow detectors to choose transverse or longitudinal beam polarizations. These spin rotations are achieved through the use of *helical dipole magnet* based spin rotators (Figure 3.1).

Year	[GeV]	Integrated Luminosity[pb^{-1}]	Polarization[%]	FOM
2005	200	3.4	49.0	19.6
2006	200	7.5	55.0	68.6

Table 3.1: RHIC achieved polarization and luminosity for the years relevant for the measurements presented in this work. One pico barn (pb) is equal to 10^{-36}cm^2. The figure of merit ratio between the 2006 and 2005 data-set was 3.5. Figure of merit (FOM) is defined as the polarization squared times the relative luminosity in units of inverse nano barns (P^4L).

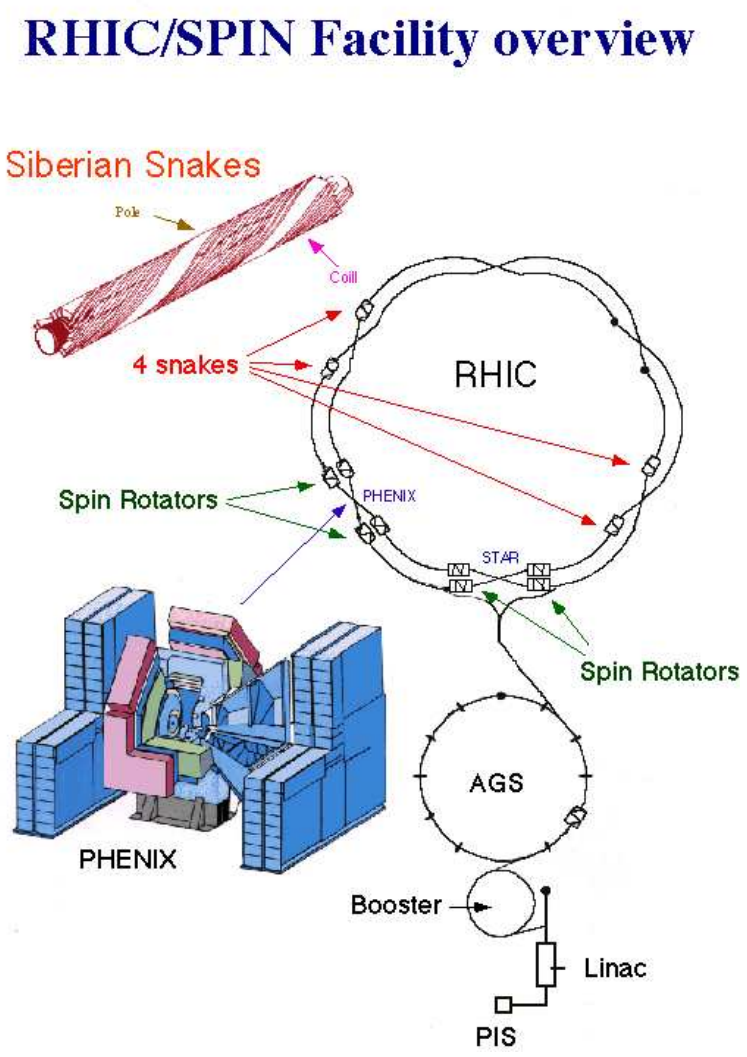

Figure 3.1: RHIC Schematic view. Siberian snakes at each of the two RHIC rings. These avoid depolarization resonances (imperfection resonances and intrinsic resonances) during the relativistic acceleration of polarized protons. This novel technique generates 180 degree spin rotations, canceling out depolarizing resonances and allowing stability of beam. The PHENIX and STAR detectors have the added capability of choosing both transverse or longitudinal polarization through spin rotators. Figure taken from[20].

Chapter 4

The PHENIX Detector

The PHENIX detector is located at the 8 o'clock position at RHIC. It weighs 4,000 tons and has three large steel magnets which produce high magnetic fields to bend charged particles along curved paths. Drift chambers, which track charged particles, record hits along the flight path to measure the curvature and thus determine each particle's momentum. PHENIX is a limited acceptance detector. It has two forward arms (bottom of Figure 4.1), and two central arms[1] with a pseudorapidity acceptance of $|\eta| < 0.35$ (Figure 4.1). These are equipped with fine-grained calorimetry 100 times finer than previous collider detectors, making particle electromagnetic cluster identification excellent. The granularity of the electromagnetic calorimeter (EMCal) is $\Delta\eta \times \Delta\phi = 0.01 \times 0.01$ [3]. Triggering on the central arms allows one to select a variety of particles at high- p_T, including $\pi^{\pm}$. The PHENIX muon arms (bottom region of Figure 4.1) cover

[1] the central arms are relevant for this work

$1.2 < |\eta| < 2.4$, they surround the beams and include $\mu^{\pm}$ identifiers, tracking stations and iron sheets with detectors in the gaps in each sheet.

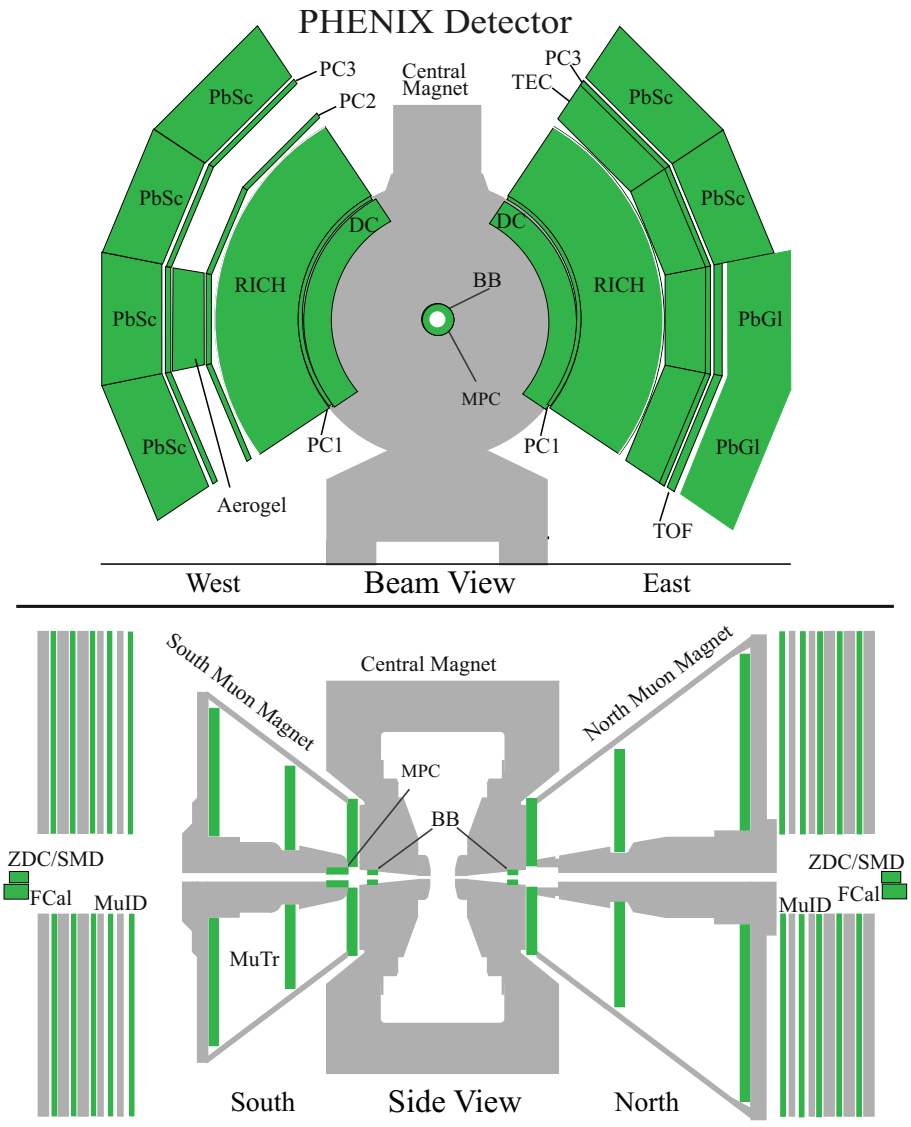

Figure 4.1: PHENIX detector data taking setup for the years 2006/2005. Note that for the year 2005, the MPC detector (muon piston calorimeter) was absent.

4.1 Detector Components

The sub-detectors used for the $\pi^{\pm}$ measurements of this work included the following:

- Beam Beam counters (BBC) (Section 4.1.1).
- Zero Degree Calorimeters (ZDC) (Section 4.1.2).
- Drift Chambers (DC) (Section 4.1.4)
- Ring Imaging Čerenkov counter(RICH) (Section 4.1.6).
- Pad Chambers 1 and 3(PC1, PC3) (Section 4.1.3).
- Electromagnetic Calorimeter (EMCal) (Section 4.1.7).

Other detectors were also used for studies and will be briefly discussed. However, after careful studies they were deemed not useful to the analysis in terms of statistics and pion identification quality.

4.1.1 Beam Beam Counters

Proton-proton collisions at 99.9% the speed of light can produce many types of events, some are more common than others. Event selectivity is thus an important component to screen interesting events in comparison to more pedestrian ones. Triggering, as this selection of events is called, can be achieved by detection of specific raw data patterns

with PHENIX's fastest sub-detectors. Algorithms using information from these detectors produce a first estimate of the transverse energy, event multiplicity, interaction time, collision vertex and the number or species of particles (i.e. electrons, photons, hadrons etc). One of these important fast detectors in PHENIX is the Beam-Beam Counter (BBC) subsystem. The BBCs consist of two arrays each consisting of 64 photomultiplier tubes equipped with quartz Čerenkov radiators on either side of the interaction region. This detector can determine the collision vertex to be used as the initial point of charged particle tracking as well as event characterization. The beam-beam counters can be thought of as the start of a stopwatch for an event. The BBCs can also provide a minimum bias trigger (Section 4.2.2) when coupled with the zero degree calorimeters (ZDC).

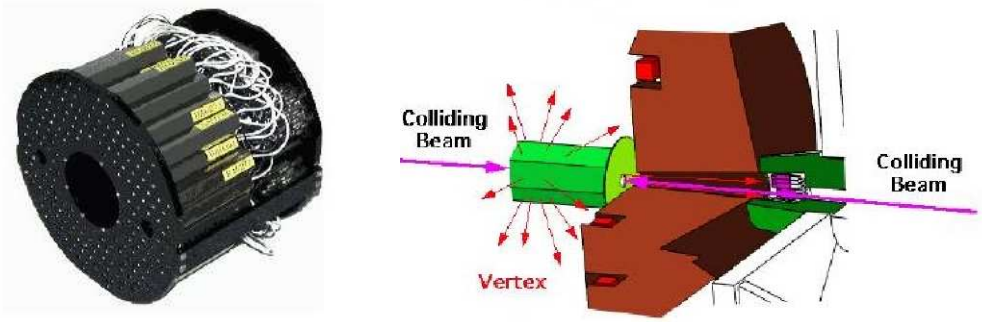

Figure 4.2: Beam Beam Counters.

4.1.2 Zero Degree Calorimeter

The Zero Degree Calorimeters (ZDC) are small transverse area hadron calorimeters located downstream of the DX dipole magnets in each of the experiments at RHIC[2]. The detectors measure neutral energy within a 2 mrad cone about the beam direction[3]. They are located $\sim$ 18m from the interaction point, with a horizontal acceptance of $\pm$5 cm. Both in heavy ions and in proton-proton collisions, the ZDC's measure energy to count the number of free spectator neutrons, which is used for event-by-event characterization in conjunction with the BBC.[3] Coincidence signals from detectors on either side of the interaction region are also used for luminosity monitoring.

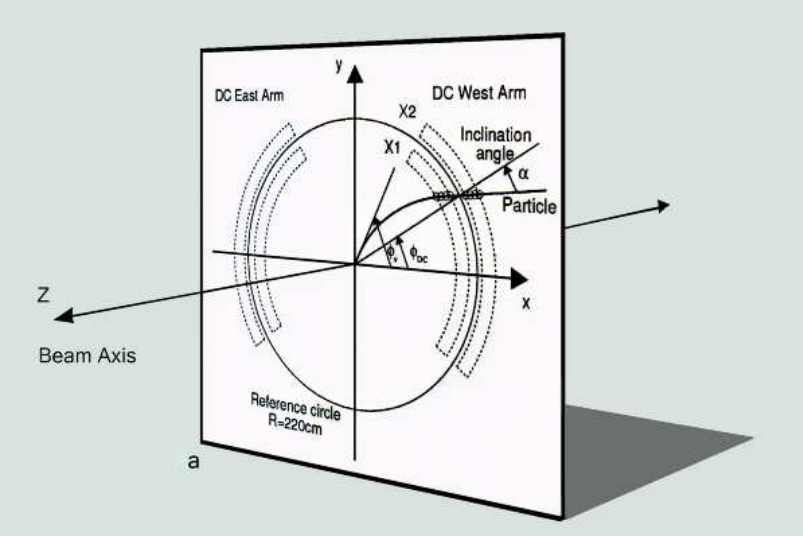

Figure 4.3: Charged tracking in the detector region is calculated by using a Hough transform of the tracks left by passing particles in the drift chamber, an assumption made is that the track is straight in the detector region. See also Figure 5.15.

[2]DX magnets are used to steer bunches so they collide.
[3]As charged particles are bent away by the DX magnetic field.

4.1.3 Pad Chambers and Tracking

PHENIX's Pad Chambers (PC) are multiwire proportional chambers which form two (East arm) and three (West arm) separate layers of the central tracking system. Each pad chamber contains a single plane of wires inside a gas volume bounded by two cathode planes. One cathode is finely segmented into an array of pixels. When a charge is induced on a number of pixels from a charged particle transversing, an avalanche starts on an anode wire and its read out through the readout electronics. Since there are no sub-detectors within the magnetic field of the central region, the pad chambers can provide points in space along straight lined charged particle trajectories which are outside of the magnetic field. This capability is of special importance to the measurements in this work (Figure 4.1). The innermost pad chamber plane, called PC1, is located between the drift chamber and the RICH on both East and West arms, while pad chamber 3 (PC3) is located in front of the calorimeter. There is an additional a pad chamber (PC2) behind the RICH, however it is present in the West arm only and was not used for the measurements described here. The PCs are the only non-projective detectors in the central tracking system and thus are critical elements of the pattern recognition. PC1 is also essential in determining the three-dimensional momentum vector by providing the z coordinate at the exit of the drift chamber [3]. One of the crucial capabilities of the pad chambers is particle track identification, particularly for reduction of the electron background proceeding from particles not originating from the collision vertex. The in-

formation from PC1 gives direction vectors through the ring imaging Čerenkov counter, while PC2 and PC3 are used to resolve track ambiguities in the outer detectors.[4] By accurate recognition of three points forming a straight line track through the central spectrometer, response from charged particle identifying detectors (RICH) is ensured as well as correct correlation of momentum and identification of the track's charge sign from the drift chamber.

4.1.4 Drift Chamber

The drift chambers (DC) provide a high resolution momentum measurement by tracking charged particle trajectories in the $r - \phi$ direction of the central arms (Figure 4.3). They are located in the region from 2 m$< r <$ 2.4 m from the *z* axis and have a total length (*d*) of 2 m along the beam direction. They are placed in a region of minimal residual magnetic field. Tracks which transverse the gas volume of the DC are thus expected to be straight (Figure 4.3). Each arm of PHENIX has two identical drift chambers, with volumes defined by cylindrical titanium frames which bound the azimuthal and *z* (beam-axis) acceptance of the detector. Each frame is divided into twenty equal sectors which have wire modules stacked radially. These wire modules can help discern the quality of the traversing track by recording hits in space. There are six types of these wire modules: X1, U1, V1, X2, U2 and V2. Each module contains 4 anode planes and 4 cathode planes

[4]Track model ambiguities can occur when decay particles outside the drift chamber tracking volume, and low-momentum primary tracks curve around PC1 in the magnetic field and strike PC2 and PC3. These can also strike the calorimeter, producing false tracks or energy depositions.

forming cells with a 2-2.5 cm drift space in the ϕ direction. The X1 and X2 wire cells run in parallel to the beam to perform tracking measurements in the $r-\phi$ plane (Figure 4.4). These wire cells are then followed by two sets of small angle "U" and "V" wire planes which are used in pattern recognition. U1, V1, U2, and V2 wires have stereo angles of about 6° relative to the X wires and measure the *z* coordinate of the track. The stereo angles in the U and V wire planes can minimize track ambiguities by matching the *z* resolution of the pad chambers [3]. Electronically what this means is that when the pad chamber 1 receives a unique hit in the beam axis coordinate *z*, the stereo wires try to verify. When verification occurs a unique UV wire hit will be recorded. When a unique UV hit is not found then UV wires are then consulted for the closest hit. The bit pattern for hits in the wires are binary and they are defined as follows:

- 0 (1) X1 used.
- 1 (2) X2 used.
- 2 (4) UV found.
- 3 (8) UV unique.
- 4 (16) PC1 found.
- 5 (48) PC1 unique.

As it can be seen from the above binary patterns, the best track match is 63 followed by 31. 31 indicates that the PC1 may be ambiguous but the UV has a preference among

choices. In this work, only tracks which had a drift chamber and PC1 quality of 63 or 31 were considered.

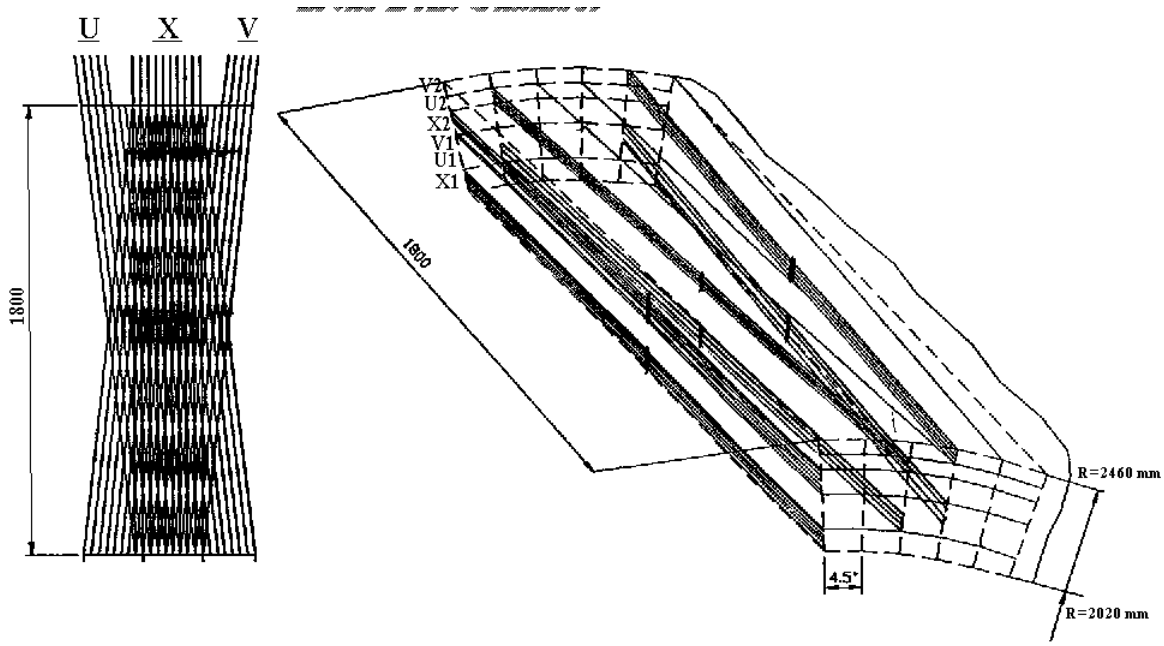

Figure 4.4: Schematic Drawing of X, U, and V planes on PHENIX's Drift Chamber.

4.1.5 Magnetic Field and Inner Tracking System

PHENIX central magnet is composed of two concentric coils with a field integral of roughly 8000 Gauss-meters , which provides a field near the interaction vertex and parallel to the beam. Charged particles will curve in the presence of the magnetic field and will enter a minimum field integral region which coincides with the radius of the first tracking detector: the drift chamber (DC). The design of PHENIX magnets called for a requirement of not having mass in the apertures of the central spectrometer. While this

requirement minimizes multiple scattering and the interactions with material from particles, it also means that there is no magnetic field tracking within the inner detectors. One of the requirements for example, was that the field integral on the ring imaging Čerenkov counter (which lies within a radial distance from the vertex of 2.4m to 4m) was less than 100 Gauss-m. This was required to minimize the smearing of the rings associated with low momentum tracks. The inner PHENIX charged tracking system consists of Drift Chambers (DC) and Pad Chambers (PC1). These tracking detectors measure charged particle trajectories in the θ and ϕ direction to thus obtain 3 momentum of the particle. The DC are cylindrically shaped and located in the region from 2 to 2.4 m from the collision point and 2 m along the beam direction. This places them in a residual magnetic field with a maximum of 600 Gauss-m. Due to the lack of magnetic field tracking within the DC and the PC region, charged tracks in the central spectrometers are reconstructed assuming a collision vertex in the geometrical center of the detector. Hit associations in the DC and PC1 in conjunction with a track reconstruction model is used to associate hits within a window of the track. In order to obtain accurate momentum reconstruction of charged tracks, offline corrections are made to the collision vertex and these will discussed with more detail in Section 5.2.4.

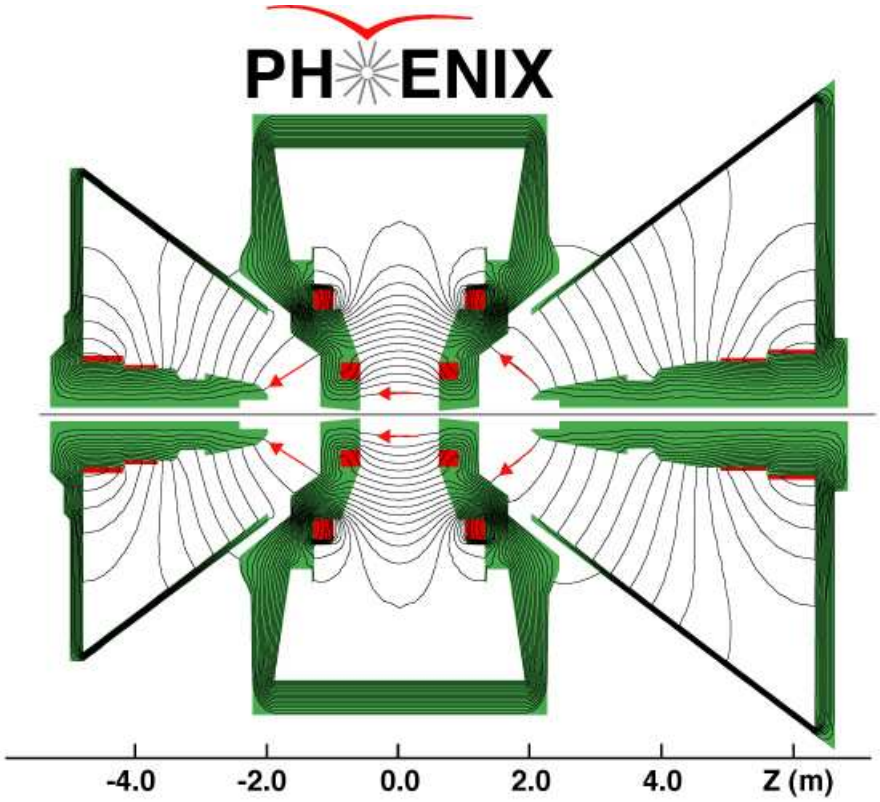

Figure 4.5: Magnetic field lines for the two central magnet coils in combined $++$ mode.

4.1.6 RICH

The Ring Imaging Čerenkov Counter (Figure 4.6) is a subsystem from PHENIX central arms, occupying a radial region between 4.1 m$>$ r $>$2.58 m from the beam line. When a charged particle passes through the RICH's gas volume, electromagnetic radiation is emitted. These occurs when particles pass through the gas volume at a constant speed greater than the speed of light and energies above light emitting (Table 4.1) threshold. Čerenkov photons are emitted from the charged particle and reflected by spherical mirrors. These photons are then focused on arrays of photo multipliers (2560 per arm) as a

ring (electrons) or disk (pions) shaped pattern[5]. Position of the Čerenkov ring, or disk then gives the direction of the charged particle track. Each arm of PHENIX has one RICH detector both identical and flanked by the inner and outer tracking stations. The RICH has a charged pion threshold of 4.7 GeV/*c* and while electrons can also fire the RICH at this threshold, pion behavior can be different than that of electrons. Electron production of photons to electrons due to the photo electric effect above 500 MeV/c is a constant while charged pion's is not. Electrons produce rings, or a "corona," while pions fire the RICH over a disk due to their smaller light cone. Moreover, an electron will fire 6 PMTs in average, while a charged pion's firing will increase with p_T and plateau around 5 PMTs. In this analysis, light emitted from pions is studied over a disk ($n1$), rather than a ring ($n0$) to help identify charged pions. $n1$ represents a disk of a radius of 11 cm circling the projected hit location of an identified track inside the drift chamber. To ensure that charged pion tracks are selected, a requirement $n1 > 0$ PMTs is enforced as this ensures that pions in the sample are above (or equal) the RICH's light threshold.

Particle	Threshold [GeV/c].
e^+, e^-	0.017
μ^+, μ^-	3.5
π^+, π^-	4.7
K^+, K^-	16
p^+, p^-	30

Table 4.1: RICH thresholds.

[5]Electrons will emit light in a cone radius larger than pions (Section 5.3).

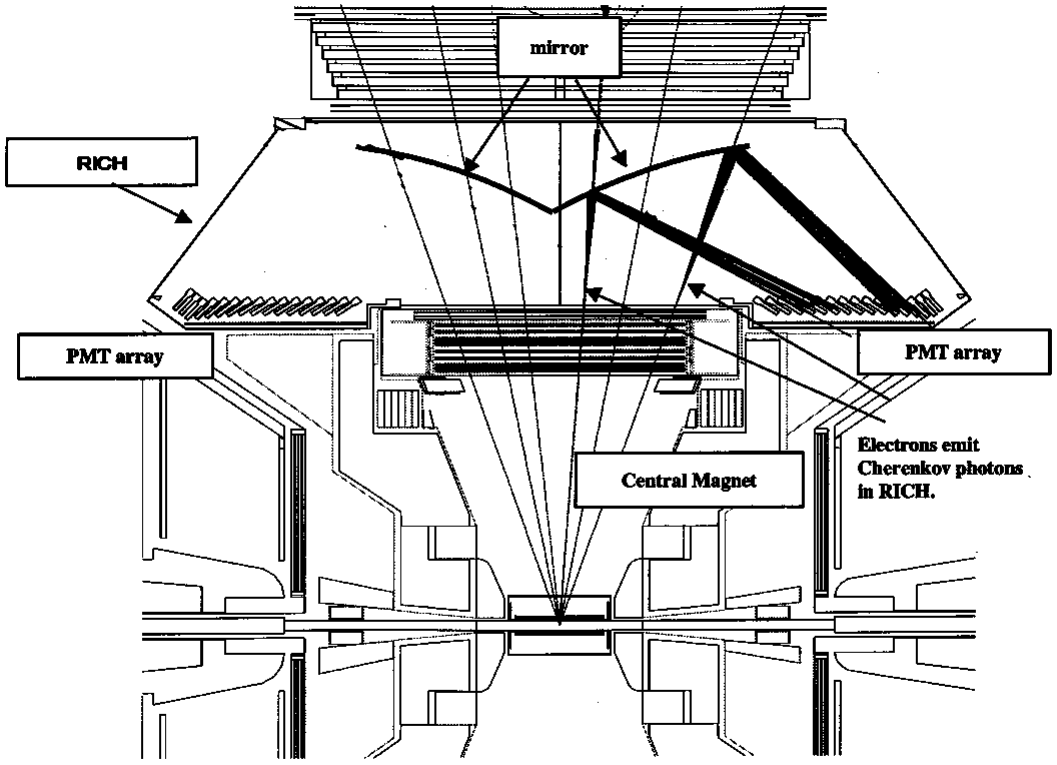

Figure 4.6: Illustration of the Ring Imaging Čerenkov Counter which shows the reflecting mirror collecting the light emitted by particles above light emitting threshold. Arrays of photomultiplier tubes (PMT) will collect the light and convert the photons to photoelectrons due to the photoelectric effect.

4.1.7 Electromagnetic Calorimeter

The electromagnetic calorimeter (EMCal) is a laterally segmented array of approximately 25,000 individual towers each with photomultiplier tube (PMT) readout [14]. The EMCal measures the spatial position and energy of particles produced in collisions. It covers the full pseudorapidity (η) of the central arms ($70^\circ \leq \theta \leq 110^\circ$). Each of the EMCal's two arms cover 90° in azimuth. The West arm is composed of four sectors of a lead-scintillator (Pb-Sc) sampling calorimeter, while the East arm has two sectors of Pb-Sc and two of a Pb-glass Čerenkov calorimeter. The designs of both Pb-Sc and Pb-Gl are different as the Pb-Sc is a sampling calorimeter while the Pb-glass is a Čerenkov detector. The EMCal plays an important role in particle identification, in particular in shower cluster resolution of particles. The EMCal also provides an important element to the triggering system as the EMCal can trigger on rare events with high transverse momentum (p_T) and one can resolve the trigger particle due to the fine granularity. Signals from the EMCal are incorporated in Level-1 triggers (Section 4.2.1). The EMCal system consists of a total of 24768 individual detector modules divided between the Pb-Sc calorimeter[6] and the Pb-glass. The Pb-glass calorimeter consists of two sectors on the east arm. Both sub-detectors are read out with photomultiplier tubes (PMT) and are equipped with good energy resolution[7]

[6]The Pb-Sc provides six sectors of azimuthal coverage.

[7]The calorimeter has energy and position resolutions of 8% and 7 mm, respectively, for 1 GeV photons and electrons at normal incidence and gives a π^0 mass with resolution of 15 MeV[14].

4.2 From Raw Data to Reconstructed Files

Proton-proton collisions at RHIC can produce many events. Fast detectors in PHENIX can perform selectivity to more interesting events with the use of triggering. Triggering allows data storing to remain within capacity by rapidly deciding which events are interesting enough to keep. The front end electronics (FEE) process sub-detectors by converting detector signals into digital event fragments. Once the event is accepted, the data fragments from the FEM's then move via optical fibers to the data collection modules (DCM). The detector subsystems use the following methods to collect and digitize data for transmission to the DCMs:

1. The data is digitized in real time. The BBC, ZDC, DC, PC, Time Expansion Chamber (TEC) and Muon Identifiers (MuID) use this method.

2. The data is sampled and stored in analog form in analog memory units (AMU). The analog data is only digitized after receipt of an accept from the LVL1 trigger. The Time of Flight (ToF) detectors, Ring Imaging Čerenkov Detectors (RICH), Electromagnetic Calorimeter (EMCal), and the Muon Trackers (MuTrk) use this approach [3].

In this work, two types of triggered data were used: Minimum Biased data (MB), where the data is triggered by the BBC alone (method 1 above) and EMCal-RICH(ERT) triggered data, where the EMCal and RICH (method 2 above) are used as part of the trigger

coupled with the BBCs (method 1)[8].

Triggered data is collected and reconstructed offline. It takes several months to go from raw data to reconstructed events which can be of use for a physics analysis such as this work. Once the data is reconstructed and PHENIX data access framework implemented (called Fun4All), the data files are classified according to types of Data Storing Tapes (DST), for example:

- CNT data from tracks reconstructed in PHENIX Central Arm.
- EWG data that for every track there is a hit in RICH.
- MWG data from tracks reconstructed in PHENIX Muon Arm.
- PWG data from EMC clusters.

CNT, EWG, MWG, PWG, types of DST in addition have other ”flavors” according to trigger selection (MB, ERT etc). These allows saving disk space for outputs, since the PHENIX analysis framework gives an opportunity to read multiple data inputs simultaneously during physics analysis. In this work, CNT files as well as PWG files were accessed for data analysis.

[8]The ratio of the trigger rate to the event rate is referred to as the selectivity of the trigger.

4.2.1 ERT Trigger

The ERT trigger was used for the analysis of the $\pi^{\pm}$ asymmetries. The ERT trigger consists the EMCal and the RICH acceptance region separated into 16 trigger segments. Each of these segments consist of 9-PbSc-RICH and 16-PbGl-RHIC trigger tiles. When a particle deposits energy in one or more of the 144 Trigger EMCal towers, the energy of the towers in a 2 by 2 or 4 by 4 neighboring towers is summed as the shower of the deposited energy will typically spread over several towers. Different energy threshold values are assigned depending on whether the trigger is in a 4×4 or 2×2 towers overlapping energy sum configuration. When a particle deposits energy above these set thresholds a trigger signal of ERTLL1 4×4 or ERTLL1 2×2 is issued. The ERTLL1 4×4 has 3 versions based on threshold energy, $4 \times 4a$, $4 \times 4b$, and $4 \times 4c$. Each trigger type requires a 2.1 (*a*), 2.8 (b) and 1.4 (c) GeV energy deposit in a 4×4 tower block made up of 4 neighboring basic tiles. In this work the 4×4 trigger of types (c) and (b) were used.

4.2.2 Minimum Bias Trigger

In minimum bias triggering events are selected when a coincidence PMT hits on the BBC modules are recorded. As the vertex of the beam particles is rapidly calculated, the electronics calculate if the vertex is within the desired interaction region of ($|z| < 37.5$ cm). Output bits of accepted collision points. Timing of the events is sent to global level

1 systems which in conjunction with other level 1 data and data acquisition information, will accept the signal that is sent to the electronics of the other PHENIX subsystems. In this work, the MB trigger with BBCLL1[9] was used.

[9] A minimum requirement was made that more than zero PMT tubes fired in the BBCs.

Chapter 5

Measurements - Differential Cross-sections $E\frac{d^3\sigma}{dp^3}$

Two main measurements from charged pions in the PHENIX detector central arms are presented, asymmetries and cross-sections. The goal of these measurements is to establish that the measurements of A_{LL} can be interpreted in a factorized pQCD framework (Section 2.3.1) and to understand detector response. The reaction of interest is: $pp \longrightarrow \pi^{\pm}X$. Measurements of A_{LL}, as mentioned in Section 2.3.1, contain three ingredients under a factorized pQCD framework: the unpolarized (polarized) parton distribution functions $f_{q,g}(\Delta f_{q,g})$, the fragmentation functions (for charged pions in this case) $D_{\pi^{\pm}}$, and the unpolarized (polarized) hard scattering cross-section $\hat{\sigma}(\Delta\hat{\sigma})$. Two of the three terms which describe the cross-sections in the asymmetries of pion production

are non-perturbative: the parton distribution functions and the fragmentation functions. Both of these quantities are typically measured from scattering of leptons in nuclei or lepton-lepton scattering. One key assumption of the factorization framework is that the parton distribution functions and fragmentation functions are treated as universal. This means that one set of FF and PDFs can predict a larger set of values which can be applied to proton-proton collisions. It is a goal of the measurements presented to verify that the identified charged pions are consistent with the factorized framework used to interpret asymmetries. This goal is accomplished by measuring charged pion differential cross-sections which will be the subject of this chapter. The asymmetry measurements will be the subject of the next chapter.

Asymmetries require a clean pion sample and sub-detector efficiencies are less important. The measurements of asymmetries use calorimeter triggered data and require calorimeter background removal techniques. Detector efficiencies introduce uncertainties in measurements, however, since asymmetries are ratios of identified yields, they cancel in the asymmetry, A_{LL}. In cross-section measurements efficiencies do not cancel so its important they are known with precision. Therefore, in this work events triggered by the calorimeters and data from the calorimeters are not used for the cross-section measurements as the response of these detectors to charged pions are not well known. The measurements presented in this chapter discuss the method for determining differential cross-sections for unpolarized charged pion production.

Preliminary steps were taken to assess the quality of data collected, i.e. momentum resolution studies. Detector response and efficiency studies were performed with the aim of understanding detector effects which may affect the identification of charged pions at high transverse momentum. The data used was MB data from 2006 year running.

The organization of this chapter will be as follows:

- Description of $E\frac{d^3\sigma}{dp^3}$.
- Global quality checks: Monte Carlo simulations, efficiency calculations and calibrations.
- Sub-detector requirements (Identification cuts).
- Detailed description of differential cross-section results and comparisons to pQCD predictions.
- Background estimates ($E\frac{d^3\sigma}{dp^3}$).
- Errors.
- Ratios of π^-/π^+.

5.1 Differential Cross-sections $E\frac{d^3\sigma}{dp^3}$

Measurements of invariant yields of charged separated pions were performed as a complementary measurement to the measured spin asymmetries. These measurement provide a verification of the use of the pQCD framework with the comparison to next-to-leading order (NLO) pQCD predictions. The factorized pQCD framework, as previously defined, predicts that the unpolarized parton and polarized quark distribution functions, obtained from DIS, as well as the fragmentation functions, obtained from semi-inclusive DIS, can be used for the interpretation of A_{LL}. Minimum bias data from year 2006 was used for the cross-section analysis. The corresponding integrated luminosity of the charged pion sample was: $\int Ldt$ =1258366234 cm^{-2}s^{-1}.

The Lorentz invariant form and experimental descriptions for the calculation of this quantity are as a follows.

Invariant yield or differential cross-section:

$$E\frac{d^3\sigma}{dp^3} = \frac{d^3\sigma}{p_T d\eta dp_T d\phi} = \frac{1}{2\pi p_T}\frac{d^2\sigma}{dp_T d\eta} \quad \text{Lorentz invariant form} \tag{5.1}$$

$$\tag{5.2}$$

$$E\frac{d^3\sigma}{dp^3} = \frac{1}{2\pi p_T}\frac{N_{\pi^\pm}(p_T)}{\int Ldt\,\epsilon_{reco}\epsilon_{geo}\epsilon_{bias}\Delta p_T\Delta\eta}\ \text{Experimental definition} \quad (5.3)$$

Statistical uncertainty in $E\frac{d^3\sigma}{dp^3}$:

$$\Delta(E\frac{d^3\sigma}{dp^3}) = E\frac{d^3\sigma}{dp^3}\sqrt{\left(\frac{\Delta N_{\pi^\pm}}{N_{\pi^\pm}}\right)^2 + \left(\frac{\Delta N_{MB}}{N_{MB}}\right)^2} \quad (5.4)$$

Where:

- p is the momentum of the particle. For the present measurements, this quantity is approximately equal to p_T as particles are scattered in the central region of the PHENIX detector:$|\eta|$ <0.35.
- η is the pseudorapidity, described as $\eta = -ln[tan(\frac{\theta}{2})]$, where θ is the between the particle momentum $\vec{p}$ and the beam axis[1].
- p_T is the transverse momentum of the particle, defined as $p_T = \sqrt{p_x^2 + p_y^2}$. As the present measurements are produced in central rapidities, p_T is approximately equivalent to *p*.
- ϕ is the azimuthal angle (see Figure 5.1).

[1]In PHENIX $|\eta|$ =0.35, however for the measurements of this work, this value was normalized to one.

- $N_{\pi^{\pm}}$ is the number of reconstructed pions (charge separated for this work) in a p_T bin.

- ϵ_{geo} is the total efficiency of the geometrical acceptance, momentum smearing, as well as the reconstruction algorithm.

- ϵ_{reco} is the total efficiency of the identification technique (cuts).

- ϵ_{bias} is the bias of the BBC trigger.

- Δp_T is the bin width.

- $\int Ldt$ is the integrated luminosity defined as $\int Ldt = \frac{N_{MB}}{\sigma_{p+p}\epsilon_{BBC}^{p+p}}$, where:

  N_{MB} is the equivalent number of sampled minimum bias (MB) events. During the course of data taking a prescale is typically set on clock and MB triggers. This means only a fraction of the collisions is sampled to remain within bandwidth limits. N_{MB} is properly accounted for prescales, which would typically reduce the fraction of recorded events.

  σ_{p+p} is the total inelastic cross-section of proton collisions and ϵ_{BBC}^{p+p} is the BBC trigger efficiency. The quantity $\sigma_{p+p}\epsilon_{BBC}^{p+p}$ has been determined at $\sqrt{s}$ =200 GeV energies to be **23.0**$\pm$**2.2 mb** (Section 4.1.1) and this will be the value used in this work.

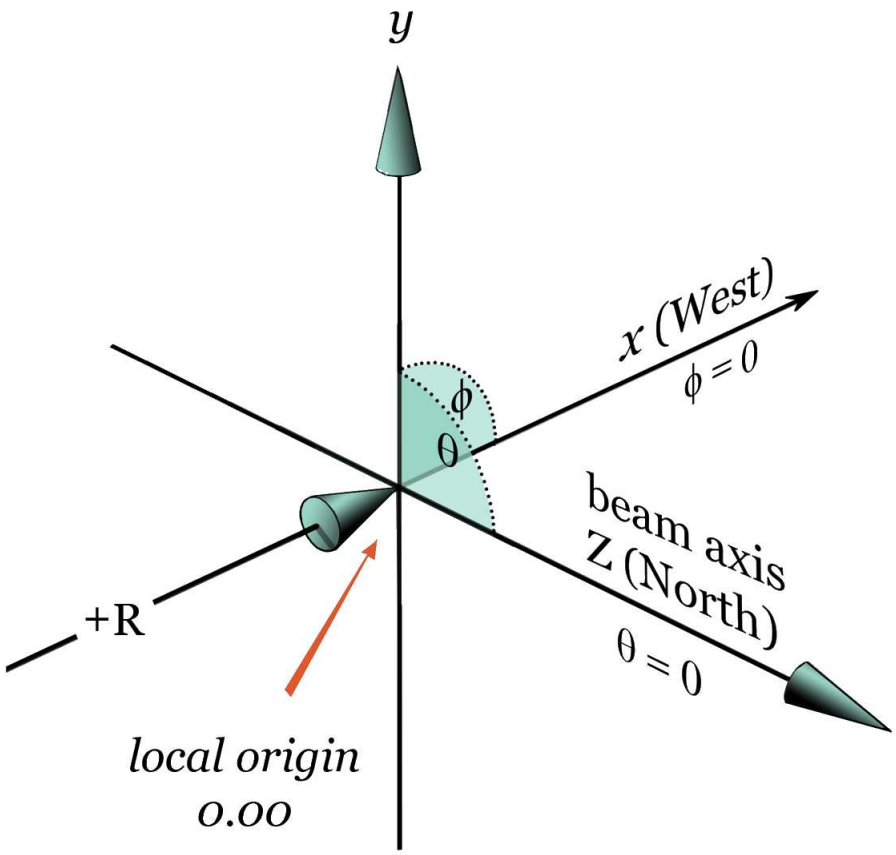

Figure 5.1: Representation of PHENIX coordinate system.

5.2 Sub-detector Requirements (cuts), Studies and Calibrations

This section provides an introduction to the data quality studies and calibrations that were performed before the final cross-sections were measured. Data from polarized p+p collisions at RHIC was extensively studied to determine the efficiency and quality of charged pion identification and calibrations specific for charged particle detection at

PHENIX. Simulated data was also generated to allow comparisons to real data and to study the detector response.

Cross-sections were measured by identifying a charged pion sample and studying with great detail the detector response in each sub-detector utilized in the measurement. Efficiencies in each sub-detector were calculated using both data and simulation each which will be discussed in this chapter. Identification of pions considered for a cross-section measurement consisted of the following detector requirements (cuts). Refer to the introduction of this chapter for the motivation of these cuts:

- Collision vertex measured from the BBC of less than 30 cm (absolute value).
- High drift chamber quality track (Referred to as quality of 63 or 31).
- Charged particle above RICH light emitting threshold for pions (4.7 GeV/c).
- Number of RICH photomultiplier tubes fired above zero and below five within a disk shape (referred to as $|n1| >$0).
- Transverse momentum range of charged particles between 5 and 10 GeV/c.
- z matching of charged track to the radial plane of less than 40 cm (absolute value). Referred to as $|zed| <$ 40cm. (Figure 5.2).
- Drift chamber (DC) track projections to pad chamber and EMCal. Projections should not deviate from actual hits by more than 2σ in dϕ and dz (Figure 5.3).

5.2.1 Simulation Data

In order to study detector response to charged pions a full simulation was performed. Simulated data was generated first by the use of a Monte Carlo simulation (PYTHIA, version 6.2)[18] and second by a full GEANT [15] simulation of the PHENIX detector. The main motivation of the simulation was to study detector response for the cross-section measurements. PYTHIA is a program which models the phase space distribution of relevant particles under study. The model includes hard and soft interactions parton distributions, initial, final state parton showers, multiple interactions, fragmentation and decays. In this work single pions[2] were generated and allowed to travel freely within the detectors geometrical acceptance. The generated charged pions were subsequently passed through a full GEANT [15] simulation of the PHENIX detector (PISA[3]), which took into consideration multiple scattering, material interactions, as well as detector dead areas. Finally the simulated data files were reconstructed as if they were real data and a full analysis was performed.

The **simulation** chain order was as follows:

Single particle $\pi^{\pm}$ (PYTHIA)$\rightarrow$ Detector (PISA) $\rightarrow$

Track Reconstruction (CNT files Section 4.2)$\rightarrow$ Analysis.

Dead areas from the DC (Section 4.1.4), PC (Section 4.1.3) and Čerenkov counters were

[2]No polarization information was simulated in any of the Monte Carlo studies performed in the work presented.

[3]PHENIX Integrated Simulation Package

implemented in the simulation. The goal was to try to be as close as possible to the real PHENIX detector. The **simulation** data was generated with the following initial parameters:

- 10^5 particles for each charge ($\pi^{\pm}$) per 1 GeV p_T bin.
- $|\eta| < 0.5$.[4]
- Collision vertex as measured by BBCs: $|BBCvertex| <$ 30 cm.
- 2$< p_T <$13 GeV/c.
- 0$< \phi <$2π.

[4]Note that PHENIX $|\eta|$ is within $\pm$ 0.35.

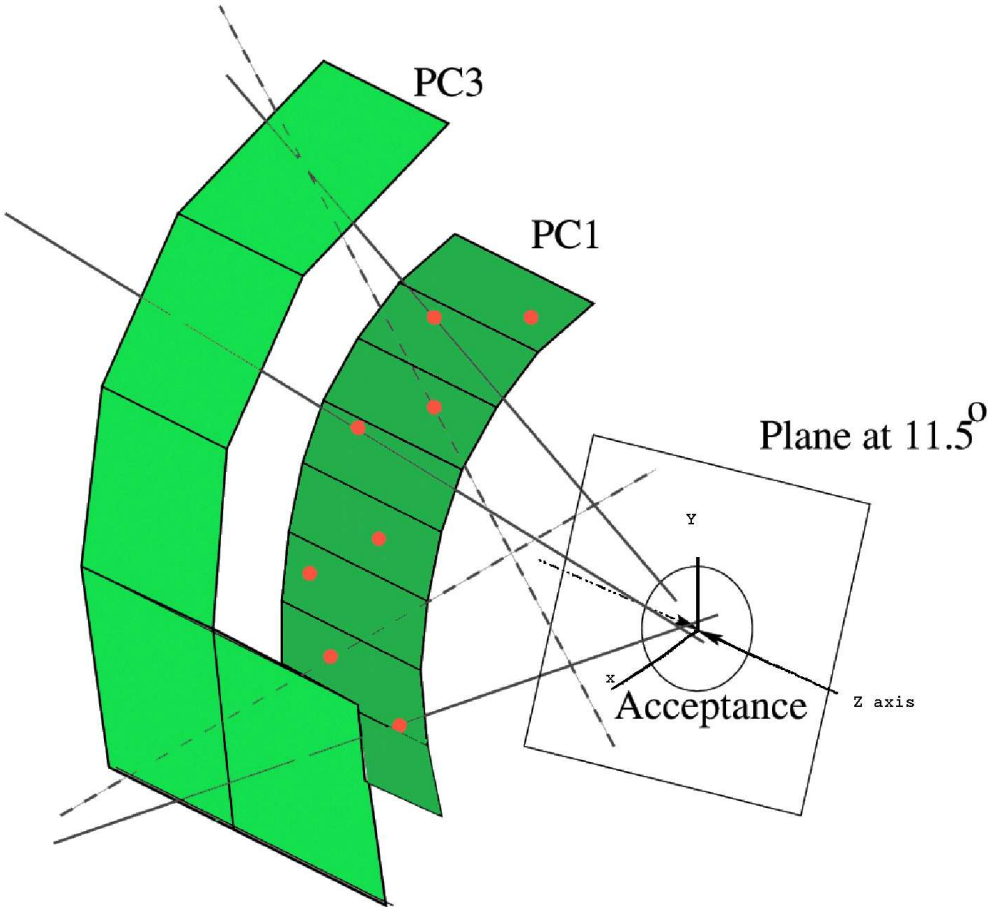

Figure 5.2: ZED. z coordinate at which the DC track crosses the PC1 (zed). When a charged track crosses the z coordinate, the vertex position is determined by combining all PC1 and PC3 hits to lines. These lines are projected to the plane and will be saved within an appropriate x and y window. The peak position of the z distribution will then be calculated.

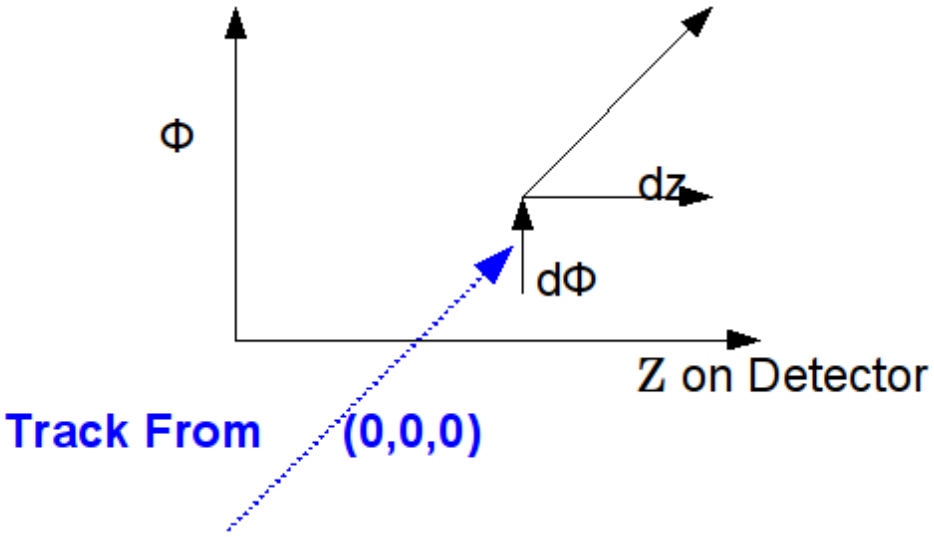

Figure 5.3: Illustration of projections of reconstructed DC tracks to the EMCal and the PC. The distributions of the difference between projection points and hits (called residuals) are fitted with a Gaussian. These projections can be used to minimize the background from particles not originating from the collision vertex.

Comparison of data and simulation was made to ensure that the initial simulated conditions matched the data fiducial maps and general geometry. To accomplish this, minimum bias data taken during the 2006 proton-proton run was examined and compared to the generated simulation. Apart from dead maps, simulated files were analyzed in the exact same manner as data. Minimal requirements used to analyzed **real** events included the following:

- Minimum beam collision vertex (using BBC) of $|bbcVtx| < 30$ cm.
- Minimum and maximum p_T requirements[5].
- Strict DC quality of charged track, $quality\,31\,or\,63$ (Section 4.1.4).
- Strict EMCal matching distributions cuts in σ, $|emcsd\phi| < 2, |\,emcsdz| < 2$ (Section 4.1.7 and Section 5.4).
- Strict PC Matching cuts in σ, $|pc3sd\phi| < 2, |pc3sdz| < 2$ (Sections 4.1.3 and Section 5.4).
- Fiducial Cuts (for the complete set of studies showing these fiducial cuts see the Appendix B) on the DC acceptance as follows:

  $((cos(\theta) > -0.002 * BBCVtx + 0.016)$[6].

[5]The selection of p_T depended of the study performed. The measurements of interest were performed within a momentum 5 GeV/c <p$_T$ <10 GeV/c (Section 6.1) whilst the simulation window was extended to lower and higher values to properly account of momentum smearing effects which push particles to lower or higher momentum bins.

[6]These cuts correspond to linear functions which describe physical empty areas and/or parts of the frame which hold the drift chamber see Figure 5.6.

$(cos(\theta) < -0.0019 * BBCVtx - 0.007))$

$((cos(\theta) > -0.0046 * BBCVtx + 0.016)$

$(cos(\theta) < -0.00467 * BBCVtx - 0.014))$

$abs(cos(\theta)) < 0.4$

$(cos(\theta) < -0.0044 * BBCVtx + 0.302)$

$cos(\theta) > -0.0042 * BBCVtx - 0.302)$

- Dead area maps on the DC and PC which were implemented from real data to the simulation.
- RICH detector firing in a disk shape: $n1 > 0$ (Section 4.1.6).
- Drift chamber minimum $|z|$ (defined as $|zed|$) tracking position of less than 65 cm (to 30cm depending on the study performed).

Definition of zed Cuts

A useful tracking cut that is done on the measurements presented is a cut in zed. The *zed* is defined as the *z* coordinate that a charged track crosses in the *x* and *y* plane. Alternatively it can be defined as the match of the z axis to the radial plane of a transversing charged track (Figure 5.2). When a charged track crosses the z coordinate, the vertex position is determined by combining all PC1 and PC3 hits to lines. These lines are projected to the plane and will be saved within an appropriate x and y window. The peak

position of the z distribution is then calculated. For the measurements of this work the main sources of background consist of electrons and positrons which do not originate from the collision vertex. These type of backgrounds have a strong zed dependence which will not be typically be found in particles originating from the collision vertex. Figure 5.4 illustrates these dependencies on simulated background, whilst Figure 5.5 shows the relative flat distributions of simulated charged pion signals.

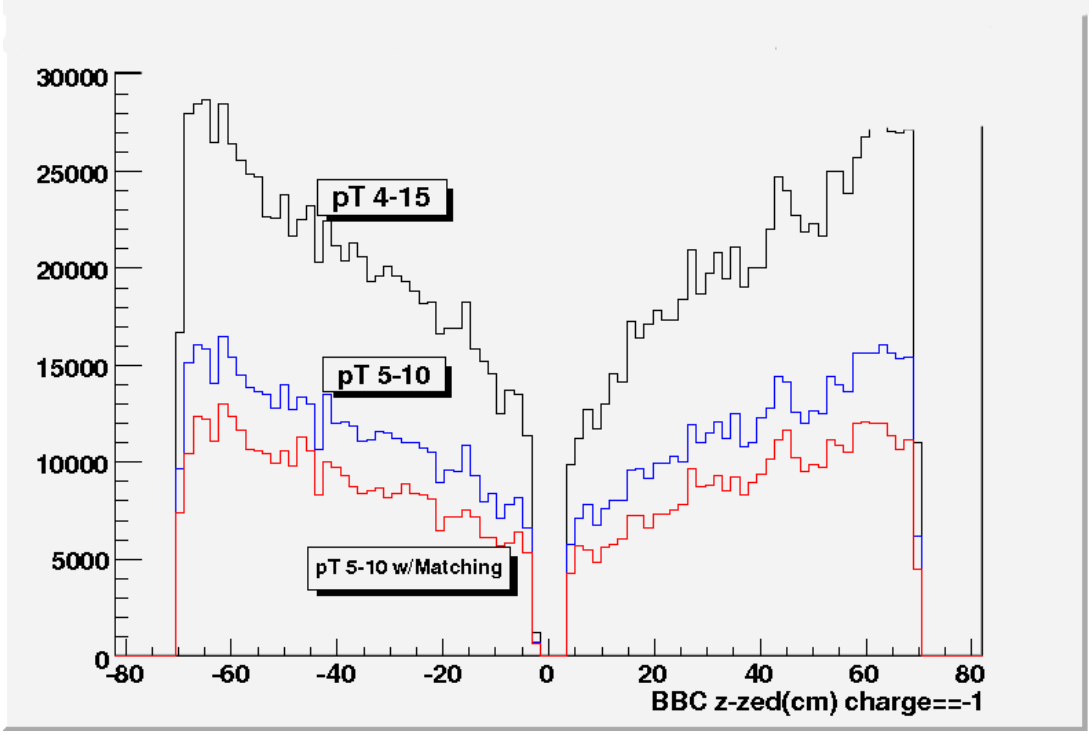

Figure 5.4: *zed* distributions of data in different bins of p_T, which displays the high tails at high and low *zed* (see also Figure 5.15), indicating the presence of secondary electron/positron background. The data used for this study was minimum bias with standard identification cuts, including a loose matching (Section 5.4) cut of 3σ (red lines).

The generated simulation was consistent with the detector configuration as it can be inspected from Figures 5.6, 5.7 and 5.8 as well as the figures found in the Appendix B,

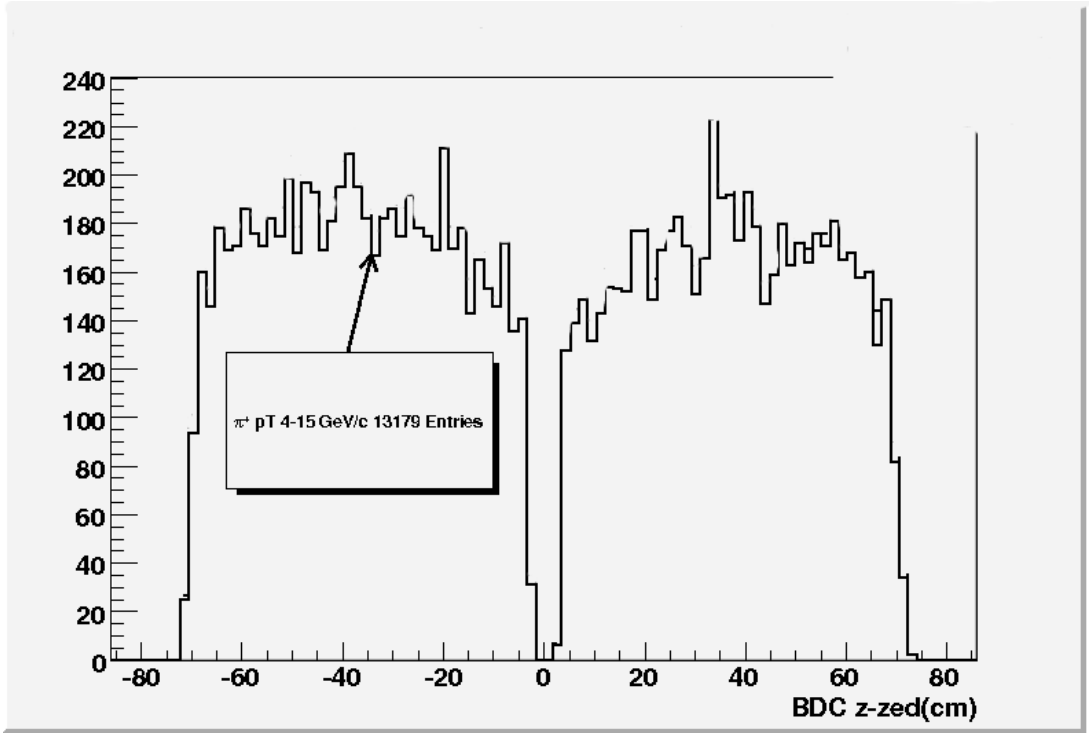

Figure 5.5: Simulated drift chambers *zed* distributions for π^+. The simulation found in these figures contain minimal cuts, as the goal was to inspect the shape of the *zed* distributions. As it is shown above the distributions are relatively flat.

more details can be read in the captions of these figures. Simulated p_T spectra after flat momentum input can be found in Figure 5.9. The conclusion of these figures is the reproduction of a realistic spectra of pions from simulation. In addition to the general geometrical setup, tracking of the generated background particles were also inspected, as these posed an opportunity to test the identification method. Background particles were generated. Secondary particles were also tracked in the simulation. Background particles from decays as they traveled/generated through the acceptance region can be summarized in Section 5.2.1.

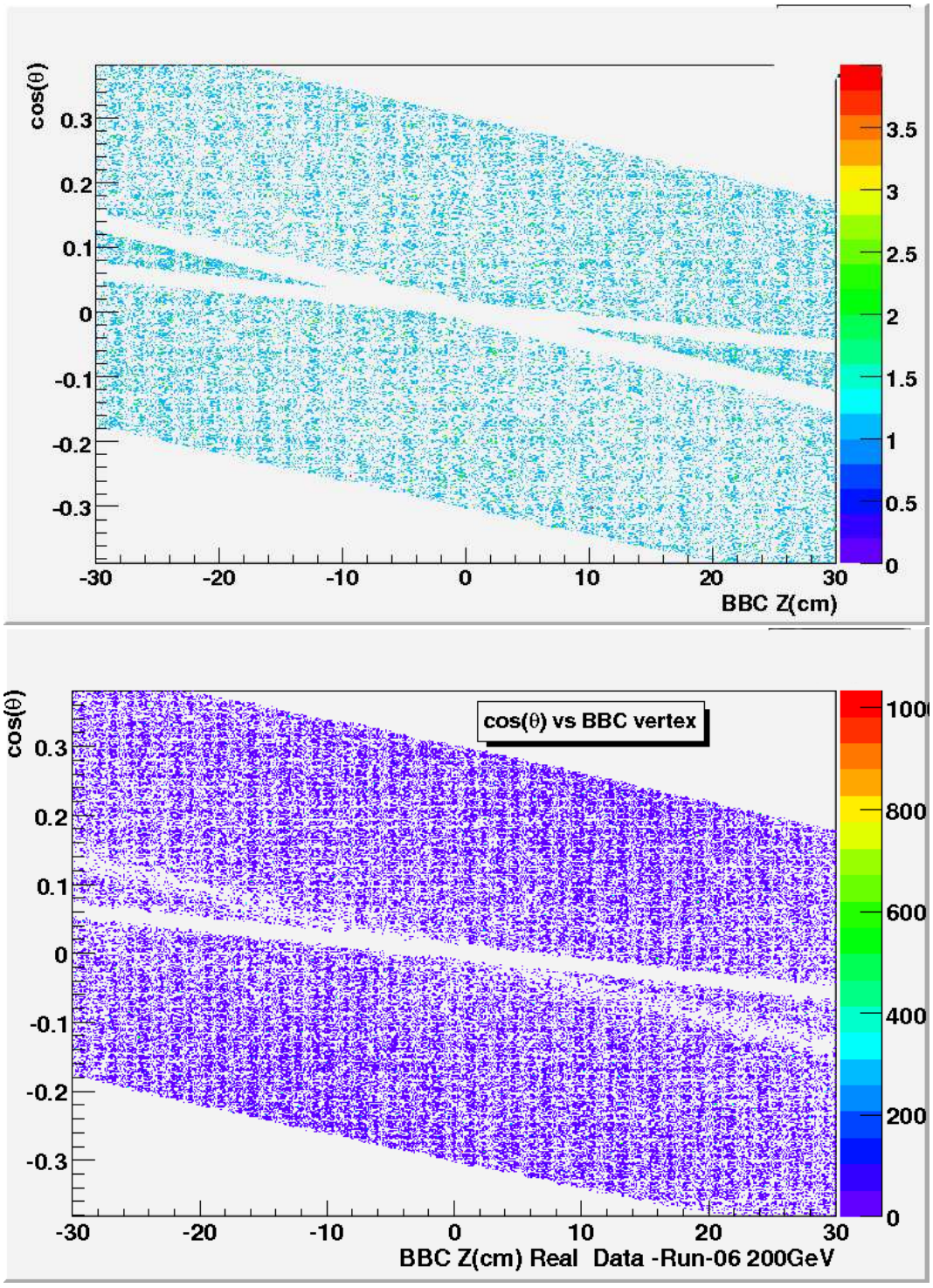

Figure 5.6: Acceptance plots in $cos(\theta)$ used to make fiducial cuts. These show the drift chamber's (both arms) and RICH gaps in simulation (top) and real (bottom) data. Additional studies can be found in Appendix B.

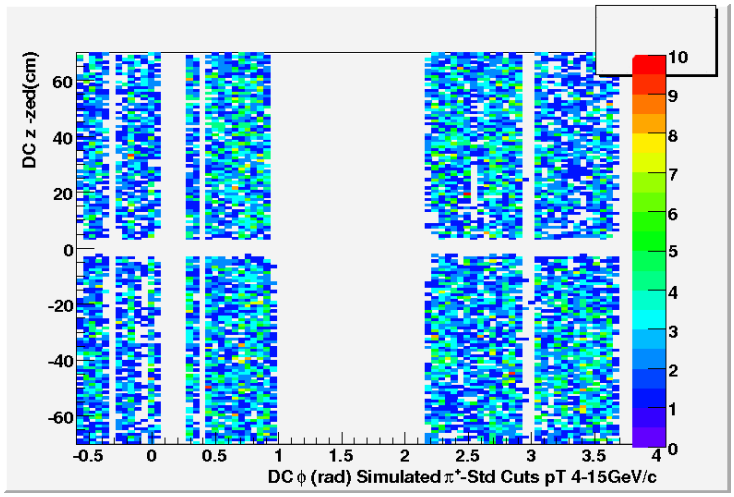

Figure 5.7: Simulated drift chamber's ϕ vs *zed* π^+. The white gaps found in the figures combine physical gaps in the detector as described above (Section 5.2.1), as well as dead maps caused by broken wires within the sub-detectors, and dead electronic channels. Additional studies can be found in Appendix B and Figure I.16.

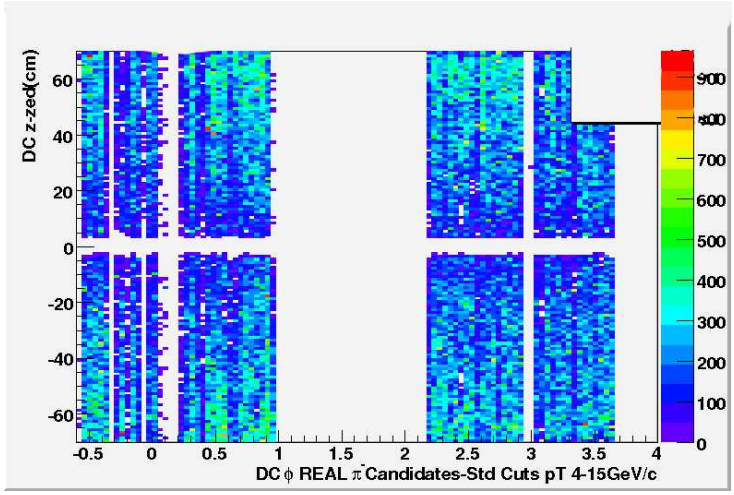

Figure 5.8: Real drift chamber data's ϕ vs *zed* π^-. These figures demonstrate the reproducibility of the implemented dead maps from real data onto simulation. Additional studies can be found in Appendix B and Figure I.17.

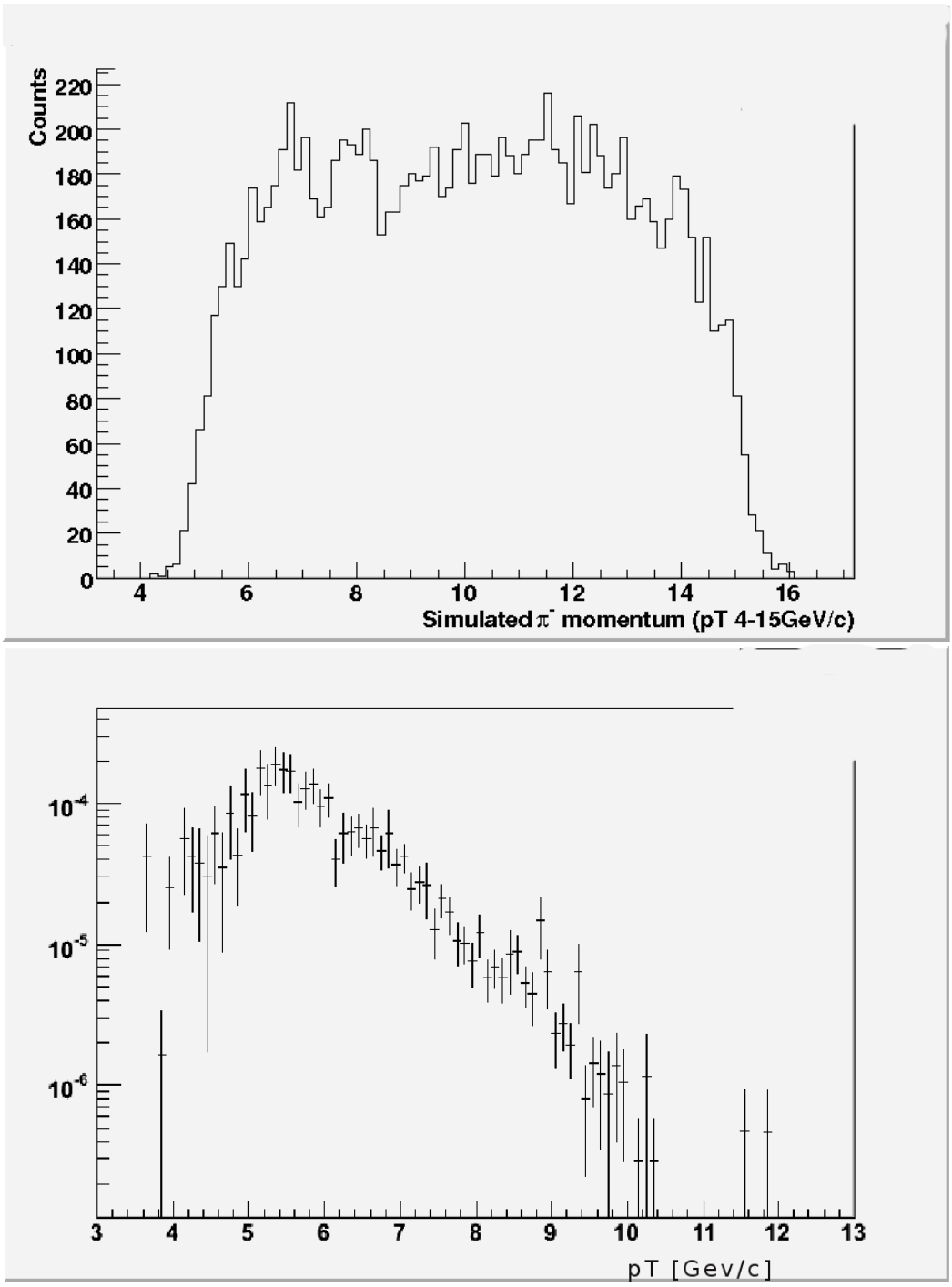

Figure 5.9: π^- simulated momentum distributions within 4 GeV/c $< p_T <$15 GeV/c. Top figure shows the spectra after a flat momentum distribution is used as input. The bottom figure has momentum weighted distributions by the function 14.43/$p_T^{8.1}$[5] to simulate a realistic decaying particle spectra in the detector. Errors on bottom figure are histogram bin entries. Abscissa is p_T in units of GeV/c. Refer to Figure I.20 for positive particles.

Of 100,000 single π^+ generated using a single particle Monte Carlo generator, within a rapidity of $|0.5|$ and a ϕ acceptance of $0 - 2\pi$, 58,007 make it through the detector region. The reconstruction algorithm is 83% efficient, with the remaining losses accounted by the larger η ($|0.5|$) of the simulation with respect to the PHENIX central rapidity η of $|0.35|$. 10,532 particles from the simulation do not originate from the vertex. These particles originate from decays and material interactions. These decay particles consist of the following species:

- 3969 (7938 pairs) - $\gamma \longrightarrow \mathrm{e}^+ e^-$.
- 2441 - failed to reconstruct at the end of the simulation chain.
- 6, 1 - μ^+, μ^-.
- 7, 8, 9 - π^0, π^+, π^-.
- 15, 37, 37, 22 - K_{long},K_{Short}, K^+, K^-.
- 13 -Neutrons
- 154, 2 - Protons, Anti Protons.
- 42 λ
- 4,3 σ^+, σ^-.
- 1 χ^-

- 25 Anti Neutron

- 1 anti Ξ^0

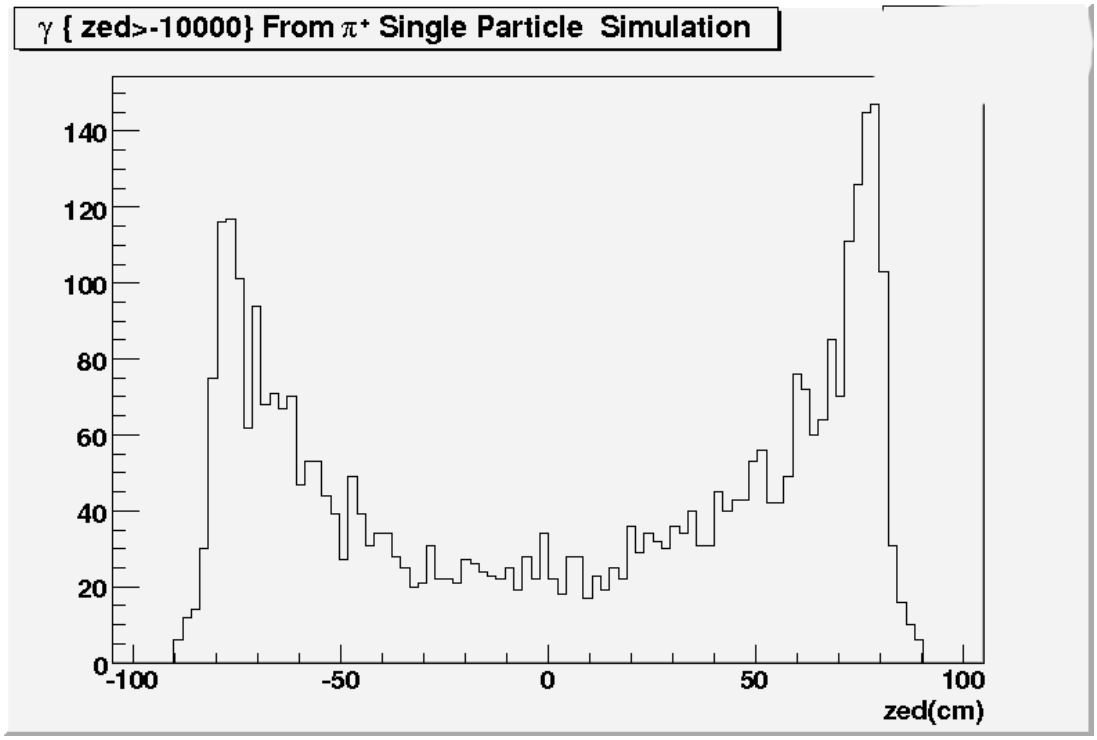

Figure 5.10: zed distribution of secondary electron positron pairs proceeding from γ conversions showing the high *zed* tail dependence.

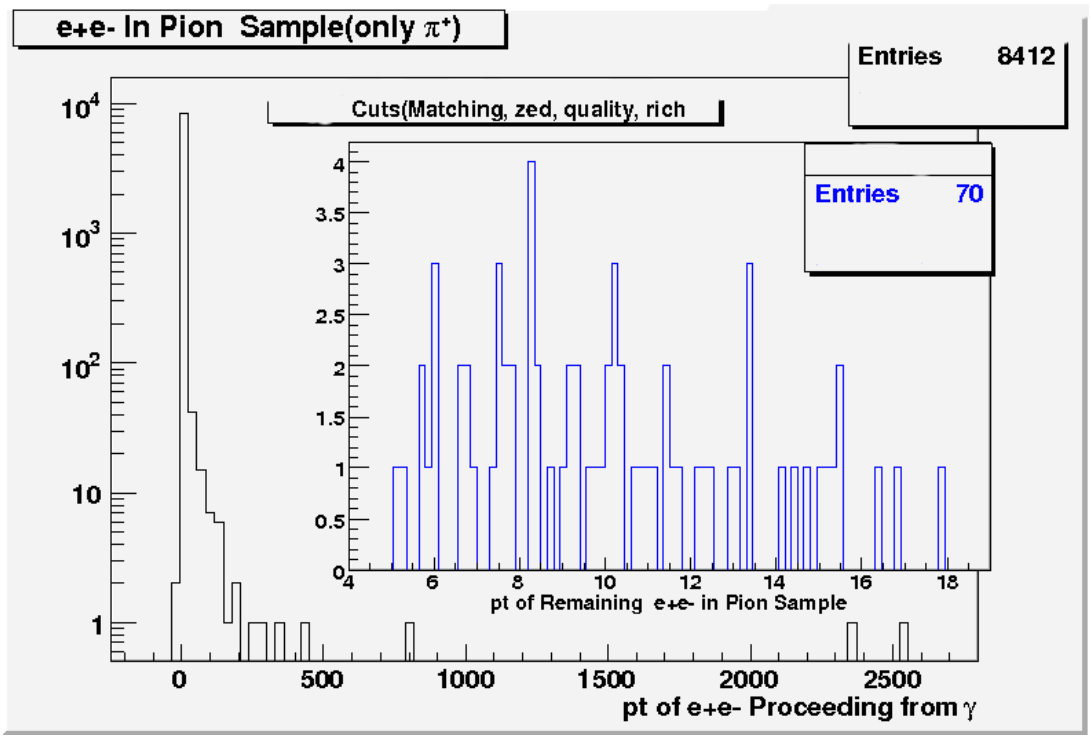

Figure 5.11: Momentum spectra of secondary electron-positron pairs proceeding from γ, inset shows the remaining pairs in the sample after preliminary pion identification cuts are implemented. Input p_T is 2 to 13GeV/c. Output p_T is center of bin.

Of particular interest are the 3969 γ primary particles that end up as e^+e^- pairs in the acceptance region. These e^+e^- pairs are in fact the type of background which is most relevant for the identification of pions. Photons will interact with the material in front of the drift chamber and produce a copious number of low energy e^+e^- pairs. These pairs are generated close to the DC and within the residual magnetic field. The e^+e^- pairs then mimic high momentum pions, when in fact their energy is close to 500 MeV. The *zed* distributions in Figures 5.10 and 5.11 show that they have a strong *zed* (Figure 5.2) dependence and over 98% can be removed by a $|zed|$ cut of 65 cm. A study using standard cuts (drift chamber quality, matching to pad chambers, *zed*, RICH) show that of the original 3969 γ which produce e^+e^- pairs, only 70 remain in the identified π^+ sample. This type of background will be again the subject of further discussion.

Pad chamber (PC) reconstruction shows that many simulated pions do not make it through and are flagged as not recognized or tracked in the sub-detectors. These flags can be caused by not having a probable hit in the pad chambers (or the EMCal) in either the ϕ or z directions. Many of these unrecognized tracks are due to dead areas in the sub-detectors themselves. Exploiting the existence of a tertiary tracking detector, the PC2, in addition to PC3 and EMC on the West arm, showed that the number of tracks salvaged by the use of this additional sub-detector was not sufficient to justify its use (Figure 5.12). Table 5.1 summarizes how many pions are lost in the matching distributions. Figure 5.13

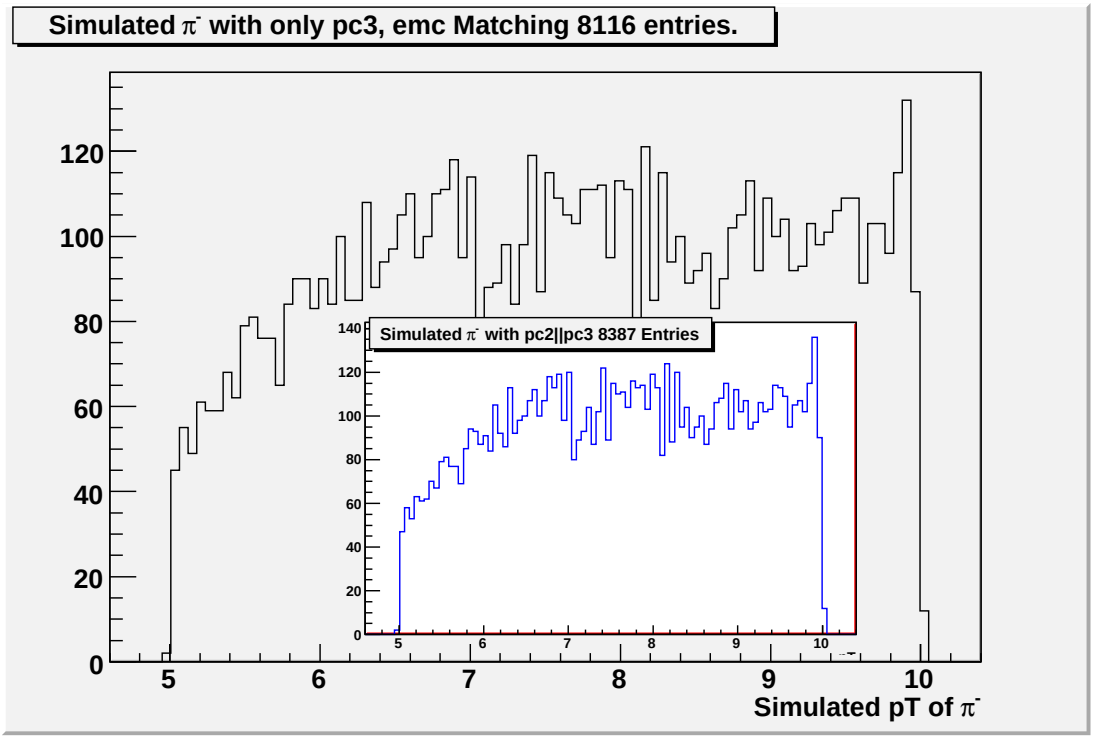

Figure 5.12: Number of tracks saved by using $PC2$ or $PC3$ rather than just $PC3$ and EMC sub-detectors. Only an extra 3% or particles are salvaged by the use of $PC2$. The momentum of the particles is 5 GeV/c to 10 GeV/c.

Un-reconstructed Tracks		
Cut	Counts π^+ (25777)	not reconstructed($\%$)
Emcsdϕ	388	1.5
pc3sdϕ	2411	9.4
pc2sdϕ	13703	53.2
Emcsdz	390	1.52
pc3sdz	2411	9.4
pc2sdz	13706	53

Table 5.1: Tracks that do not make the residual distributions, Detailed efficiencies of these distributions will be discussed in 5.4.

shows one of this sample distributions which show typical values for lost and accepted tracks. Refer to Appendix C for more figures regarding this study.

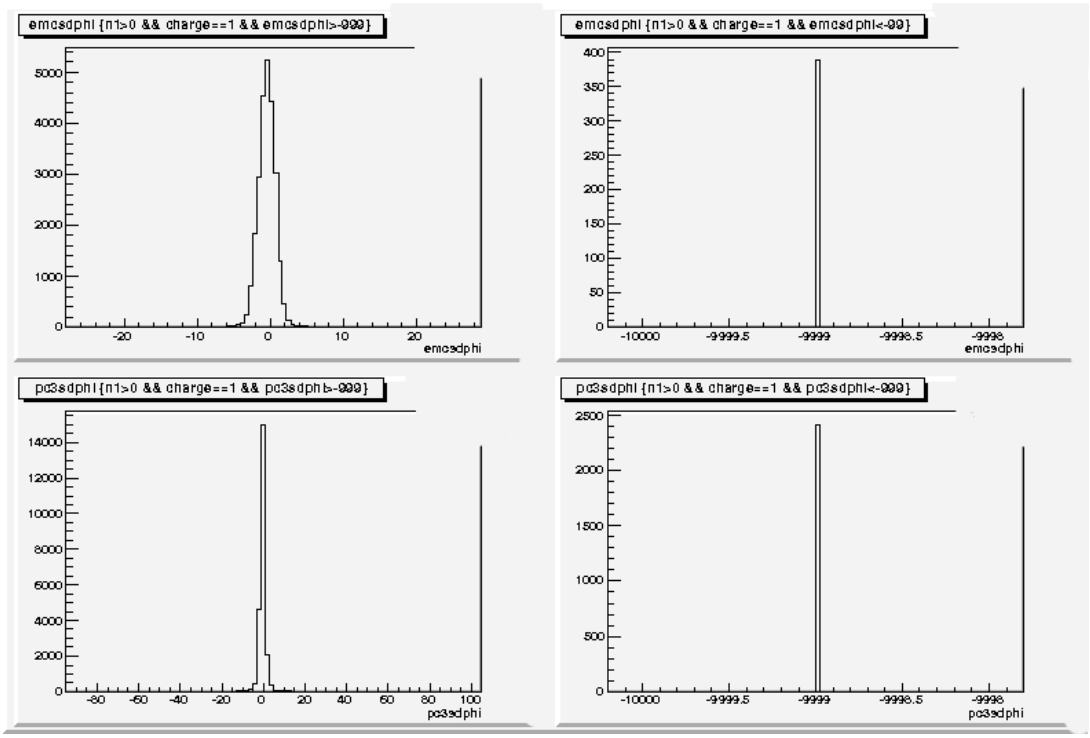

Figure 5.13: ϕ matched tracks that missed reconstruction recognition in the EMCal and PC3. The left panel show typical Gaussian distributions of accepted tracks, whilst the right panel shows the single binned values of those tracks that failed reconstruction. More figures can be found in the Appendix C.

5.2.2 Energy and Momentum Studies

The PHENIX integrated GEANT[15] package has not incorporated the hadronic response to the calorimeter. This is mainly due to lack of EMCal test beam data[7], and the lack of diverse and dedicated charged hadron detection at p_T larger than 2GeV/c[8]. As explained in last section and in the introduction of this chapter, precise detector response knowledge is needed for the cross-section measurements. Energy deposition studies were performed to evaluate the ERT sample[9], and this will discussed in Section 6.5.2.

5.2.3 Geometrical Acceptance Efficiency

Not all charged pions which are produced in proton proton collisions will be detected in the geometry of the detector or by the reconstruction algorithms. The detector acceptance depends on the design geometry. In this work it is assumed that the efficiency of detecting a pion can be decomposed into the geometrical acceptance and each subsystem's detection efficiency. The detector efficiency, which includes the event reconstruction efficiency, is summarized in Table 5.2. Figure 5.14 shows a typical trend of the geometrical acceptance. Most of the lost of particles can be atributed to the fact that there is very limited detector coverage, i.e. there are large empty areas of space which

[7]There exists test beam data at very large momentum, however, even this data was unavailable for analysis.

[8]In recent years which are not applicable to the data used for this work, there have been new detectors installed in PHENIX. These new detectors have diversified the hadron identification techniques, as well as increased the momentum identification capabilities for protons, kaons, and pions.

[9]The ERT sample in this work did not require detailed efficiency studies of the calorimeter as this sample focused on ratios of yields.

Fractional Efficiencies		
p_T[GeV/c]	π^+	π^-
5-6	0.26	0.26
6-7	0.24	0.23
7-8	0.22	0.21
8-9	0.20	0.19
9-10	0.17	0.17

Table 5.2: Geometrical acceptance efficiency of charged pions obtained through simulation of single particles.

have no detectors. The efficiencies found in this study show that as charged pions with larger momentum travel to the detector region, the efficiency drops. Ratios of pions ($\frac{\pi^+}{\pi^-}$), however, do not seem to change much across p_T.

5.2.4 Beam Shift Correction

Since there is no magnetic field in the tracking sub-detector regions (i.e within the drift chamber (DC), RICH and the pad chamber (PC) regions), charged tracks in the central spectrometers are reconstructed assuming a collision vertex in the geometrical center of the drift chamber. Hit associations in the drift chamber and first pad chamber (PC1) compared with a track reconstruction model are used to associate hits within a window of the track. In order to obtain accurate momentum reconstruction of charged tracks, offline corrections are made to the collision vertex. Displacements of the collision vertex from the detector's center can be caused by a shift of the beam of proton's axis or detector mis-alignment as the central spectrometers in PHENIX can roll in the *x* direction during detector access periods and normal beam operations. These vertex displacements,

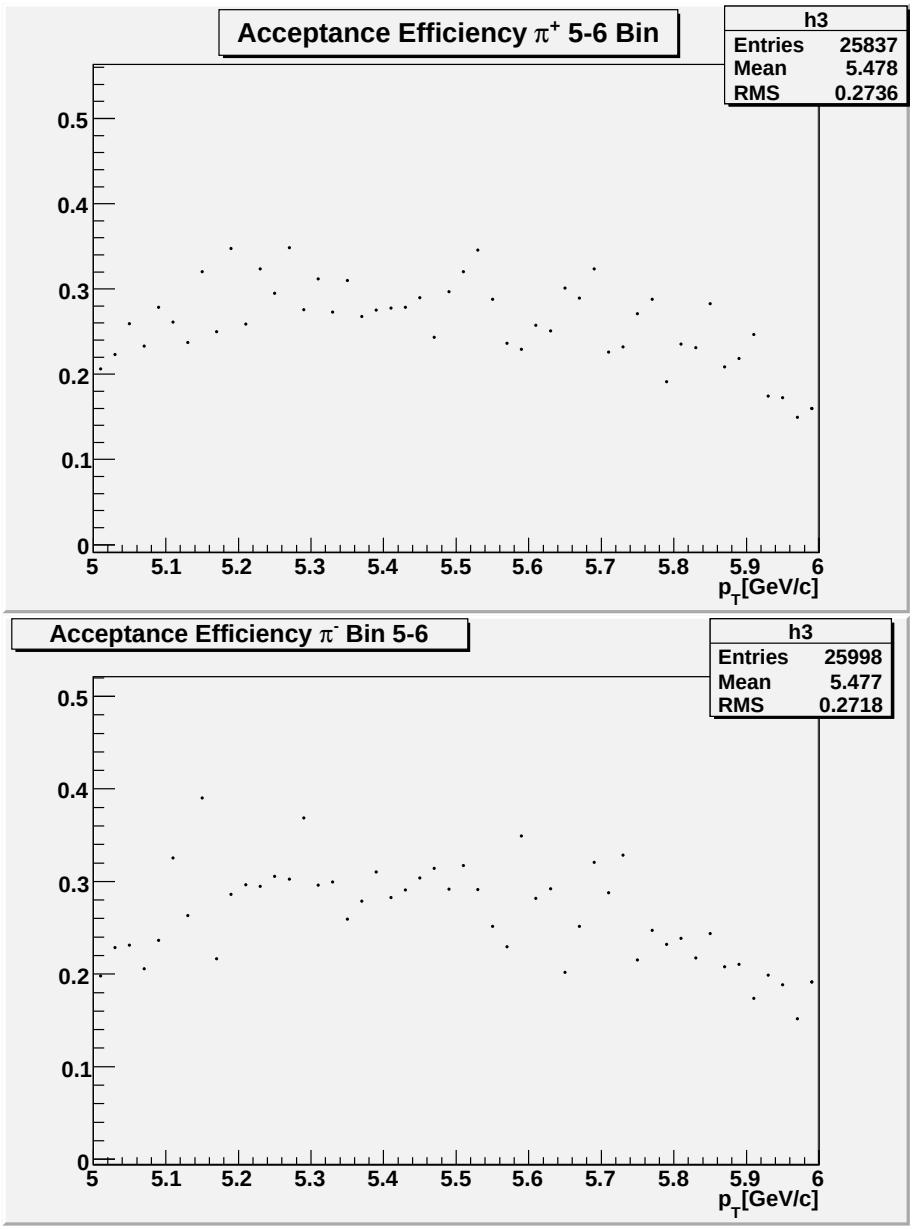

Figure 5.14: Detector acceptance within a p_T window of 5$< p_T <$6. Top panel are π^+, whilst bottom panel are π^-. Fluctuations point to point in histogram are due to histogram binning. Similar studies can be found in Appendix D.

which are called offsets, affect the *x* and *y* coordinates as they are related to the r-ϕ (Figure 5.15) slope, which are in turn used during momentum track reconstruction. To

calculate the amount the collision vertex was off-centered in the data[10], proton data under zero field conditions were analyzed. Zero field data is taken under zero magnetic field settings in the PHENIX detector, therefore the magnetic force will not act on the charged particles which otherwise bends their trajectory. To center the distribution of the shifted vertex of the expected straight tracks, the α and ϕ of charged tracks recorded by the drift chamber were studied. Since tracks are expected to be straight in the central arms, any ϕ-dependence of the measured track's azimuthal angle (α) gives a numerical measurement of the offsets in *x* (XOffset) and *y* (YOffset). Two main components were corrected in this portion of the analysis: an actual beam shift and a misalignment caused by the detector central arms being moved during detector access periods[11]. A beam shift is indicated by measuring non-zero *x* and y contributions which are equal in magnitude in East and West arms. A non-zero x component that has a different magnitude in the West and East arms is an indication of a detector misalignment. Corrections to both effects are done simultaneously as these effects are not decoupled in this analysis. In addition, a momentum scale correction was extracted from the offset measurements. By plotting α vs ϕ, one can then transform from polar coordinates to Cartesian to extract the remaining *x* and *y* offset components. The values thus obtained can be then applied to the applicable data via a master recalibrator that takes these calibration constants and

[10]Only 2006 data was calibrated for beam shift effect by the author of this work, 2005 data was not calibrated.

[11]During the beam operations, access to the detector is forbidden, as short lived radiation is present, when the beam is not present -or it is "dumped" in collider language-researchers and technicians can access the detector and make adjustments or repairs by rolling out the central arms.

recalculates the momentum. These corrections were made available to all physicists, and in addition, the method of calibrating the beam shift in PHENIX was standardized. Geometrically, an actual offset can be defined as a ϕ dependence on the α of the traveling charged particle:

$$\alpha\,\text{offset} = \frac{XOffset * \sin(\phi)}{R_{DC}} + \frac{YOffset * \cos(\phi)}{R_{DC}} \tag{5.5}$$

where R_{DC} = Drift Chamber radius = (220 cm). In this calibration, only drift chamber tracks of highest quality and probability were selected, the plots of α vs ϕ were first examined and fitted run by run[12], and finally were examined and fitted by fill[13] to combine statistics (Figure 5.16).

Beam Offsets			
XOffset	West	fill 7621:	-0.27 cm
XOffset	East	fill 7621:	-0.03 cm
YOffset		fill 7621:	0.19 cm
XOffset	West	fill 7641:	-0.29 cm
XOffset	East	fill 7641:	-0.05 cm
YOffset		fill 7641:	0.20 cm

Table 5.3: Drift Chamber's non-zero *x* and *y* values found after analysis of zero field runs. The *y* values are representative of both East and West arms, whilst the *x* values are separated by arm.

[12]A run is topically a fully data file which records several hours of proton collisions, when the proton beam is circulating the beam under stable conditions.

[13]A fill is defined as the time period encompassing one complete machine cycle. This includes the injection, acceleration, storage of colliding beams and ends with a beam dump.

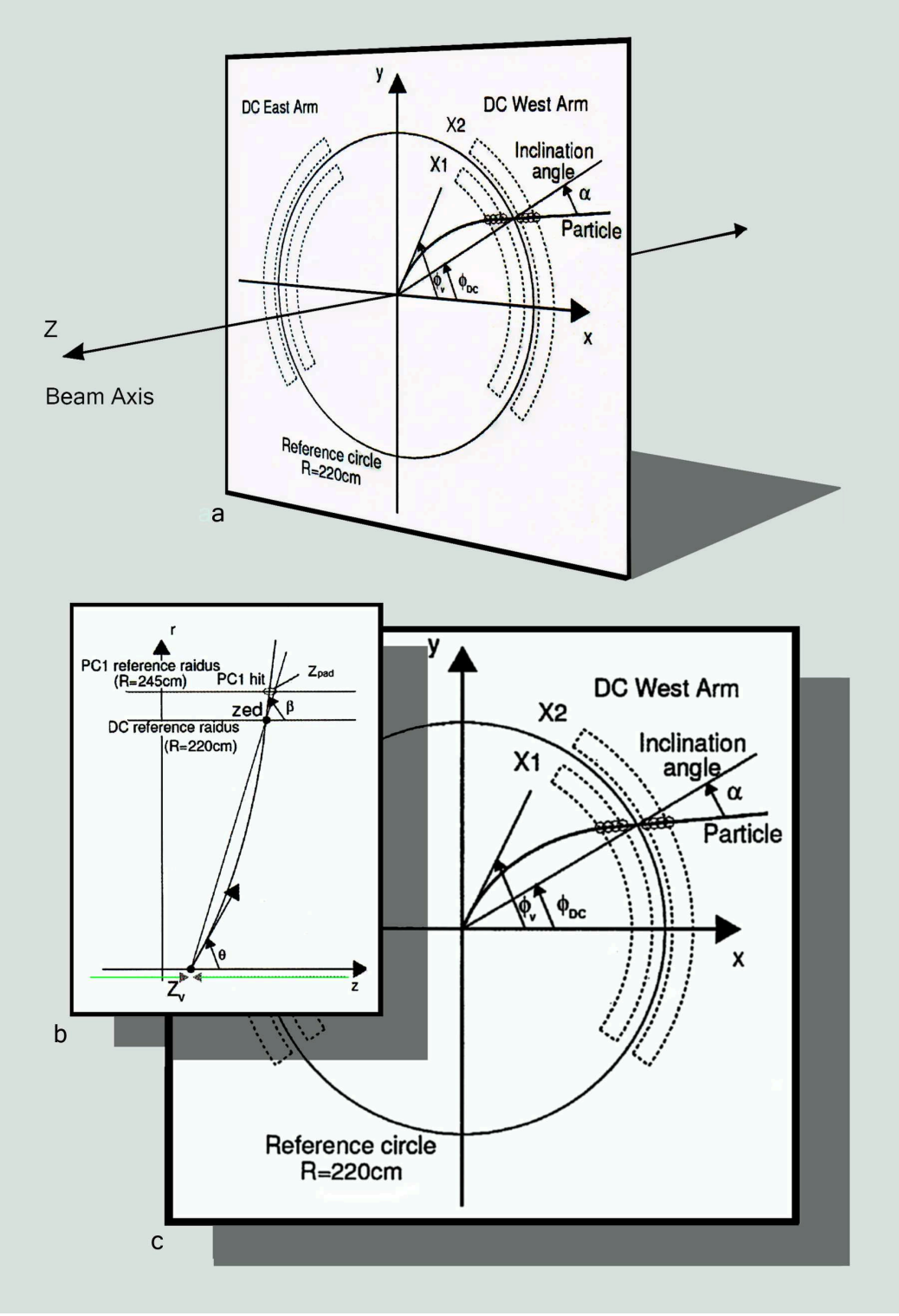

Figure 5.15: Schematic depiction of the DC's geometry. a) Shows the coordinate system, where *z* is defined by the proton beam's travelling direction. b) Shows the match of the z axis to the *x* and *y* DC coordinate. c) Shows the definition of DC angles which determine a particle's momentum.

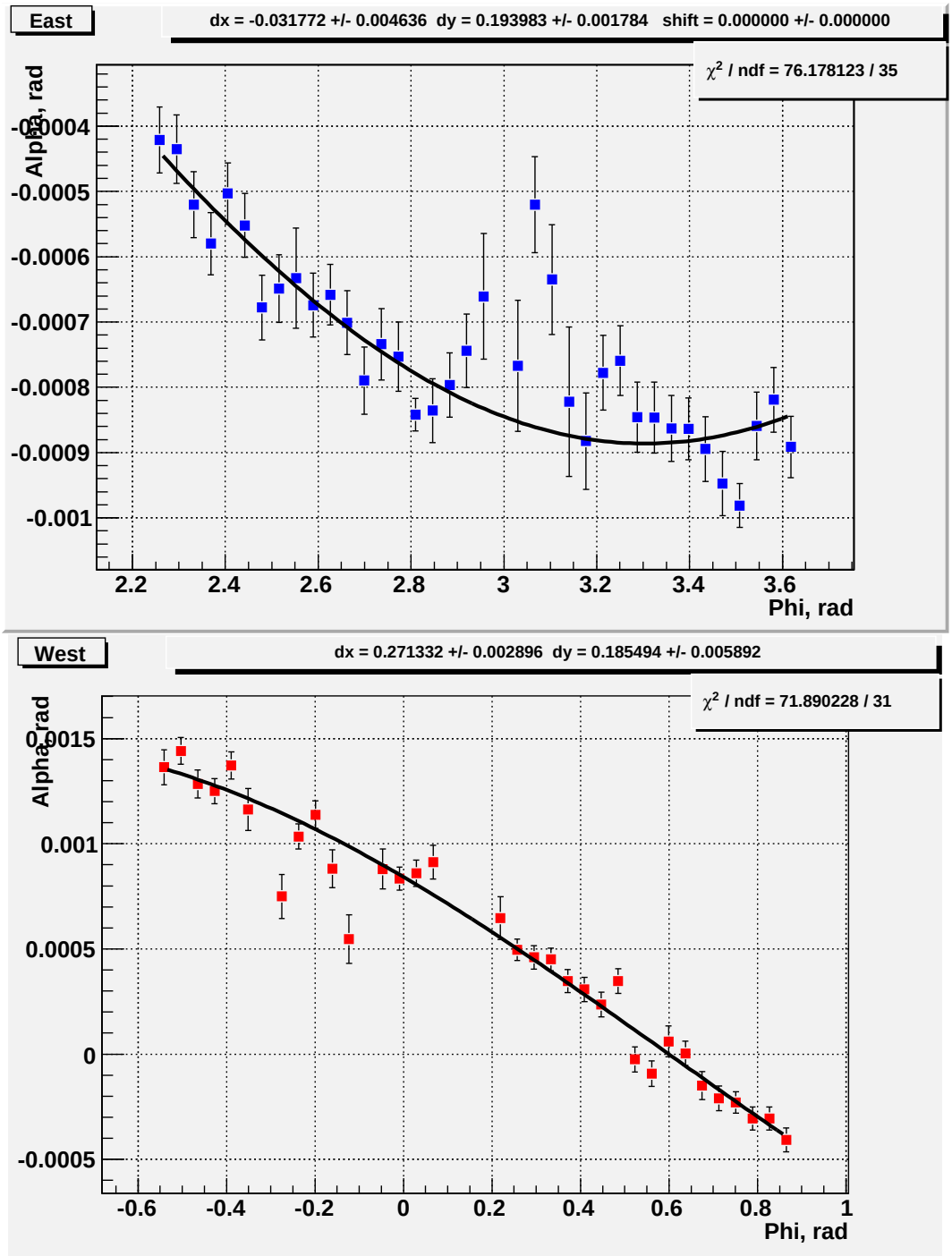

Figure 5.16: Fill combined fit of α vs ϕ plots. top (bottom) figure is East (West) arm. The points which seem to be out of range of the fit on the top figure are due to a large dead segment of the drift chamber, and thus statistics are limited in this region. (Figure 5.8 and Appendix B).

Figure 5.16 revealed that whilst the offset values in *y* were consistent in magnitude in both East and West arms, the *x* offset values were not (Section 5.3). This gave an indication of a detector shift as described above and the need to have corrections for the *x* offsets separated by PHENIX's West and East arms. There were two cross checks made to determine if the corrections obtained were accurate. The first one required the submission of the found offset values to a localized copy of the PHENIX calibration database. This applied corrections over the zero field data via a beam center recalibrator module[14]. Once the recalibrator corrected for the beam shift, inspection of ϕ were repeated to observe any dependence on α (Figure 5.17). If these dependencies disappeared and the transversing charged particles did not show any α dependencies, then the corrections were made permanent to PHENIX's official database and available to all physicists interested in the same data-set.

[14]This part of the calibration was only visible to the author of this work.

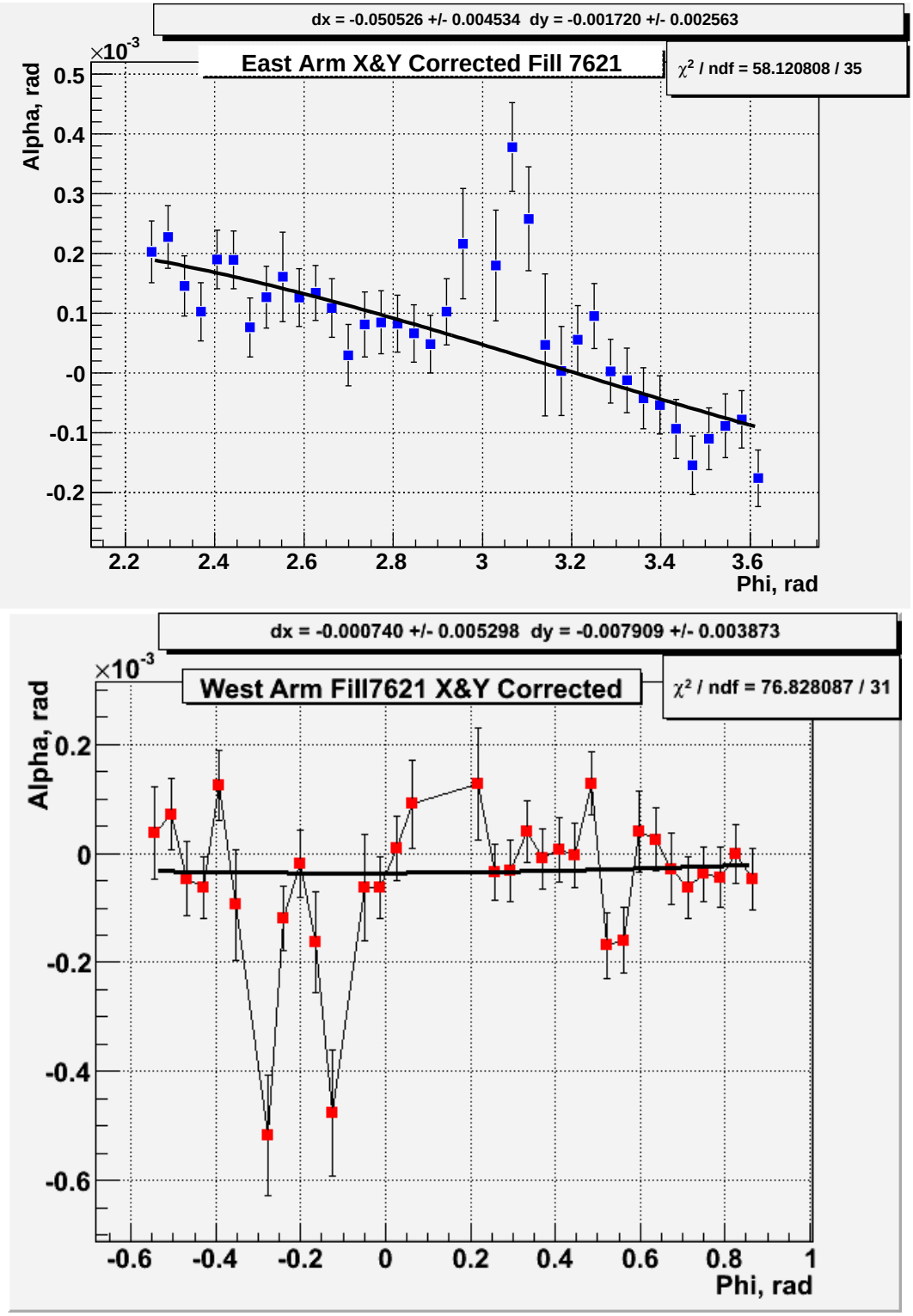

Figure 5.17: Drift Chamber's α vs ϕ distributions after corrections. Top (bottom) panels, represent the East (West) arms.

A second verification was performed to the beam shift calibrations over all data collected in 2006 for proton proton collisions at $\sqrt{s_{NN}} = 200$ GeV with the magnetic field on. Using other charged particle detectors, particles whose mass resolution is well known were identified. The mass-squared of protons and anti protons[15] was measured using the Time of Flight. (The time of flight is a limited acceptance detector in PHENIX, which can identify a variety of charged particles[3] at low momentum ranges). A beam shift in the data can be detected by looking for a shift in the mass squared value in opposite directions for protons and anti protons due to the magnetic bend the charged particles experience. The mean of the p and $\overline{p}$ mass distributions will not only differ from the established world value referred in the particle data book (PDG)[13], but these p and $\overline{p}$ values will be shifted in opposite directions according to their charge (Figure 5.18, top panel). Once the beam calibrations were applied to the data (Figure 5.18, bottom panel), one can see that not only do the mass values become aligned for the p and $\overline{p}$, but the width of their mass distributions were also narrower, indicating higher precision. The actual m^2 value obtained from calibrated p and $\overline{p}$ tracks is then used to obtain a momentum scale correction, which will be described in the following section.

[15]This is known at PHENIX to high resolution with other detectors and is used as verification of the tuning of the detectors.

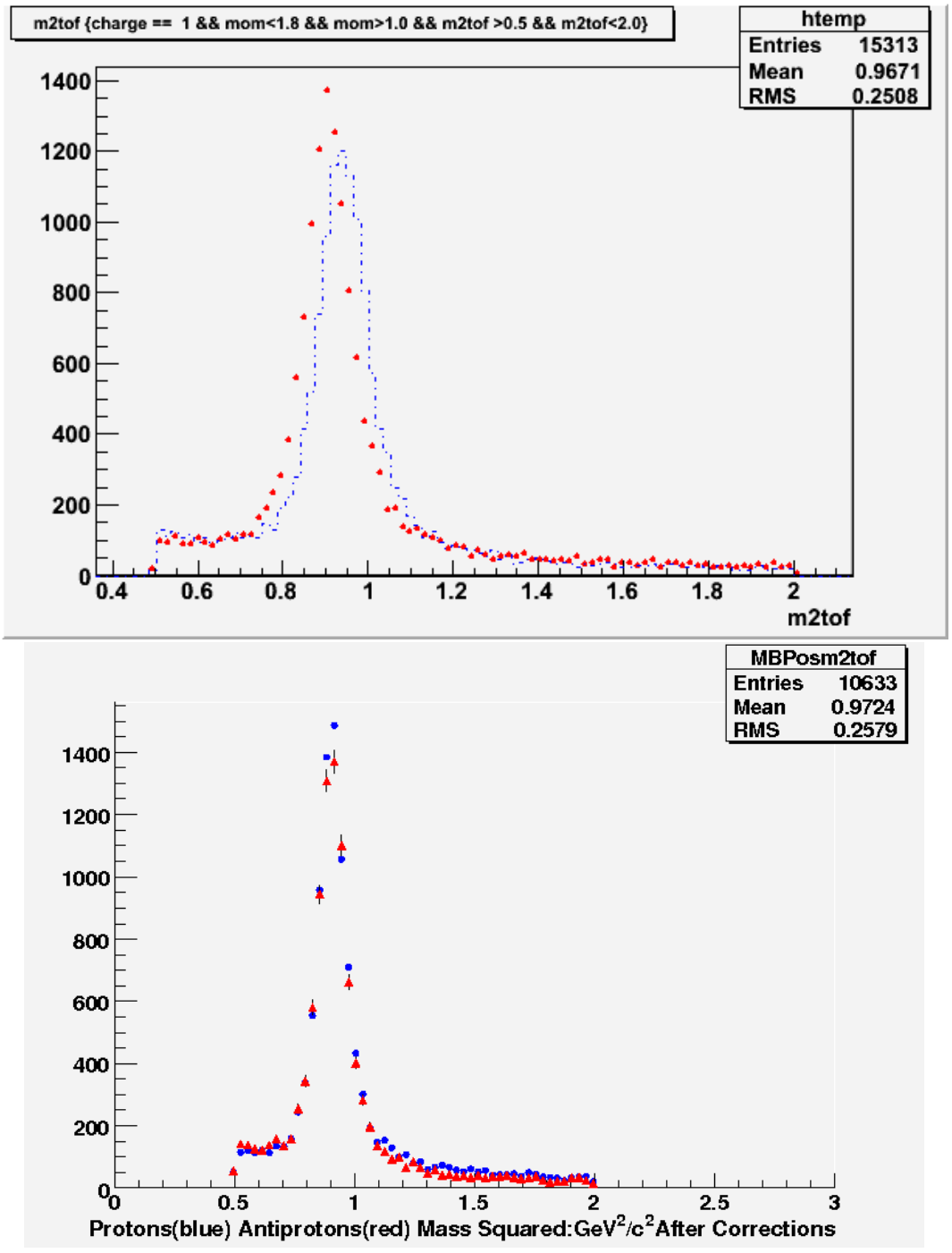

Figure 5.18: Mass-squared using the time of flight of identified protons (blue) and anti-protons (red). Before (top) and after (bottom) beam shift corrections.

5.2.5 Momentum Scale Correction Using Protons and Anti-protons

Using the Time of Flight sub-detector, the mass-squared distribution of protons and anti-protons was measured and compared to that from the particle data book [13]. Charge separated mass-squared distributions within an mass-squared range of 2 (GeV/c^2)^2 $>$ m^2 $>$(0.5 GeV/c^2)^2, measured with high quality drift chamber tracks within a momentum range of 1.0 GeV/c $<$p$<$ 1.8 GeV/c, were studied (Figure 5.19). A clear narrow peak was obtained and the signal and background was fit to a second degree polynomial plus a Gaussian. The mass-squared values obtained from the fit for protons and anti-protons was 0.906 $\pm$0.001 (GeV/c^2)^2. Using the Time of Flight as the main detector for identification, a simple relation (Equation 5.6) connects the m^2 obtained to the momentum of the particle:

$$m^2 = p^2 * \sqrt{t^2/(L^2 - 1)} \tag{5.6}$$

where *t* and *L* are known variables indicating time of flight (*t*) of particle and distance (*L*) from collision to detector respectively. The peak of 0.906 (GeV/c^2)^2 compared to the PDG value of 0.880 (GeV/c^2)^2 yields a scale of $\sqrt{0.97}$ or 2% from unity.

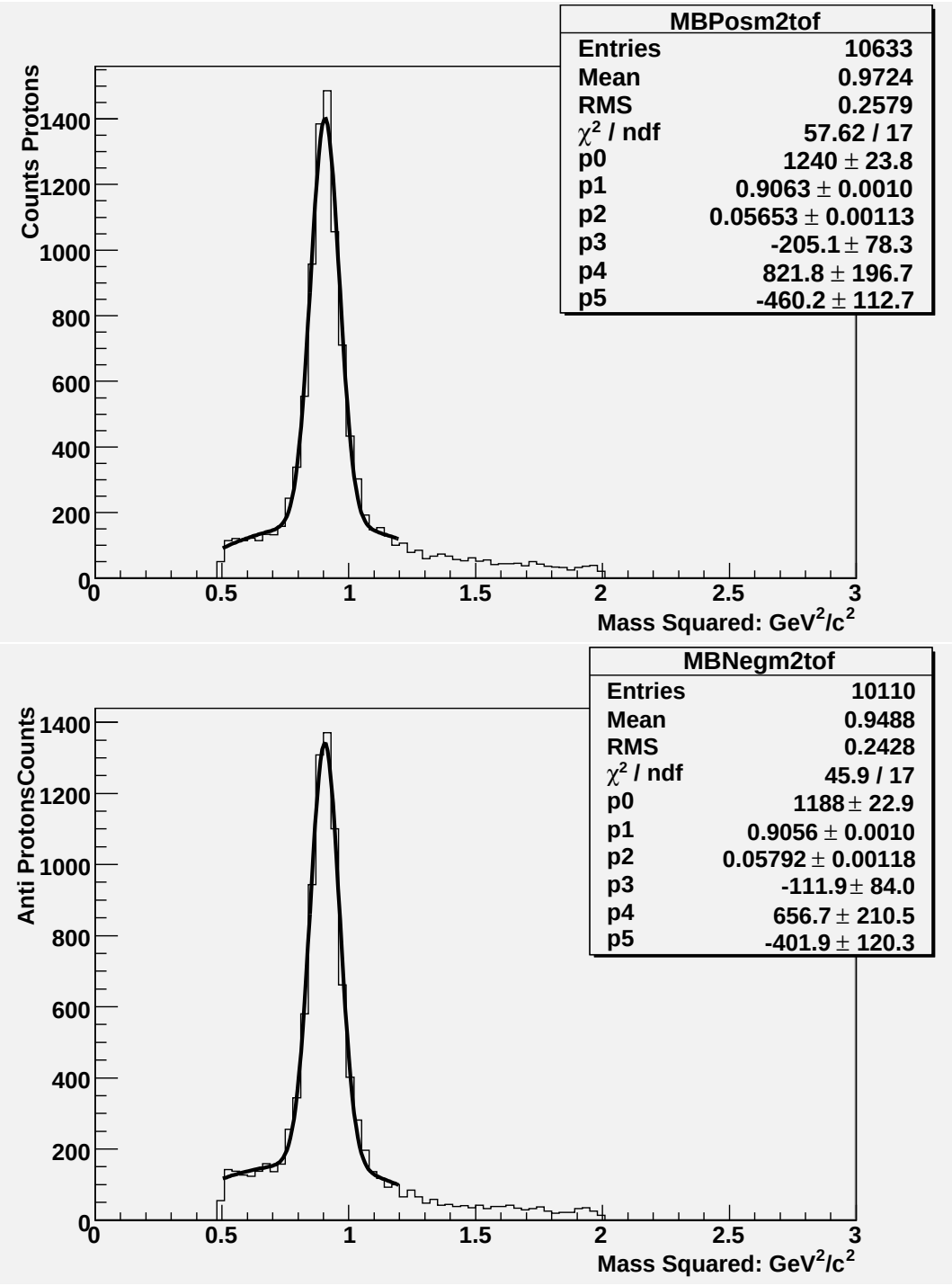

Figure 5.19: Mass peak squared of protons(top) and anti-protons (bottom), fitted to a second degree polynomial plus a Gaussian.

5.2.6 Beam shift Cross Check Using Charged Pions

A final validation of the calibration was performed by inspection of high-p_T charged pion candidate spectra. As pions fire the Čerenkov counter at around a p_T of $\sim$4.7 GeV/c, a mismatch of the turn on curves could be an indication of beam center misalignment. The verification, in particular, tested the longitudinally polarized data, which was the data collected towards the end of the 2006 data taking period.[16] Verification was done with inspection of the Čerenkov light turn-on threshold for charged pions. This light turn on could be clearly seen around 5 GeV/c for both charged species matched at the same Čerenkov radiation threshold of 4.7 GeV/c (Figure 5.20).

[16]The calibrations performed, were applicable to a wide data-set which included both transverse polarized and longitudinally polarized proton beams.

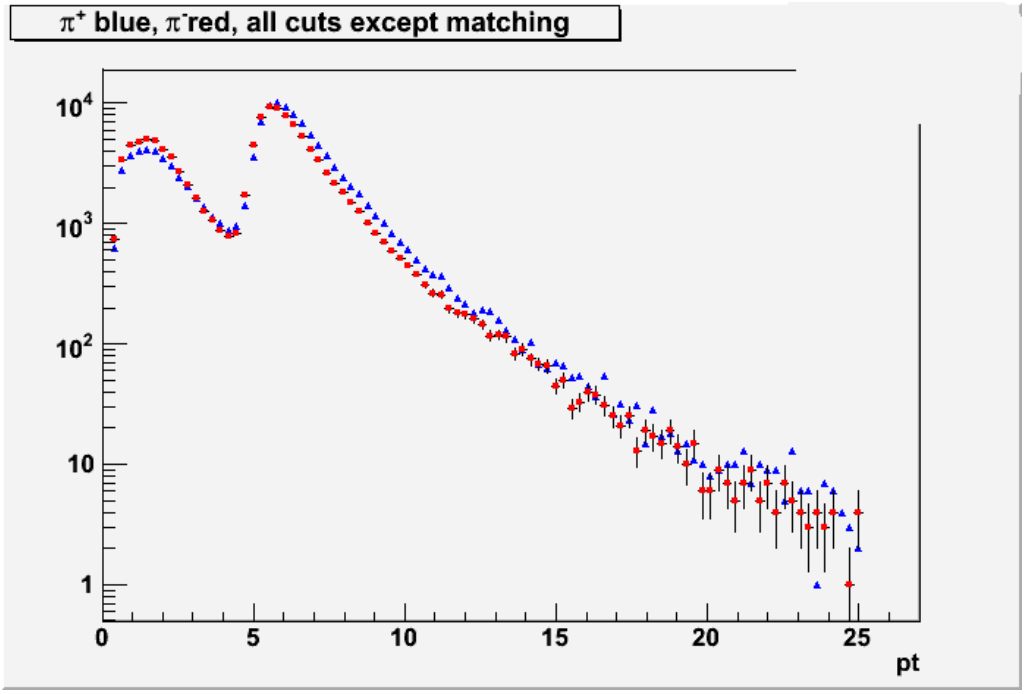

Figure 5.20: High-p_T charged pion candidates firing the RICH. RICH threshold for pions highlight the peaks of both π^+ (blue) and π^- (red) at 4.7GeV/c as expected.

5.2.7 Momentum Resolution of the Charged Tracking

The DC in PHENIX's central arms provides the tracking for high resolution transverse momentum measurements of charged particles. The drift time of ionization electrons in the gas is used to calculate the position of the ionizing particle, thus there are factors than can degrade the spatial resolution of the momentum measurement, such as electron diffusion and electronics signal time start uncertainty. To measure the resolution of the momentum for the charged tracked data used in this work, two methods were developed. The momentum resolution, using the same zero field data discussed on the previous section, was calculated and compared to a simulated detector response data with similar detector dead channels and/or maps as those found in the data under study. The main motivation for this measurement was primarily to establish and standardize the procedure. The results obtained are used as a systematic error quantification of the momentum, as well as accountability of detector's finite momentum resolution for a cross-section measurement.

Procedure for Momentum Resolution Determination

The procedure entailed comparing the azimuthal angle (α) resolution to that found in simulated data. To first order the momentum is measured by α according to Equation 5.7, where the constant in the formula corresponds to a magnetic field integral kick of K_1:

$$K_1 = \frac{constant}{R_{DriftChamber}} \int lBdl \tag{5.7}$$

$$\alpha = K_1 * \frac{1}{p} \tag{5.8}$$

As a result of Equation 5.7, a first derivative will give a first order measurement of the momentum resolution:

$$\begin{aligned} \frac{\partial \alpha}{\partial p} &= K\left(\frac{1}{p^2}\right) \\ \delta\alpha * p_T &= K(\frac{\delta p_T}{p_T}). \end{aligned} \tag{5.9}$$

The constant can be extracted from data and compared to values obtained in simulation. In this measurement, MB data was used at $\sqrt{s} = 200$ GeV. The results of measuring α and comparing data and simulation can be found in Figure 5.21 for π^- and Figure 5.22 for π^+. The magnitude of the values of the constant from these figures is $|0.10|$, a value consistent for both charges and in perfect agreement between samples. The consistency between data and simulation indicates accuracy in the B field configuration.

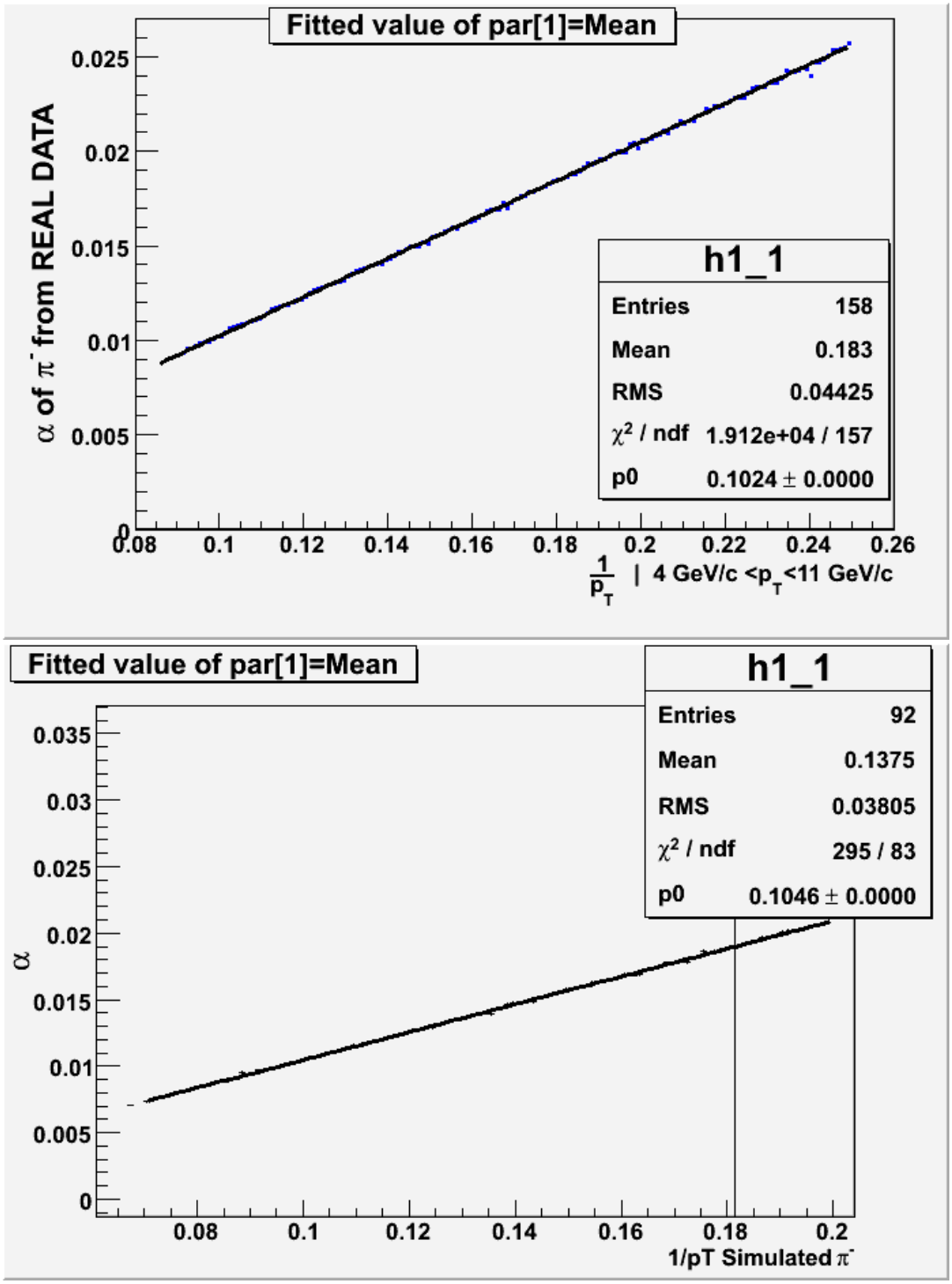

Figure 5.21: α vs $\frac{1}{pT}$ of π^- and negative charged tracks. Comparison of data collected from 2006 with a minimum bias trigger (top panel) and simulation (bottom panel.) Simulation consists of single particle pions.

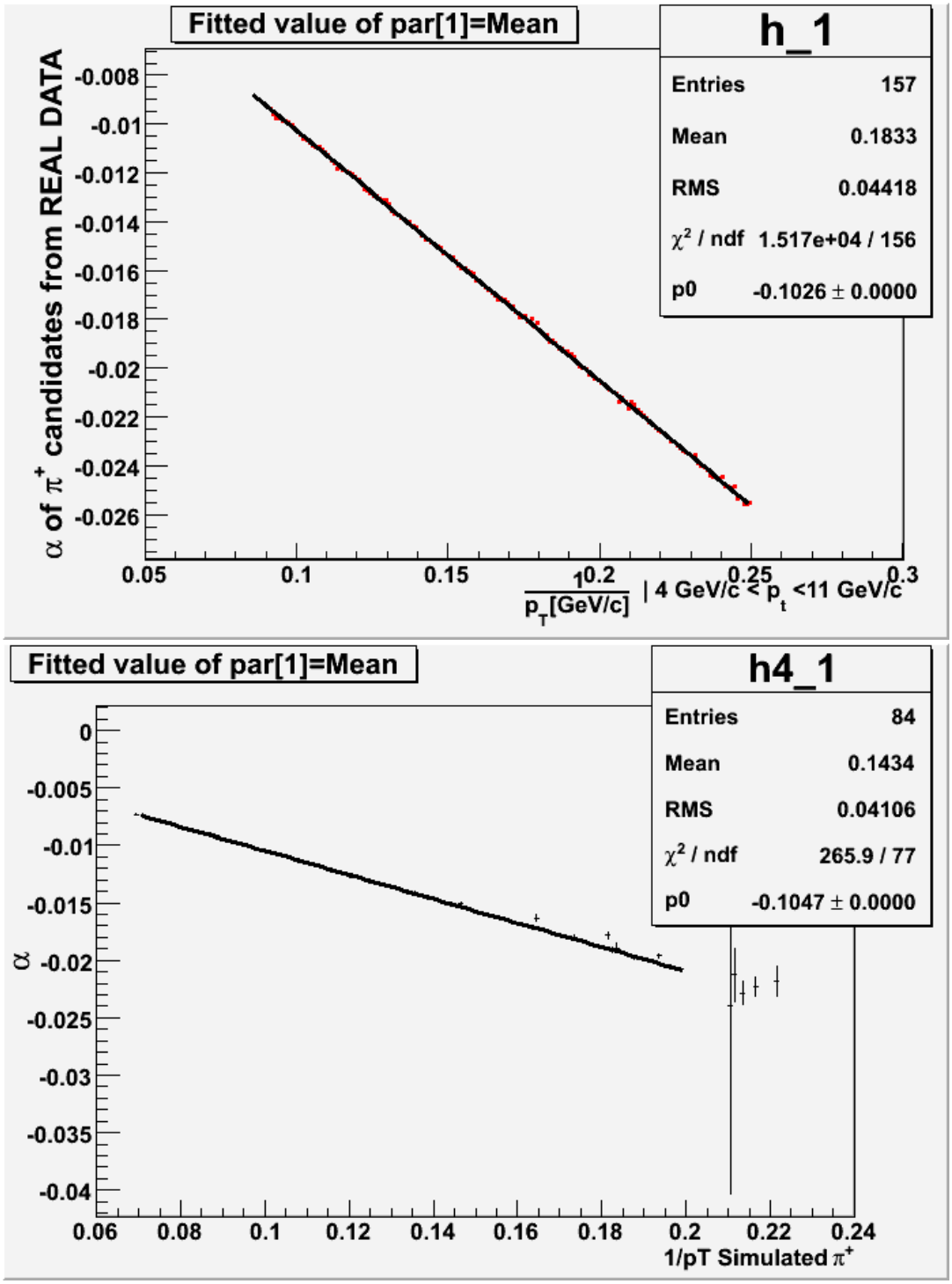

Figure 5.22: α vs $\frac{1}{pT}$ of π^+ and positive charged tracks. Comparison of data collected from 2006 with a minimum bias trigger (top panel) and simulation (bottom panel.) Simulation consists of single particle pions.

Momentum Resolution Obtained from Zero Magnetic Field Data

As mentioned several times in this work, the momentum scale depends on the magnetic field in the path of the charged particles. Momentum reconstruction is performed assuming the beam vertex is located at the geometrical center of the drift chamber (Figure 5.15). This means that momentum will also be affected by misalignment of the central arms or a shift of the beam vertex. Calibrations were performed to these misalignments and the results of these were already discussed in Section 5.2.4. Similar to previous sections, the α distributions were inspected, however for this part of the measurement, the precision of α was important as the momentum resolution was under study. Figure 5.23 shows the measured α distribution for the data sample relevant for the measurements presented in this work. The distributions of α is fit with a double Gaussian function and the fitting parameters yield the resolution given by the drift chambers and the charged tracking reconstruction. The width of the distribution for Figure 5.23 is **1.3mrad** (Equation 5.9). The Figures 5.24 show similar distributions with minimum energy requirements of of 500 MeV (top panel) and 800 MeV (bottom panel). Since the measured angle distributions are taken with zero magnetic field conditions, a multiple scattering term exists which is mainly caused by low momentum particles. A minimum energy requirement can thus help estimate this scattering term emerging from the otherwise low energy particle background. The resolution with a minimum energy requirement of 500 MeV is **1.1 mrad**. Similarly, a cut of 800 MeV gives an α resolu-

tion of **1.1 mrad** which summarizes to a resolution of $1.1\%p_T$ obtained from real data (Equation 5.9).

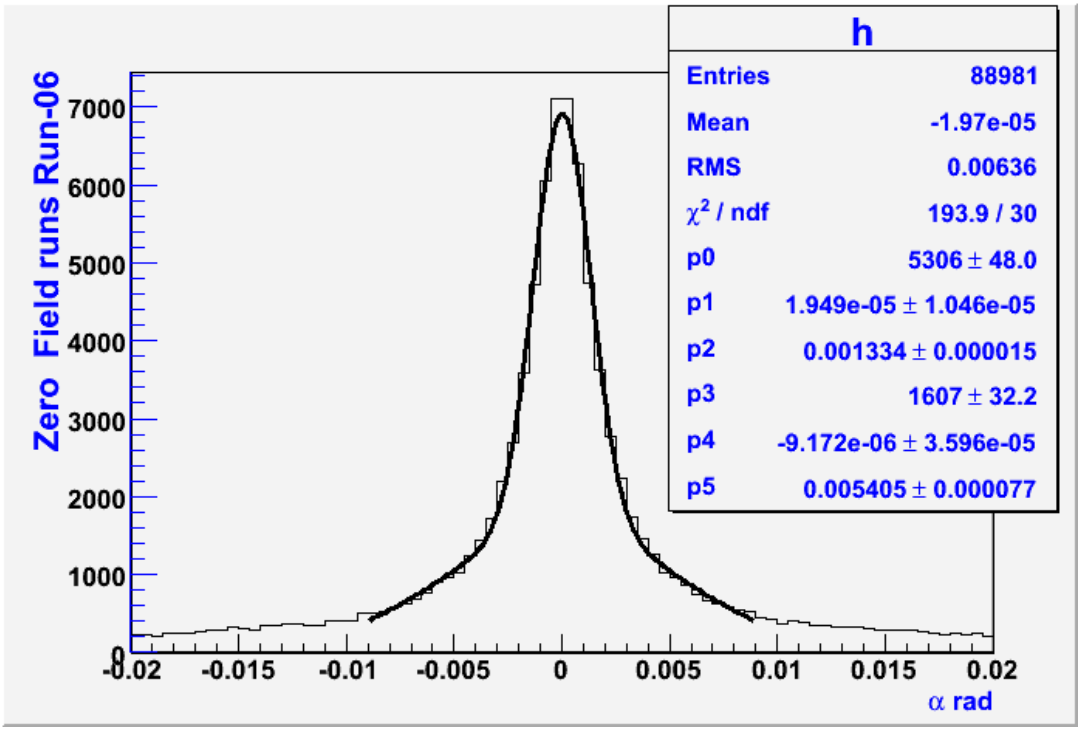

Figure 5.23: α (rad) resolution and yields from zero magnetic field data. The first three parameters correspond to the result of the Gaussian fit. *p2* in this case is the width of the Gaussian and it represents the resolution in *mrad* of the drift chamber's α. (Figure 5.15).

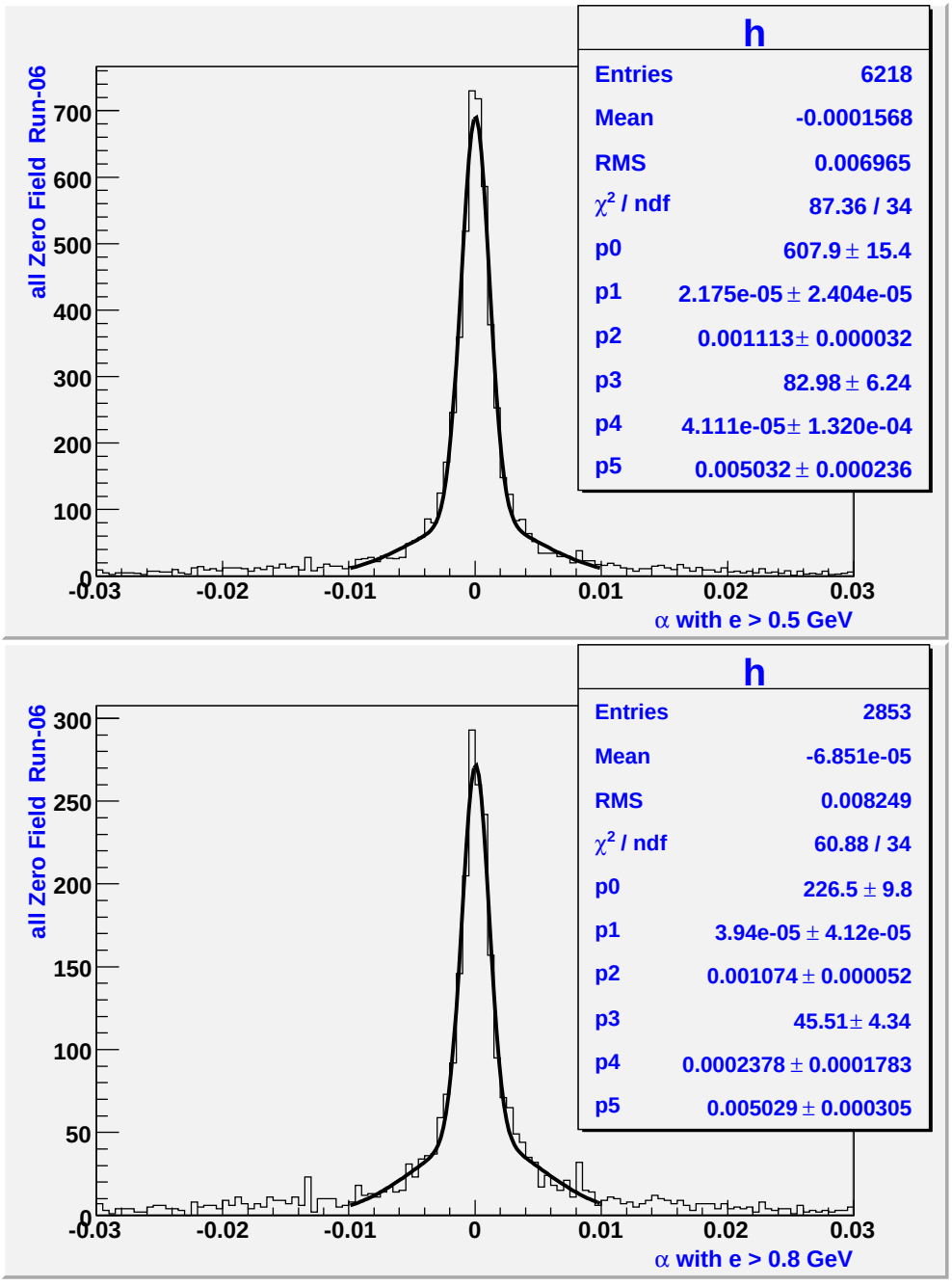

Figure 5.24: α (rad) resolution and yields of data with a minimum energy cut of 500GeV (top panel) and 800MeV (bottom panel.) The first three parameters correspond to the result of the Gaussian fit. *p2* in this case is the width of the Gaussian and it represents the resolution in *mrad* of the drift chamber's α (See Figure 5.15).

Momentum Resolution from Simulated Zero Field Data

Simulated single pions were generated and exposed to detector geometrical conditions as it was discussed in Section 5.2.1. PHENIX sub-detector configurations were incorporated with the notable exception of the magnetic field, which was set to zero to allow comparisons to data presented in previous section. The simulated p_T distribution was flat in a range 2-10 GeV/c. The measurement of α from these studies showed a resolution of $0.63\% p_T$ and $1.1\% p_T$ when the tails of the distribution were not ignored. The value of 0.6% from the limited range Gaussian shown in Figure 5.25 and Figure 5.26 is lower than the resolution obtained from zero field data, however the larger Gaussian from a double Gaussian fit matches the data. Note that the simulated sample consists of pure charged pions at high p_T. In contrast, zero field data from real proton proton collision events contain a much wider p_T range. Furthermore, data consists of all charged particles proceeding from proton proton collisions combined with an underlying background and a multiple scattering term[17]. It is thus a reasonable find that the momentum resolution is lower in a simulation of pure charged pions. In the next subsection, the multiple scattering term is estimated based on material interaction lengths.

[17]For real data, a narrow Gaussian is selected. For simulated data consisting of pure high $p_T \pi^{\pm}$ selecting the narrow Gaussian of a double Gaussian fit may be misleading an ignoring the tails may give a too good of an α, thus a limited range Gaussian or the bigger Gaussian may give a more accurate description in this case.

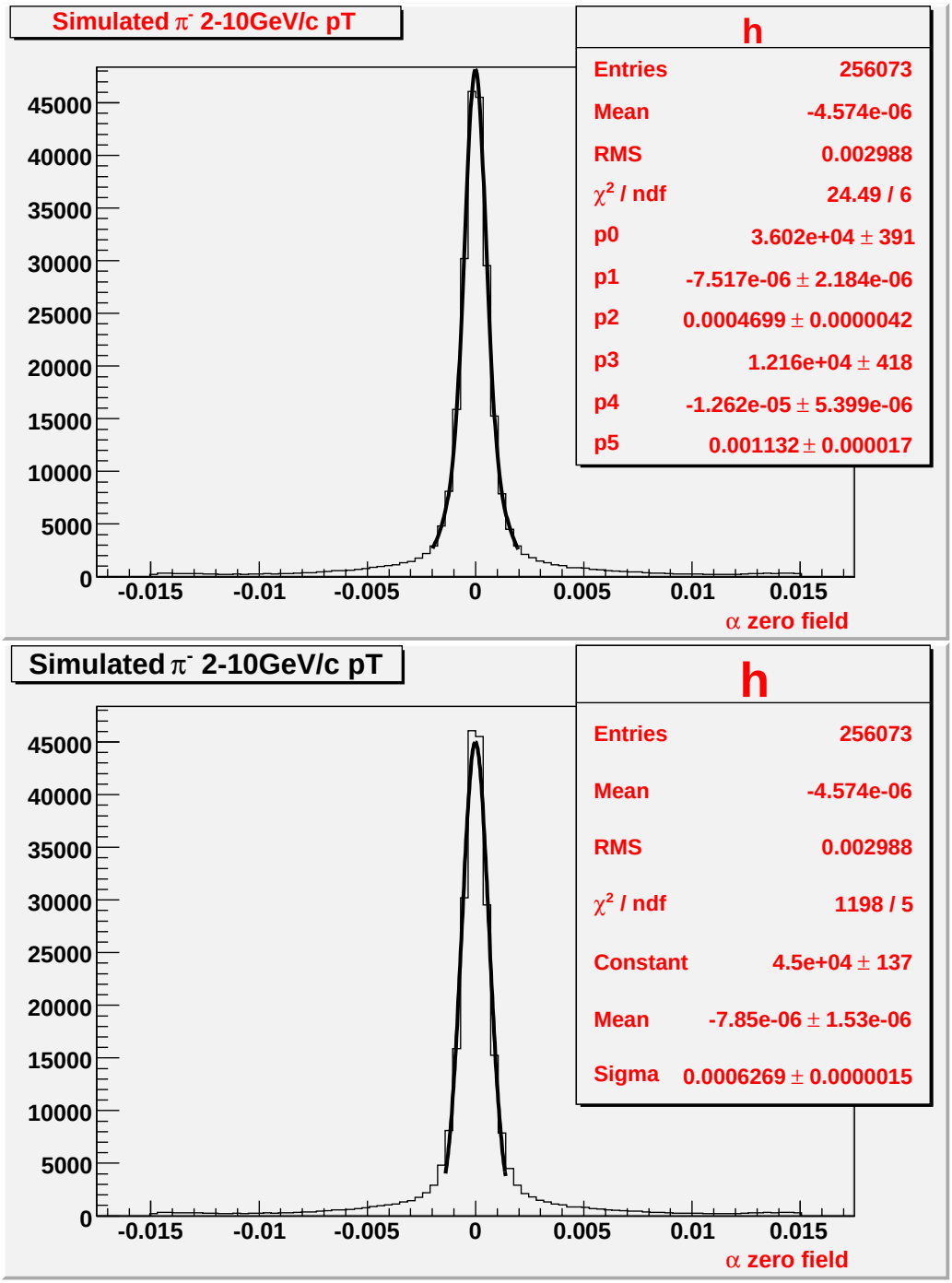

Figure 5.25: α (rad) distribution of simulated zero field run conditions. Top panel shows the α resolution of π^- obtained from a Gaussian fit for the p_T range of 2-10GeV/c. Bottom panel shows similar distribution with a fit to a limited range Gaussian function.

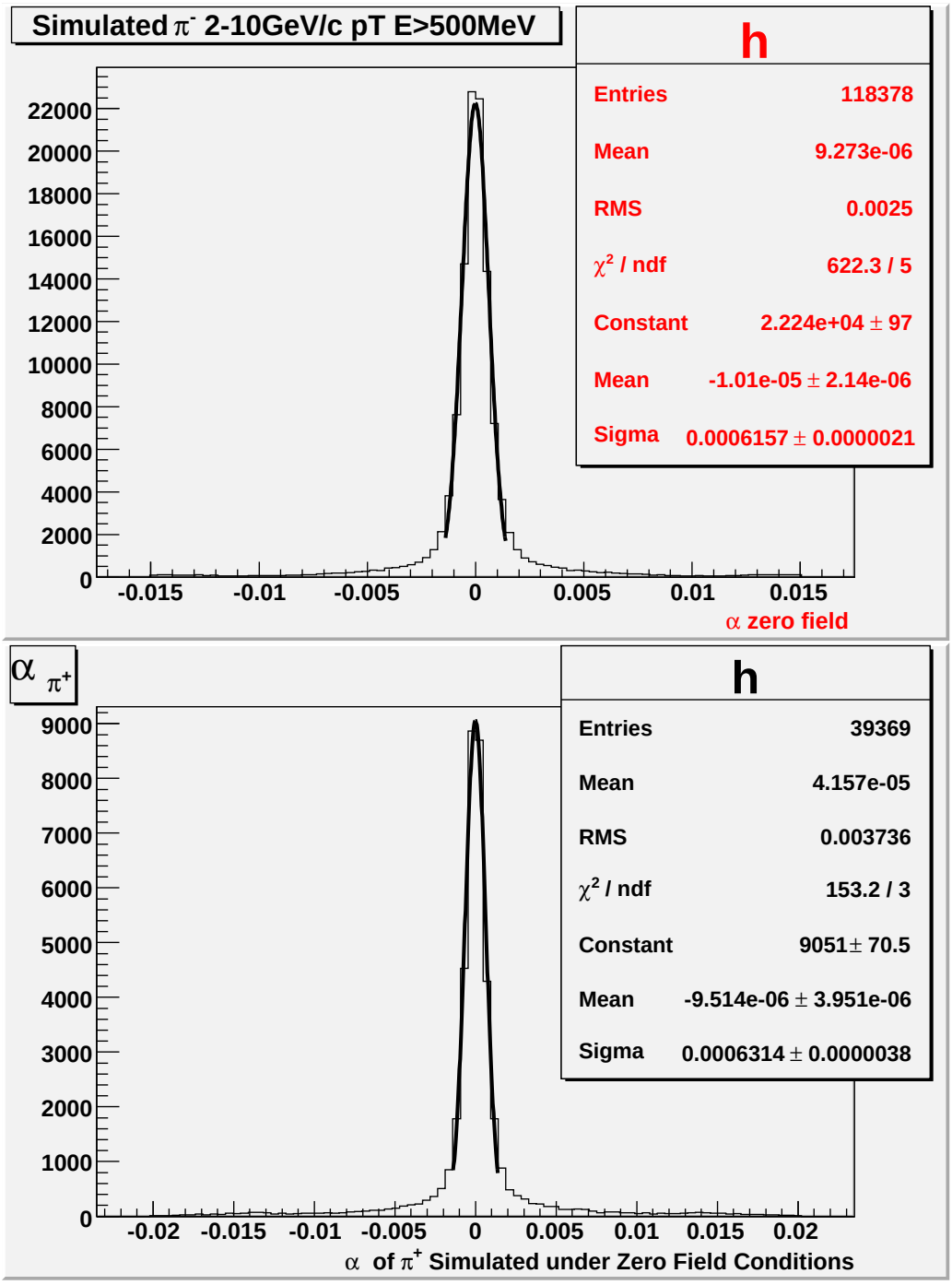

Figure 5.26: Simulated zero field run conditions. α (rad) resolution of π^- (top panel) and π^+ (bottom panel) with a minimum energy cut of 500 MeV.

5.2.8 Estimate of the Multiple Scattering Contribution to the α Resolution

As revealed in the previous section, the momentum resolution of charged tracks at PHENIX is limited at high momenta by the drift-chamber's resolution and at low momenta by multiple scattering. A minimum energy deposition requirement of 500 MeV and 800 MeV from the measured α in the data can give an estimate of the multiple scattering term (Figure 5.27) as this affects low momentum particles scattering of detector material. Two energies are used to check the variations on the multiple scattering term estimate. The hadronic interaction energy, which becomes important above the minimum ionizing particle threshold of 300 MeV, is not known in the PHENIX simulation package. No high energy test beam data exists which would be needed to understand the detector response to hadron energy depositions in the electromagnetic calorimeter. Another method is used to measure the multiple scattering term estimated by the minimum energy deposition requirement of 500 MeV in reconstructed charged particles. The average multiple scattering contributions at an angle θ_{ms} and at the distance R in the drift chamber radius, which is 220 cm (Figure 5.2.8), can be expressed as:

$$\Delta_{\alpha} = \theta_{ms} R / R_{dc} \tag{5.10}$$

The multiple scattering contribution can be calculated using using the interaction

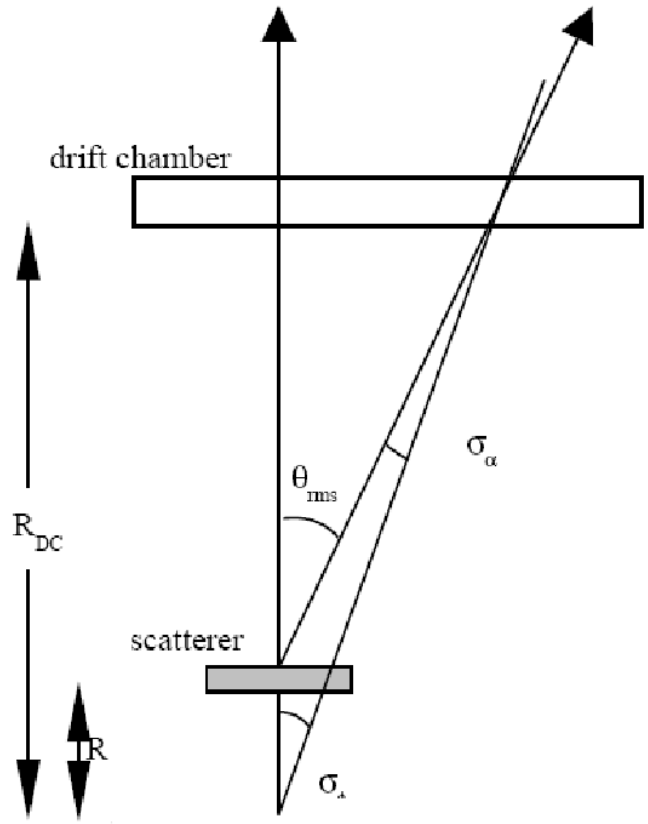

Figure 5.27: Illustration showing the multiple scattering interactions.

data on materials which are relevant for the PHENIX detector settings (Table 5.4). The estimated scattering combined term from materials is 0.26 mrad, which is consistent with the estimate made with the minimum energy requirement previously (0.23 mrad and 0.26 mrad). In the simulation, it is not expected that a multiple scattering term should contribute as particles are selected at high momentum from a pure sample of charged pions.

Multiple Scattering Contributions					
Material	Thickness (cm)	σ(X/Xo-mrad)	R(m)	θ_{ms}(mrad)	δ_α(mrad)
Be Beam pipe		0.3	0.04	0.58	0.01
DC Mylar Window	0.2	0.07	2.0	0.26	0.24
Total		0.37	-	-	0.26

Table 5.4: Materials in front of the drift chamber and their estimated contribution to δ_α. The values correspond to the uncertainty in the momentum as explained in Formula 5.9. Resolution in mrad directly translates to an uncertainty on the momentum. X/Xo is the contribution due to the radiation length.

5.2.9 Summary of Momentum Resolution Studies

The momentum resolution obtained from data for high p_T charged tracks was $\delta_\alpha/p_T = 1.1\%p_T$. The multiple scattering term was measured with a minimum energy requirement and material data interaction information. The obtained value of 0.3 mrad only affects low p_T tracks (which are not the subject of this work). The low p_T and high p_T resolution is thus $\delta_\alpha/p_T = 0.3\% \otimes 1.1\%p_T$. The simulated data yields a high p_T angular resolution of $0.6\%p_T$ using single high p_T charged pions as input to detector simulations. The difference of the momentum resolution from data and simulation is assigned as a systematic uncertainty.

5.3 Ring Imaging Čerenkov Counter (RICH) Studies

The main method of identifying charged pions in PHENIX, at the transverse momenta of interest, is by looking at produced Čerenkov light in the Ring Imaging Čerenkov Counters. This gas detector has a high angular segmentation with pions emitting light

Particle	Emitting threshold(GeV/c)
e^+, e^-	0.017
μ^+, μ^-	3.5
π^+, π^-	4.7
K^+, K^-	16
p^+, p^-	30

Table 5.5: PHENIX RICH thresholds for various charged particles.

above 4.7 GeV/c because of the CO_2 radiator within the RICH gas vessel. All particles that produce light in the RICH are listed in Table 5.5. For light emitting particles, the charged track will be identified in the drift chamber. This initial drift chamber information will be used by the Čerenkov counter to reconstruct a projected hit around a ring or a disk corresponding to the cone of light from the traveling particle which will begin to radiate light. The measurements presented in this work are only concerned with 5 GeV/c $<$p$_T$ $<$10 GeV/c as this range provides the maximum gluon-quark scattering contribution (Figure 2.3). Within this momentum range only $\pi^{\pm}$, $e^{\pm}$ and $\mu^{\pm}$ can produce Čerenkov light. Primary electrons and positrons as well as muons have lepton to pion production ratios around 10^{-4}. Thus primary $e^{\pm}$ and $\mu^{\pm}$ which emit light in the RICH pose little contamination threat. e^+e^- which do not come from the vertex will emit light at nearly 99$\%$ efficiency. It is these Čerenkov light emitting particles which are studied further in the following sections.

5.3.1 Separating Pions from Electrons with the RICH

The RICH has a charged pion threshold of 4.7 GeV/c, and whilst electrons can also fire the RICH at this threshold, pions can be distinguished from electrons. Exploiting these differences can help in estimating the electron positron background. Production of photoelectrons (electrons released or ejected from a photoelectric substance having absorbed energy from incoming light) in the RICH proceeding from electrons above 500 MeV/c is constant whilst the number of photomultiplier (PMT)[18] tubes firing increases steadily for pions with a plateau around 5 GeV/c. Electrons produce distinct rings or a "corona," while pions, having a smaller cone radius, will fire the RICH over a disk. Moreover, an electron will fire six PMTs in average, while a charged pion's firing will increase approximating the efficiency of electrons with increasing p_T and plateau around five PMTs. The radius of the Čerenkov cone of light was studied by analyzing the disk of light produced by particles. The variable which measures this disk is called $n1$. $n1$ represents a disk of radius 11 cm encircling the projected hit location of an identified drift chamber track. To ensure that charged pion tracks are selected, a requirement of more than zero PMTs is made (Figure 5.28). Figure 5.29 shows the expected turn on curve for charged pions around 5 GeV/c. A ring of detected light ($n0$) (Figure 5.30) was also studied. $n0$ represents hit PMTs in a ring with inner radius 3.4 cm and outer radius of 8.4 cm around the projected track on the PMT plane of the RICH. The expected

[18] Photocathodes that convert photons to photoelectrons via the photoelectric effect.

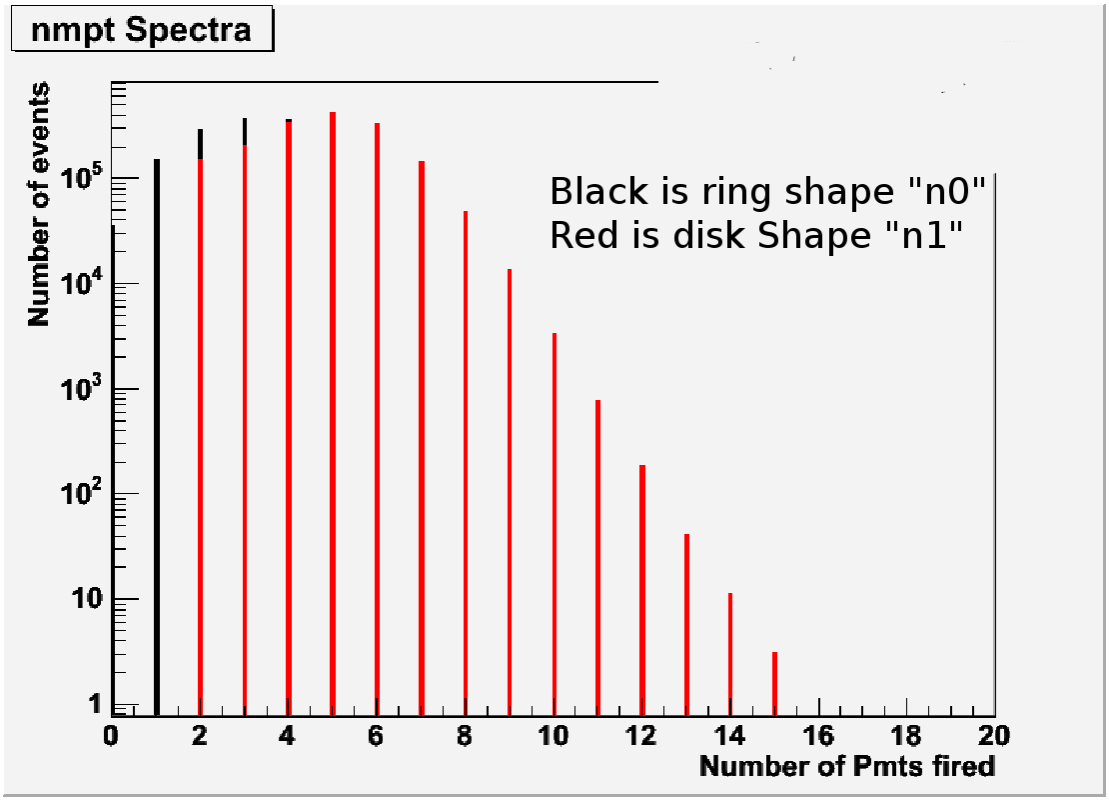

Figure 5.28: Number of RICH photomultiplier tubes firing in the vicinity of a projected DC track. The red histogram shows the number of tubes fired in a disk area ($n1$), while black is a ring ($n0$). Data correspond to the full 2005 data sample. The x axis represent the integer number of PMTs being fired, while the y axis represents the number of particles. Black histograms start at x values of zero while red histogram start at x values of two.

radius of a Čerenkov ring emitted by an electron is expected to be 5.9 cm, and the width of $\pm$ 2.5 cm around this corresponds to the position resolution of the PMT. Figures 5.30 to 5.32 show the RICH turn on curves as a function of p_T for $\pi^{\pm}$ and $e^{+}e^{-}$. The pions are separated from the $e^{\pm}$ as can be clearly seen in the distributions. These figures will also be relevant in the next section.

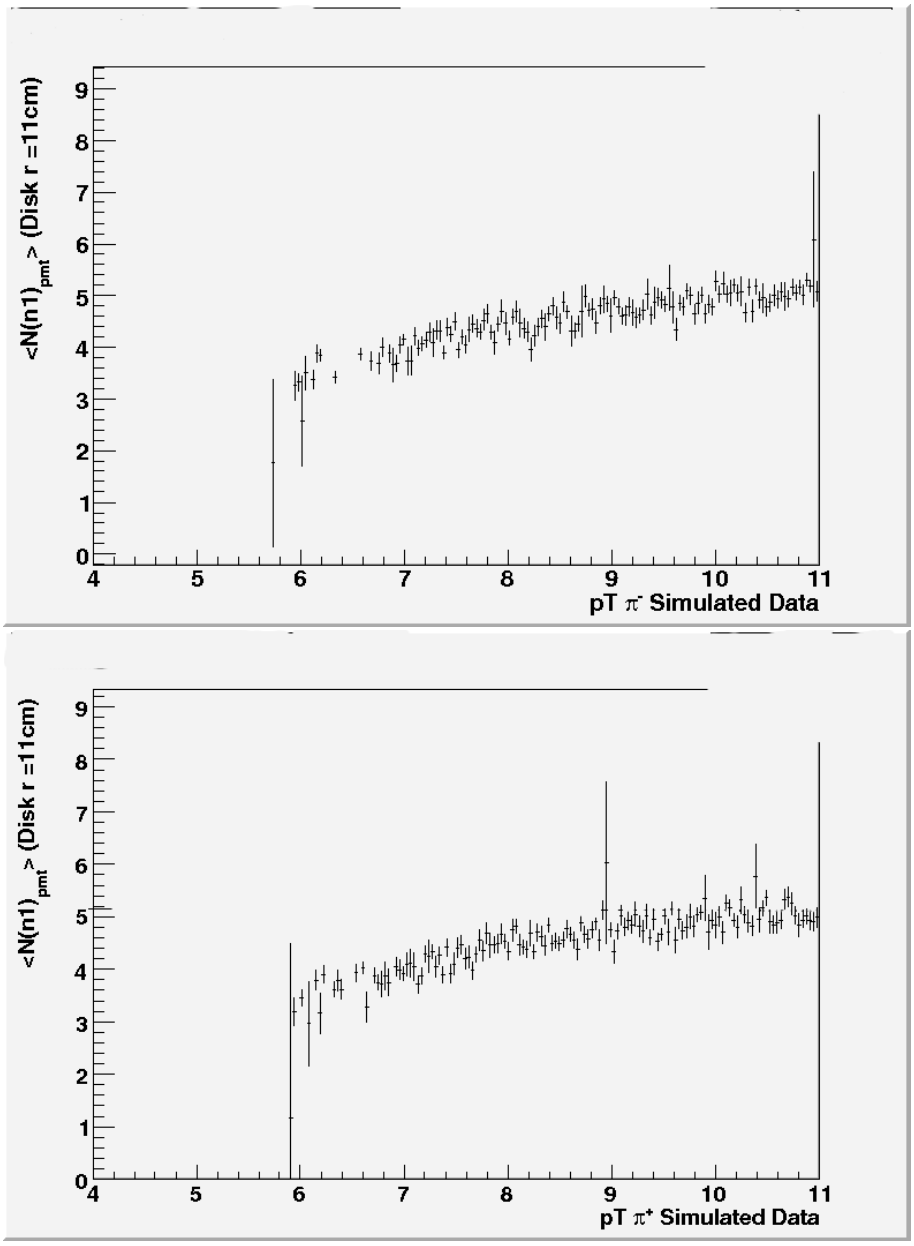

Figure 5.29: RICH turn on for pions using a disk ($n1$), abscissa is the p_T and the y axis is the average number of PMTs being fired. The top plot shows π^-, while the bottom shows π^+. Error bars are spread of mean σ values.

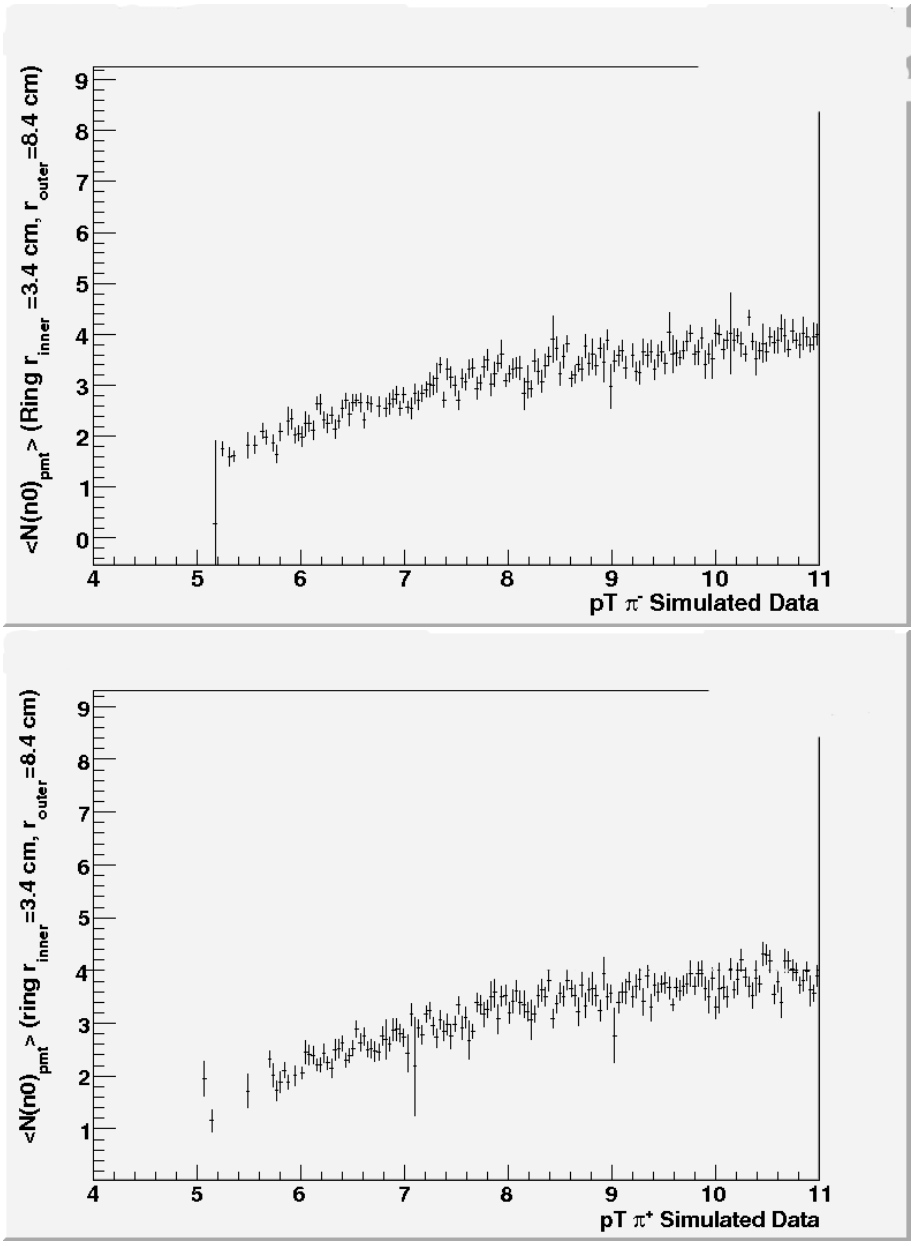

Figure 5.30: RICH turn on for Pions using a ring ($n0$) abscissa is the p_T and the y axis is the average number of PMTs being fired. The top plot shows π^-, while the bottom shows π^+. Error bars are spread of mean σ values.

Fractional Efficiencies				
$< N >_{pmt}$	$e^{\pm}$ n1	$e^{\pm}\, n0$	$\pi^{\pm}\, n1$	$\pi^{\pm}\, n0$
pmt> 0	0.98	0.98	0.71	0.67
pmt> 1	0.95	0.98	0.71	0.54
pmt> 2	0.86	0.96	0.58	0.33
pmt> 3	0.65	0.89	0.38	0.16
pmt> 4	0.39	0.71	0.17	0.06
pmt> 5	0.14	0.40	0.05	0.01

Table 5.6: RICH efficiencies within the momenta range of interest for this work of 5 GeV/c <p$_T$ < 10GeV/c. $n1$ represents a disk size while $n0$ represents a ring size, refer to the text for details.

5.3.2 Efficiencies of RICH-$e^{\pm}$ and $\pi^{\pm}$

With the use of a Monte Carlo simulation, the efficiency of selecting zero to six or more photomultiplier tubes (PMT) in the RICH was evaluated. Figures in the previous section showed typical firing trends (Figure 5.30). The simulation entailed generating both pions and electrons and selecting a minimal number of tubes required. The results of these studies are in Table 5.6 and also in Figure 5.31.

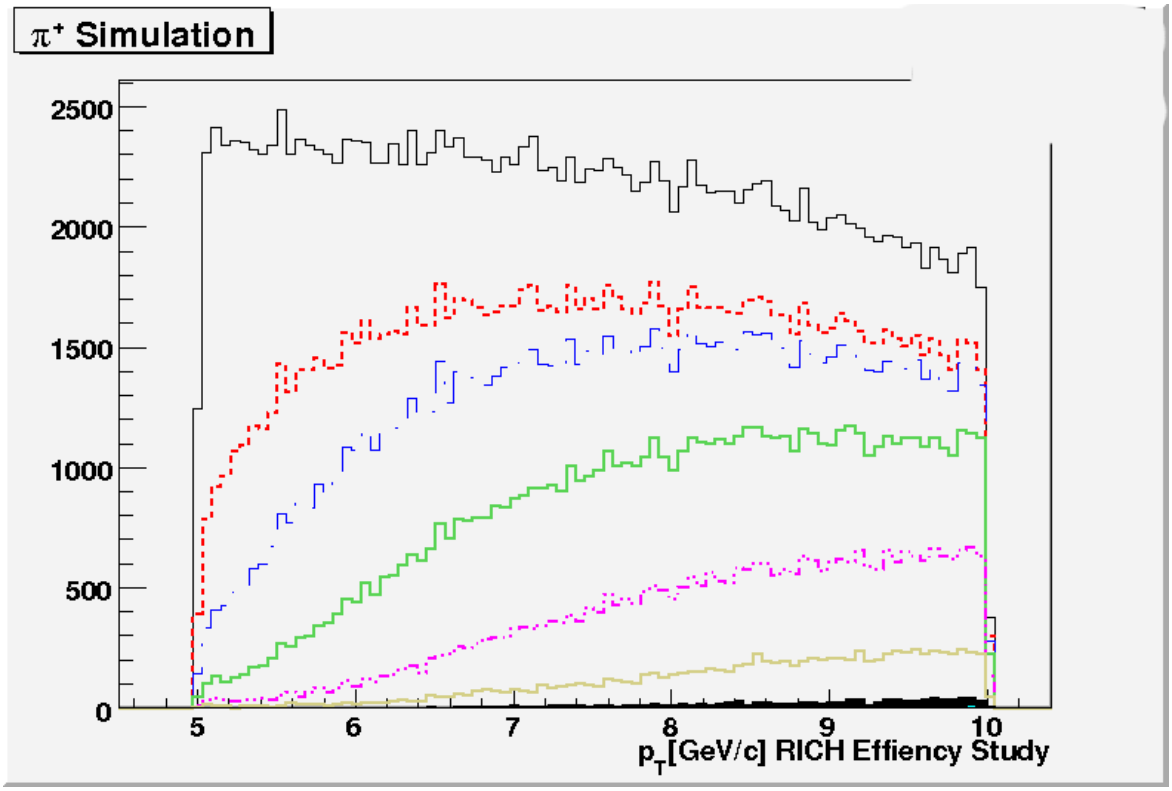

Figure 5.31: RICH simulation response to pions versus p_T at different photo multiplier tubes firing requirements versus p_T, Black is no requirement, red > 1, blue > 2, green > 3, pink > 4, mustard > 5, black fill > 6.

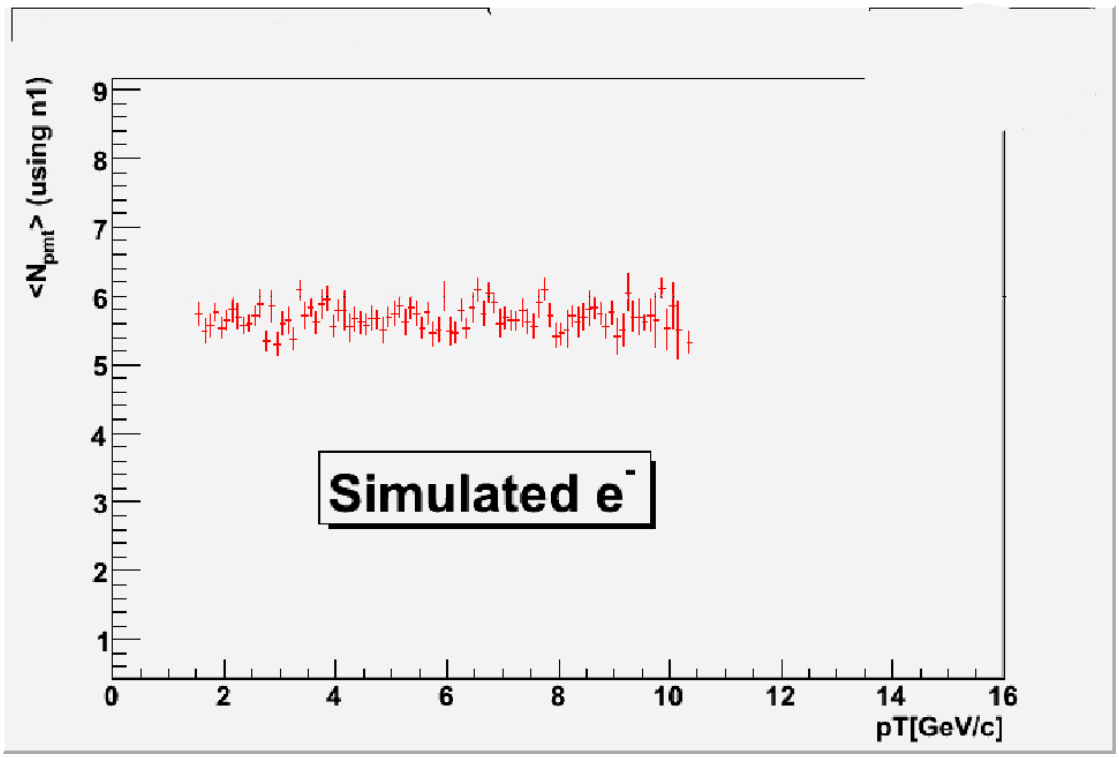

Figure 5.32: RICH turn-on for electrons using a disk ($n1$). Abscissa is the p_T and the y axis is the average number of PMTs being fired.

It is clear that using a disk ($n1$) retains more charged pions that a ring ($n0$). It is also evident that a RICH firing requirement greater than five PMTs retains only 5% of pions in the sample, while it keeps 40% of electrons (Figure 5.32 and Figure 5.33). A detailed study of the disk ($n1$) efficiencies can be found in Table 5.7, where the efficiencies are calculated in 1 GeV/c p_T increments. The electron's efficiencies are also calculated in the low p_T region, as it is the low momenta electron originating from material interactions that become the main source of background for high p_T charged pion measurements (Figure 5.31).

Real data taken with the ERT trigger (Section 4.2.1) was also studied to calculate

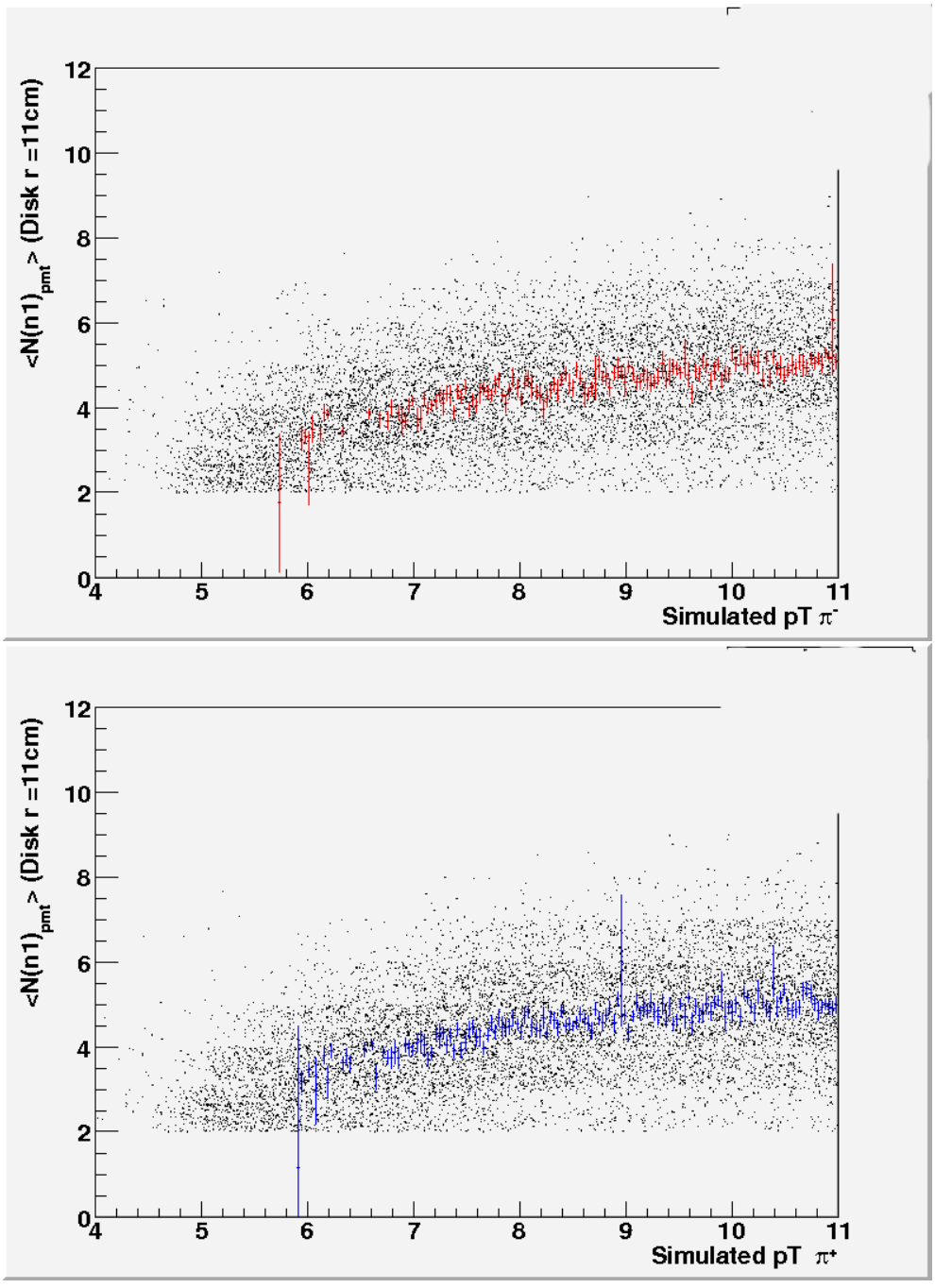

Figure 5.33: Spread of PMT tubes fired for charged pions π^-(top), π^+ (bottom). This figure illustrates the typical number of PMTs that will produce electronic signals from a transversing pion in the detector gaseous dielectric.

Fractional Efficiencies						
p_T[GeV/c]	$n1_{e^\pm}$ >0	$n1_{\pi^\pm}$ >0	$n1_{e^\pm}$ >4	$n1_{\pi^\pm}$ >4	$n1_{e^\pm}$ >5	$n1_{\pi^\pm}$ >5.
2-3	0.98	-	0.71	-	0.38	-
3-4	0.98	-	0.71	-	0.38	-
4-5	0.98	-	0.69	-	0.40	-
5-6	0.98	0.57	0.69	0.02	0.42	$< 1\%$
6-7	0.97	0.71	0.69	0.09	0.40	0.02
7-8	0.98	0.77	0.67	0.18	0.37	0.05
8-9	0.98	0.80	0.67	0.26	0.38	0.08

Table 5.7: Simulated RICH efficiencies by p_T bin of $n1$ for low and high reconstructed momentum electrons, and high momentum pions. Efficiencies were calculated using clean DC tracks from simulation.

the efficiency of the RICH detector. However, this study mainly focused on background electrons from γ conversions (Section 5.6) which occur away from the vertex. The efficiency obtained for these electrons and positrons is estimated to be 40%. Details of this efficiency will be discussed in Section 6.7.

5.4 Track Matching

Track matching is used as a background removing tool. Matching distributions (Figure 5.3) are projections of reconstructed DC tracks to the EMCal and the pad chambers. The outer detector in PHENIX's central arms are two dimensional: in azimuth and in beam direction. When drift chamber hits are tracked, their trajectories are projected to each of the outer detectors. The distributions of the difference between projection points and hits (called residuals) are then fitted with a Gaussian. The mean and the sigma of the distribution depends on the track momentum and on the charge and direction of the track.

These projections can be used to reduce the background from secondary particles, such as decays and conversions or any particle not originating from the assumed vertex. One can then apply cuts on the deviation of the position of the actual associated hits from the track model projection. This is usually evaluated relative to the momentum (and, in the case of the EMCal, incident angle) in standard deviations. Close matching cuts make an excellent tool for eliminating background coming from conversion pairs. In this analysis, a matching cut of $\sigma_{cut} < 2$ was required for the cross-section analysis. A looser matching cut of $\sigma_{cut} < 3$ was additionally required for the asymmetries as this sample was less contaminated than the cross-section data sample. The remaining data was then studied to estimate the background correction (Section 6.6). The mean of the distributions are expected to be centered at zero with a σ width of one for a normalized

σ distribution. This is generally true for the signal region. However, as studies for this work show, particularly when using the 2005 data - see Appendix F and Table E.0.3, the background may not have matching distribution centered at zero and typically will be non-Gaussian. Furthermore the signal region may have the wrong parametrisation and thus will incorrectly have broader Gaussian shapes. Corrections to such distributions are crucial if they are to be used as part of the background reduction. Corrections were done to all the data samples under study, including the following data-sets:

- Simulated data (Section 5.2.1).
- ERT triggered data from 2005 (Section 4.2.1).
- Data from 2006 both MB trigger and ERT trigger.

The summary of corrections can be found in following sections. These corrections are calculated in bins of p_T and charge. See Tables A.9 and A.10 for the corrections performed to MB data and Tables A.11, and A.12 for the ERT sample. Additional corrections can be also found in the Appendix. Simulated data was also studied to check the efficiency of requiring a matching window and also to verify that the widths of the simulated distributions had a mean zero and σ of one. The efficiency of the pad chamber (PC) requirements were found to be consistent across p_T and charge in σ units of dz and dϕ. The distributions were not exactly the expected values, in particular the distributions for simulated π^+ were shifted slightly off centered. Both fits of π^+ and π^- were narrower

than the expected σ of one by about 20%. The summary of the mean and σ of matching distributions for the simulated sample are in Tables A.1 and A.4. To calculate the efficiency of maximum σ tolerance, the distributions were first normalized to a mean of 0 and σ of one before the efficiency was calculated.

5.4.1 Study of Matching Distributions by zed

The efficiency of the *zed* cuts[19] was described in Section 5.2.1. What are mainly considered in this section are the inspections of the matching distributions (deviation of track and projected hit) in minimum bias (MB) data to estimate an adequate requirement on the *zed* that will minimize the background contribution to the signal. Figure 5.34 shows a typical distribution of high particle hit densities (many particles preferentially hitting one area of the detector) at *zed* greater than 40 cm and outside a matching window of 2σ. These lie on the negative or positive mean of the pad chamber matching distributions depending on the charge under study. These studies, in combination with the studies found in Figure 5.35, where the high density areas in dark maroon, also show the high particle hits on the *zed* edges (above $|40\,\mathrm{cm}|$). These distributions were cut in *zed* slices and fit with single Gaussians. The mean of the matching distributions show a trend of mean shift which is also charge and *zed* position dependant. The complete studies of all p_T bins and *zed* intervals of interest can be found in Appendix G. Another observation

[19]The *zed* is defined as the *z* coordinate which a charged track crosses within an *x* and *y*, *z* (*x* and *y* being the central plane and z being the direction of the beam) coordinate system with a radius *r* of 220 cm.

which becomes evident by looking at Figure 5.36 is that the matching variables in z are not as sensitive to a *zed* dependence as the matching distributions in ϕ. The summary of these observations lead to a maximum $|zed|$ requirement of $\pm$40 cm on the MB data sample. The ERT (Section 4.2.1) triggered data used for the asymmetry measurements also has a maximum $|zed|$ requirement, however, this one is a looser requirement of 70 cm and will be discussed in Section 6.5.

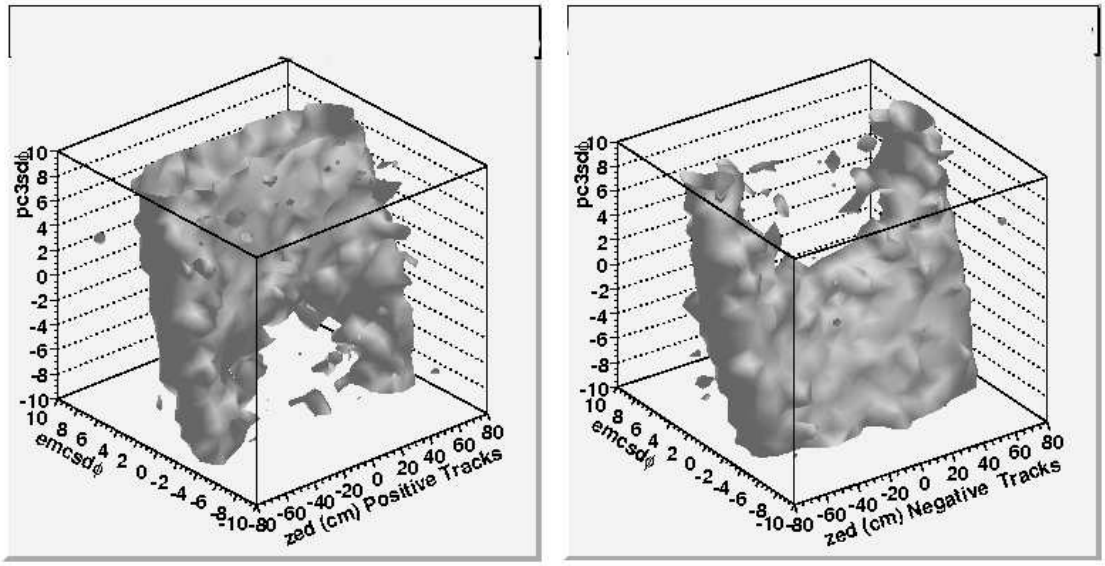

Figure 5.34: Correlation of high density hits of PC and EMCal matching distributions in ϕ. The units of the matching are in σ, while the units of *zed* are in cm. Left panel are positive tracks, while the right panel are negative tracks. The distributions correspond to minimum bias data from the year 2006. p_T is 5 GeV/c to 10 GeV/c.

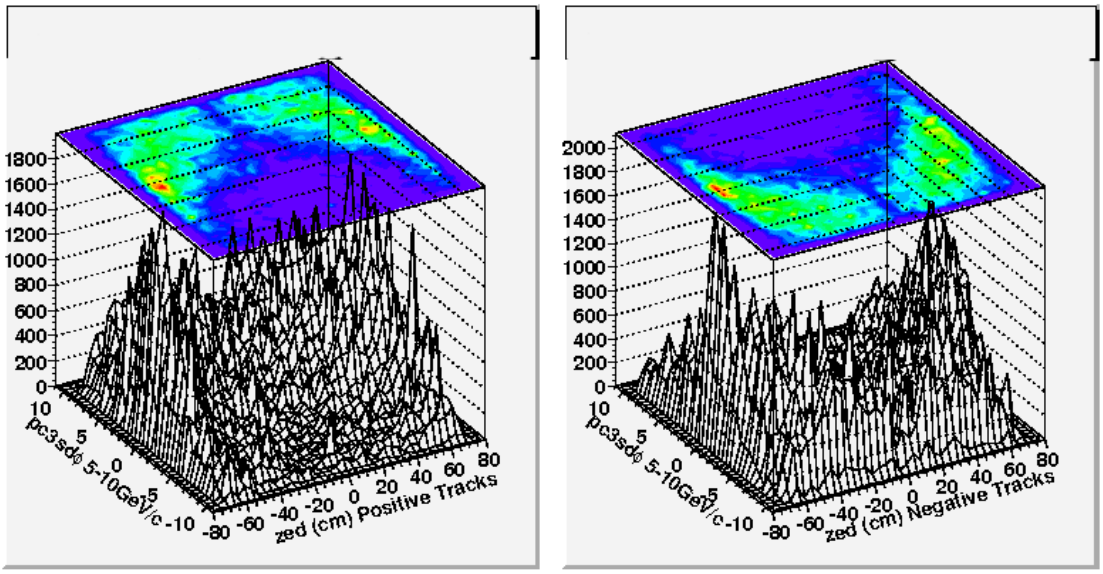

Figure 5.35: Correlation of high density hits of pc3sdϕ vs *zed*. The units of the matching (deviation of track and projected hit in ϕ) are in σ, while the units of *zed* are in cm. Left panel are positive tracks, while the right panel are negative tracks. The distributions correspond to minimum bias data from the year 2006, p_T is 5 GeV/c to 10 GeV/c. To note from these figures are the high tails and red areas which represent high concentration of particles and background contributions.

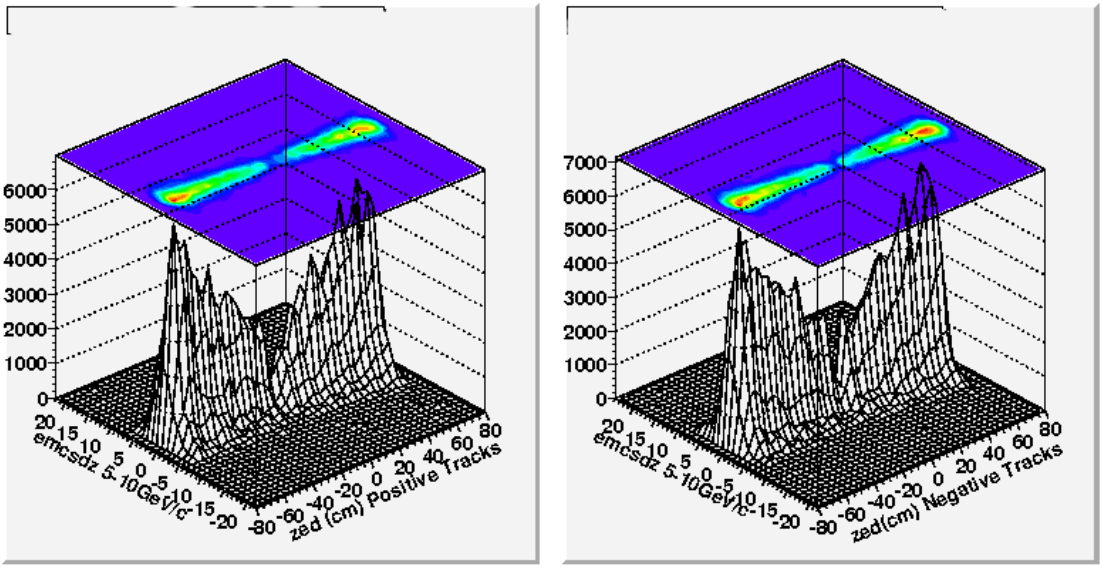

Figure 5.36: Correlation of high density hits of emcsdz vs *zed*. The units of the matching (deviation of track and projected hit in z) are in σ, while the units of *zed* are in cm. Left panel are positive tracks, while the left panel are negative tracks. The distributions correspond to minimum bias data from the year 2006, p_T is 5 GeV/c to 10 GeV/c.

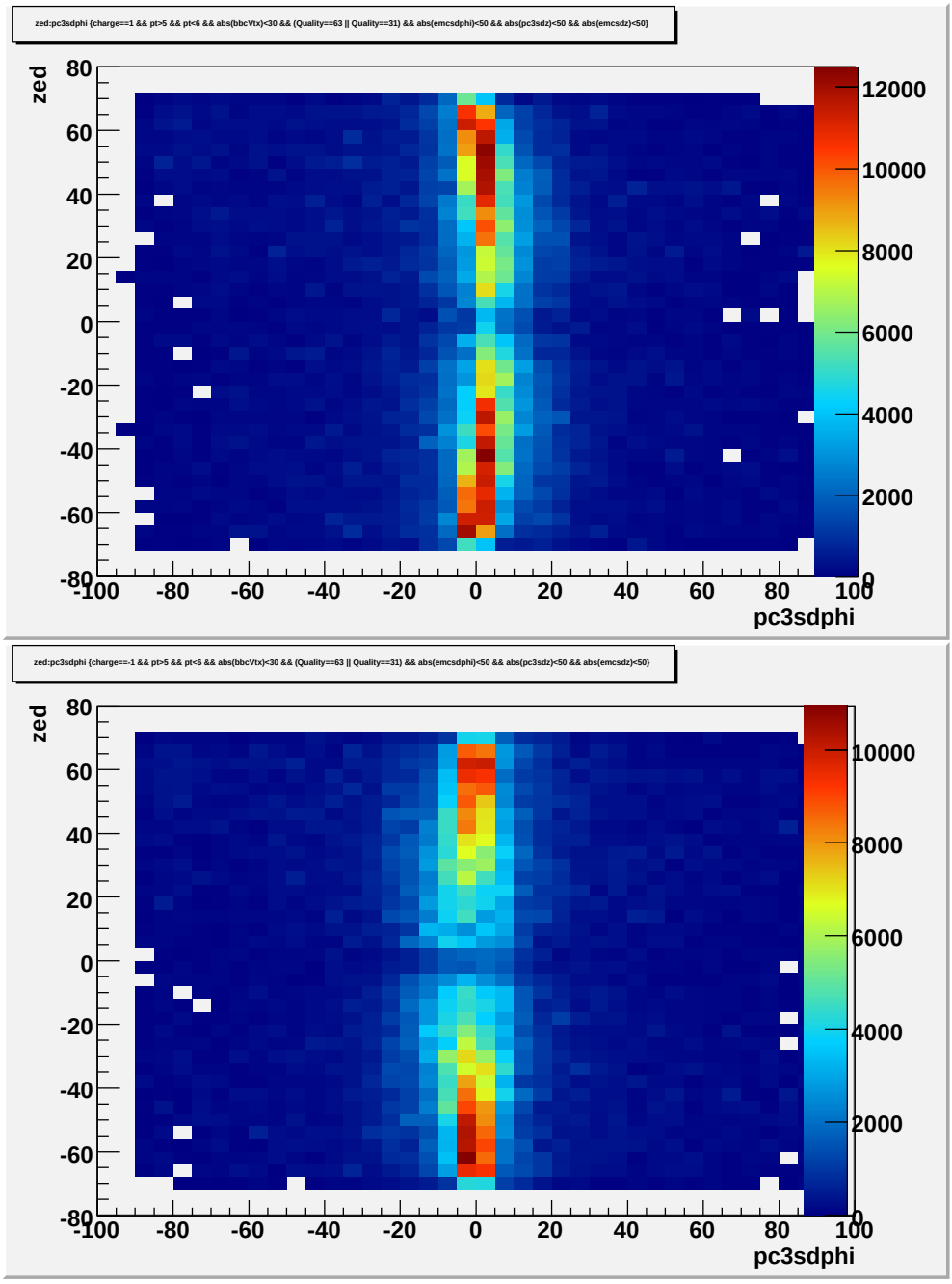

Figure 5.37: Zed vs pc3s$d\phi$ of positive and negative tracks showing the areas of high density track matches on the p_T region of 5 GeV/c to 6 GeV/c. Similar studies can be found on Appendix G.

The matching distributions were more carefully inspected in 10 cm *zed* intervals and fitted to double Gaussians. These inspections were first attempts to search for indications of how the background is changing and verify that the high particle hit trends on the edges of the zed distributions observed in Figures 5.34, Figure 5.35 and Figure 5.37 at a 10 cm *zed* interval level. The results of these inspections can be found on Appendix G and on Tables A.13 through A.20. The narrow Gaussian fits are representative of the signal region, while the broad Gaussian represents the background.

5.5 Drift Chamber Efficiency Study

The drift chamber is important in the detection of charged tracks and their momentum. The efficiency of using different drift chamber track quality cuts was calculated using simulated pions which survived the detector simulation conditions (i.e. magnetic field settings, identification cuts). The result of requiring a high quality DC track (Section 4.1.4) resulted in an average efficiency across p_T for both charged types of $\sim 85\%$. Refer to Section 4.1.4 for more details on the drift chamber. Refer to Table 5.8 for a summary of the efficiencies.

Drift Chamber (DC) High Quality Cuts		
Charge	p_T[GeV/c]	Fractional Efficiencies
π^+	5-6	0.82
	6-7	0.85
	7-8	0.86
	8-9	0.86
	9-10	0.88
π^-	5-6	0.82
	6-7	0.85
	7-8	0.86
	8-9	0.87
	9-10	0.87

Table 5.8: Efficiency of drift chamber extracted from simulated charged pions. Quality is described in Section 4.1.4.

5.6 Efficiency of *zed* Cuts

zed is used as a background elimination tool in the present work. The *zed* is defined as the z coordinate which a charged track crosses the radial plane, which corresponds to a radius r of 220 cm and the drift chamber (DC) position from the origin (Figures 5.15 and 5.1). The *zed* is determined by using information from unambiguous PC1 pixel clusters. If a pad chamber cluster is ambiguous, then wire information from the DC is used. In this work an upper $|zed|$ limit is applied (i.e. $|zed| < 40$ cm), which proves to be a powerful tool in eliminating background from particles that decay far from the vertex or particles which are produced within the residual magnetic field and thus are bent. The efficiency of cutting on the outer edges of the *z*[20] coordinate of a track is summarized in Table 5.9.

Fractional Efficiencies									
	p_T[GeV/c]	<70cm	<65cm	<60cm	<55cm	<50cm	<45cm	<40cm	<35cm
π^-	5-6	0.84	0.79	0.72	0.67	0.61	0.55	0.49	0.42
	6-7	0.85	0.79	0.73	0.67	0.6	0.54	0.48	0.42
	7-8	0.85	0.8	0.74	0.68	0.62	0.55	0.49	0.43
	8-9	0.85	0.79	0.73	0.67	0.61	0.55	0.49	0.43
	9-10	0.86	0.8	0.74	0.67	0.61	0.55	0.49	0.42
	p_T[GeV/c]	<70cm	<65cm	<60cm	<55cm	<50cm	<45cm	<40cm	<35cm
π^+	5-6	0.84	0.78	0.72	0.66	0.6	0.54	0.48	0.42
	6-7	0.85	0.79	0.73	0.67	0.61	0.55	0.48	0.42
	7-8	0.85	0.85	0.79	0.73	0.67	0.61	0.55	0.48
	8-9	0.85	0.79	0.73	0.67	0.61	0.54	0.48	0.42
	9-10	0.86	0.8	0.74	0.67	0.61	0.55	0.49	0.42

Table 5.9: Efficiency of *zed* cuts extracted from simulated charged pions, where $|zed|$ <N is applied, N being distance from the vertex in cm.

In addition to the simulated pions *zed* efficiency calculations, γ from 0-10GeV/c p_T

[20]Geometrically, the maximum absolute value of *z* in the central detector region is 75 cm.

were simulated to investigate the *zed* efficiency of electrons proceeding from low momentum photons $\gamma \longrightarrow e^+e^-$ which interact with the material. Of 1,964 γ, 334 e^+e^- were produced. The efficiency of the *zed* for these particles can be summarized in Table A.22. Simulated primary electrons and positrons were also studied for *zed* efficiency, as well as the e^+e^- pairs proceeding from $\gamma \longrightarrow e^+e^-$ which were also produced through material interactions in this electron sample. The results of these studies are found in Table 5.4.

5.7 Cross-section Measurement

As described in Section 5.1, the experimental measurement of $E\frac{d^3\sigma}{dp^3}$ for charge separated pions entailed extracting pion yields detected at PHENIX. Yields were normalizing by various quantities, many which were obtained through efficiency calculations using simulations already discussed in great detail in Section 5.2.1, while other efficiencies were obtained using data. The elements which will be further discussed before the results are presented can be summarized as follows:

- Pion yields normalized by p_T and bin: $\frac{N_{\pi^\pm}}{p_T \Delta p_T}$
- Integrated luminosity $\int Ldt$. Details calculated in Section 5.7.2 (Formula 6.9)
- Efficiency corrections. $\epsilon_{reco} \times \epsilon_{geo} \times \epsilon_{triggerbias}$. (Table 5.11)

5.7.1 Pion yields Normalized by Momenta and Bin Size - $\frac{N_{\pi^\pm}}{p_T \Delta p_T}$

As mentioned in Section 5.7, $\Delta\eta$ was normalized to one in the simulation. In this part of the work the summary of the yields obtained for π^+ and π^- are presented. The yields obtained in Table 5.10 are background subtracted, which means the background had to be estimated (Section 5.8.1) and subtracted from the yields which are used for the calculation of $E\frac{d^3\sigma}{dp^3}$ (Section 5.1). The p_T at which yields are calculated are not at the center of the bin, but rather at the integral mean p_T.

Pion Yields			
p_T[GeV/c]	π^+	p_T[GeV/c]	π^-
5.47	1699	5.48	1501
6.49	938	6.47	712
7.49	278	7.46	191
8.46	100	8.48	70

Table 5.10: Pion yields by charge and integral mean p_T normalized by bin width and p_T. Errors are discussed in Section 5.9.

5.7.2 MB Integrated Luminosity - $\int Ldt$

The integrated luminosity, as described in Section 5.1, is the ratio of total MB triggered events and BBC trigger efficiency normalized by the total inelastic cross-section. The equivalent number of events corrected by prescales[21] sampled with the MB trigger was **28,942,423,390**. The integrated luminosity was: $\int Ldt$ =1258366234 cm^{-2}s^{-1}, calcu-

[21] During the course of data taking a prescale is typically set on clock and MB triggers. This means only a fraction of the collisions is sampled to remain within bandwidth limits. N_{MB} is properly accounted for prescales, which would typically reduce the fraction of recorded events.

lated with the MB triggered proton - proton cross-section of $\sigma_{p+p}\epsilon_{BBC}^{p+p}$ =23 $\pm$2 mb.[22]

5.7.3 Efficiencies Corrections $\epsilon_{reco} \times \epsilon_{geo} \times \epsilon_{triggerbias}$

Proper accounting for efficiency corrections, which included geometry considerations, cuts and reconstruction algorithms (including momentum smearing), are summarized in this section. Refer to Section 5.2.1 for the detailed study on how the efficiencies presented here were derived. The three main corrections were:

1. ϵ_{geo}, which is a geometrical correction which accounts for reconstruction efficiency, geometry of PHENIX, as well as momentum smearing.

2. ϵ_{eff}, which is an efficiency correction to the pion identification cuts.

3. ϵ_{bias}, which is a correction that takes into account the probability or rather preference, of a hard scattered process to be accepted and treated as a trigger in the finite acceptance of the BBCs. This value used in this work is 0.79$\pm$0.02, as determined in [2].

5.8 Measured Differential Cross-sections

Three cross-sections were calculated and corrected for all effects as described in the last section and are summarized in Table 5.19 and Table 5.20. Cross-sections for π^+ and

[22]Where the error here is a systematic.

Fractional Efficiencies			
p_T	ϵ_{bias}	ϵ_{geo}	ϵ_{eff}
π^+			
5-6	0.79	0.26	0.034
6-7	0.79	0.24	0.046
7-8	0.79	0.22	0.053
8-9	0.79	0.20	0.053
π^-			
5-6	0.79	0.26	0.037
6-7	0.79	0.23	0.053
7-8	0.79	0.21	0.052
8-9	0.79	0.19	0.053

Table 5.11: Efficiency corrections by charge and mean p_T, refer to the text and Section 5.2.1 for a description of each.

π^- were calculated separately and charge averaged summed cross-sections were also obtained $(\pi^+ + \pi^-)/2$. The dominant error for these measurements was the background estimation which was derived from RICH efficiencies of data. Background removal techniques and errors will be discussed in more detail. The final measured cross-sections can be found in Figure 5.39, Figure 5.40 and Figure 5.42.

5.8.1 Background Estimate Cross-sections

Conversion electrons comprise the main background contribution to the sample, as these can have similar signatures as high p_T $\pi^{\pm}$. The conversion background is composed of electron pair tracks generated close to the drift chamber and deflected by the magnetic field. The pair will split in the main bend plane and can potentially be reconstructed as a high momentum track. However, as stated in Section 4.1.6, electron behavior and charged pion behavior can be different as the light cone radius is larger for electrons than

pions. An electron will fire on average six PMTs in the RICH, while for charged pions, with their more compact light cone, the mean number of PMTs quickly increases and plateaus around five PMTs. In addition, the matching distributions of $e^{\pm}$ and $\pi^{\pm}$ also differ: charged pion distributions are narrow and centered around zero, while background electron distributions are broader and centered to the right or the left of zero depending on their charge.

The background estimate for a cross-section measurement proved to be a challenging task as the sample available using MB data was heavily contaminated. The approach to estimate the remaining background was similar for both the asymmetries (Section 6.6.1) and cross-section measurements. The latter differs by requiring stricter background separation methods than in the asymmetry case. Furthermore background yields are subtracted in the cross-section analysis. The method entailed separating electrons and positrons from pions based on RICH firing behaviour. This behaviour was based on the efficiency studies already presented in Section 5.3.1, which demonstrated that requiring more than five PMT tubes will kill 99$\%$ of the pion signal. Using the requirement of more than five PMTs firing in a disk area ($n1 > 5$) was used in order to maximize pion retention while still removing a large portion of the background. The remaining background was estimated using Equation 5.12 and was subtracted. The RICH efficiencies for conversion electron positron pairs were calculated from data as follows:

$E\frac{d^3\sigma}{dp^3}$					
p_T[GeV/c]	π^+ (mb-GeV$^2c^2$)	p_T[GeV/c]	π^-(mb-GeV$^2c^2$)	p_T[GeV/c]	$\frac{\pi^+ + \pi^-}{2}$(mb-GeV$^2c^2$)
5.46	0.00001539	5.48	0.00001242	5.47	0.000013901
6.49	0.00000680	6.47	0.00000467	6.48	0.000005738
7.49	0.00000191	7.46	0.00000140	7.48	0.000001655
8.46	0.00000076	8.48	0.00000056	8.47	0.000000657

Table 5.12: Measured $E\frac{d^3\sigma}{dp^3}$ values by p_T of π^+, π^- and (π^++π^-)/2. Errors are discussed in the following Section 5.9.

$$R_e = \frac{N_e \,\text{within}\,(n_1 > 5) \text{and}\, \text{pc3sd}\phi\,(\sigma > 5, \sigma < 15)}{N_e \,\text{within}\,(n_1 > 0)\,\text{and}\, \text{pc3sd}\phi\,(\sigma > 5, \sigma < 15)} \tag{5.11}$$

$$Spectra_{5\geq n_1>0} = Signal_{5\geq n>0} + Background((\frac{n_1 > 5}{R_e}) - N_{e^\pm}(n1 > 5))$$

The charged pion sample was found to be heavily contaminated by conversion electron pairs, and furthermore, the values for R_e efficiencies vacillated across p_T bins giving an indication of a systematic uncertainty. It is expected that RICH efficiencies are flat for electrons and should not depend on p_T. Any trends observed are assigned as a systematic uncertainty due to large variations on the already contaminated sample. Background levels were estimated to vary from seventy two percent to one hundred percent (Figure 5.38) in the highest momentum bin which was discarded. The value of R_e, which corresponds to the efficiency of the RICH, was found to be $= 48\% \pm 2\%$. The background in the sample, as well as the remaining signal in each p_T bin are all summarized in Tables 5.13, 5.14 and 5.15.

Fractional Efficiencies		
p_T[GeV/c] Bin	R_{e^+}	R_{e^-}
5-6	0.45	0.51
6-7	0.48	0.48
7-8	0.45	0.46
8-9	0.47	0.48
9-10	0.46	0.51

Table 5.13: Efficiencies of the RICH by p_T bin of conversion electrons pairs, where the mean of the values obtained are used for the background estimate.

Positive Spectra			
p_T[GeV/c] Bin	$n_1 > 0$	5≥n1>0	n1>5
5-6	66224	38930	27294
6-7	52947	30482	22465
7-8	38139	20826	17313
8-9	26470	14172	12297
9-10	16086	8130	7956
Negative Spectra			
p_T[GeV/c] Bin	$n_1 > 0$	5≥n1>0	n1>5
5-6	70009	40058	29951
6-7	46672	26153	20520
7-8	31871	17149	14722
8-9	25673	13611	12062
9-10	21775	10596	10578

Table 5.14: Uncorrected statistics in each p_T bin separated by RICH response. Errors are discussed in Section 5.9.

Positive Spectra			
	$N_{\pi^+ + e^+}$	N_{π^+}	$N_{e^+}(\%)$
5-6	7079	1699	76
6-7	4691	938	80
7-8	2777	278	90
8-9	1667	100	94
Negative Spectra			
p_T[GeV/c]	$N_{\pi^- + e^-}$	N_{π^-}	$N_{e^-}(\%)$
5-6	7920	1501	81
6-7	4745	712	85
7-8	2734	191	93
8-9	1755	70	96

Table 5.15: Background estimates and signal levels of charged pion sample. Background is subtracted in each p_T bin. Yields are corrected for p_T, Δp_T and bin shift. $N_{e^+} + N_{\pi^+}$ is the spectral region within a RICH response of $5 > n > 0$. Errors are discussed in Section 5.9.

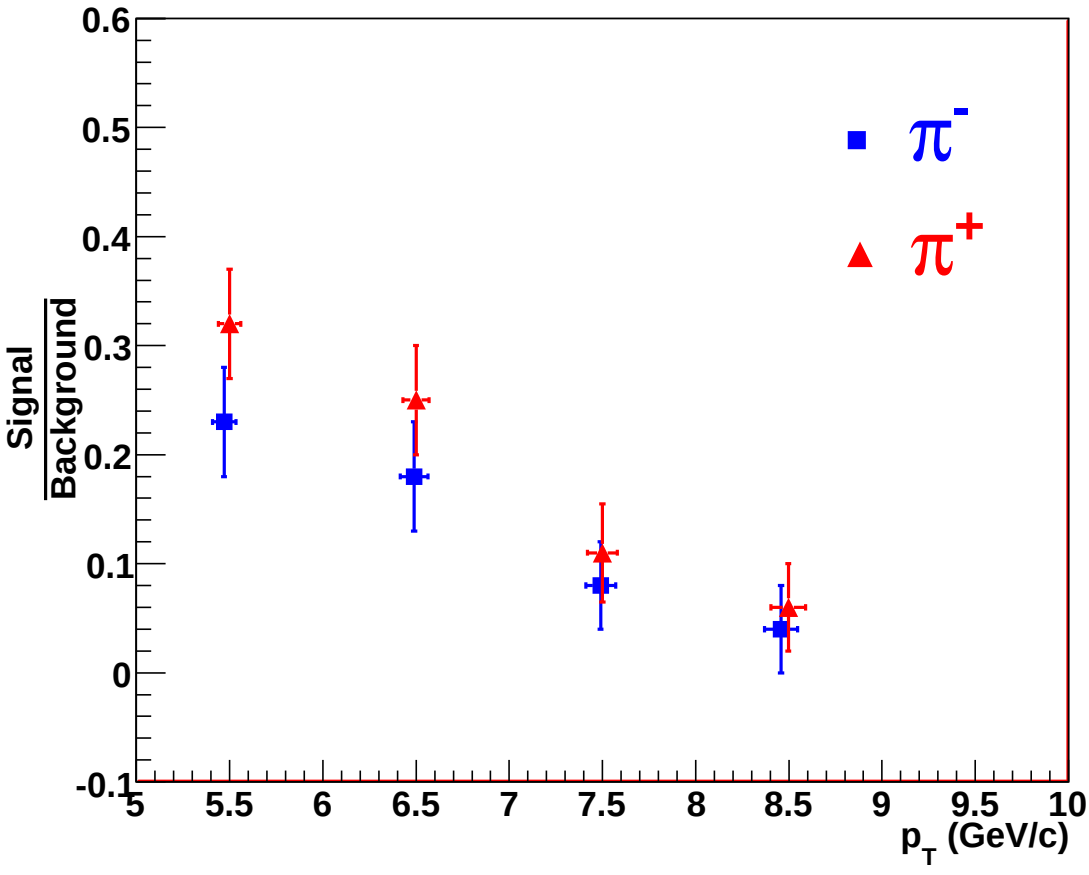

Figure 5.38: Signal and background ratios for π^- and π^+ with statistical errors included. The largest uncertainty comes from the background estimate at large p_T.

5.9 Errors in $E\frac{d^3\sigma}{d\vec{p}^3}$

The dominant source of error in this measurement is systematic and it emerges from the uncertainty of the background estimate. As pion yields become less numerous with increasing p_T the background, which remains flat, begins to dominate and its estimate introduces an uncertainty. The errors presented in this work were an estimate based on the studies and data available. The errors presented here are just an estimate and it is understood that many improvements could be made. Other studies that could be made to improve the systematic errors are cross-checks of the RICH efficiencies. This cross-checks can be done with a clean data sample from other particles besides charged pions. A clean data sample could be obtained from primary electrons. Electrons used for cross-checks could be obtained from more current data-sets with better identification. Another improvement that can be made to the systematic errors in future data-sets is the identification technique. Better identification can be achieved by the use of new sub-detectors at PHENIX unavailable for the data analyzed in the present work. Complete understanding of the EMCal response to hadrons could also aid in the identification method of high momentum charged tracks. Hadron response to the calorimeter would require test beam data at appropriate energy ranges. Alternatively, one could parametrise the response to the calorimeter with a clean charged pion sample from real data using several identification cross-checks. Identification cross-checks would need to be independent of the calorimeter. Comparisons of energy distributions and simulation could then be

parametrised. A more appropriate cross-section measurement could be made once the calorimeter response to hadrons is understood with the ERT trigger. Asymmetries presented in this work are measured with the ERT trigger. A complementary cross-section should also be made with a calorimeter triggered sample.

Errors on the differential cross-sections can be divided also into systematic and statistical. The statistical error summary can be found in Table 5.16. Systematic uncertainties that will be discussed include the following:

- Integrated luminosity, which is propagated from the systematic uncertainty in $\sigma_{p+p}\epsilon_{BBC}^{p+p}$ and has been determined to be **23.0**$\pm$**2.2 mb** (Section 4.1.1).

- Background estimate. This type of systematic arises from the RICH efficiencies calculated for the conversion background. Efficiencies for electrons, either primary or conversion, are expected to be flat above the transverse momenta of 1GeV/c. In the calculation of the RICH efficiencies of the conversion electron sample, it was found that the efficiency (R_e) fluctuated. The mean of this efficiency was taken for the background estimate calculation, and the variation of the mean was used as systematic uncertainty which was propagated to the final cross-section measurements.

- Momentum resolution, which has been discussed in Section 5.2.4 and included here for completeness.

$\sigma_{statistical}$			
p_T[GeV/c]	$\Delta E\frac{d^3\sigma}{d\vec{p}^3}_{\pi^+}$(mb-GeV$^2c^2$)	p_T[GeV/c]	$\Delta E\frac{d^3\sigma}{d\vec{p}^3}_{\pi^-}$(mb-GeV$^2c^2$)
5.47	0.00000037 (2%)	5.48	0.00000032 (3%).
6.49	0.00000022 (3%)	6.47	0.00000018 (4%).
7.49	0.00000011 (6%)	7.46	0.00000010 (7%).
8.46	0.00000007 (10%)	8.48	0.00000007 (12%).

Table 5.16: Summary of statistical errors of $E\frac{d^3\sigma}{d\vec{p}^3}$ by mean p_T and charge.

$\sigma_{systematic}$			
p_T[GeV/c]	$\sigma E\frac{d^3\sigma}{d\vec{p}^3}_{\pi^+}$(mb-GeV$^2c^2$)	p_T[GeV/c]	$\sigma E\frac{d^3\sigma}{d\vec{p}^3}_{\pi}$(mb-GeV$^2c^2$)
5.47	0.00000116(8%)	5.48	0.00000167(13%)
6.49	0.00000152(22%)	6.47	0.00000102(22%)
7.49	0.00000117(62%)	7.46	0.00000098(70%)
8.46	0.00000048(64%)	8.48	0.00000036(65%)

Table 5.17: Summary of systematic errors (standard deviations) of $E\frac{d^3\sigma}{d\vec{p}^3}$ by mean p_T and charge obtained by varying the background according to the uncertainty obtained in R_e.

The summary of these errors, which are added in quadratures, are summarized in Tables 5.16, 5.17 and 5.18.

$\sigma_{systematic}$ (%)			
p$_{T\pi^+}$[GeV/c]	π^+ (%)	$p_{T\pi^-}$[GeV/c]	π^-(%)
5.47	11	5.48	16
6.49	24	6.47	23
7.49	62	7.46	70
8.46	65	8.48	66

Table 5.18: Total systematic errors of $E\frac{d^3\sigma}{d\vec{p}^3}$ by mean p_T and charge. Errors include momentum, background estimate and uncertainty in total inelastic cross-section.

5.10 Summary of cross-section results

Results obtained were compared to pQCD calculations using the latest fragmentation functions available[11]. Charged separated results can be found in Figure 5.39 and Figure 5.40. The comparison to pQCD fits an be found in Figure 5.41. These results show consistency within errors indicating that the unpolarized distribution functions as well as the fragmentation functions describe the data. Figure 5.42 shows the summed average cross-section compared to published π^0 results from the PHENIX detector[5]. These results also show that within the errors (Figure 5.43), the measurements are consistent with each other. Table 5.19 and Table 5.20 summarize the results.

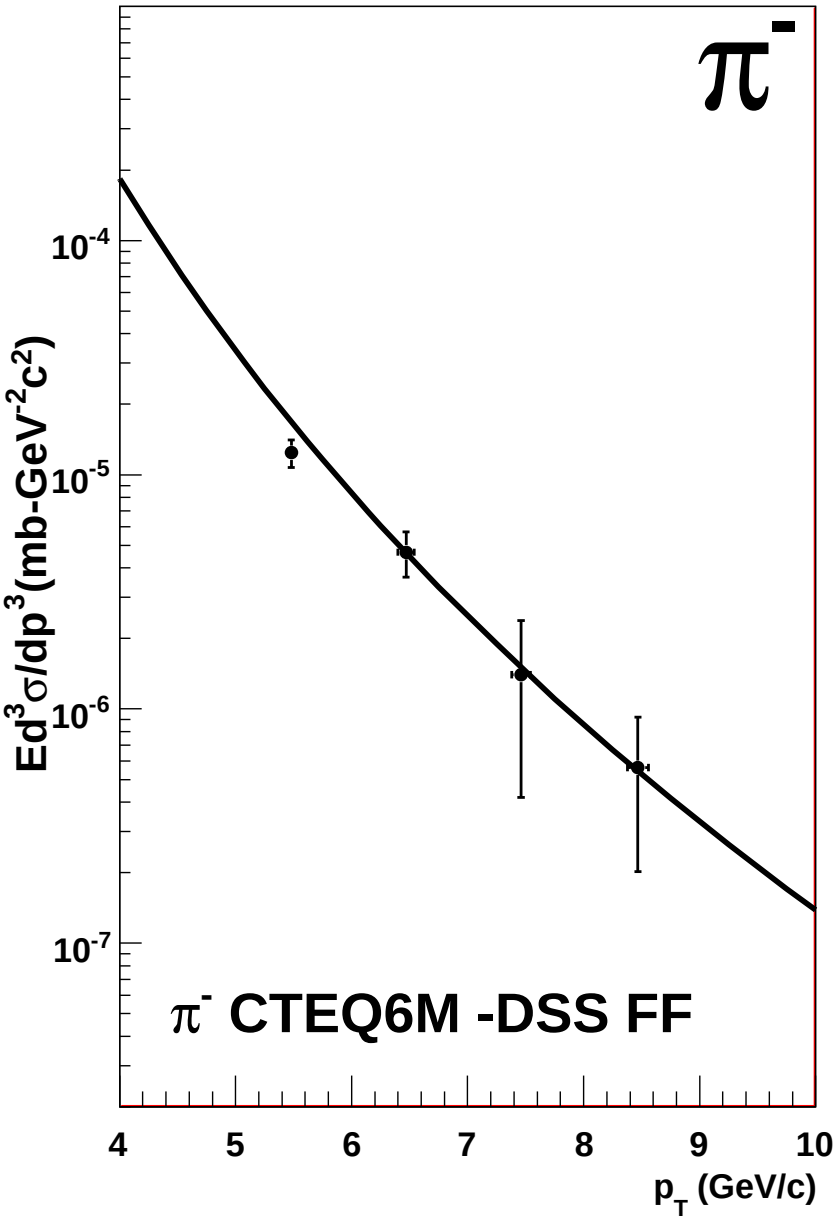

Figure 5.39: Measured cross-sections of π^- with Statistical and systematic errors included. Statistic errors are too small to see, while systematic errors are in black. Dominant errors are systematic, with the largest uncertainty coming from the background estimate at large p_T. The curves represent pQCD parametrisations using the DSS[11] fragmentation functions.

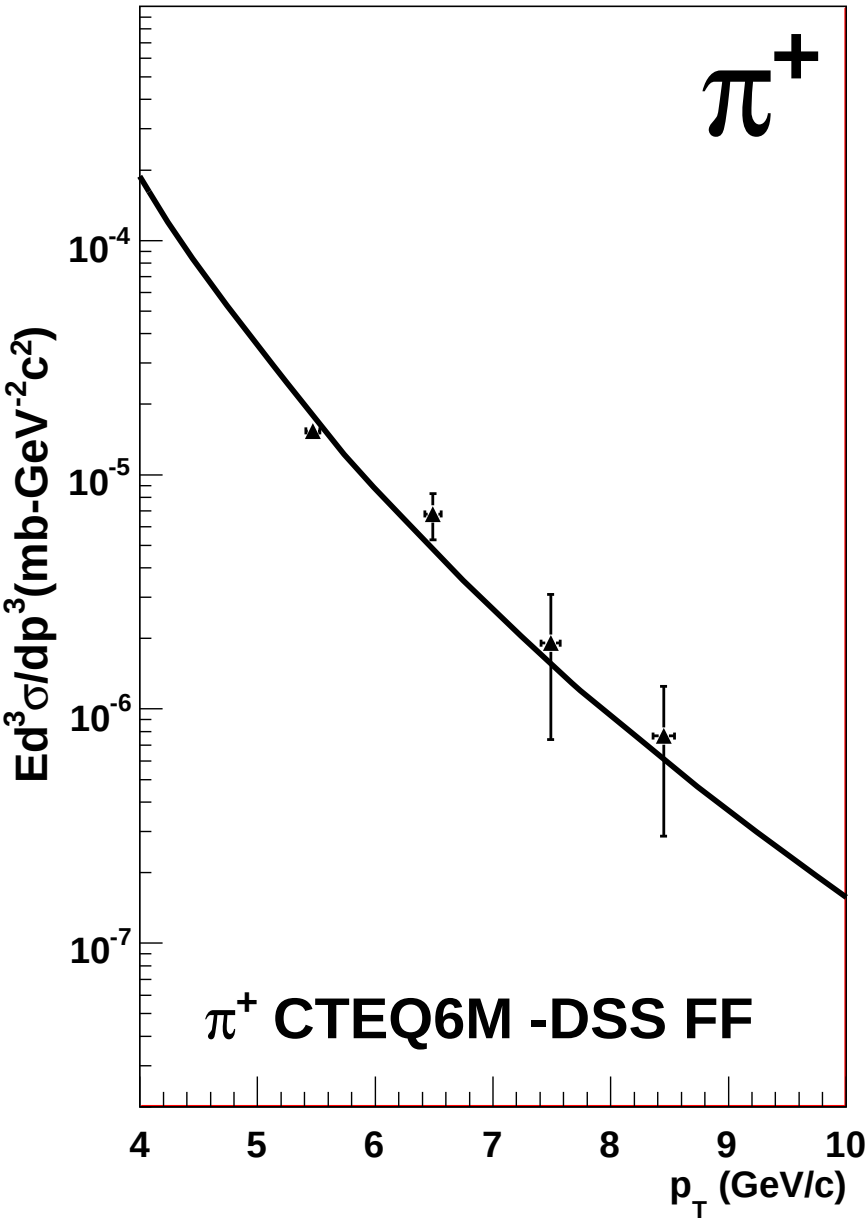

Figure 5.40: Measured cross-sections of π^+ with statistical and systematic errors included. Statistic errors are too small to see, while systematic errors are in black. Dominant errors are systematic, with the largest uncertainty proceeding from the background estimate at large p_T.The curves represent pQCD parametrisations using the DSS[11] fragmentation functions.

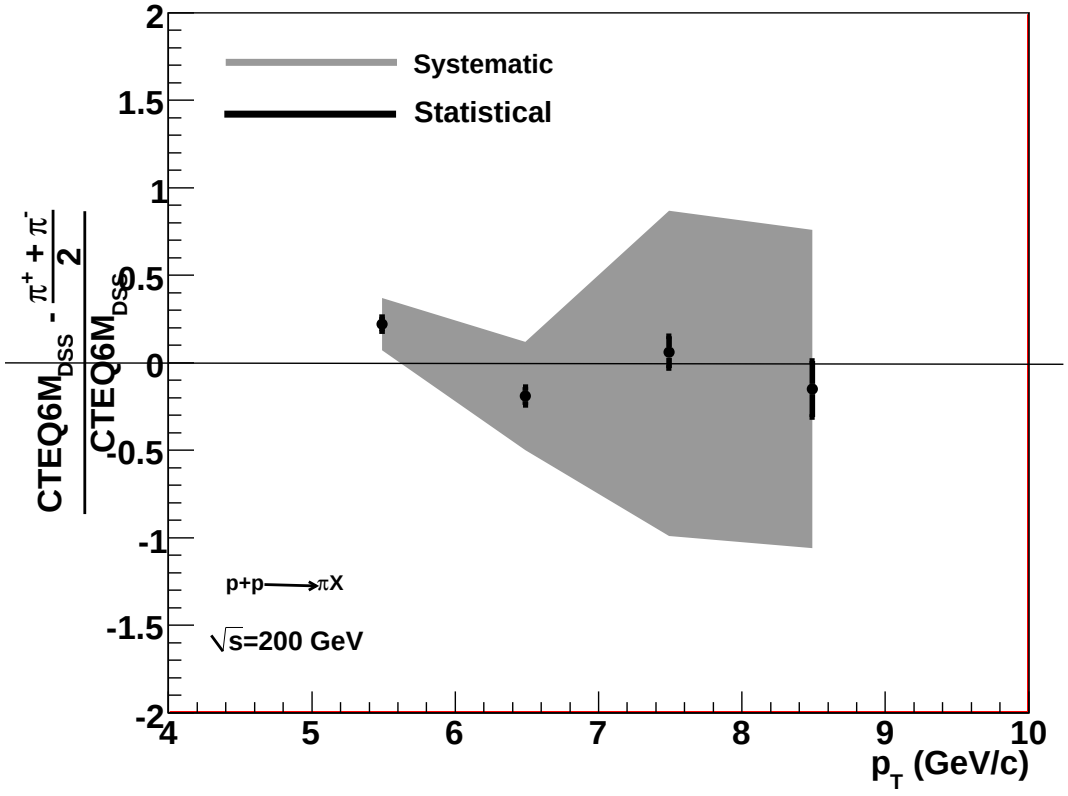

Figure 5.41: Comparisons of averaged summed pion measurement to pQCD predictions, using CTEQ6M unpolarized data and DSS fragmentation functions.

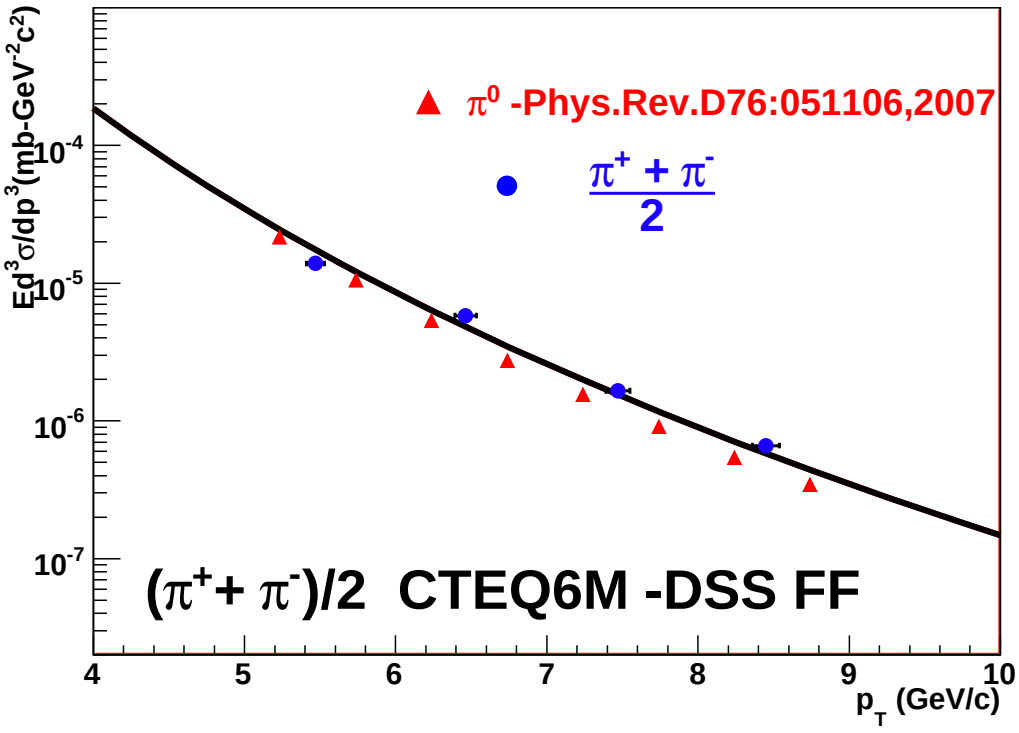

Figure 5.42: Comparison of measured cross-sections in this work with published neutral cross-sections from the PHENIX detector. Errors are shown in Figure 5.43.

$E\frac{d^3\sigma}{dp^3}$ Summary π^+.					
p_T[GeV/c]	Total Yields	Background Subtracted	ϵ	$E\frac{d^3\sigma}{dp^3}$ (mb-GeV$^2c^2$)	$\sigma_{sys} \otimes \sigma_{stat}$ (%).
5.47	7079	1699	0.0878	0.00001539	$8 \otimes 2$
6.49	4691	938	0.1096	0.00000680	$22 \otimes 3$
7.49	2777	278	0.1158	0.00000191	$62 \otimes 6$
8.46	1667	100	0.1052	0.00000076	$64 \otimes 10$

Table 5.19: Summary of π^+ yields, associated backgrounds and errors for $E\frac{d^3\sigma}{dp^3}$. Backgrounds can be found in Table 5.15. ϵ represents the efficiencies and constants described in Formula 5.3. Integrated Luminosity ($\int Ldt$ =1258366234 cm^{-2}s^{-1}) can be found in Section 5.7.2.

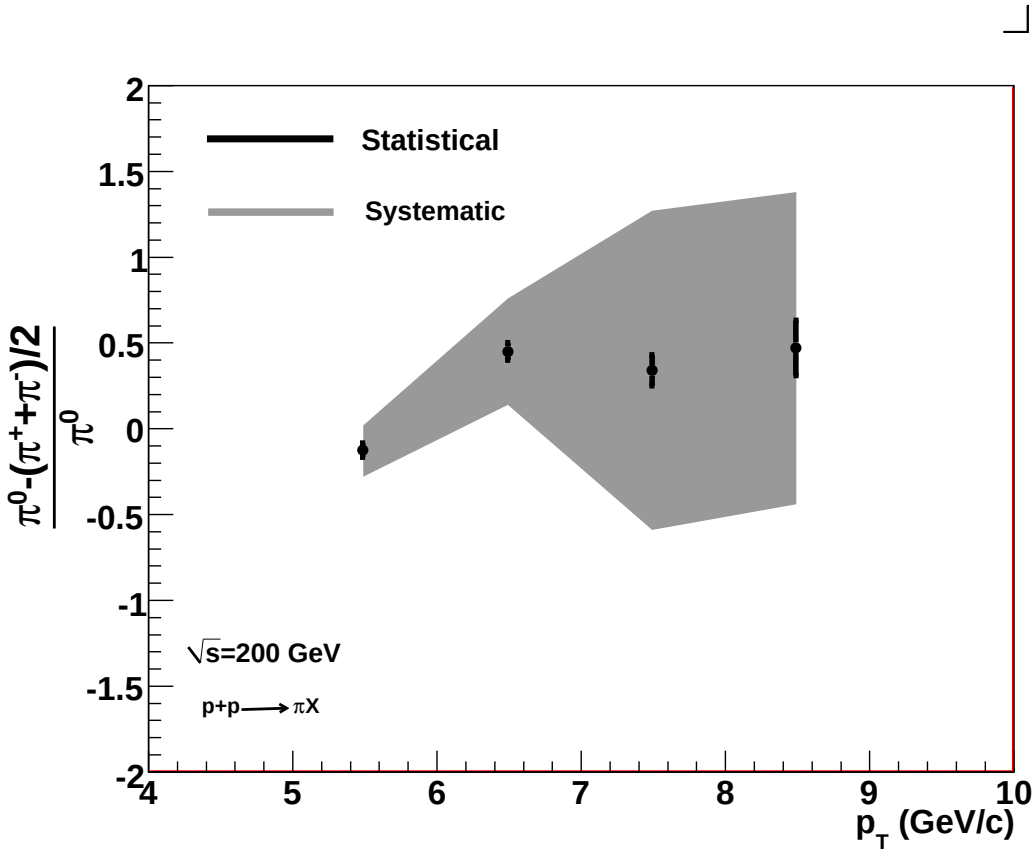

Figure 5.43: Comparisons of average summed charged pion cross-sections, with published cross-sections from neutral pions[2]. Systematic and statistical error bars are included. Errors are discussed in the following Section 5.9.

$E\frac{d^3\sigma}{dp^3}$ Summary π^-.					
p_T[GeV/c]	Total Yields	Background Subtracted	ϵ	$E\frac{d^3\sigma}{dp^3}$(mb-GeV$^2c^2$)	$\sigma_{sys} \otimes \sigma_{stat}$ (%).
5.47	7920	1501	0.0961	0.00001242	$13 \otimes 3$
6.49	4745	712	0.1210	0.00000467	$22 \otimes 4$
7.49	2734	191	0.1084	0.00000140	$70 \otimes 7$
8.46	1755	70	0.1000	0.00000056	$65 \otimes 12$

Table 5.20: Summary of π^- yields, associated backgrounds and errors for $E\frac{d^3\sigma}{dp^3}$. Backgrounds can be found in Table 5.15. ϵ represents the efficiencies and constants described in Formula 5.3. Integrated Luminosity ($\int Ldt$ =1258366234 cm^{-2}s^{-1}) can be found in Section 5.7.2.

5.11 Ratio of π^-/π^+

As briefly mentioned in Sections 6.1 and 2.9 charged pions form an isospin triplet. Due to charge conservation in proton proton collisions, it is predicted that a ratio different from one should dominate above 5GeV/c momenta. In addition to charge conservation, the partonic contributions in charged pion production at mid-rapidity can help predict the size of the charge asymmetry. Figure 2.3 illustrates the different partonic contributions to charged pions at the relevant p_T range of interest. g-g dominates the low momenta region giving an expectation of pion ratio of one. As the production momenta increases, q-g scattering begins to contribute to the probability of up quarks within the proton to fragment into π^+. At large momenta q-q and q-$\bar{q}$ scattering begins to take place, this naturally leads to an expectation of increasing charge asymmetry in favor of positive pions. This production rate expectation among the pions species make the isospin triplet an interesting quantity to measure. Measurable differences can provide an insight to the quark and gluon content and the fragmentation process. In this section a summary of pion ratio is made based on two different data-sets from proton proton collisions. This data will then be compared to theoretical predictions using two different fragmentation functions: DSS[11] and modified KKP [27]. Figure 5.44 shows the trends expected from these models.

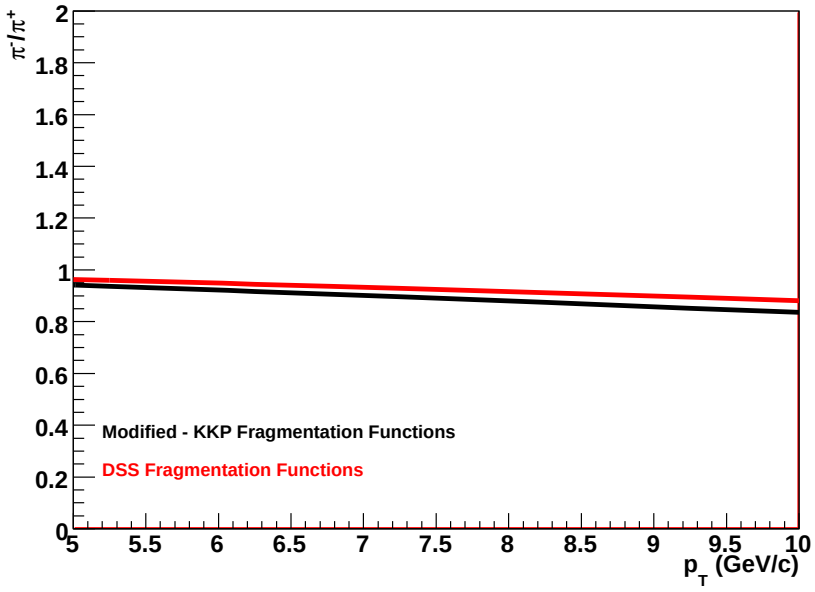

Figure 5.44: Ratio of π^-/π^+ as expected from theoretical inputs using two different fragmentation functions.

p_T[GeV/c] Bin	$\frac{\pi^-}{\pi^+}$	σ_{stat}
5-6	1.00	0.010
6-7	0.82	0.009
7-10	0.68	0.009

Table 5.21: Pion ratios measured with ERT triggered data after all cuts by charge and p_T bin.

p_T[GeV/c] Bin	$\frac{\pi^-}{\pi^+}$
5-6	1.03
6-7	1.03
7-10	0.93
7-8	0.90
8-9	0.96
9-10	0.96

Table 5.22: Simulation. Pion ratios after all implemented cuts (Section 5.2.1) by charge and p_T bin.

Preliminary Studies of π^-/π^+ with Simulation Data

A study using single particles as described in Section 5.2.1 did not display a strong charge asymmetry caused by detector effects. What was found instead was a slight excess of π^- for the p_T bins less than 7 GeV/c and an excess of π^+ for the bins above 7 GeV/c. Table 5.22 summarizes the findings from the Monte Carlo simulation. Another preliminary check that was performed involved testing the MB and ERT trigger for potential biases on the triggering mechanism itself. Again, this test showed that the MB trigger and the ERT trigger did not differ too much in the preference of which charge they would fire on. To test the effect of using different triggers on the pion identification, a study was performed which involved looking at all pions identified with the minimum biased data and collecting from this larger data-set all of the pions that also fired the ERT triggers. Charged pions in this sample were identified using standard cuts as will be described in Section 6.1:

$$\frac{N_{\pi^\pm} ERT\_trigger}{N_{\pi^\pm} Minimum\, Bias\, Trigger} \tag{5.12}$$

The results from this ratio showed that the identification of π^+ was similar to π^-, so we conclude that the PHENIX trigger does not significantly bias the π^+ and π^- measurements. Other ERT trigger studies were performed to explore potential biases and these will be discussed in Section 6.3. An additional study of the MB and ERT trigger

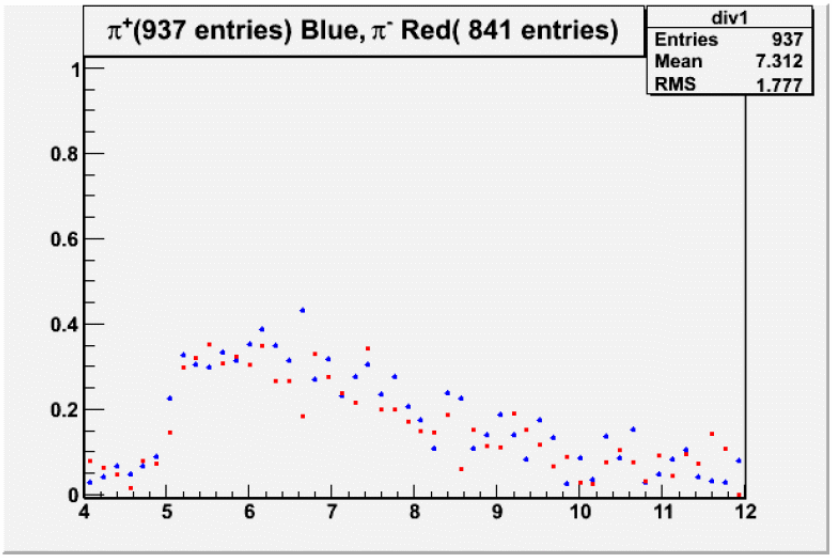

Figure 5.45: Ratio of pions vs p_T. Identified pions using the ERT Trigger and pions identified using the MB trigger. Blue points are π^+ candidates, while red are the π^- candidates. No dependence on the trigger is seen based on charge alone. The simultaneous decrease of both curves as a function of p_T is taken to be a systematic uncertainty as both triggers used the beam beam counters. Thus this is a further inefficiency which is introduced. Consequently, Equation 5.12 does not represent the efficiency of the ERT trigger

was performed with 2006 data and the results are shown in Figure 5.45.

Ratios from ERT Data and MB Data

A non trivial point to highlight is that the sample using the ERT trigger provided the cleanest and purest sample of charged separated pions, as will be seen in the next chapter (also Table 6.4). The method of identifying pions using ERT data which will be discussed in the next chapter utilized strict calorimeter cuts which removed completely all the minimum ionizing particles (MIP) and retained only those pions with a energy deposit above the MIP energy. The lowest energy pion accepted using this method was

$0.3 + 0.15 * (5GeV/c)$ or 1.05 GeV. The momentum dependent energy cut is close to the ERT trigger threshold of 1.4 GeV (Section 4.2.1); this energy cut will be discussed in Section 6.5.2. As the calorimeter's response to hadrons is not understood due to a lack of reliable test beam data, the efficiencies of these calorimeter based cuts are not known. Nevertheless, a ratio of pions was studied and found to be decreasing with p_T. This is summarized in Table 5.21 and in Figure 5.46. The ratio measured with MB data after large backgrounds were subtracted also showed this decreasing trend[23]. The rate of change appears consistent between samples and within the estimate of errors. Error bars of charged pions identified in the MB sample are dominated by systematic errors, mainly due to large uncertainty in the background which is calculated through RICH efficiencies. Table 5.21 and Table 5.23 summarize these results. Figure 5.47 compares the ratios measured thus far at the other experiment within RHIC, STAR[24]. The results in this work are consistent within errors to the results measured with the STAR detector[26]. This shows that the data measured in this work is consistent with measurements at STAR and with pQCD expectations.

[23]Systematic and statistical errors were too large to determine precisely the trend, as with errors included, all samples in this work agree with pQCD predictions.

[24]Solenoidal tracker at RHIC.

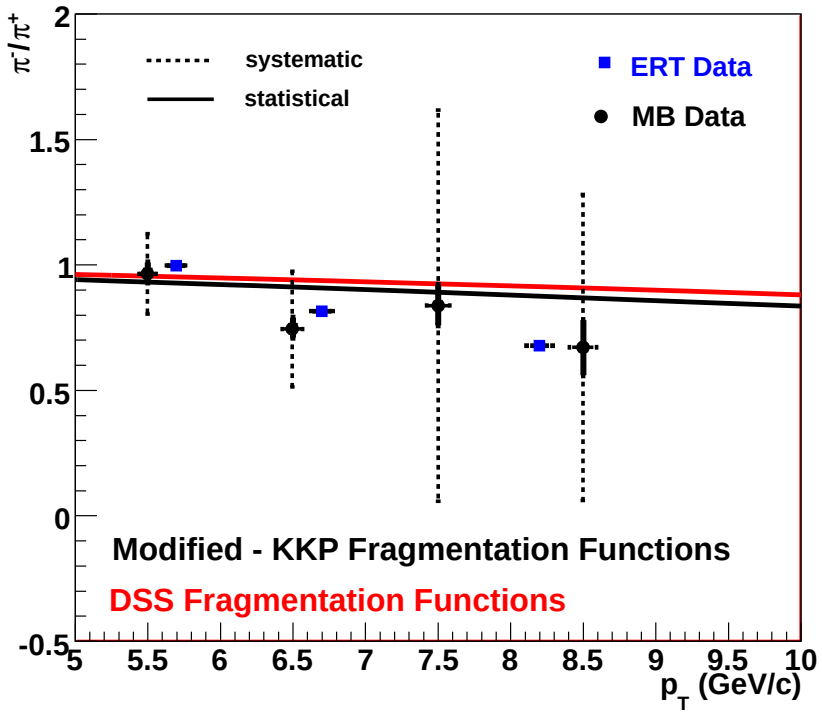

Figure 5.46: Measured ratio of π^-/π^+ using ERT and MB data.

Errors ($\frac{\pi^-}{\pi^+}$)			
p_T[GeV/c] Bin	$\frac{\pi^-}{\pi^+}$	σ_{stat} (%)	σ_{sys}(%)
5-6	0.97	0.04 (4)	0.16 (16)
6-7	0.75	0.04 (5)	0.23 (31)
7-8	0.84	0.08 (10)	0.78 (93)
8-9	0.67	0.11 (16)	0.61 (91)

Table 5.23: Identified pion ratios measured with minimum bias data by charge and p_T bin corrected for background using method 5.8.1 and with no calorimeter cuts implemented. Ratios are also corrected by the simulation ratios in Table 5.22.

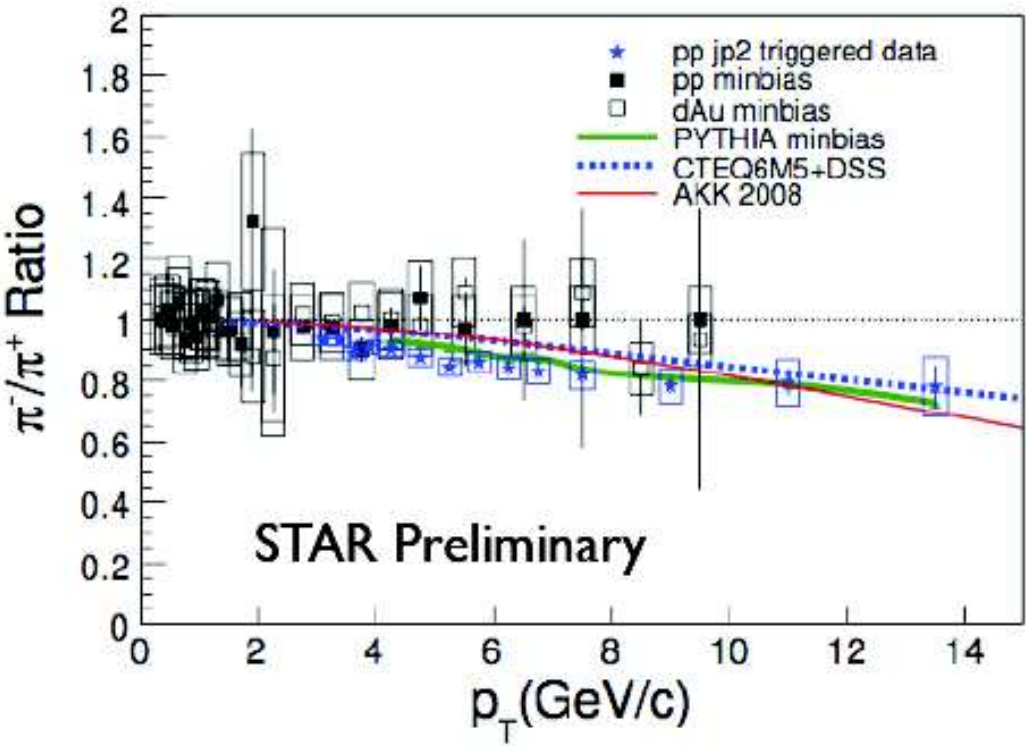

Figure 5.47: Measured ratio of π^-/π^+ by the STAR detector at RHIC. The pions measured at STAR are not necessarily a one to one comparison the pions measured in this work, as their triggering mechanism is substantially biased towards neutral particles. In addition, the newest charged pion measurements do not look at inclusive pions, but rather at away side jet fragments. Pions are detected after triggering in a large jet sum of energy, nevertheless, it is instructive to compare results. See[26] for more details.

Chapter 6

Charged Pion Spin Asymmetries A_{LL}, A_L

The measurements presented in this section will focus on the analysis of charged pion double spin asymmetries (A_{LL} Section 2.7) using both longitudinally polarized proton beams collided at $\sqrt{s} = 200$ GeV. The physics motivation behind the measurements of charged pion asymmetries is to help constrain both the sign and magnitude of the gluon polarization ΔG. Preferential fragmentation of up quarks (u) to π^+ and down quarks (d) to π^- leads to the dominance of up-quark-gluon and down-quark-gluon contributions. This dominance of u or d combined with the different signs of their polarized distributions translates into asymmetry differences for the different pion species π^+ , π^0 and π that depend on the sign of ΔG.

Before identifying charged pions with the PHENIX detector, preliminary steps were taken to assess the quality of data collected. The results of these quality checks are in Section 5.2.4 and also in Appendix E.0.2. In the previous chapter the main focus was to identify pions with a precise understanding of the detector response in the identification technique. Efficiencies were studied as each one of these cuts would introduce a systematic uncertainty if it were not well known. In contrast, this chapter emphasizes sample purity with disregard to detection efficiencies. Asymmetries consist of ratios of identified particle yields which cancel detector efficiencies as they are typically present in the numerator and denominator of the definition of A_{LL} (Formula 6.2). The focus will thus be to minimize background without precise knowledge of the number of candidate pions removed from the sample. The main motivation is to minimize systematic uncertainties in A_{LL} arising from sub-detector cuts. It is also desirable to obtain as pure of sample as possible as this will ensure that the measurement can be accurately described by the partonic fractions in Figure 2.3. As it will be shown at the end of the chapter, the charged pion sample obtained is of high purity with systematic errors below the current statistical precision.

The organization of this chapter will be as follows:

- Description and motivation of quantities measured: A_{LL} and A_L.
- List of sub-detector requirements (referred to as $cuts$).
- Trigger Studies.

- Identification studies.
- Background estimates (A_{LL}).
- Detailed description of the measured results for A_{LL} using two different methods and compared to pQCD predictions.
- Errors.

6.1 Double and Single Spin Asymmetries- A_{LL}, A_L

It was described in Section 2.9 that double spin asymmetries can yield valuable information about the role gluons play in the total spin of the proton. The first charged pion asymmetries at high p_T measured with the PHENIX detector were done in the year 2005 by the author of this work. These asymmetries were measured again in the year 2006 with higher accumulated statistics and new background removal techniques. The figure of merit ratio between the 2006 and 2005 data-set was 3.5. Figure of merit (FOM) is defined as the polarization squared times the relative luminosity in units of inverse nano barns (P^4L). Parity violating spin asymmetries (A_L) were also measured as a cross check for systematic errors as the process under study is not parity violating.

6.1.1 Asymmetries

A_{LL} (Section 2.3.1) are measurement ratios of particle yields. In this work two methods were used: χ^2 method and summed method. The standard χ^2 method calculates asymmetries fill by fill where a fill is defined as the time period encompassing one complete machine cycle[1]. The summed method calculates asymmetries by summing over all fills. Summing over fills is particularly useful in the measuring of small asymmetries with low statistics. The standard χ^2 method typically uses all bunches available where a bunch is an accumulation of particles of various energies over a determined longitudinal dimension[2]. There are up to 120 bunches in each RHIC ring with the bunches 30 meters apart. The summed method looks at deviations of the relative luminosity ratio R. R is the ratio of relative luminosities in each beam helicity configuration (L_{++}/L_{+-}) which is typically known to 10^{-4} precision. Bunches that have an R value outside tolerance (Section 6.10) are discarded. Single spin asymmetries are also measured with the standard χ^2 method. A_L asymmetries only take into account one of the beam's polarization while discarding the information of the second beam. A_L is typically calculated separately for the yellow and blue beams. Since the beams at RHIC are not in pure helicity states, beam polarization is accounted in the measurements of asymmetries. P_B and P_Y are the polarizations of the blue and the yellow beam which are known to $\sim 95\%$ certainty. N_{ij} are the particle yields in different proton beam helicity configurations. R is the ratio

[1] This includes the injection, acceleration, storage of colliding beams and ends with a beam dump.

[2] This is so that a vast majority of them can be accelerated by the RF cavity with the correct voltage and phase.

of relative luminosities fill by fill in each proton bunch helicity state. While R's units cancel in the ratio of luminosities, luminosity L units are given in cm^{-2}s^{-1}.

Standard χ^2 method:

$$A_{LL} = \frac{1}{P_B P_Y} \frac{N^{++} - RN^{+-}}{N^{++} + RN^{+-}}, \tag{6.1}$$

$$\text{Where, } R = \frac{L_{++}}{L_{+-}} \tag{6.2}$$

A_{LL}'s Summed[3] method:

$$A_{LL} = \frac{1}{< P_B P_Y >} \frac{\sum_{fills} (N^{++})_i - < R > \sum_{fills} (N^{+-})_i}{\sum_{fills} (N^{++})_i + < R > \sum_{fills} (N^{+-})_i} \tag{6.3}$$

Single Longitudinal Asymmetries A_L:

$$A_L = \frac{1}{P} \frac{N^{+} - RN^{-}}{N^{+} + RN^{-}} \tag{6.4}$$

Uncertainty (statistical) in A_{LL}:

$$\Delta A_{LL} = \frac{1}{P_B P_Y} \frac{2RN^{++}N^{+-}}{(N^{++} + RN^{+-})^2} \sqrt{(\frac{\Delta N_{++}}{N_{++}})^2 + (\frac{\Delta N_{+-}}{N_{+-}})^2 + (\frac{\Delta R}{R})^2} \tag{6.5}$$

[3]Also referred to in this work as a bunch subtraction method

Uncertainty (statistical) in A_L:

$$\Delta A_L = \frac{1}{P_{BY}} \frac{2RN^+N^-}{(N^+ + RN^-)^2} \sqrt{(\frac{\Delta N_+}{N_+})^2 + (\frac{\Delta N_-}{N_-})^2 + (\frac{\Delta R}{R})^2} \tag{6.6}$$

6.2 Data Quality Checks

In this section different cuts and detector identification techniques for charged pion A_{LL} are discussed. While some studies may overlap with the cross-section analysis, some differences remain in the identification techniques. The data sample under study was minimum bias for the cross-section measurements. A_{LL} measurements make use of ERT triggered data as the trigger provides greater certainty of DC track energy. Cross-section studies make no use of calorimeter cuts, while for asymmetries calorimeter is extensively used as an aid for background removal.

6.2.1 Sub-detector Requirements for Identification of Charged Pions

Polarized proton proton collisions at RHIC in the years 2005 and 2006 provided the longest longitudinal polarization running time available for the work presented. Asymmetries were measured by identifying a clean charged pion sample. The data used was calorimeter triggered data taken in two consecutive years of longitudinally polarized

p+p collisions at $\sqrt{s}$ =200 GeV. Cross-sections differed from the asymmetries in that no electromagnetic calorimeter based cuts or triggers were used. Omitting the calorimeter sub-detector in the previous chapter was based on lack of precise knowledge of the hadronic response. In the measurements presented here many calorimeter based cuts are employed as well as looser zed, matching and RICH cuts than in the cross-section analysis. Since asymmetries are ratios of yields, efficiencies typically cancel in the measurement. Identification of pions consisted of the following complete list of sub-detector requirements (cuts):

- Collision vertex measured from the BBC of less than 30 cm (absolute value).
- High drift chamber quality track (Referred to as quality of 63 or 31).
- Charged particle above RICH light emitting threshold for pions (4.7 GeV/c).
- Number of RICH photomultiplier tubes fired above zero within a disk shape (referred to as $|n1| >$0).
- Transverse momentum range of charged particles between 5 and 10 GeV/c.
- z matching of charged track to the radial plane of less than 70 cm (absolute value). Referred to as $|zed| <$ 70 cm (Section 5.2.1).
- Electromagnetic shower shape probability of deposited energy in calorimeter to be less than 20$\%$ (referred to as $prob < 0.2$).

- Ratio of deposited energy in calorimeter to measured transverse momentum of charged particle of less than 90% (Referred to as e/p <0.9, where energy is in units of GeV or MeV and momentum p in units of GeV/c).

- Energy deposition (in units of GeV or MeV) of identified charged particle to be greater than 300 MeV plus 15% of its measured transverse momentum (Referred to as $e > 0.3GeV + 0.15 * p_T$-Section 6.5.2).

- Drift chamber track projections to calorimeter and pad chambers. Deviations between projections and actual hits were required not to deviate more than 3σ in dϕ and dz (pc3sdϕ, pc3dsz, emcsϕ, emcdz. Figure 5.3).

6.3 Trigger Study

The 2006 and 2005 spin asymmetries utilized the *Electromagnetic calorimeter - RICH* Trigger (ERT Section 4.2.1). The ERT trigger is not a dedicated charged pion trigger but rather a trigger based on electromagnetic energy deposition. Before discussing the identification method of pions for the asymmetry measurements, a study checking for potential biases of the ERT trigger will be discussed. The study will address the following questions:

- Are charged pions triggered in the central region of PHENIX, biased towards more quark like jets?

- How often are secondary particle clusters which correspond to more than one energy shower associated with a single charged track?

Quark jets are expected to be small and compact while gluon jets are expected to have a larger angular distribution. Indeed, studies by the OPAL collaboration[17] have shown that there are angular distribution differences between quark and gluon jets. In addition, gluon jets seem to have higher particle production but are of softer character. In PHENIX the geometrical acceptance is limited and reconstructed full jets and their energies is a challenging task. The expected full jet cone radius is larger than the actual geometrical acceptance of the PHENIX detector. The 4x4c (Section 4.2.1) trigger used for A_{LL} has an energy threshold of 1.4 GeV. A high threshold of 1.4 GeV would perhaps bias the data sample with multiple particle energies coming from compact jets.

The issue that is investigated in this section is the contribution of energy from multiple particles overcoming the trigger energy threshold. These multiple contributions would be associated with a single DC track or single triggered event (i.e multiple electromagnetic shower clusters associated with one trigger). Multiple clusters associated with a single DC track could presumably be caused by the smaller angular distributions of particles coming from quark vs gluon jets. Observing a high cluster multiplicity would indicate that the charged pions measured in this work with the ERT trigger did not represent an unbiased sample of the pQCD partonic contributions in Figure 2.3. The detector's trigger would preferentially sample quark jets over gluon jets. A PHENIX de-

tector response simulation was performed to understand if the PHENIX detector could discriminate between particles coming from quark-quark, gluon-quark or gluon-gluon scattering. Additionally, a study was also made with triggered data taken in the year 2006. The data studies consisted of measuring how many times the trigger associated more than one shower cluster to the same unique drift chamber track. The conclusions of these trigger studies are that the measurements presented in this work are not biased by the trigger.

6.3.1 PHENIX Response to Simulated QCD Jets

To study the detector response to QCD jets a PYTHIA[18] Monte Carlo simulation was made specifically selecting: $qq \longrightarrow qq$, $qg \longrightarrow qg$ and $gg \longrightarrow gg$ (3000 events each). These processes were studied both as QCD jets and as individual hard scattering processes. Each generated QCD sample was then used as an input to a full detector simulation with detector configuration matching the year 2006 proton proton collisions settings. The average distribution of particles detected by each electromagnetic calorimeter arm [3] was studied. The distributions showed that events coming from gluon generated events had higher (although nearly indistinguishable) particle production on average than the quark generated events. The excess of particles coming from gluon-gluon scattering became indiscernible when a minimum momentum requirement of 0.5 GeV/c was applied. Particle counts were comparable between samples in the pQCD "safe" re-

gion above 1.5 GeV/c. This similarity between scattering processes can be explained by the removal of particles coming from soft components which tend to be in the low momentum region and cannot be described well with pQCD[4]. Figure 6.1 shows the drift chamber tracks projected to the calorimeter in the y and z coordinate of the EMCal. Particle distribution in each PHENIX track arm is also shown in these figures while Table 6.1 summarizes the findings.

Each point in Figure 6.1 is a simulated particle which managed to make it through the PHENIX detector. Particle distributions are comparable when QCD jets are generated from quark-quark, gluon-gluon or quark-gluon scattering processes. Similarly, when single processes are generated, particles produced in the reaction are detected without strong preference of one process over another.

Simulation of QCD processes. Minimum parton p_T of 2.0 GeV/c.		
Process	Total Particles Detected	Particles after a p_T of cut > 0.5 GeV/c
$gg \longrightarrow gg$	102	38
$qg \longrightarrow qg$	92	48
$qq \longrightarrow qq$	72	35

Table 6.1: Number of particles detected in the central arms compared with low p_T cuts for 3 different QCD Processes.

[4]In PHENIX, the momenta region below 1.5 GeV/c is considered to be the ”unsafe” non perturbative soft region, for an estimate of this see Reference[5]

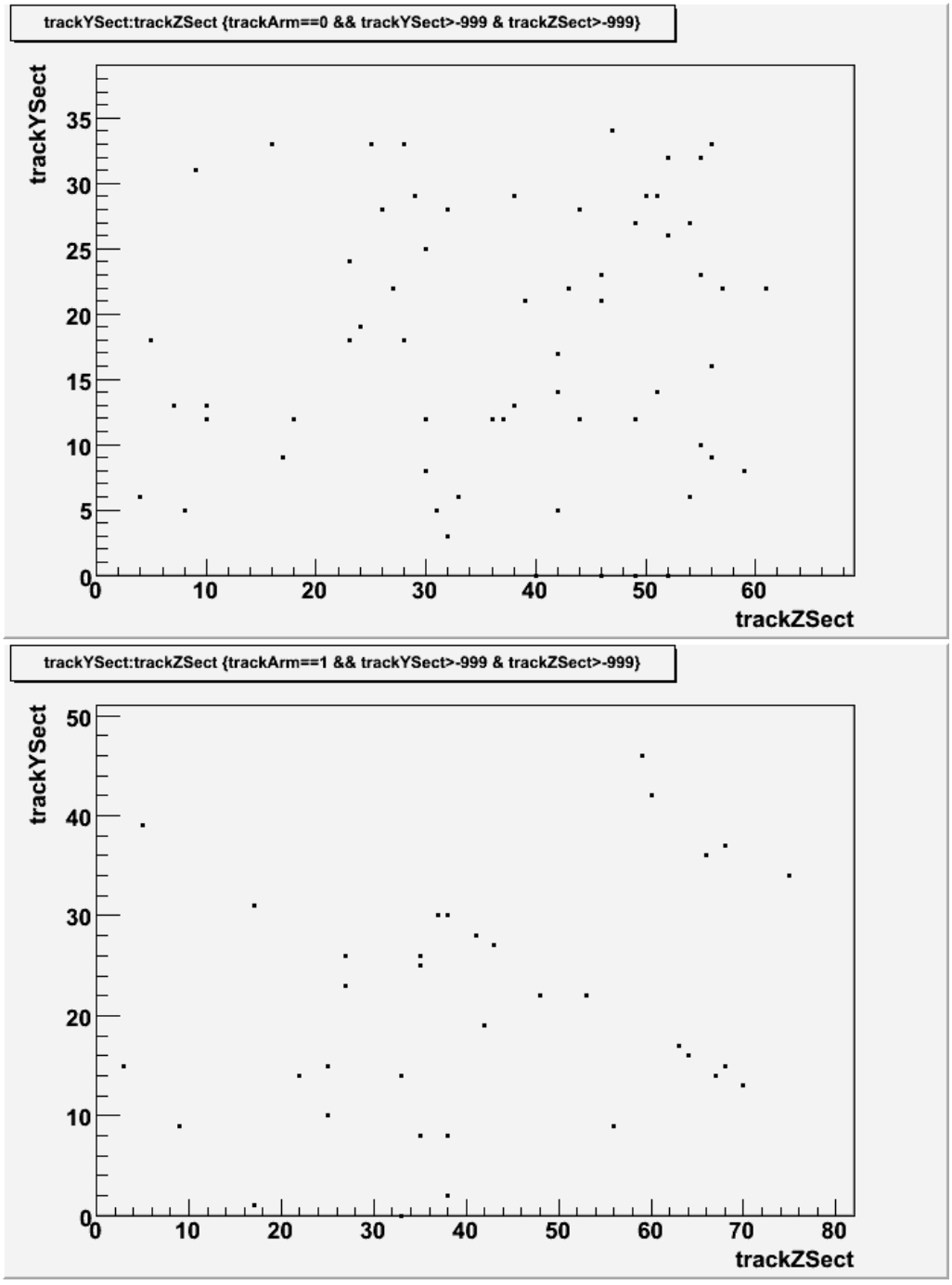

Figure 6.1: Number of simulated particles detected in the central arms. Events are gluon-gluon scattering. Each point in the scattered plot is a particle energy deposition cluster measured in cm length in the *x* and z plane. As a reminder the EMCal has position resolution of about 7 mm. EMCal Arm West is shown in the top panel while the East arm is shown on the bottom panel. Total number of particles produced and tracked with the drift chamber are 63 in the West arm and 39 in the East arm. More studies can be found on the Appendix J.1.

6.3.2 ERT Trigger Charged Track Clustering Study

To study possible biases imposed in ERT triggered data, events containing charged tracks were analysed. This study utilized the 2006 proton proton collision[5] data taken with the ERT 4x4 trigger (Section 4.2.1). Events were analysed for recorded triggers. Once a trigger was found, all charged tracks associated with the trigger were inspected.

The number of energy clusters associated with the same trigger which pointed towards the same geometrical region (super module) as the drift chamber track were analyzed. 282 triggered events were found. Of these events, 8.5$\%$ had a secondary cluster associated with the same track, same geometrical region, same event and trigger (See Table 6.2). When a requirement was made that the energy of the track were to be equal or greater than the energy of the matched cluster, the multiplicity of clusters dropped to about 6$\%$. Multiple cluster associations were separated into 3 categories:

1. Clusters with a high central tower deposition containing a tower having energy higher than the energy of the DC track (1.5%). An example of this energy mismatch follows. One may have a track with energy 1 GeV but there may be two central towers associated with the same trigger and thus two energy clusters[6](Section 4.1.7). The cluster energies were recorded as: $central - Tower_1 = 1.5\,GeV$ and $central - Tower_2 =$

[5]Only one segment from each run was analyzed. This is similar as analyzing a few percent of the data in each data taking period which is typically a few hours. A few percent of the whole data accumulated is usually made readily available by locally storing it. This is to enable quick studies with a representative sample of the whole data-set.

[6]Once the towers are calibrated, adjacent ones are grouped together to form clusters with the central tower holding the center, thus highest energy fraction of the total shower deposition

$0.8\,GeV$. Clearly 1.5 GeV is higher than the total energy of the track E_{track} =1 GeV.

2. Clusters of comparable high central tower energy but less energy than the total DC track energy (6%). An example of this central energy inconsistency follows. One trigger may have two clusters with two central towers of values: $central - Tower_1 = 0.78$ GeV and $central - Tower_2 = 0.7$ GeV. These will have two different cluster energies: $energy_1 = 1.96$ GeV and $energy_2 = 1.4$ GeV. The energy of the track in this case was found to be $E_{track} = 1.9$ GeV.

3. Clusters with a low energy central tower near a high energy central tower (1%). The DC track is associated with the lower energy cluster rather than the cluster the central tower containing the highest energy. E.g., one triggered track may have two or more clusters with two central towers. One tower will have energy of 0.2 GeV and the other tower 1 GeV. The triggered track energy points at the lower energy cluster rather than the cluster containing the high energy central tower.

Process	Number found
Triggered N_{Events} with a track associated with a SM	282
Triggers with only one cluster	258
Triggers with more than one cluster	24
Triggers with more 2 clusters	3

Table 6.2: Number of triggers with more than one cluster in the super module.

Figure 6.2 shows the ratio of energy of triggered tracks with the energy of triggered cluster. One can clearly see that there are a number of events in which the cluster energy exceeds that of the track energy. This effect only occurs when there is more than one

cluster associated with the same trigger. PHENIX's ERT trigger provides the option of verifying the particle that produced the trigger signal. This is typically verified by the deposition of energy within the geometrical constraints of the super-module where a trigger is found. The particle that caused the trigger signal can be verified to be the particle being analyzed. In all of the ERT measurements and studies contained within this work, particle trigger verification was performed and only trigger particles were considered candidates for the physics measurements. Figure 6.3 shows the consistency between the selected region by the ERT and the super-module where the particle was found. Figure 6.3 also shows consistency between the geometrical region of the DC track coinciding with the triggered EMCal module.

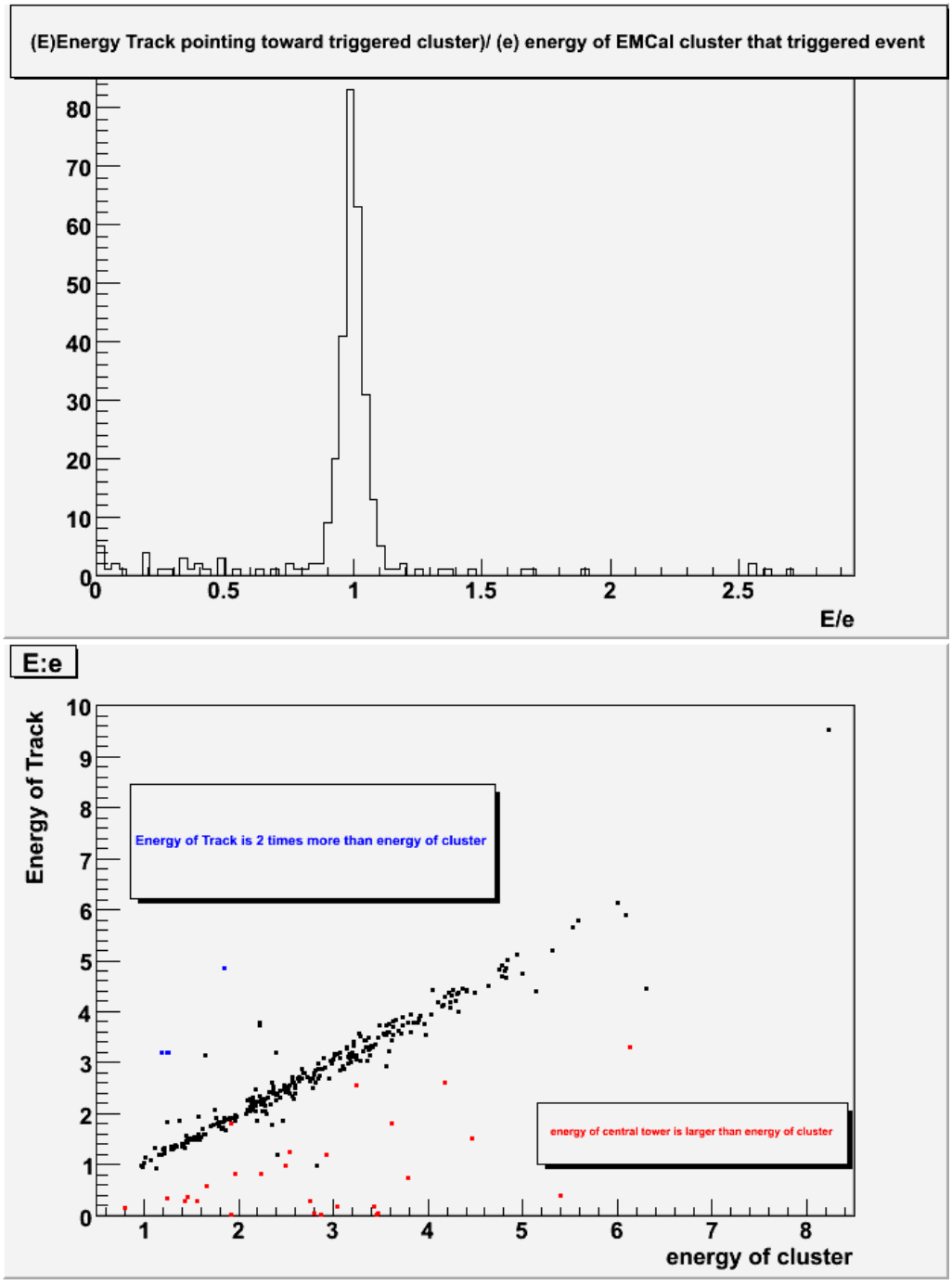

Figure 6.2: Energies of tracks associated with a trigger that fired and went inside a super module compared to associated clusters that also fired the trigger. Blue points are track energies that exceed cluster energy by a factor of ~ 2 or more. Red points are central tower energies which exceed the overall cluster energy. Top panel shows the ratio of DC track energy over EMCal cluster energy. Bottom panel shows energy of the track vs. energy of cluster.

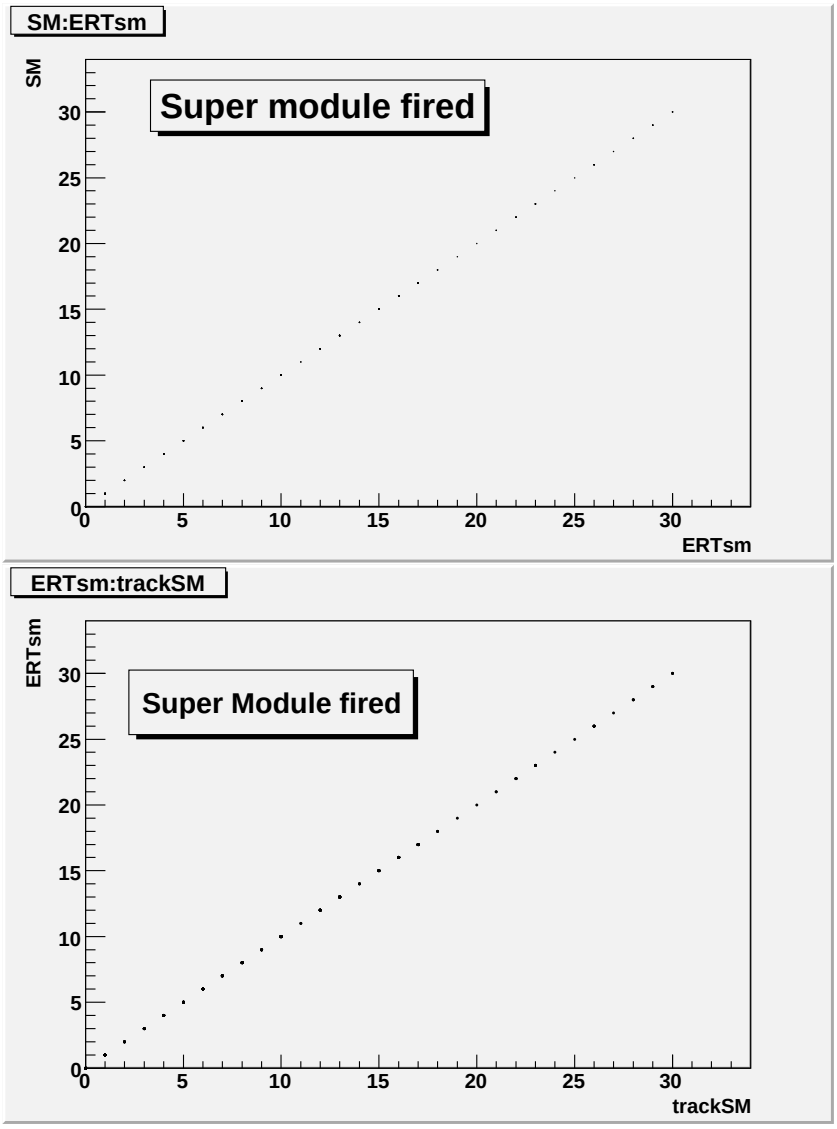

Figure 6.3: Matching of modules where the trigger was found, clusters modules vs ERT modules (top) and track modules vs ERT modules (bottom). A clear match is made which shows that the selected particle was measured with consistency in the modules.

6.3.3 Summary of Trigger and QCD Jet Study

The QCD jet simulation study showed that the PHENIX detector with its limited acceptance cannot differentiate particles coming from quark or gluon jets. The spatial

resolution of particles produced in each QCD process appeared to be comparable and of similar detection probability. The particle distributions showed that while a gluon jet may produce more particles than a quark jet, these particles cannot be easily discerned after travelling through the PHENIX acceptance region. This may be explained by the limited acceptance of PHENIX and the high granularity of the calorimeter. In the presented work inclusive charged pions are measured. These pions are expected to be dominated by quark-gluon scattering in the momenta region 5-10 GeV/c. Each process: quark-gluon, gluon-gluon and quark-quark, is carefully taken into account using pQCD. A potential bias occurring from artificially selecting one type of process over another does not seem to be supported by the detector response simulation. The ERT trigger study using real data showed that when it was required that a triggered particle is associated with a drift chamber track, 8.5% of the time the ERT trigger will associate more than one shower cluster to a single trigger. An energy requirement on the shower clusters can reduce the shower association multiplicities to 6%. These results can be viewed as knowing the particle under study with 94% certainty.

6.4 Selection of Data and Identification Studies

The 200 GeV data has been calibrated for proton beam shift and drift chamber (DC) momentum scale. Refer to Section 5.2.4 for details on how this was performed. Charged track reconstruction within the central arms in the PHENIX detector assumes straight tracks outside the effective magnetic field and within the sub-detector regions. The charged track momentum is obtained by measuring α (Figure 5.15) formed by the transversing track which will ionize the gas in the DC producing an electronic signal induced by drifting electrons hitting the anode wires (wire hits). α is proportional to first order to the inverse to the momentum and the charge of the particle - see Reference [3] for detailed information on the drift chamber's principles of operation. The magnetic field configuration and the coordinate system used for the DC relates a positive α to a positively charged particle and a negative angle to a negatively charged particle. The resolution of the four momentum assumes particle production originating from the collision vertex (0,0,0) (Figure 6.4). If the vertex origin is changed by a physical shift of the beam or by the PHENIX central arms rolling in the *x* direction, the momentum of the tracks as well as their matching to the outer detectors will be incorrect. A full calibration analysis was performed to correct for these effects. Besides calibrating the vertex origin several data files (runs) were discarded due to unacceptable quality. Criterion for discarding data included: bad polarization values, too many drift chamber dead areas, inconclusive or wrong relative luminosity values. The A_{LL} analysis consisted of ERT triggered

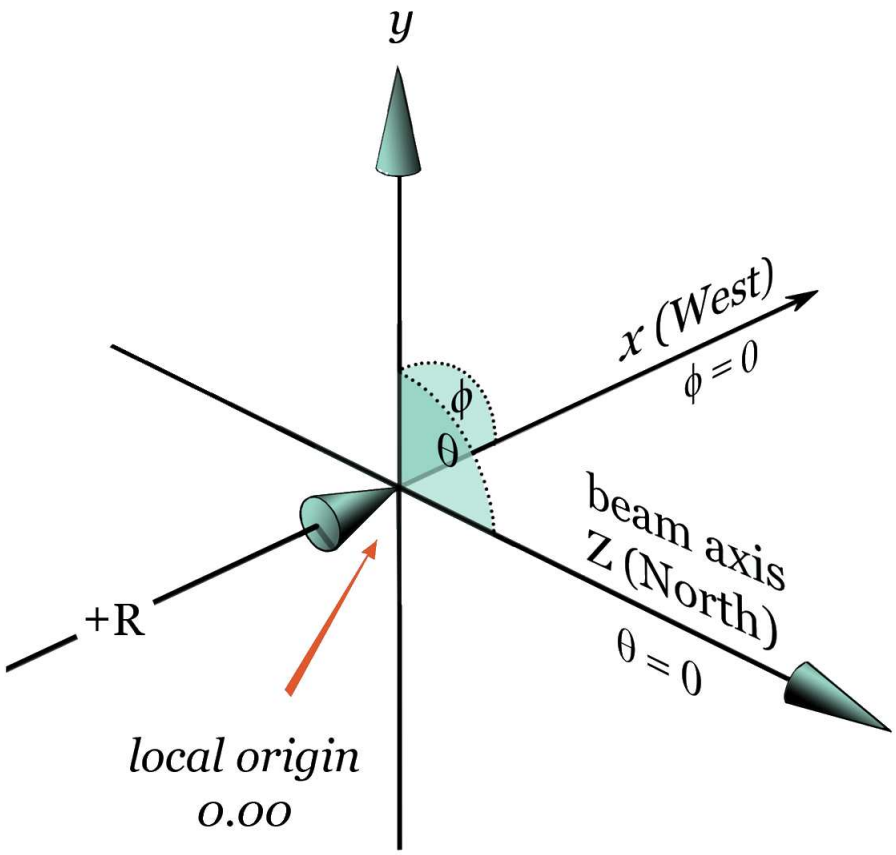

Figure 6.4: Representation of PHENIX coordinate system

.

data (Section 4.2.1). Calorimeter triggered data was used because this provided higher statistics and certainty in the energy and projection of the DC track. ERT trigger configurations selected were 4x4c and BBCLL1 (Section 4.2.2) with a 1.4 GeV threshold (energy deposition). The data range selected for the measurements of this chapter included two separate years of proton proton longitudinal data at $\sqrt{s} = 200$ GeV. Only tracks with high DC quality (Section 4.1.4) were analyzed. In addition a requirement

was made such that the triggered particle was found in the electromagnetic calorimeter geometrical area under study (super module). This is also called a trigger bit check and it ensures that the trigger particle is selected rather than clusters in the vicinity of the triggered particle[7]. Figure 6.5 illustrates the effect of verifying the particle in the ERT trigger. The low momentum region indicative of minimum ionizing particles is greatly suppressed. The total number of events analyzed were 56,527,853 for the 2006 data-set. Details of the charged pion identification cuts and studies will be discussed in following sections.

[7] A trigger electronic bit can be set to zero or one if a particle that triggered the event can also be found in coincidence with a super module hit.

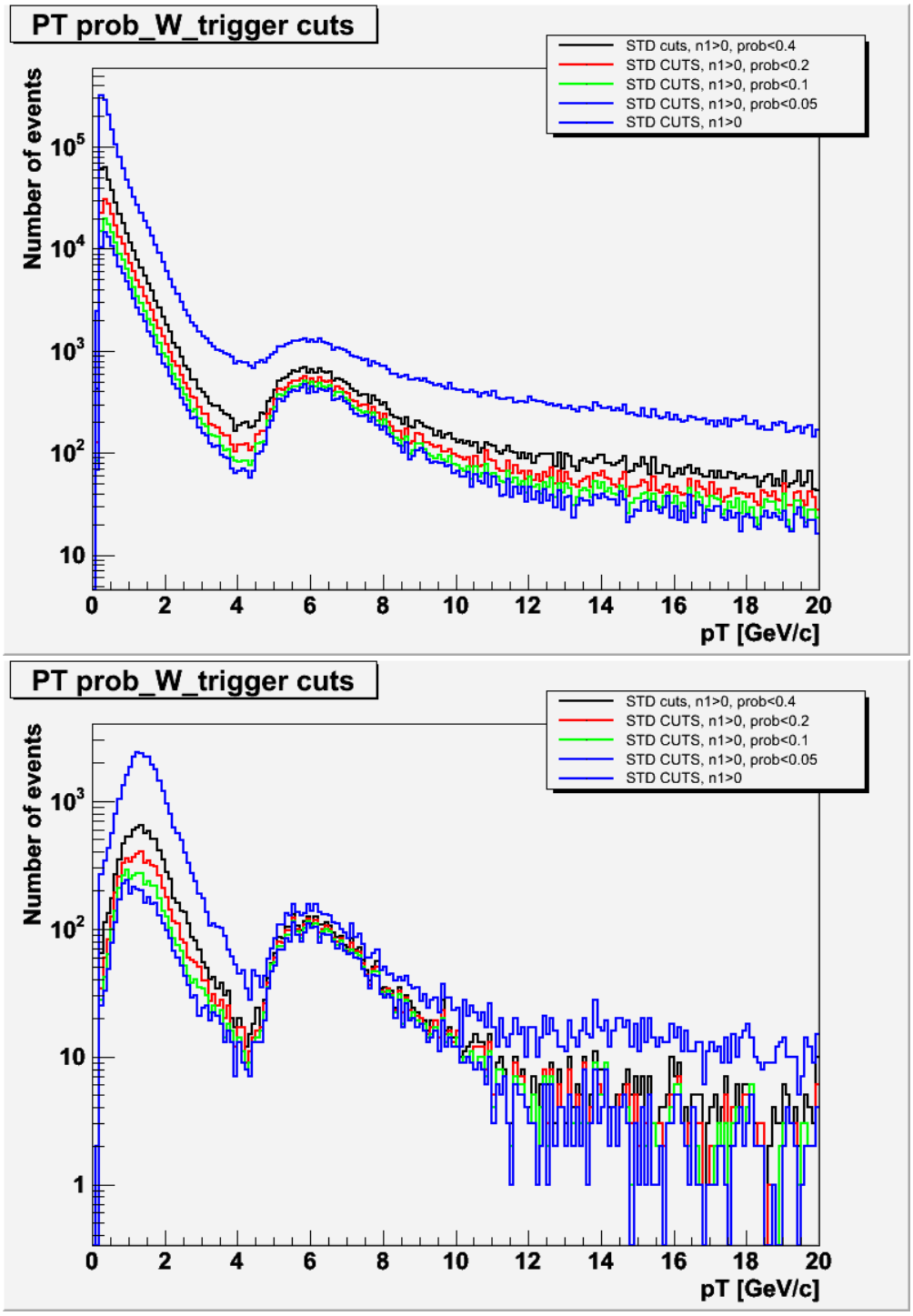

Figure 6.5: p_T spectra of pion candidates with low probability of electromagnetic type showers and different RICH *n1* (Section 5.3.1) disk tube firing requirements. Top plot shows all triggered data while bottom plot requires that the triggered event contains the triggering particle (trigger bit was set). The reduction in statistics in the p_T region below 1 GeV/c indicates a significant reduction of minimum ionizing particles. STD cuts refers to beam beam vertex cut less than 30 cm as well as $|zed|$ less than 70 cm. Refer to Section 6.2.1.

Beam	Energy (GeV)	Uncertainty	$< P >$ (%)
Blue	100	4.7%	53
Yellow	100	4.8%	53
$\frac{\Delta P_B \Delta P_Y}{P_B \times P_Y}$	100	8.3%	55

Table 6.3: Official polarization global uncertainties for each polarized proton beam on $\frac{\Delta P}{P}$ and $\frac{\Delta P_B \Delta P_Y}{P_B P_Y}$. Where B (blue) and Y (yellow) indicate the labeling convention of the rings where beams are stored.

6.4.1 Polarization information for the selected data-set.

The polarization values were obtained from the final polarization[8] analysis performed by the RHIC CNI[9] group. Polarization data along with some supporting material can be obtained from CNI web page[9]. Assuming errors correlated for all fills, the global uncertainties are taken from CNI's official release of numbers and are summarized in Table 6.3.

[8]Final polarization values were implemented for the asymmetries measured using 2006 data. asymmetries measured using 2005 data-set used on-line polarization values with a scale uncertainty of 20% on each colliding beam

[9]CNI stands for Coulomb nuclear interference region, it is in this interaction point at RHIC (the 12 O'clock region -Figure 3.1)- where polarization is measured and made official to all RHIC experiments. CNI refers to certain energy range in the elastic p-p scattering process, in which the strong and electromagnetic forces are part of

6.4.2 Relative Luminosity of Selected Data-set

The relative luminosity for the sum of bunches with a given polarization combination is used to normalize the input yields in the asymmetry calculation $R = L_{++}/L_{+-}$. A bunch is an accumulation of particles of various energies over a determined longitudinal dimension so that a vast majority of them can be accelerated by the RF cavity with the correct voltage and phase. Run-by-run relative luminosity information was obtained from PHENIX's internally approved calibrated files which were also used for the 2006 π^0 results[5]. Luminosity is defined as the number of particles per unit area per unit time times the opacity of the target, while integrated luminosity is the integral of the luminosity with respect to time, the latter which is used to characterize collider performance.

6.5 Specific Identification Cuts Used to Measure Charged Pion A_{LL} and A_L

Several of the cuts listed at the beginning of the chapter will be discussed in this section in greater detail. These cuts are more specific to the asymmetry measurements as calorimeter cuts are included. There are sub-detectors that are common for cross-sections and asymmetry measurements. These common sub-detector cuts are looser in this section than in the cross-section measurements in the previous chapter.

These cuts will include the following:

- Identification cuts - RICH. (Section 6.5.1).

- Background removal cuts - EMCal (Section 6.5.2).

  prob< 0.2.(Section 6.5.2).

  e$> 0.3GeV + 0.15 * p_T$.(Section 6.5.2).

  e/mom < 0.9.(Section 6.5.2).

- Charged tracking - background removal cuts.

  $|zed|$ cuts (Section 5.2.1).

  Matching cuts.(Section 6.6.1).

6.5.1 Using the RICH to Identify Charged Pions

To identify charged pions the primary sub-detector used is the RICH (Section 4.1.6). Light emitted by charged particles above charged pion Čerenkov light emitting threshold is used as the primary form of identification. Charged pions will create a disturbance in the (carbon dioxide radiator) dielectric medium contained in the RICH vessel. Light emitted by charged pions will typically will be in the shape of a disk ($n1$) of Čerenkov light associated with a Drift Chamber (DC) charged track. This $n1$ disk is defined by a radius of 11 cm encircling the projected hit location of an identified track inside the DC. Details of the choice of a disk of light $n1$ over a ring of light $n0$ as a identification technique and the associated efficiencies can be found in Section 4.1.6. To ensure

that charged pion tracks are selected, a requirement is made that all particles are above the light emitting threshold for charged pions ($n1 > 0$). This can be clearly seen in Figure 6.6 regarding the expected turn on curve for charged pions around 4.7 GeV/c. The efficiencies as function of p_T of the RICH are known from the previous chapter Section 5.3.1.

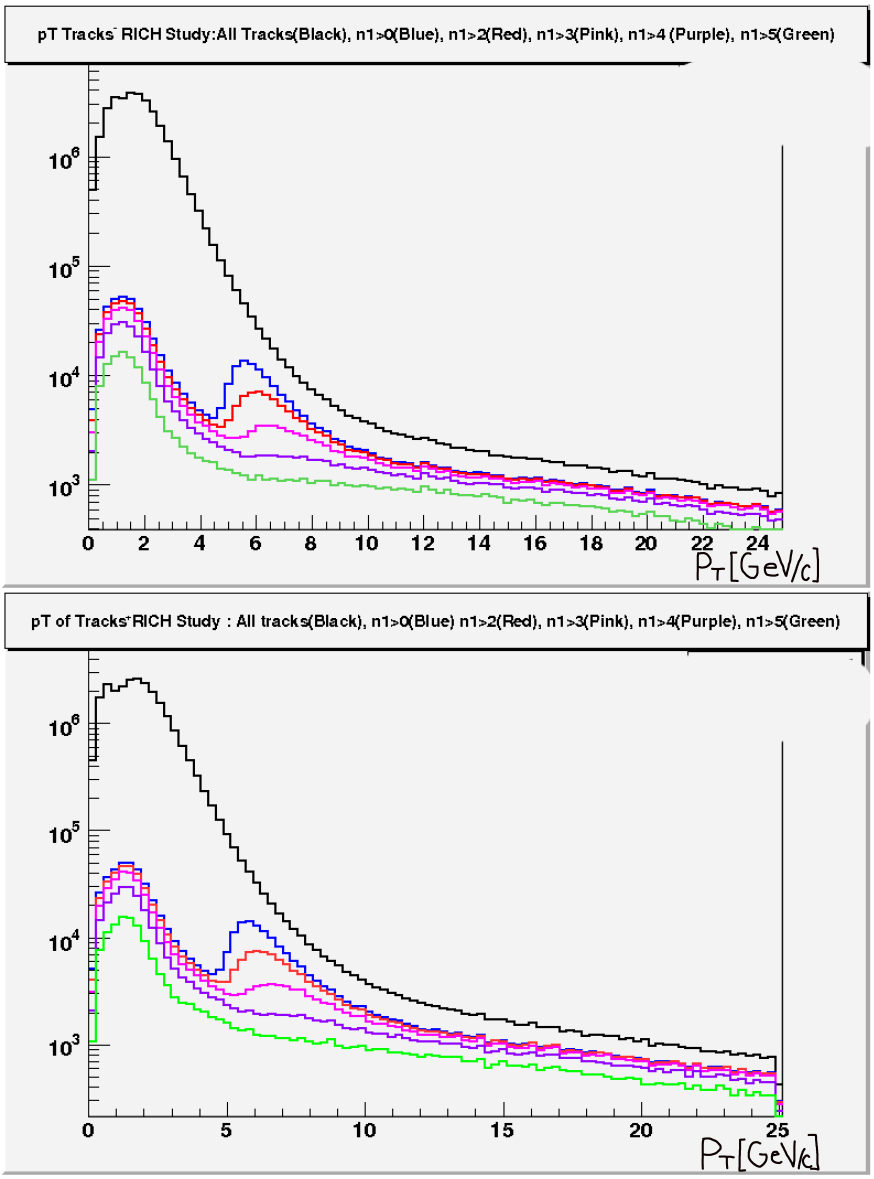

Figure 6.6: Study of RICH Čerenkov light emitting threshold within a disk of light $n1$. The $n1$ disk corresponds to the shape of the light as detected by the photomultipler tubes (PMTs) proceeding from charged pion candidates disturbing the transversing dielectric medium in the detector volume. The top panel corresponds to π^-, while the bottom panel corresponds to π^+ candidates. A clear turn on curve can be seen around the RICH p_T threshold of ~ 5 GeV/c when requiring that $n1 > 0$ (blue line). Note that the turn on diminishes at $n1 > 4$ (purple line) and completely disappears for n1> 5 (green line). Other curves represent different PMT from $n1 > 2$ to $n1 > 6$ tube firing requirements. See Section 6.7 for a detailed discussion of the background which remains in the sample.

6.5.2 EMCal Cuts

For the asymmetry measurements three cuts on the calorimeter were performed which shall be discussed in further detail:

- Strict maximum electromagnetic shower likelyhood (*prob*).
- Strict minimum p_T dependent energy deposition (*e*).
- Loose maximum ratio of energy and momentum requirement (*e/p*).

Probability on the Electromagnetic Shower Profile (prob).

A *prob* cut is used to reject electromagnetic type showers. *Prob* is a normalized photon probability from EMCal χ^2 (emcchi2) obtained by calculating the predicted energy distribution in the EMCal towers (based on electromagnetic shower parametrisation). It is obtained by comparing it with the measured deposited energy. Since electromagnetic showers remain compact while hadronic showers are diffused, χ^2 has a significant rejection power: typical respective χ^2 for hadrons should be large, while that of photons (electrons) are small. By design this cut has been optimized to reject hadrons. This cut is an effective tool yet its efficiency is unknown. EMCal based cuts are unknown as hadronic showers have not been studied nor reproduced successfully due to lack of test beam data at PHENIX. In this analysis the $prob$ cut is used to reject showers that are highly electromagnetic in nature as this variable has been parametrized to accurately

recognize them. Figure 6.7 shows the effect on the charged particle sample, and in in particular, the effect at lower p_T (below 5 GeV/c) and at high p_T (above 8 GeV/c). Some hadrons will be rejected by this method, however as asymmetries require high purity the sacrifice of some hadrons is made as a trade off for the purity of the sample. Several ratios of probability cuts were made leading to a conclusion that stricter probability cuts were unnecessary. Stricter $prob$ cuts reduced the efficiency without additional charged pion purity (See Figure 6.7 and Figure 6.8). For further ratio studies of the *prob* cut see the Appendix I.

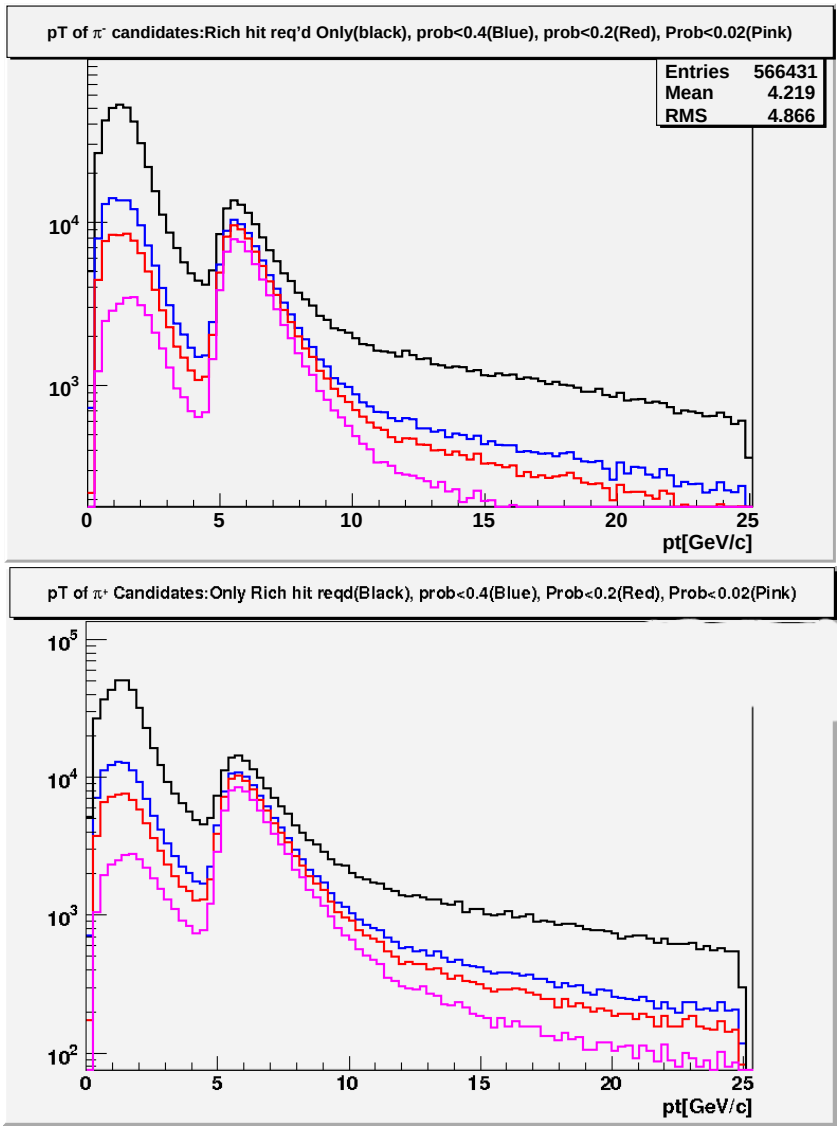

Figure 6.7: Study of the $prob$ variable: probability < 0.2 was selected (red) as optimal. Notice how the distribution changes at high p_T as the electromagnetic-ness of the particles decreases when one requires a small *prob* cut. Top panel are π^- candidates while bottom panel are all π^+ candidates within a region of $0 < p_T < 25$ GeV/c. Data from year 2005.

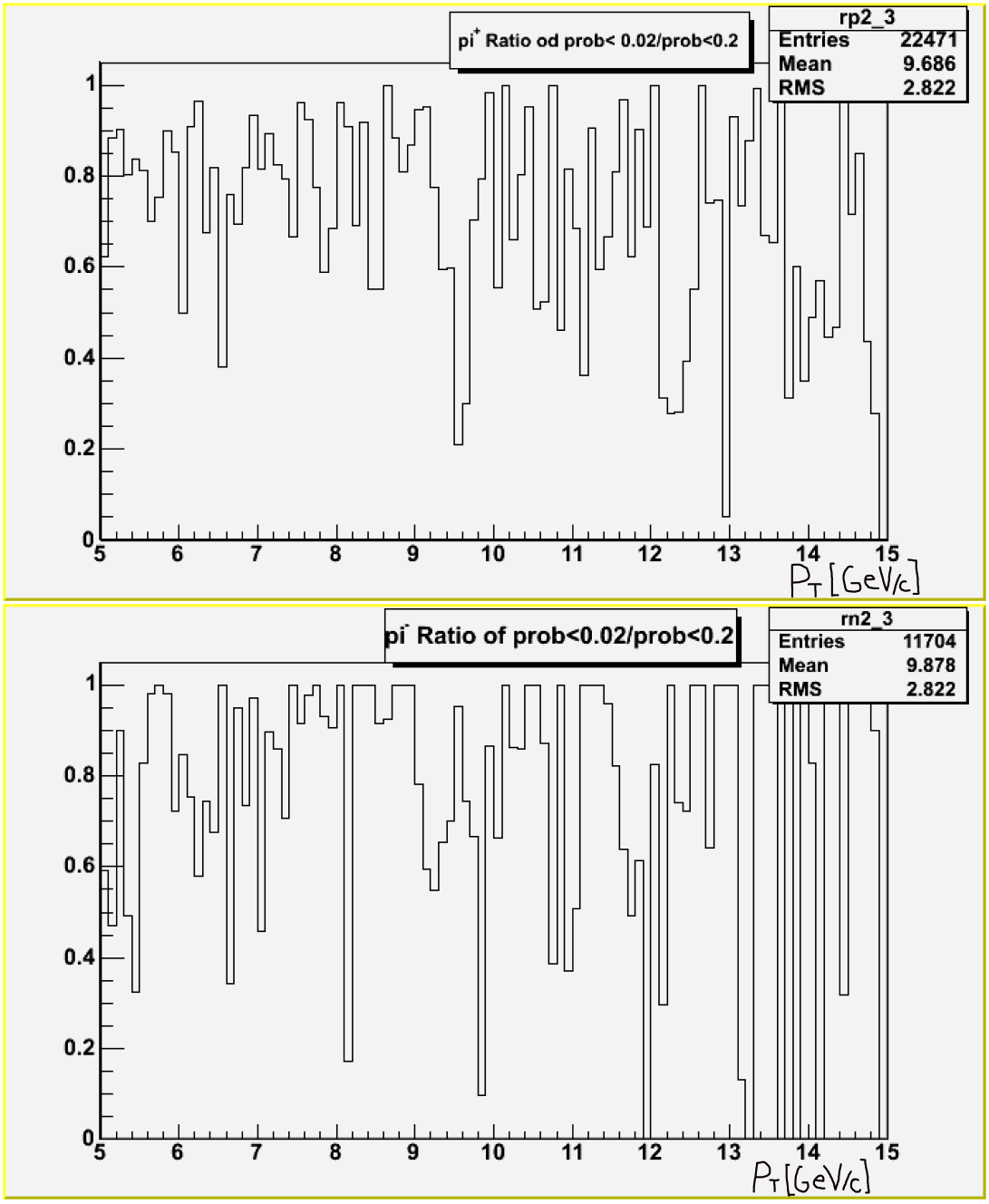

Figure 6.8: Ratio of data with a probability of electromagnetic shower $\frac{prob<2\%}{prob<20\%}$ for positive (top) and negative (bottom) pion candidates. The ratios are based on the data from Figure 6.7 concentrating in a smaller p_T range. Units on x axis are GeV/c, corresponding to bins in p_T, y axis are the ratio of yields $\frac{prob<2\%}{prob<20\%}$. Data from year 2005.

p_T Dependent Energy Cut

Since the average p_T of an electron coming from photon conversion is 500 MeV and an electron will typically deposit all of its energy in the calorimeter, a constant minimum high energy deposition requirement will reduce the background at high p_T. This constant energy[10] will also select only nuclear interacting particles with large energy depositions, therefore reducing the overall pion reconstruction efficiency. For this portion of the analysis a p_T dependent energy deposition requirement of pion energy $> 0.3GeV + 0.15 * p_T$ is chosen over a constant energy requirement. Figure 6.9 shows the effects of requiring different energy depositions with $> 0.3GeV + 0.15 * p_T$ being the optimal choice for this work (purple curve). Refer to the figure for more details. This cut corresponds to a study based on test beam data which determined that a momentum dependent energy requirement was more adequate at maintaining constant efficiency as a function of p_T[11]. By taking a look at an energy/momentum (e/p) distribution (Figure 6.11), one can see that indeed this cut effectively removes all low energy depositions which includes both electrons and hadrons. For an asymmetry measurement purity is considered a priority even at the expense of removing a potential large hadron contribution and thus purity is chosen over the loss of hadronic statistics.

[10] Constant referring for example to a 500 MeV minimum energy deposition

[11] The pion test beam data referred to, was restricted momentum below 3 GeV/c, a range useful for this type of inquiry, however not useful for calibrations over the whole momentum range studied in this work. As a consequence the efficiency of this cut is not known in the full region of $0 < p_T < 25$ GeV/c

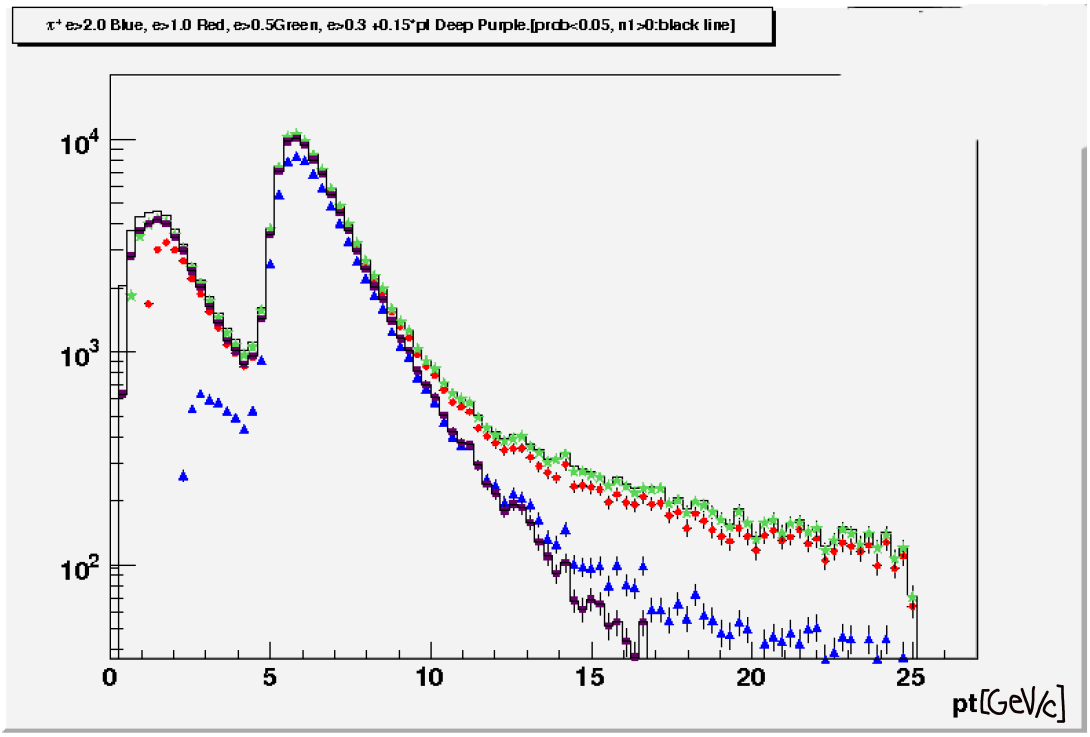

Figure 6.9: π^+ candidates with different minimum energy deposition requirements. Green, red and blue curves are minimum constant energy requirements $e >$2.0 GeV, 1.0 GeV and 0.05 GeV respectively. A large portion of the background can be suppressed while maintaining a clean signal by requiring that the minimum energy deposition of the particle is greater than $0.3GeV + 0.15 * p_T$ (purple curve). The p_T region of interest is $5 < p_T < 10$ GeV/c.

Ratio of Energy and Momentum

A e/p cut is applied to the data used for spin asymmetries. The calorimeter's interaction length is only one unit which immediately implies that while an electron may deposit all of its energy a hadron will only deposit a small fraction of their energy: 1/**e**[12] or $\sim 40\%$ of their energy. Particles with an energy to momentum ratio exceeding 90% were cut out of the sample. Figures 6.10 and 6.11 show typical distributions of e/p while Figure 6.12

[12] **e** being the constant 2.7182, not energy

shows the energy vs. momentum distributions and the effects of the EMCal cuts in different histogram colors. The distributions of *e/p* show three areas of interest:

- Gaussian type peak around one indicating the presence of primary electrons(Figure 6.10).
- A secondary peak around the expected hadronic energy deposition of 0.4 (Figure 6.11).
- A high deposition at low ratios indicating the presence of minimum ionizing particles which include both electrons and hadrons.

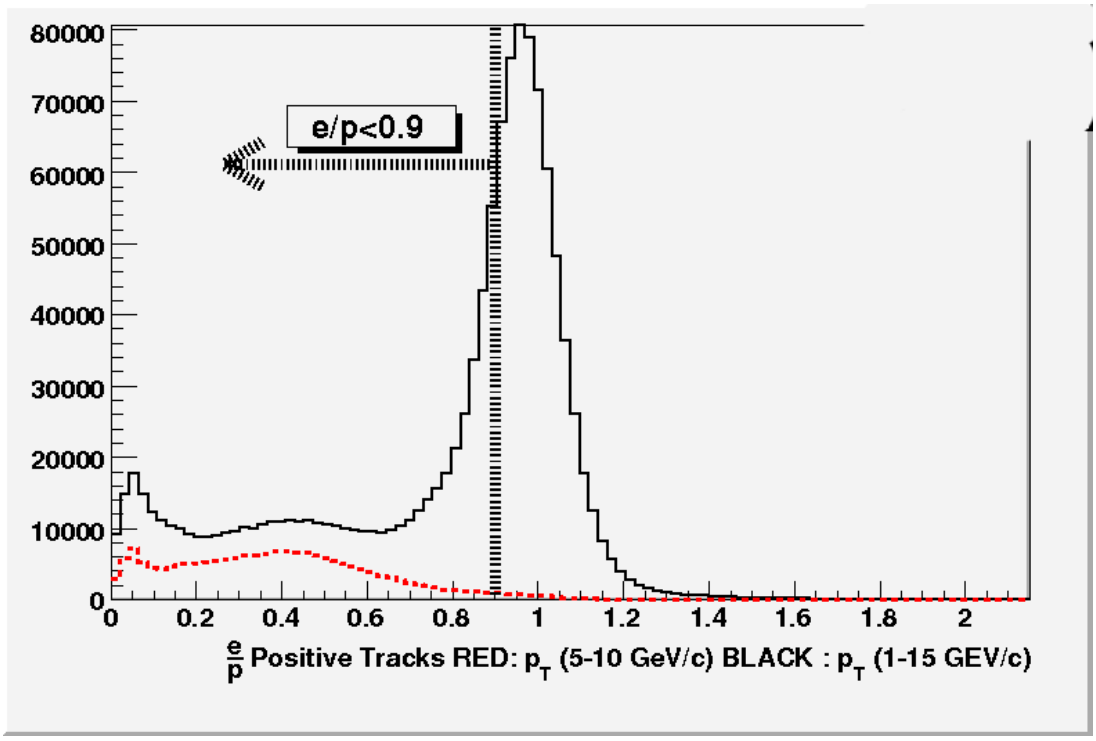

Figure 6.10: Ratio of energy and momentum of particles within a of 5 GeV/$c < p_T <$10 GeV/c (red curve) and 1 GeV/$c < p_T <$15 GeV/c (black curve). There are three distinct $\frac{e}{p}$ regions:the low ratio region is removed by the p_T dependent cut as Figure 6.11 shows, while the ratio close to unity can be reduced by a RICH $n1 > 0$ and $p_T >$5 cut. Only the region that satisfies a ratio of e/p< 0.9 is kept, further minimizing the contribution from primary electrons. See Figure 6.12 for an additional study on the removal of electrons by these cuts.

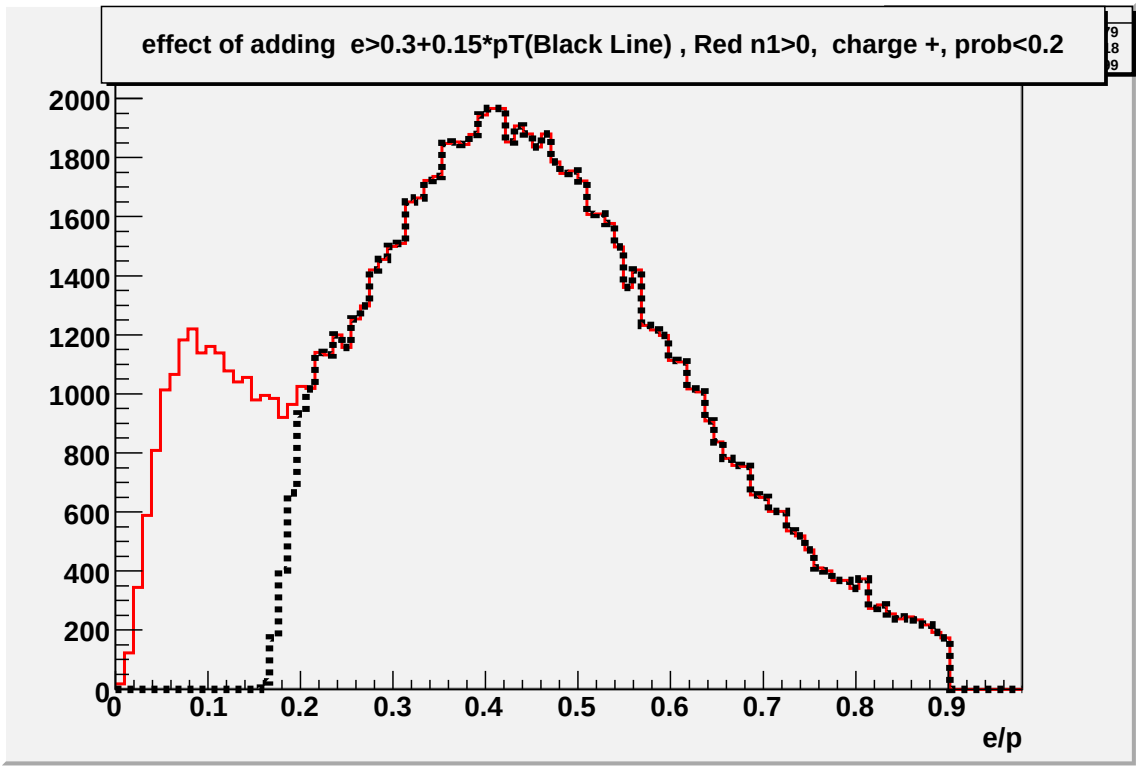

Figure 6.11: Energy/momentum distribution. Most of the energy depositions occur around 0.4 which coincides with the expected energy hadron deposition fraction given that the EMCal only has one interaction length. At very low e/p values electrons can be removed from the spectra using a p_T dependent energy cut. The low e/p spectra represents particles with momenta much larger than its energy. This region of the distribution is an indication of minimum ionizing particles and is removed from the sample.

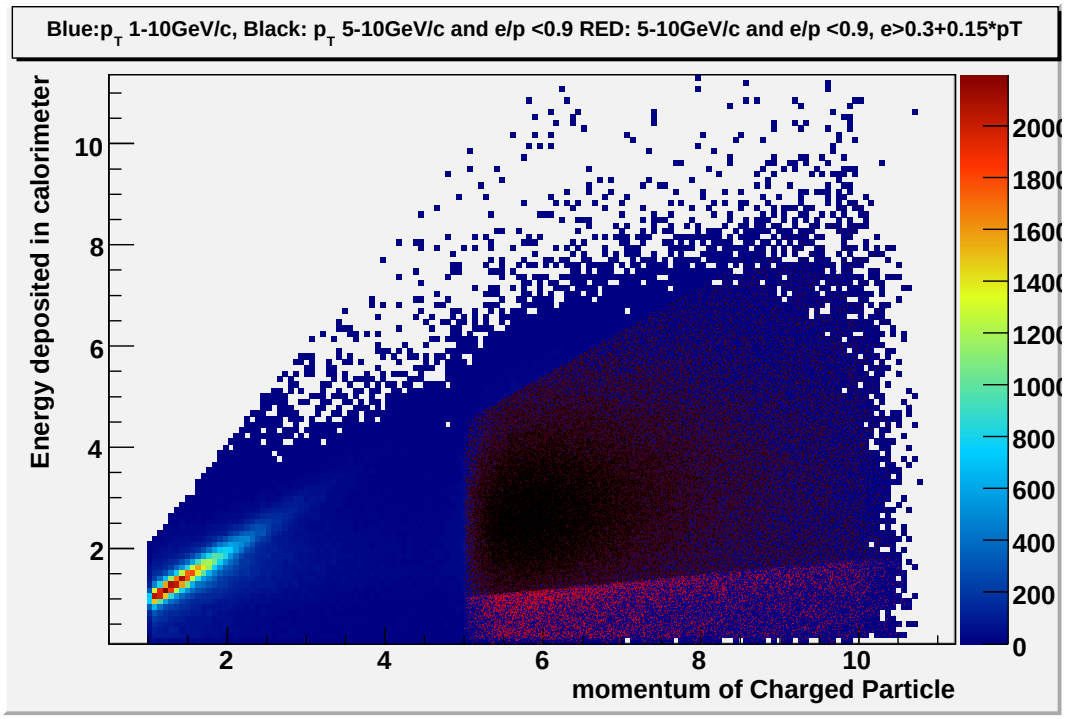

Figure 6.12: Energy vs momentum distribution showing in blue the total number of candidates within a $1 < p_T < 11$ GeV/c. Red shows the acceptance of 5-10 GeV/c pions with a $e/p < 0.9$ requirement and lastly in black is the added p_T dependent energy cut (Section 6.5.2).

6.6 Matching and Background Estimate of Asymmetries

For the data recorded in 2005 the background was estimated with an extrapolation of a power law to the low p_T charged particle yield. The argument for this method was based on the natural expectation that for hard scattered produced particles the spectrum is expected to follow a power law distribution. The signal region of p_T above 5 GeV/c in the data sample as well as the background region (below 5 GeV/c) was well described by this method. The fits to the signal and background can be seen in panels of Figure 6.13. A power-law fit was also applied to the region below the signal. This method overestimated the background as can be seen by the fact that the signal and background curves would cross at very high p_T. The fractional background contributions using this fitting method was found to be less than 5% (Table 6.5). The remainder of this section discusses the technique used in purifying the charged tracks. Briefly all EMC and PC3 matching (Section 5.4) distributions in dϕ and dz were studied by p_T bin. The matching distributions of the ERT sample were found to have minor deviations from expected values. After corrections were applied to the data sample a loose matching cut of $< 3\sigma$ was required for all tracks to eliminate contamination. The remaining sample was then meticulously studied to estimate the background correction which will be discussed on the following sections. Table 6.5 summarizes the background estimates using the power-law method. Further figures along with their fits may be found in the Appendix E.

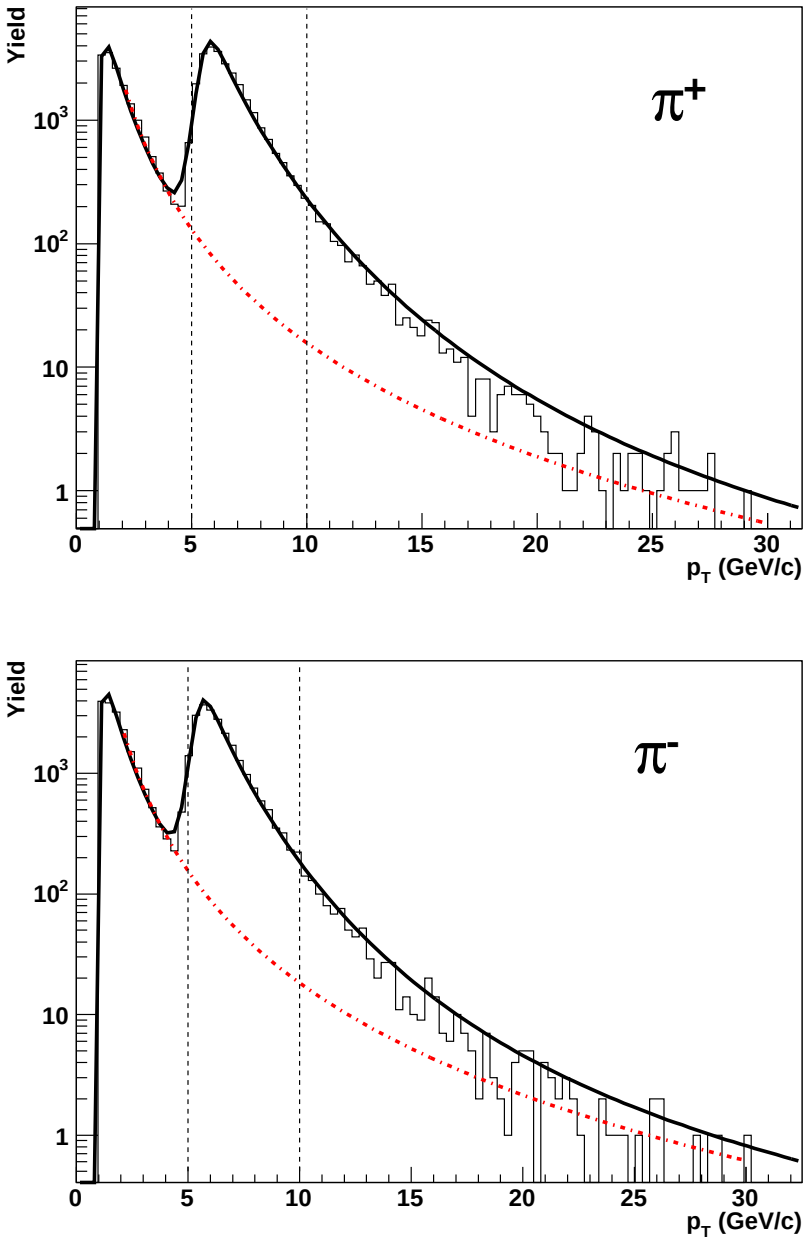

Figure 6.13: Background estimate of the 2005 data sample using a power law fit extrapolation. Top are π^+ and bottom π^-. The black curve is the signal region while the red curve is the background estimate. The dashed vertical lines are the p_T region of interest.

6.6.1 Close σ Matching Cut Study

A strict cut in the σ (Section 5.4) window on the matching distributions was performed to estimate the remaining background on the outer tracking areas of the detector's $d\phi$ distributions. The study showed that most of the distributions were Gaussians and centered around zero with very minimal tracks residing outside a 2σ cut[13]. This will be studied further in the next section as it is implicitly combined with a strict RICH cut.

6.7 Conversion electron background estimate

Conversion electrons comprise the main background contribution to the sample for both the cross-section measurements as well as A_{LL}. These background particles can have similar signatures as high p_T $\pi^{\pm}$. The conversion background is composed of electron positron pair tracks generated close to the drift chamber and deflected by the magnetic field. The pair will split in the main bend plane and can potentially be reconstructed as a high momentum track. However, as stated in Section 4.1.6, electron behavior and charged pion behavior can be different as the light cone radius is larger for electrons than pions. Electrons will fire six PMTs in average, while a charged pion's firing will increase approximating the efficiency of electrons with increasing p_T and plateau around five PMTs. In addition the residual/matching distributions (Section 5.4) of e^+e^- and

[13]Which also implies that the background was minimal, as background tends to dominate the tails , broadening the distributions

$\pi^{\pm}$ also differ: charged pion distributions are narrow and centered around zero, while background electron distributions are broader and centered to the right or the left of zero depending on their charge. While the cuts used in this analysis effectively remove a large fraction of the background as can be seen in Figure 6.9, a conversion contribution still remains. To estimate this remaining fraction particles that make all the cuts and remain within a $1 < \sigma < 3$ are studied in combination with different RICH requirements. Figure 6.14 shows these distributions with $n1 > 2$ (black) to $n1 > 4$ (blue) requirements. It is clear that requiring more than four PMTs to be fired in the RICH will remove a large portion of the signal and the conversion electrons will be selected as we can see their distributions not centered around zero but rather to the right or left of zero depending on the charge. This asymmetry which is dependent on charge is a signature of background particles which do not originate from the vertex. The efficiency of the RICH sub-detector for conversion electrons can then be calculated by safely assuming that the matching of track residual between one detector and another (say from $\sigma < 10$ and $\sigma > 4$) will be all conversion background. One can then estimate the efficiency of the $n1$ variable through the relation in Equation 6.7.[14] No charged pion background cuts are used outside of $n1 > 0, 4$ when calculating the efficiency R_e as this will bias the sample towards charged pions and the efficiency of the RICH will not be constant. R_e is an efficiency of the RICH not to be confused with previously defined R which is a ratio

[14]Efficiencies of the RICH were also calculated using simulated data. Refer to Section 4.1.6 for more details.

of relative luminosities.

$$R_e = \frac{\#\text{of particles within}(n_1 > 4)\text{and pc3sdphi}(\sigma > 4, \sigma < 10)}{\#\text{of particles within}(n_1 > 0)\text{and pc3sdphi}(\sigma > 4, \sigma < 10)} \tag{6.7}$$

$$Spectra_{n_1>0} = Signal + Background(\frac{n_1 > 4}{R_e}) \tag{6.8}$$

The remaining background estimation from the cleaned sample can be then estimated by p_T bin by requiring this $n1 > 4$ and excluding tracks that fall within 1 σ of detector matching.

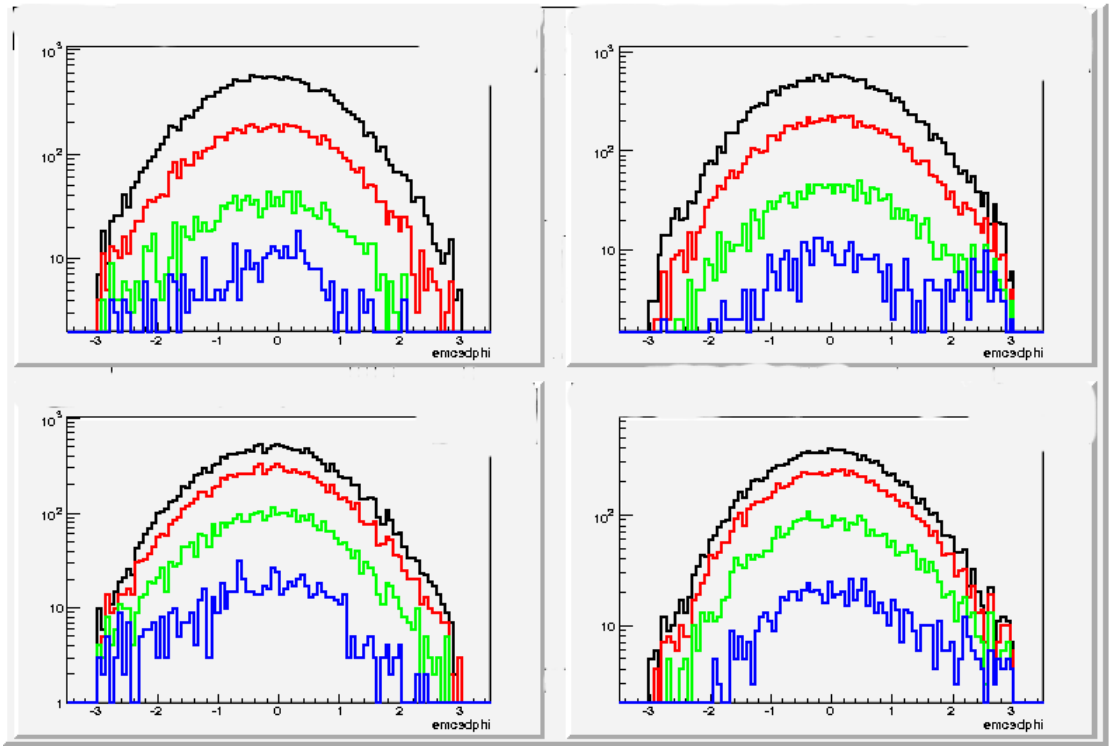

Figure 6.14: Matching distributions for different p_T bins, charges, and RICH requirements. Black, red, green and blue histograms represent n1$>$ 0,n1$>$ 2, n1$>$ 3 n1$>$ 4. The left (right) panels show $\pi^+(\pi^-)$, top (bottom) for 5 GeV/c $< p_T <$6 GeV/c (6 GeV/c $< p_T <$7 GeV/c). The blue curve starts to exhibit the off-centered behaviour expected from background electrons, which is in opposite direction for each charge sign.

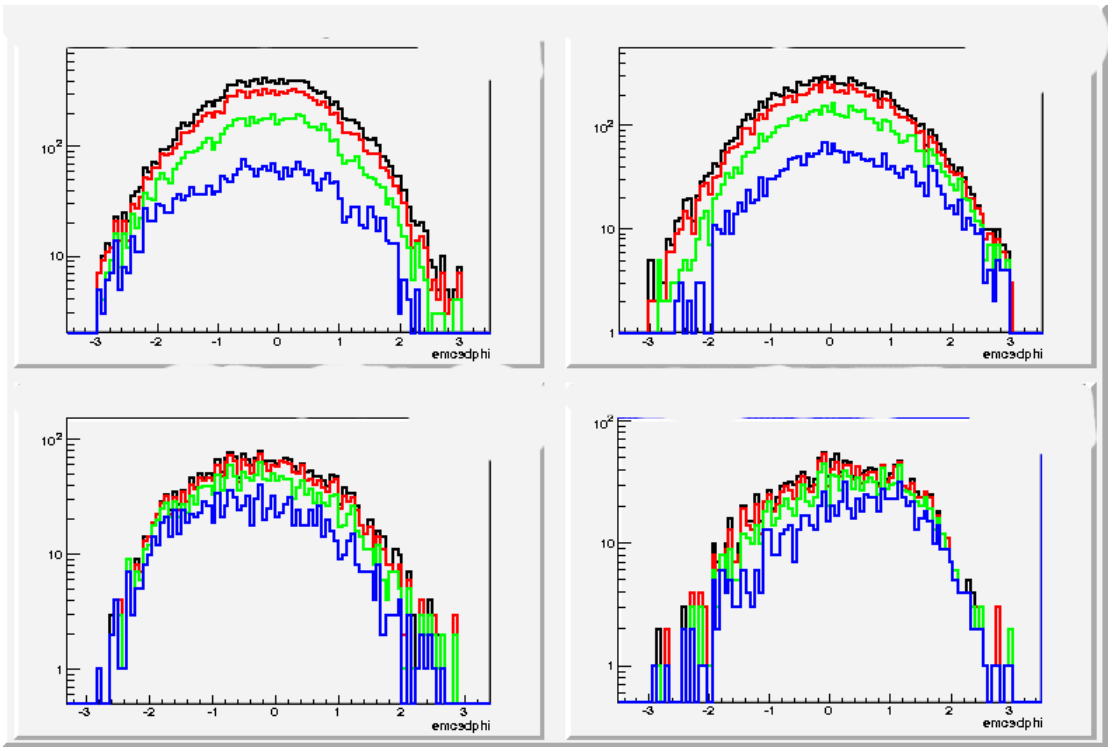

Figure 6.15: Matching distributions for different p_T bins, charges, and RICH requirements. Black, red, green and blue histograms represent n1$>$ 0,n1$>$ 2, n1$>$ 3 n1$>$ 4. The left (right) panels show $\pi^+(\pi^-)$, top (bottom) for 7 GeV/c $< p_T <$ 10 GeV/c (10 GeV/c $< p_T <$ 15 GeV/c). The blue curve starts to exhibit the off-centered behaviour expected from background electrons, which is in opposite direction for each charge sign.

The remaining background contributions can be found on Table 6.4. The last p_T bin of 10 GeV/c $< p_T <$ 15GeV/c in Figure 6.15 indicates that the technique seems to breakdown. One can see even within one σ the spectra appears to be background dominated as the whole distribution seems to be shifted from zero. This could be caused by decay particle contamination which would have to be estimated in this p_T range. A brief discussion of decay background will be made in the next section.

Background in A_{LL} (%). Year 2006				
p_T Bin[GeV/c]	π^+Remaining BK(%)	R_{e^+}	π^-Remaining BK(%)	R_{e^-}
5-6	<1	0.49	<1	0.46
6-7	<1	0.41	<1	0.41
7-10	1.6	0.43	1.8	0.49

Table 6.4: Remaining background in sample from 2006 data and RICH efficiencies "R_e" obtained per p_T. Table values correspond to the 2006 data-set.

Background in A_{LL} (%). Year 2005		
p_T Bin[GeV/c]	% Background π^+	% Background π^-
5-6	3	4
6-7	2	3
7-10	4	5

Table 6.5: Estimated background contributions using 2005 data-set using a power law extrapolation.

6.7.1 Decay Particles

Since in this analysis a RICH hit is required, decay particles are not a significant source of background within the range 5 GeV/c $< p_T <$ 10 GeV/c as they will not typically emit Čerenkov light inside the RICH. This is due to their very low momentum which will typically be below light emitting threshold. However above $p_T \sim$ 11 GeV/c decay background cannot be neglected as their energy will exceed light emitting thresholds. Decay particles are typically low energy particles. Due to particle decay kinematics and multiple scattering interactions they can only be detected in the EMCal if they have a high enough momentum kick from the parent particle. The average p_T of decay and conversion background is about 500 MeV/c and the random association background due

to decays has been estimated in PHENIX to be less than 0.5$\%$. This estimation has been further restricted to non-fired RICH track spectra ($n1 < 0$) in other analyses involving charged hadrons [4]. For the spin asymmetry analysis only one p_T bin above 10 GeV/c was studied. As the previous section demonstrated, this bin is more background dominated than the lower p_T bins. A method similar to the conversion estimate in the previous section was performed. A cut of $n1$ >6 seemed more appropriate in this p_T range as it can be seen in the spectral shapes (Figure 6.14, 6.15 and 6.16). The fractional efficiency of the RICH using the same technique as before was found to be quite low: 0.16. The number of particles scaled by this efficiency found within the three σ and subject to $n1$ >6 requirement was high (over 50$\%$). As a consequence of the uncertainty of the heavily contaminated 10-15 p_T region, the asymmetry obtained was not considered as a physics *spin* measurement and thus was not included in the results for A_{LL}. A visual inspection of bottom of Figure 6.16 shows the p_T bin determined to be too contaminated to consider for a charged pion asymmetry using the 2006 and also for 2005 data-set.

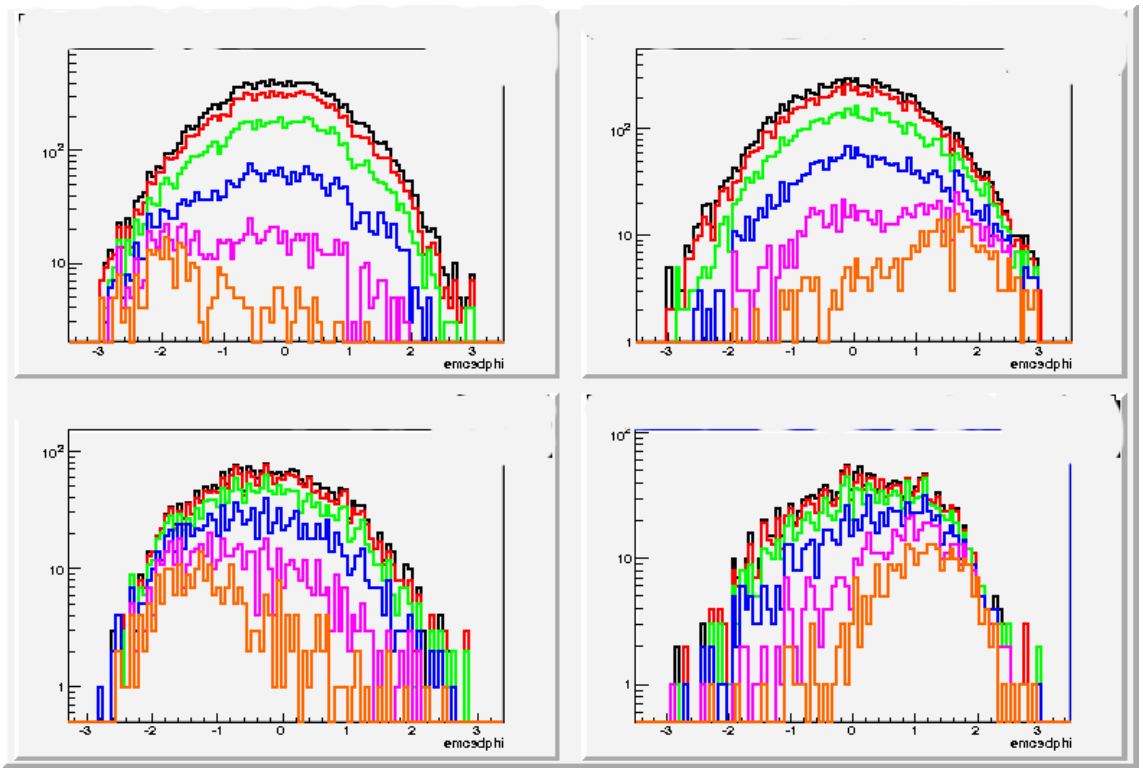

Figure 6.16: Matching distributions for different p_T bins, charges, and RICH requirements. Red, green, blue, pink and orange histograms represent $n1$ >2, $n1$ >3, $n1$ >4, $n1$ >5. The left (right) panels show $\pi^-(\pi^+)$, top (bottom) for 7 GeV/c < p_T <10 GeV/c (10 GeV/c < p_T <15 GeV/c) The curve to the orange curve start to exhibit the off-centered behaviour expected from background electrons, which is in opposite direction for each charge sign.

6.7.2 Primary Particles -$\mu^{\pm}$, e$^{\pm}$

Typical e/π and μ/π ratios from primary electrons and muons are less than 10^{-3} [16]. Particles that produce light in the RICH are listed in Table 6.6. Note that within the p_T range of 5 GeV/c-10 GeV/c only $\pi^{\pm}$ will primarily produce Čerenkov light as primary particle background originating from primary electrons or muons is considered negligible. An illustration of the typical energies of accepted particles can be found in Figure 6.11.

RICH Light Emitting Thresholds	
Particle	Threshold[GeV/c]
e^+, e^-	0.017
μ^+, μ^-	3.5
π^+, π^-	4.7
K^+, K^-	16
p^+, p^-	30

Table 6.6: RICH thresholds.

6.8 Identified Charged Pions for Spin Asymmetries

Table 6.7 lists the charged pion yields by p_T bin after all cuts were implemented. The total number of pions identified in the sample within a range of 5 GeV/c $< p_T <$10 GeV/c was 56,081 π^+ and 47,662 π^-. The total number of BBC counts in the sample was 12 billion. Using a total proton proton inelastic cross-section of 42 mb and a BBC efficiency of 52$\%$ gives an approximate integrated luminosity of 5.8 pb^{-1} (Equation 6.9). Table 6.8 lists the yields found in the 2005 data-set, where the analyzed was estimated to be 2.3 pb^{-1}.

Pion Yields ERT Data 2006		
p_T Bin [GeV/c]	π^+	π^-
5-6	21,469	21,496
6-7	18,887	15,462
7-10	15,725	10,704

Table 6.7: Pion yields after all cuts by charge and p_T bin for the 2006 data-set.

Pion Yields ERT Data 2005		
p_T Bin[GeV/c]	π^+	π^-
5-6	9589	9289
6-7	9108	7563
7-10	7399	5887

Table 6.8: Pion yields after all cuts by charge and p_T bin for the 2005 data-set.

$$\int L, dt = \frac{N_{BBCLL1}}{\sigma_{BBC}\sigma_{\epsilon_{BBC}}} \tag{6.9}$$

6.8.1 Ratio of π^+, π^- in ERT Triggered Data used for Asymmetries

The yields in Tables 6.7 and 6.8 show that the ratio of π^+/π^- changes with p_T. Similar cuts were used in the samples. Both samples show more π^+ detected than π^-. While there is a pQCD expectation for a charge asymmetry that is p_T dependent and more pronounced at high p_T (due to charge conservation in proton proton collisions, more up quarks than down quarks), there appeared to be non-physics charge asymmetry also observed. The possible causes for a non QCD asymmetry can be due to the asymmetry of the detector set-up; the drift chamber is symmetric with respect to $\phi = 90^o/270^o$ and asymmetric with respect to $\phi = 0^o/180^o$, furthermore both arms are shifted up about $\sim 1\%$. Other effects could be due to detector misalignment (either drift chamber or RICH sub-detectors) and charged track efficiency losses caused by dead areas on the drift chamber which may change from to year. While the ratio of π^+ to π^- will be of further discussion, it should not affect the spin asymmetry results as these are defined as a ratio of yields where all efficiencies will cancel out. A further discussion of the ratios for all samples studied can be found in Section 5.11.

6.8.2 Pion Yield Comparison in Years 2005 and 2006

As mentioned previously the efficiency for charged tracks changed between 2005 and 2006 data sample. Another difference between runs was the choice of the trigger (ERT 4x4c Section 4.2.1). In the year 2006, large portions of the PbGl sectors of the EMCal

were masked off causing a reduction of statistics of about 15%. The RICH detector also suffered a mirror mis-alignment in 2005 and the problem was solved by the year 2006. In addition to the trigger and efficiency changes between runs the actual correction for momentum scale was not submitted to the PHENIX database before the 2005 analysis was performed, while for the 2006 data sample all beam shift and momentum scale corrections (Section 5.2.4) were done and made available to the PHENIX collaboration before the asymmetries and yields were calculated by the author of this work. In summary, Figure 6.17 shows the ratio of yields found between the data samples in 2005 and 2006.

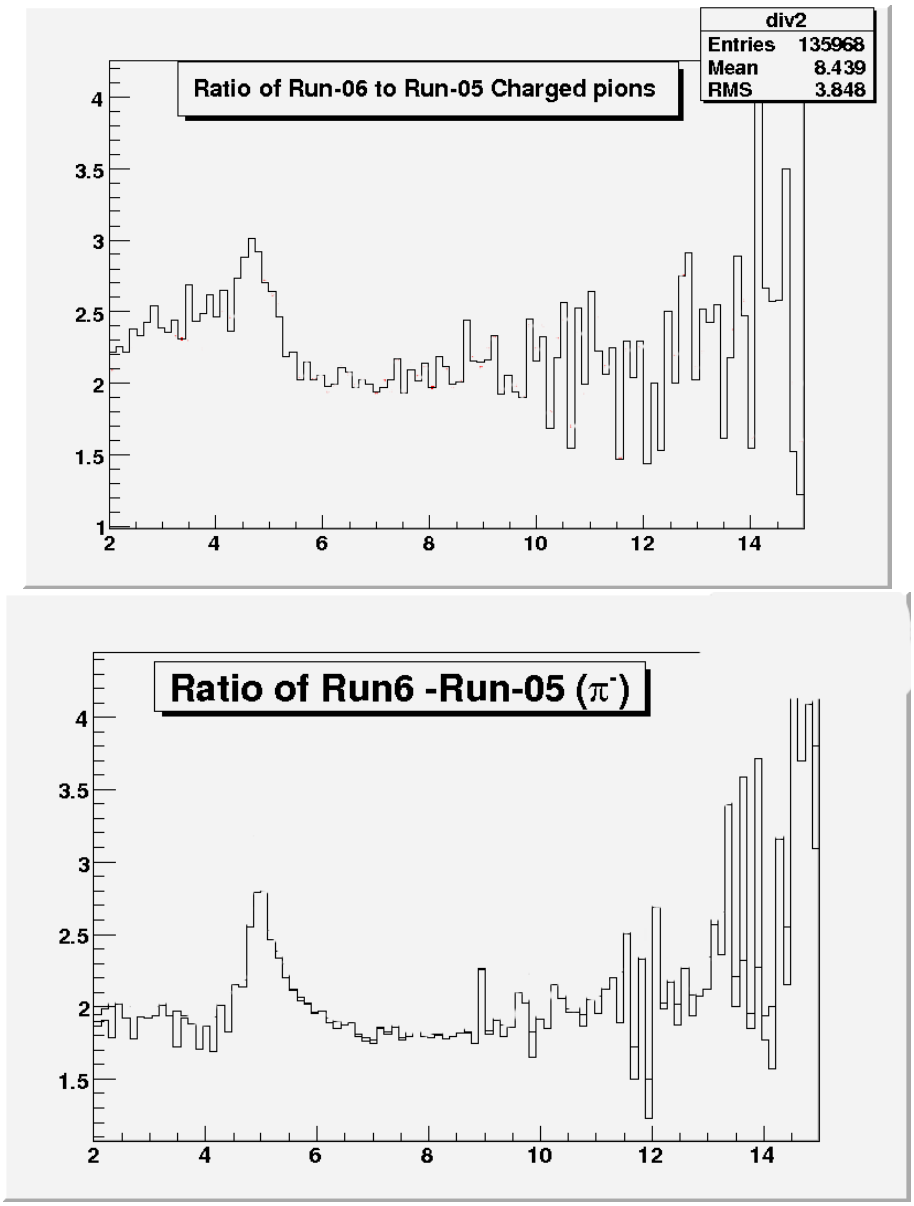

Figure 6.17: Ratio of identified $\frac{\pi^+_{2006}}{\pi^+_{2005}}$ and $\frac{\pi^+_{2006}}{\pi^-_{2005}}$ of 2005 versus 2006 data-set. *x* axis is p_T in units of GeV/c. Some pion identifying cuts were varied to test the sensitivity of the ratio shown, i.e. matching, p_T dependent and probability cuts. The large peak at the RICH threshold (4.7 GeV/c) indicates an efficiency change between data-sets associated with the RICH sub-detector. Top panel are π^+ while bottom panel are π^-.

6.9 Double and Single Spin Asymmetries: $A_{LL}^{\pi^{+/-}}$ and $A_{L}^{\pi^{+/-}}$

The double spin asymmetries were calculated using the fill by fill[15] (χ^2) method and summed method. All particles that survived the cuts discussed above and were within 5 GeV/c $< p_T <$ 10 GeV/c were considered for an asymmetry calculation. Refer to Section 6.1 for the definitions used for A_{LL}, A_L, ΔA_{LL} and ΔA_L.

6.9.1 Asymmetries with the Fill by Fill-χ^2 Method

The lower limit on transverse momentum (5 GeV/c) was applied by taking in consideration the RICH pion threshold (4.7 GeV/c) and resultant turn on curve. The upper limit was applied due to statistical limitations. An attempt was made to gain an additional higher p_T bin by using the summed method, however this did not prove practical due to limitations of the background estimate at this p_T bin as discussed in Section 6.7. The A_{LL} and ΔA_{LL} for each respecting bin were plotted by fill (Figure H.1) and fit with a constant function. The values obtained were then used as the final double asymmetry result shown in Figure H.2 and summarized in Table 6.9.

[15] As a reminder, a fill is defined as the time period encompassing one complete machine cycle. This includes the injection, acceleration, and storage of colliding beams.

A_{LL} by average p_T value using χ^2					
	π^-			π^+	
p_T[GeV/c]	A_{LL}	ΔA_{LL}	p_T	A_{LL}	ΔA_{LL}
5.6	-0.005	0.022	5.7	0.020	0.021
6.7	0.011	0.026	6.5	0.027	0.023
8.2	-0.042	0.030	8.2	0.032	0.025

Table 6.9: A_{LL} by average p_T value using χ^2. Table values correspond to the 2006 data-set.

6.9.2 Summed Method Asymmetries

Summed asymmetries were calculated using a bunch-subtraction method, where bunches[16] with relatively different luminosities in each proton helicity configuration are removed until the tolerance in *R* (See equation 6.2) value is within acceptable limits. As a reminder R is the ratio of the relative luminosity in each beam in different polarization configurations ($R = L_{++}/L_{+-}$) not to be confused with the RICH efficiency R_e. In this study the tolerance on *R* was set to 0.01. The *R* distributions graphs in even, odd and combined crossings can be seen in Figure 6.18. The asymmetries and their uncertainties using this method appear consistent with the χ^2 method. In addition an asymmetry at p_T of 11.5 GeV/c was obtained, albeit with low statistics and higher background contamination. All the asymmetries and their statistical uncertainties are summarized in Table 6.9 and Table 6.10.

[16]Rather than continuous beams, protons at RHIC travel bunched together in 120 bunches, so that interactions between the two beams will take place at discrete intervals at 106 nanoseconds (ns) apart.

A_{LL} by average p_T value using summed method.					
	π^-			π^+	
p_T[GeV/c]	A_{LL}	ΔA_{LL}	p_T[GeV/c]	A_{LL}	ΔA_{LL}
5.6	-0.012	0.021	5.7	0.012	0.021
6.7	0.008	0.026	6.5	0.023	0.023
8.2	-0.049	0.030	8.2	0.015	0.025
11.5	-0.0002	0.076	11.5	0.010	0.061

Table 6.10: A_{LL} by average p_T value using the summed method. Table values correspond to the 2006 data-set

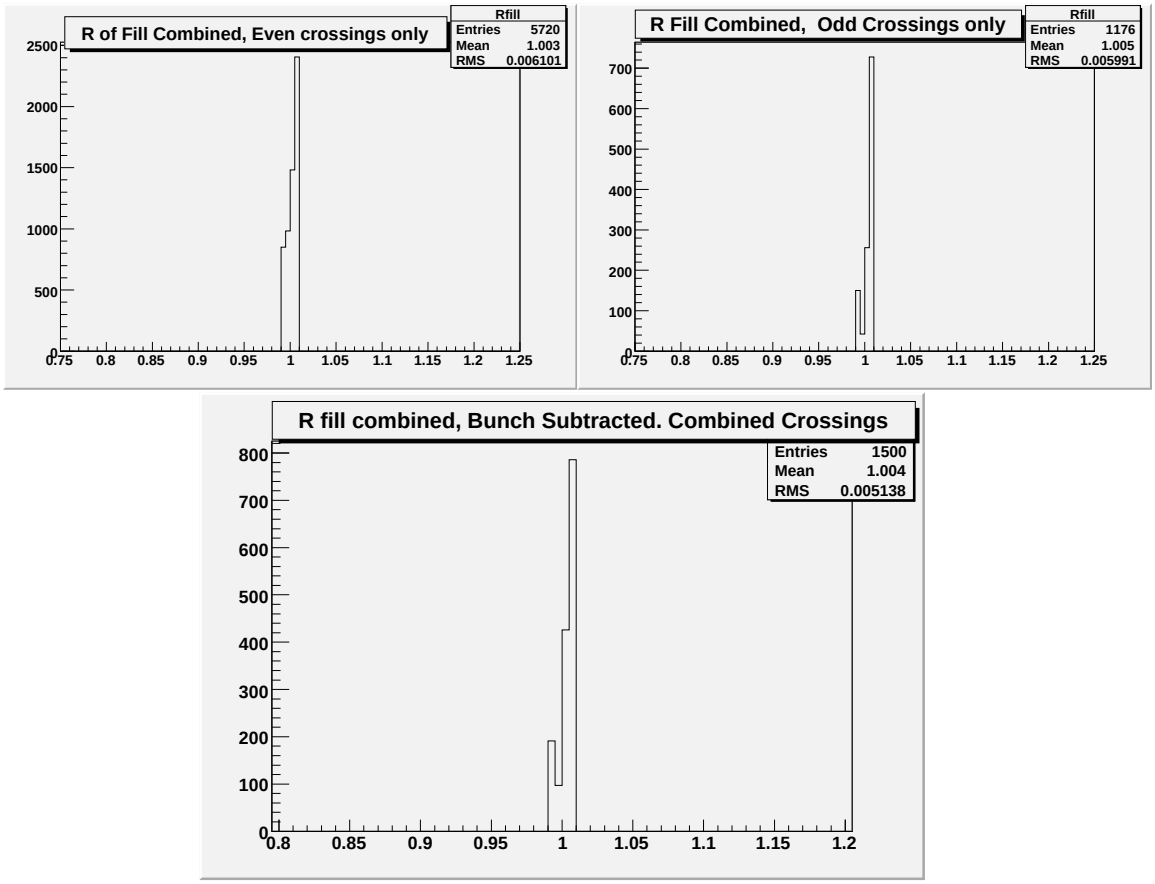

Figure 6.18: Distribution of *R* after a cut in ΔR in even, odd and combined bunch crossings after removing bunches that are outside tolerance values. R is the ratio of relative luminosities in different beam polarization configurations. The top panel shows the *R* distributions for even (top) and odd (bottom) bunch crossings, while the bottom figure combines bunches. 2006 data-set.

6.9.3 Even and Odd Bunch Separated Spin Asymmetries

The ERT trigger circuit (Section 4.2.1) consists of two separate circuits that alternates between even and odd crossings. The triggering at PHENIX (ERT) take about 140 ns to reset which is longer than the typical 106 ns between RHIC bunches. In order for the PHENIX trigger to be compatible with the RHIC bunch mode (120 bunches), the trigger was re-designed as two alternating sets of circuits which were different for odd and even crossings. For asymmetry measurements such as A_{LL} one assumes that efficiency issues are helicity and crossing independent. However a verification was made that the different thresholds did not significantly affect the asymmetry values. Asymmetries were analyzed by even and odd crossings and also by the proton beam in each collider ring -beam blue beam and yellow beam- separately for both methods used. Figure 6.19 and Figure 6.20 show the results of these studies. Measurements were also performed for both summed (Section 6.10) and χ^2 (Section 6.9.1) methods, the fill by fill asymmetries can be found on Figure I.0.14 for odd crossings and H.4 for even crossings. Single longitudinal asymmetries (A_L) of charged separated pions were also measured. Studies of even, odd and beam separated (blue, yellow) single asymmetries can be found in Figures H.5 and H.6. The measured A_L are consistent with zero indicating as expected that the process may not be parity violating. Measurements of A_L were also consistent for both years of data analyzed. Summaries of these studies can be found in Table 6.11 and Table 6.12. Additional studies can be found in the Appendix I.

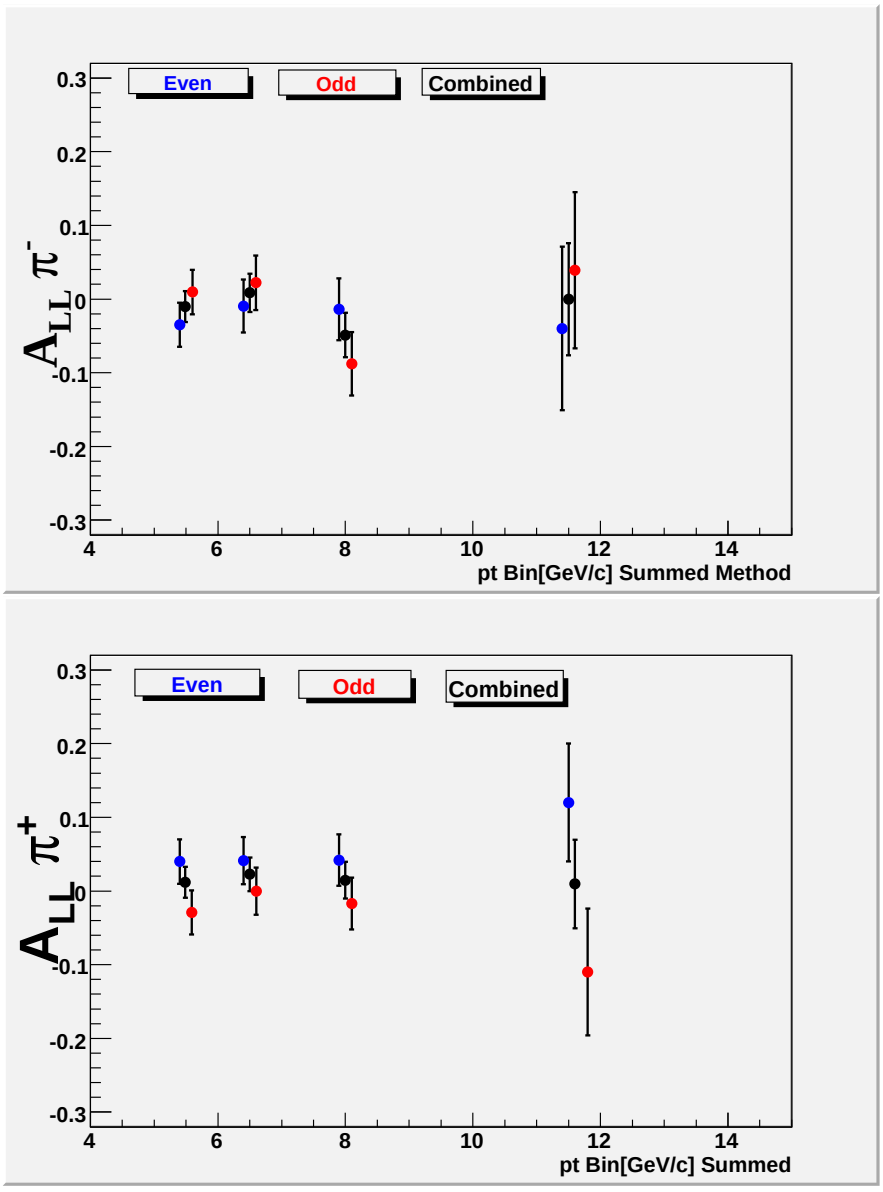

Figure 6.19: Asymmetries using the summed fill method, separated into odd and even crossings. The last momentum bin around 11.5 GeV/c will be discarded due to high background contamination. 2006 data-set.

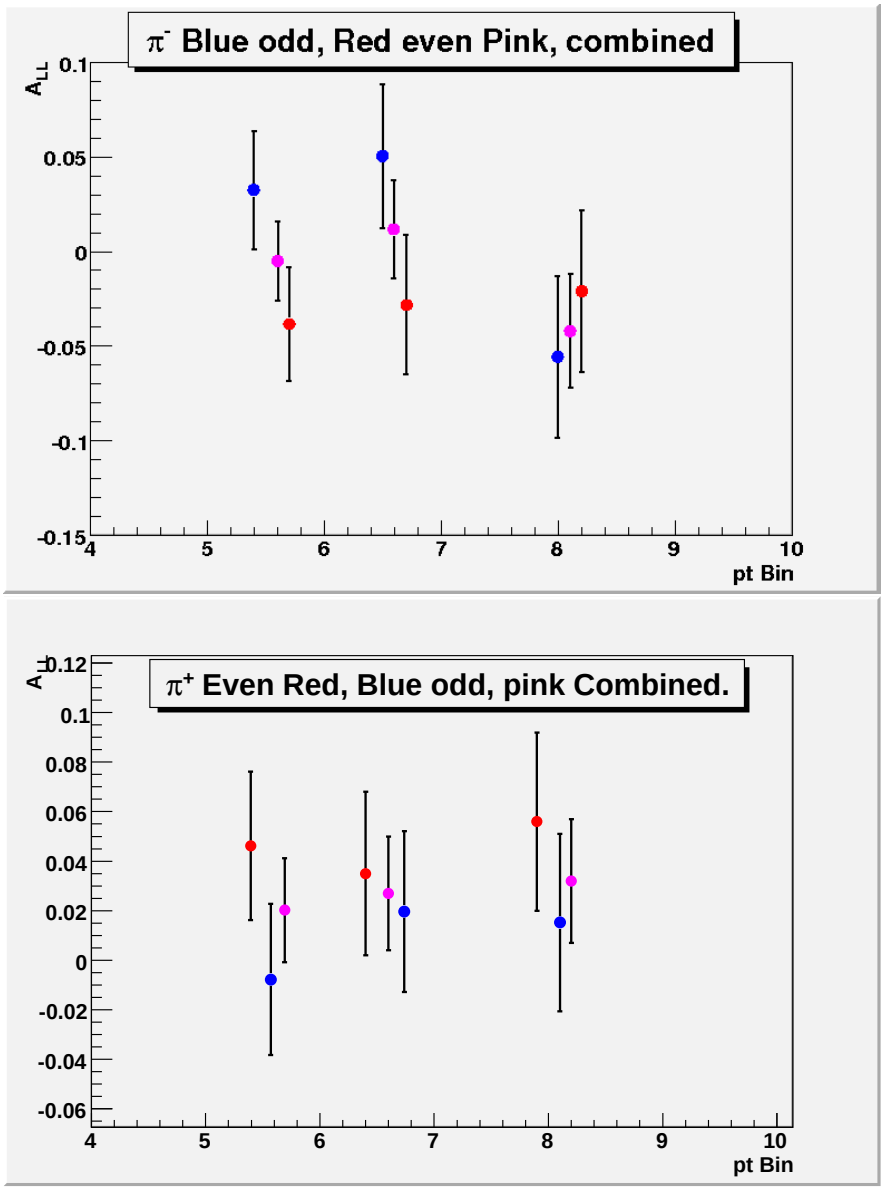

Figure 6.20: Asymmetries using χ^2 method separated into odd and even crossings. 2006 data-set.

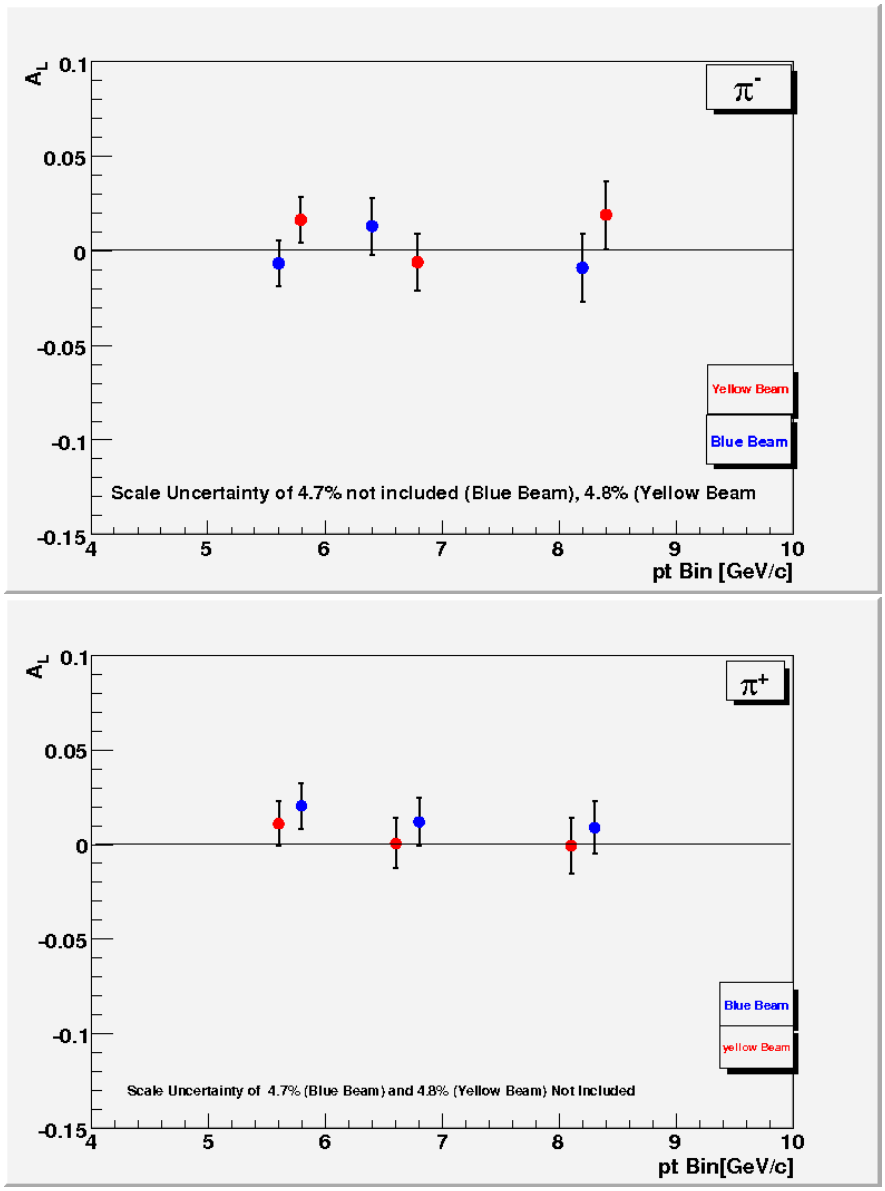

Figure 6.21: Single longitudinal asymmetries (A_L) of π^- and π^+. 2006 data-set.

A_L Yellow Beam. χ^2 method.					
	π^-			π^+	
p_T[GeV/c]	A_L	ΔA_L	p_T[GeV/c]	A_L	ΔA_L
5.6	0.015	0.0124	5.7	0.0112	0.0124
6.7	-0.006	0.0150	6.5	0.0006	0.0133
8.2	0.018	0.0175	8.2	-0.0007	0.0150

Table 6.11: A_L Yellow beam by average p_T value using χ^2 method. Table values correspond to the 2006 data-set.

A_L Blue Beam. χ^2 method.					
	π^-			π^+	
p_T[GeV/c]	A_L	ΔA_L	p_T[GeV/c]	A_L	ΔA_L
5.6	-0.0067	0.0124	5.7	0.0208	0.0120
6.7	0.013	0.0150	6.5	0.0115	0.0130
8.2	-0.009	0.0170	8.2	0.009	0.0150

Table 6.12: A_L blue beam by average p_T value using χ^2 method. Table values correspond to the 2006 data-set.

6.9.4 Summary of Measuring Methods used for Asymmetries

Both methods used for the calculations of the asymmetries were fully consistent with each other as it can be observed in Figure 6.22 for A_{LL}. The measurements of A_L was an important systematic check which showed that there were no false asymmetries. Figure 6.21 shows the results for A_L which are consistent with zero as expected. The asymmetries measured by beam also showed that there were no strong effects on the measurements caused by the different ERT circuits in each beam as it can be inspected in Figure 6.19 and Figure 6.20. These results are summarized in Table 6.11 and Table 6.12.

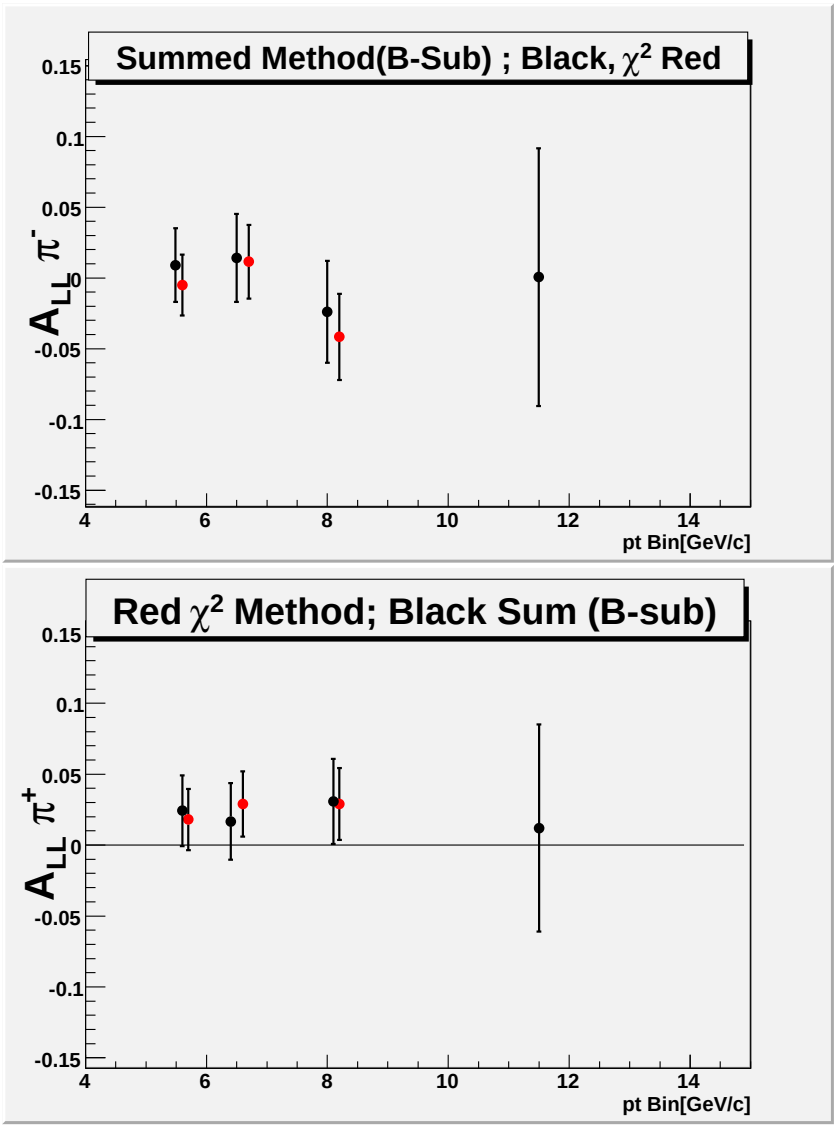

Figure 6.22: Comparison of asymmetries (A_{LL}) using the filled summed bunch subtraction method as described in 6.10, and the χ^2 method. Black circles represent the summed method while red circles the χ^2 method. The error bars are the statistical precision (ΔA_{LL}) in the measurement. Figures correspond to the 2006 data-set.

6.10 Bunch Shuffling as a Systematic Uncertainty Check of A_{LL}

Two final studies are discussed as part of the asymmetry measurements: bunch shuffling which is discussed here and background asymmetries will be saved for the next section. Bunch shuffling is performed as a technique to ensure that any systematic uncertainty from bunch to bunch or fill to fill correlations are less than the current statistical uncertainty. Since the analysis performed for the asymmetry measurements is based on one sample alone it becomes difficult to check for possible fluctuations or systematic correlations that may arise between the fills. The technique used circumvents this issue by randomly assigning the helicity of the bunches in the sample. The asymmetries are then calculated per fill and their χ^2 distributions (Figure 6.23) are inspected and fitted to its probability density, which is expected to have a mean of zero and a variance of one, provided the uncertainty is well approximated by the Poisson (Equation 6.10) uncertainty approximation. The systematic uncertainty in A_{LL} that is estimated from the bunch shuffling technique is less than 10^{-3}. The relevant χ^2 values from the bunch shuffling are summarized in Table 6.13. Figure 6.23 and Table 6.13 show that the distribution is within reasonable expectations (Formula 6.10) indicating that large systematic uncertainties are not present in the measurements. More studies can be found in the appendix.

p_T [GeV/c]	π^-, χ^2	ndf	p_T[GeV/c]	π^+, χ^2	ndf
5.6	89	56	5.7	67	65
6.7	78	55	6.5	56	67
8.2	89	57	8.2	89	65

Table 6.13: χ^2 values by p_T bin of the shuffled asymmetries. 2006 data-set.

$$f(x;k) = \frac{1}{2^{\frac{k}{2}}\Gamma(\frac{k}{2})} x^{\frac{k}{2}-1} \exp(\frac{-x}{2}) \tag{6.10}$$

Bunch shuffling allows the creation of multiple samples needed to differentiate indications of systematic uncertainties from normal fluctuations in χ^2. For this analysis 5000 shuffles were performed and fitted. All p_T bins seem in agreement within the expected fit. The complete set of figures showing all the p_T bins of interest can be found in Appendix I. The polarization pattern for bunches in RHIC can be controlled. There are four possible combinations (++,+,+ and) available for collisions at the PHENIX detector.

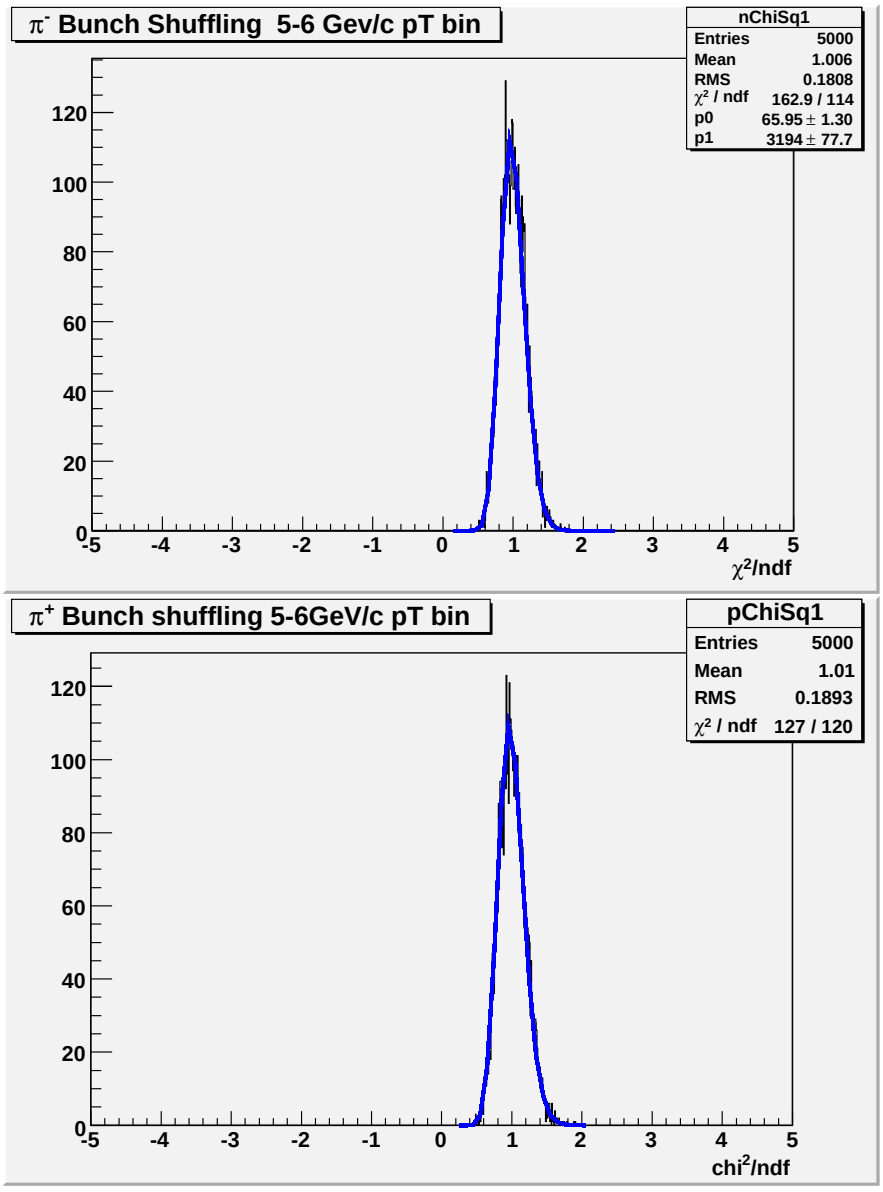

Figure 6.23: Distributions of χ^2 distributions of measured A_{LL} of randomly assigned bunch helicities and shuffled 5000 times across bunches. Top panel corresponds to π^-, while bottom panel corresponds to π^+ within $5<p_T<6$ GeV/c. 2006 data-set.

6.10.1 Background Asymmetries

Since the background in this analysis is small, it is virtually impossible to estimate a background A_{LL} according to the given statistics. However, one can use different techniques in order to estimate this quantity. When the background is from conversion electrons, the characteristic signatures of this background is well understood. One can select a "clean" conversion sample by applying inverted hard cuts upon the ones of this analysis. Example of inverted cuts are: selection of tracks having an accurate electromagnetic shower shape and studying the tracks on the outer σ window of the matching distributions and at the outer part of the $|zed|$ distribution. One can thus get an idea on how big (or small) an asymmetry can be expected from the background and therefore decide upon the importance of the percentage of contamination found within the charged pion spectra. The selected background sample is shown in Figure 6.24 where e/p (energy and momentum) is histogrammed.

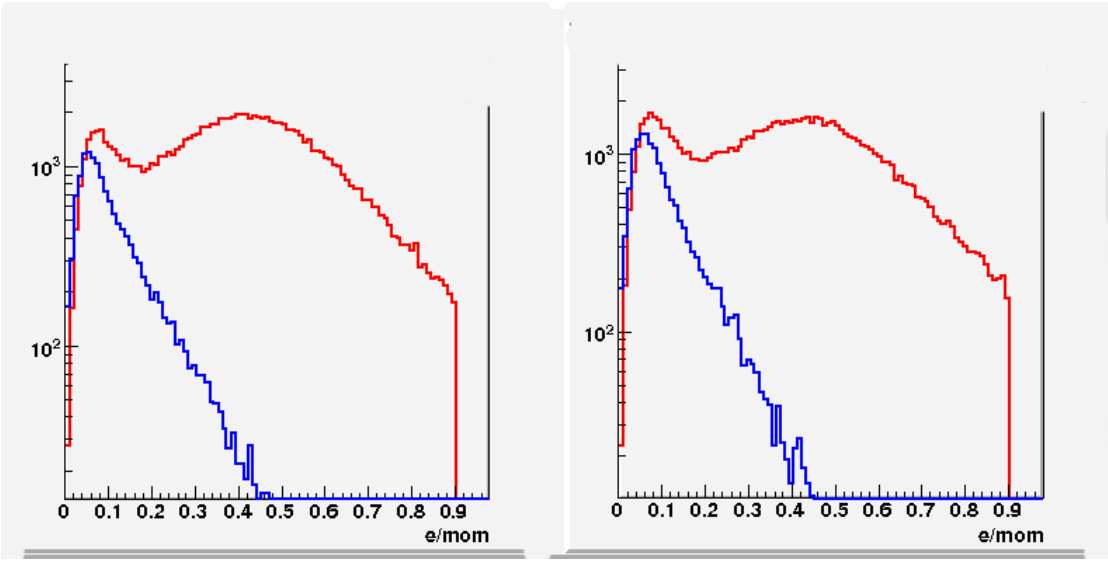

Figure 6.24: e/p distribution of selected conversion electrons, red curve is the typical charged pion distribution while the blue plot is the conversion electron (with some decays) spectra.

The resultant asymmetries are shown in Table 6.14. In the latter table it is shown that asymmetries from conversion background are not significant given the percentage background in each charged pion p_T bin. Cuts used to select conversion tracks were:

- $n0 > 4$ (see Section 6.14).
- $|zed|$ >40 (Section 5.4).
- $prob$ >0.20 (Section 6.5.2).

The method used to calculate these asymmetries was the summed method as the χ^2 required high statistics which are not available in the sample.

In addition, the e/p plot in Figure 6.24 shows that the spectra from tracks along these requirements peak at low energy and not in the mid 0.4 region (40$\%$ energy deposition) as in the charged pion case. One can thus assert with confidence that the asymmetries calculated include a high contamination sample of conversions electrons with mis-reconstructed momentum.

p_T[GeV/c]	e^- A_{LL}	δA_{LL}	p_T[GeV/c]	e^+, A_{LL}	δA_{LL}
5.5	0.008	0.086	5.4	-0.078	0.080
6.5	-0.087	0.092	6.5	0.027	0.089
8.4	-0.007	0.057	8.4	-0.032	0.057
12.3	0.035	0.050	12.4	-0.028	0.053

Table 6.14: Conversion Electron Asymmetries versus p_T bin. 2006 data-set.

6.11 Comparisons

The results obtained with the 2006 data-set are compared to GRSV[22] parametrisations. 2006 π^- and π^+ GRSV curve comparisons are updated as they are calculated using DSS[10] fragmentation functions which use the most up to date e^+e^- and RHIC data and thus contain the best information on fragmentation functions currently available. DSS unlike the previously used KKP[27] fragmentation functions which were compared with the 2005 measurements in this work also distinguish between π^+/π^-. Figure 6.25 shows the comparison between data-sets. Figure 6.26 shows the 2006 results plotted against several GSRV scenarios for ΔG. Figure 6.27 shows the 2006 results plotted against the latest parametrisations using the DSSV model which are newer than the previously GSRV models. GRSV is still a useful model to compare as it contains several scenarios of ΔG. DSSV only contains one scenario fitted from previously released data at RHIC [11].

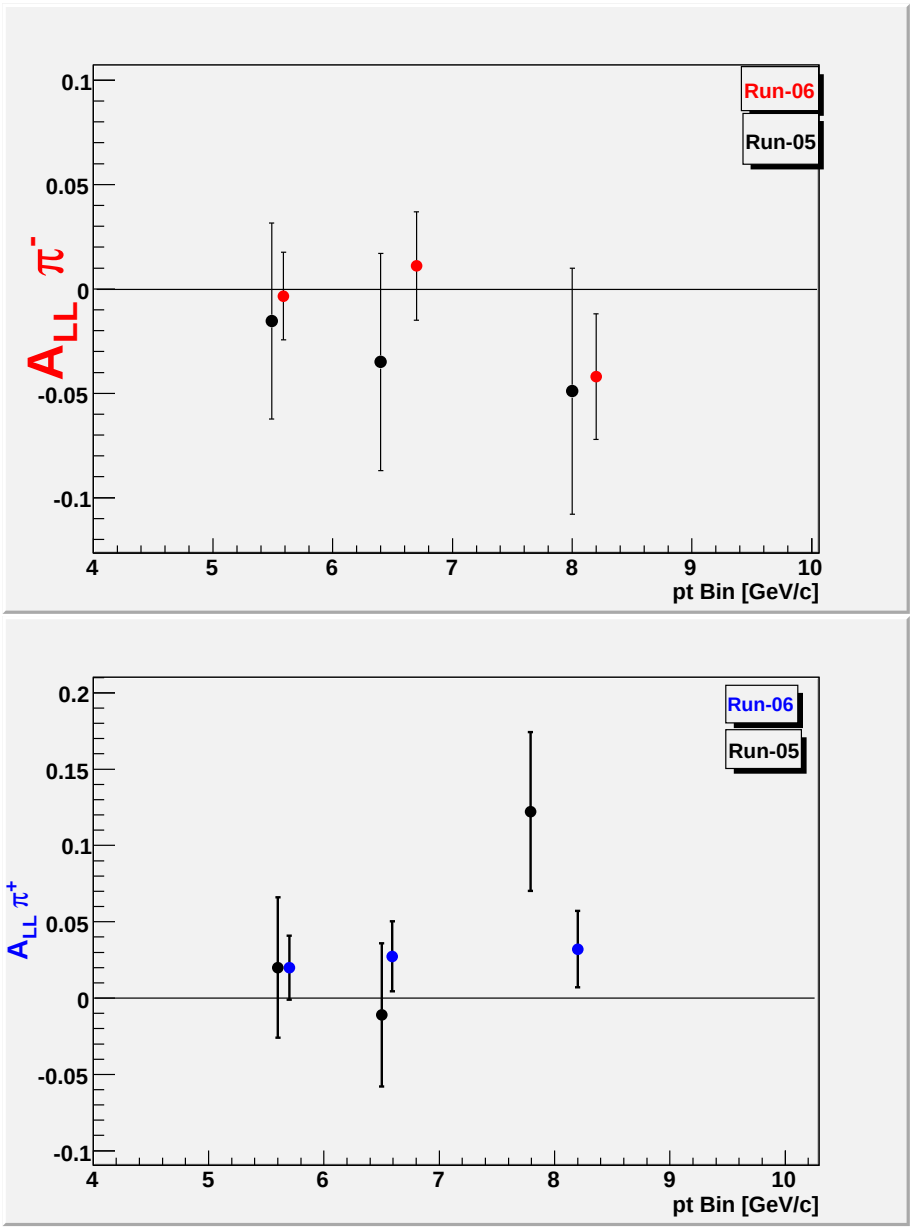

Figure 6.25: Comparison to the measured $\pi^{\pm}$ A_{LL} between the two years analyzed. 2005 data-set is depicted in black while the 2006 set is depicted in red and blue. The top panel are π^- asymmetries while the bottom panel are for π^+.

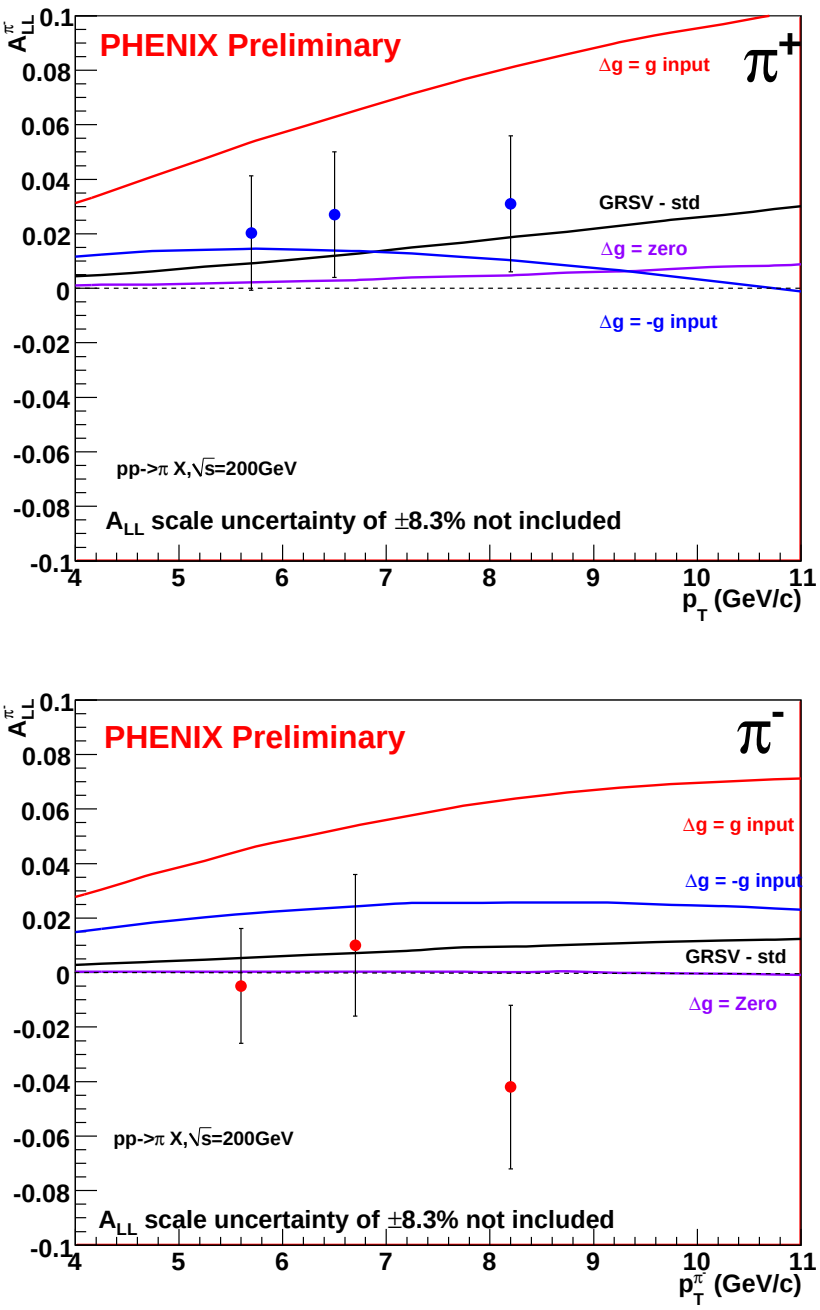

Figure 6.26: Measured A_{LL} compared to GRSV parametrisation for π^- (top panel) and π^- (bottom panel). The different curves depict estimates of gluon polarization scenarios. ΔG maximum and bounded by the unpolarized value of G obtained in DIS is the red curve, blue corresponds to a negative ΔG contribution. The purple line has zero contribution whilst the black illustrates the standard contribution, which corresponds to a contribution of 0.24 (24%) to the proton. Data corresponds to the full 2006 data-set. .

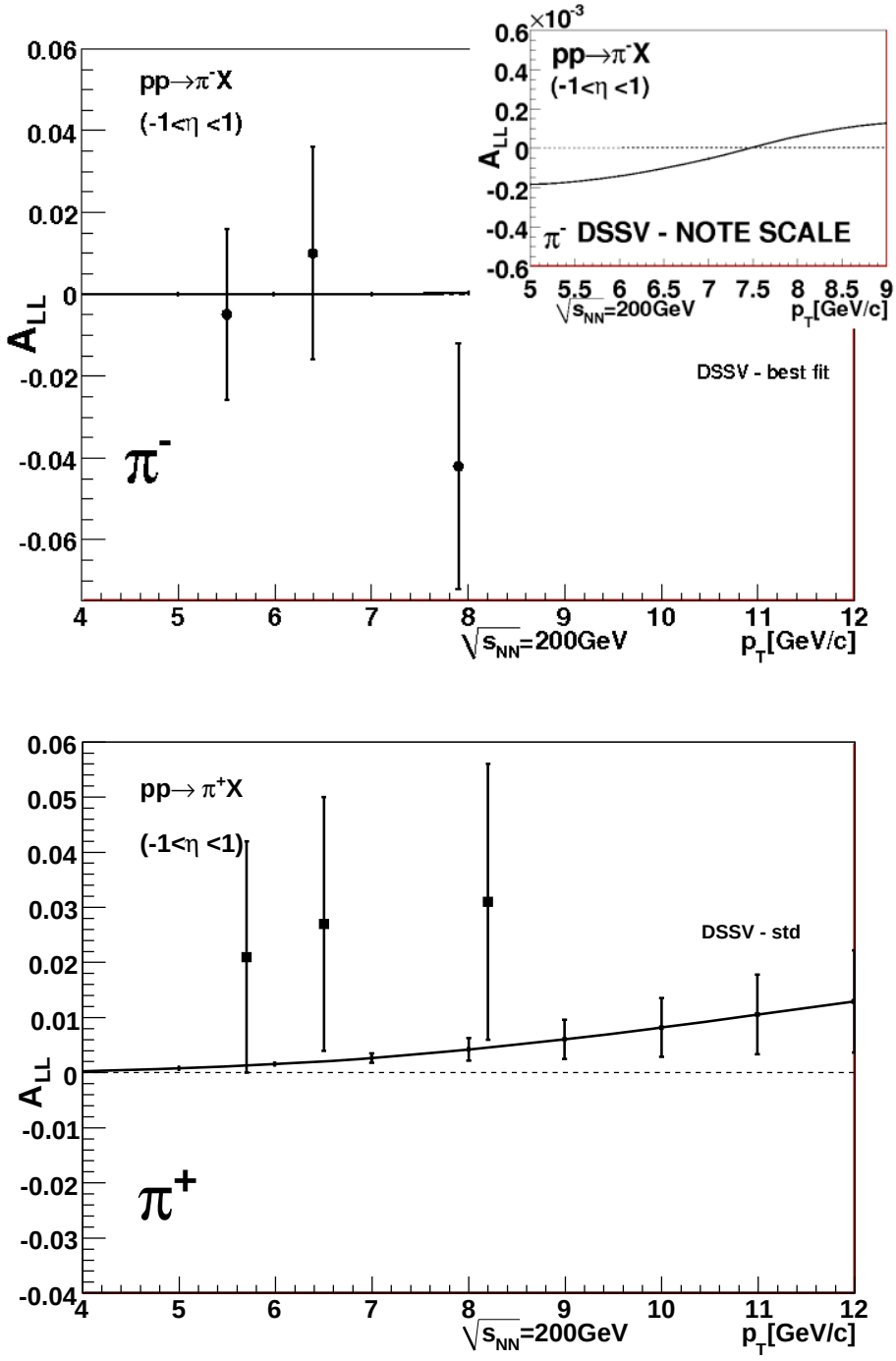

Figure 6.27: Measured A_{LL} from year 2006 compared to DSSV parametrisations for π^- (top panel) and π^- (bottom panel). The model curve depict the best fit of the gluon polarization using reference[11]. Figure corresponds to the full 2006 data-set. The scale uncertainty corresponds to the uncertainty in the beam polarization.

6.11.1 Errors in A_{LL}

The errors applicable to the measured asymmetries discussed and summarized in this section are mostly statistical. Systematic errors that have been explored include the width distributions obtained with the already discussed bunch shuffling technique (Section 6.10). The latter are of the order of 10^{-3} which is less than that current statistical precision. Other systematic errors that are present are the uncertainty in the ratio of luminosities in the two possible proton spin states:$R = \frac{L_{++}}{L_{+-}}$ (Section 6.1) which is 4×10^{-5}[5]. Systematic uncertainties that will be also be considered are momentum resolutions which, as it was noted in Section 5.2.5, are known to be $0.6\%p_T$ from Monte Carlo simulation and $1.1\%p_T$ from data. These uncertainties added in quadratures summarize to a systematic error in the momentum resolution to $1.25\%p_T$ which is a minimal source of systematic uncertainty. Momentum errors are summarized in Table 6.15 and statistical errors can be found in Table 6.16 while errors are summarized in Table 6.17.

π^-			
p_T[GeV/c]	Δp_T (GeV/c-min)	Δp_T (GeV/c-Max)	Systematic deviation [GeV/c]
5.2	5.17	5.25	$\pm$0.04
6.7	6.66	6.77	$\pm$0.05
8.2	8.15	8.29	$\pm$0.07
π^+			
p_T[GeV/c]	Δp_T (GeV/c-min)	Δp_T (GeV/c-Max)	Systematic deviation [GeV/c]
5.7	5.66	5.76	$\pm$0.05
6.5	6.46	6.57	$\pm$0.06
8.2	8.15	8.28	$\pm$0.07

Table 6.15: Summary of systematic errors in p_T of A_{LL} and A_L. Table corresponds to the full 2006 data-set.

p_T[GeV/c]	$\Delta A_{LL\pi^-}$	p_T[GeV/c]	$\Delta A_{LL\pi^+}$
5.6	0.022	5.7	0.021
6.7	0.026	6.5	0.023
8.2	0.030	8.2	0.025

Table 6.16: Summary of statistical errors of A_{LL} by average p_T. Table corresponds to the full 2006 data-set.

Summary of A_{LL} errors					
p_T[GeV/c]	$\delta_{sys} p_{T\pi^-}$[GeV/c]	$\delta_{stat} A_{LL\pi^-}$	p_T[GeV/c]	$\delta_{sys} p_{T\pi^+}$[GeV/c]	$\delta_{stat} A_{LL\pi^+}$
5.6	0.04	0.022	5.7	0.05	0.021
6.7	0.05	0.026	6.5	0.06	0.023
8.2	0.07	0.030	8.2	0.07	0.025

Table 6.17: Summary of statistical and systematic errors of A_{LL} and p_T by average p_T. Table corresponds to the full 2006 data-set.

Chapter 7

Conclusions

Investigating the structure of visible matter and getting a rare glimpse into quantum mechanical spin through RHIC's unique capabilities was the motivation of the work presented. The physics goal of this work was to measure a quantity that was sensitive to the gluon polarization ΔG. The work presented also aimed at contributing to the data of unpolarized particle production as well as to the data of polarized spin measurements. Unpolarized particle production measurements such as the ones presented in this work are important aspects of high energy collider programs. Inclusive hadron cross section measurements can add new results to existing data at different energies thus minimizing the uncertainties in the current knowledge of fragmentation function data - particularly the gluon fragmentation functions. The heart of the spin measurements in this work were the asymmetries of charged pions proceeding from polarized proton proton collisions. A_{LL} of $\pi^{\pm}$ can be used as part of a global analysis[11] to help disentangle the

contributions to the proton spin thus contributing to the current knowledge of strongly interacting matter. In order to participate in the constraint of the magnitude and the sign of ΔG, well identified charged pions were needed. A comparison of the measurements with different models (GRSV[22] and DSSV[11]) could then be made. A verification of the pQCD framework applicability was needed in order to compare model predictions. Calculating a differential cross section which could be compared to pQCD (Figure 7.1 and Figure 7.2) was a natural step to follow. These comparisons allowed verification that the unpolarized parton distribution functions used in the A_{LL} theoretical curves in Figure 7.4 and Figure 7.3 could indeed be used to compare the charged pion data obtained by this procedure. A key ingredient of QCD referred to as $universality$ provides a way for one set of measurements from DIS to make a large set of predictions in proton-proton collisions. Verifying universality in the process presented in this work was of particular importance. The job of identifying charged hadronic particles ($\pi^{\pm}$) was particularly challenging. The challenge was due to the detector which only had electromagnetic calorimetry available. The nonavailability of test beam data needed to parametrize the hadronic response of the electromagnetic calorimeter as well as the lack of a dedicated trigger meant that a methodical and diligent method had to be developed to properly account for the background. The results obtained showed that the unpolarized cross sections were consistent with pQCD production predictions. The latter meant that comparisons to different gluon polarization scenarios could be made with confidence in that

pQCD could be used for the interpretation of results presented in this work. The spin dependent measurements eliminated the maximal gluon contribution scenarios from the fits of GRSV[22]. GRSV has now been updated with the DSSV[10][11] models, which are compiled into a newer set of global analysis. These fits include neutral pion[5] measurements by the PHENIX detector as well as measurements from the STAR detector. GRSV is an older set of fits while DSSV are more current. However, these two parametrisations are constrained similarly by positivity, which will constraint the maximum ΔG contributions making the theoretical comparisons still applicable to this work.[1] Table 7.1 and Table 7.2 summarize the cross-section results, while Table 7.3 summarizes the A_{LL} measurements.

$E\frac{d^3\sigma}{d\vec{p}^3}$ Summary π^+		
p_T[GeV/c]	$E\frac{d^3\sigma}{d\vec{p}^3}$ (mb-GeV$^2c^2$)	$\sigma_{sys} \otimes \sigma_{stat}$ (%)
5.47	0.00001539	$8 \otimes 2$
6.49	0.00000680	$22 \otimes 3$
7.49	0.00000191	$62 \otimes 6$
8.46	0.00000076	$64 \otimes 10$

Table 7.1: Summary of π^+ $E\frac{d^3\sigma}{d\vec{p}^3}$ and associated errors.

$E\frac{d^3\sigma}{d\vec{p}^3}$ Summary π^-		
p_T[GeV/c]	$E\frac{d^3\sigma}{d\vec{p}^3}$(mb-GeV$^2c^2$)	$\sigma_{sys} \otimes \sigma_{stat}$ (%)
5.47	0.00001242	$13 \otimes 3$
6.49	0.00000467	$22 \otimes 4$
7.49	0.00000140	$70 \otimes 7$
8.46	0.00000056	$65 \otimes 12$

Table 7.2: Summary of π^- $E\frac{d^3\sigma}{d\vec{p}^3}$ and associated errors.

[1]The constraint of the polarized parton distribution cannot be larger than the unpolarized functions obtained from DIS.

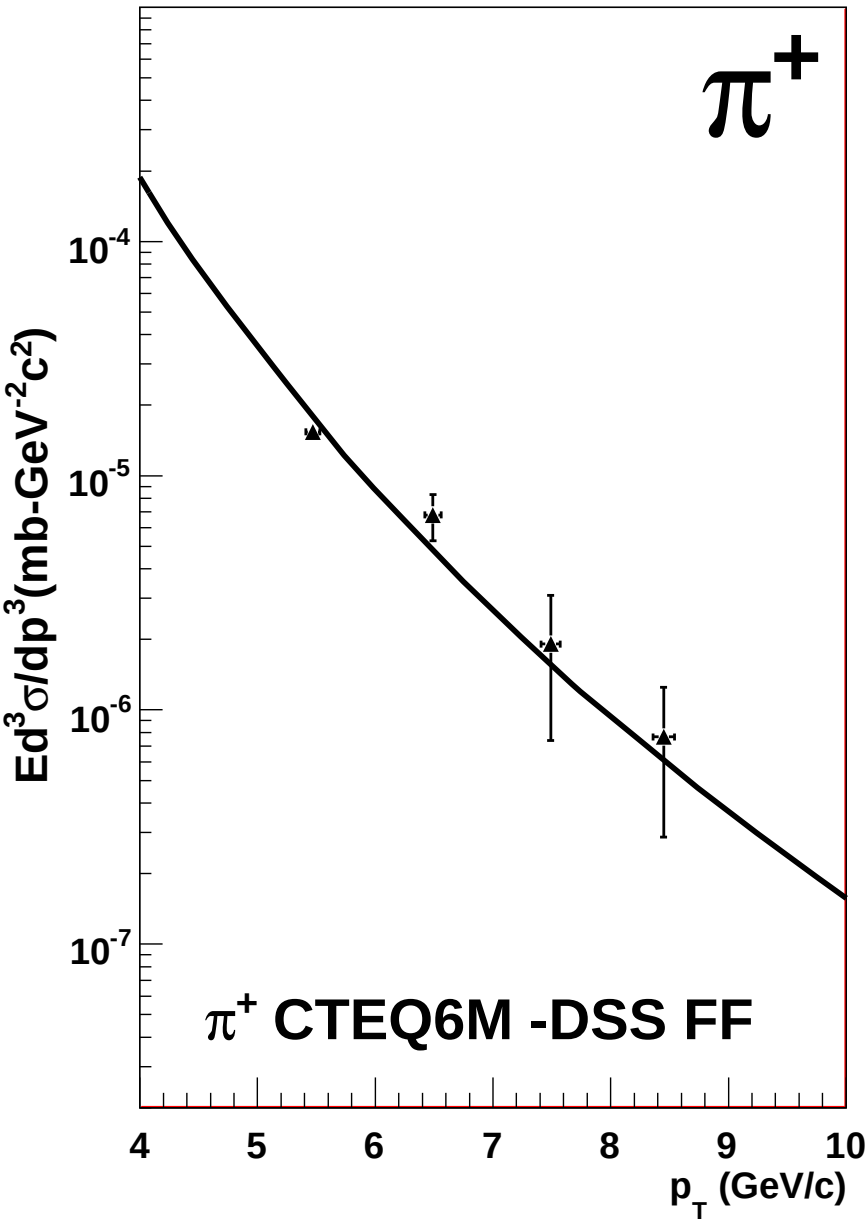

Figure 7.1: Measured $E\frac{d^3\sigma}{dp^3}$ compared to unpolarized cross section pQCD predictions that use DSS fragmentation functions for π^+.

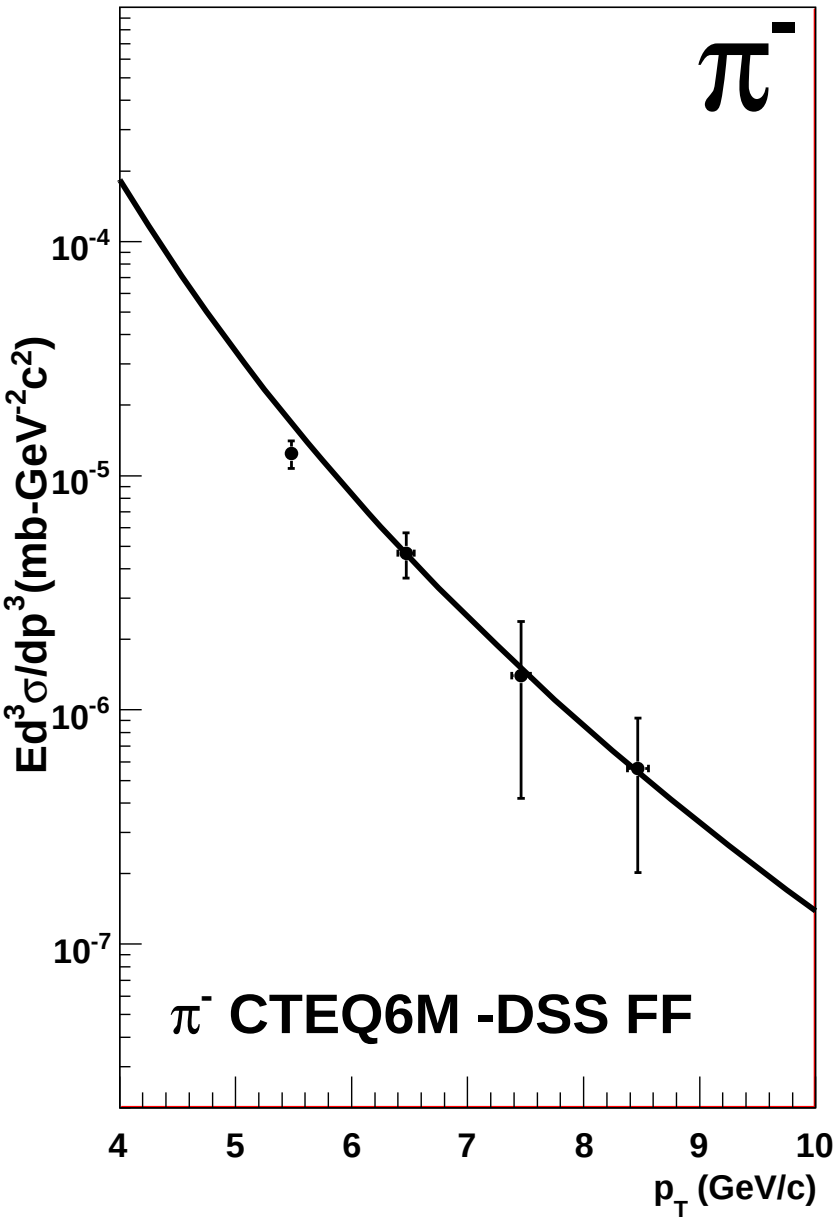

Figure 7.2: Measured $E\frac{d^3\sigma}{dp^3}$ compared to unpolarized cross section pQCD predictions that use DSS fragmentation functions for π^-.

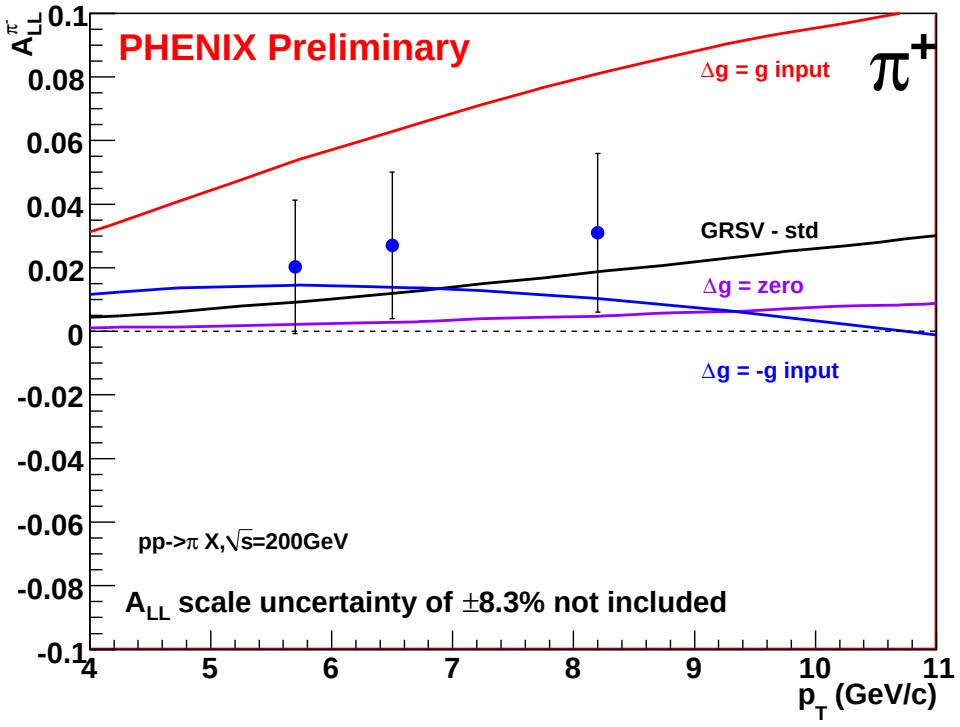

Figure 7.3: Measured A_{LL} compared to GRSV parametrisations for π^+. The red curve represents the size of the asymmetries if ΔG were the maximum value $\Delta G = g$ where g in the value of the unpolarized gluon distribution. The black curve corresponds to ΔG =0.28. The blue curve represents $\Delta G = -g$ while the purple curve represents ΔG =0 (no contribution). Measurements correspond to the 2006 data set.

Summary of A_{LL} and associated errors							
p_T[GeV/c]	$\delta_{sys(p_T)\pi^-}$[GeV/c]	$A_{LL\pi^-}$	δ_{stat} $A_{LL\pi^-}$	p_T[GeV/c]	$\delta_{sys(p_T)\pi^+}$[GeV/c]	$A_{LL\pi^+}$	δ_{stat} $A_{LL\pi^+}$
5.6	0.04	-0.005	0.022	5.7	0.05	0.020	0.021
6.7	0.05	0.011	0.026	6.5	0.06	0.027	0.023
8.2	0.07	-0.042	0.030	8.2	0.07	0.032	0.025

Table 7.3: Summary of statistical and systematic errors of A_{LL} and p_T by average p_T. Table corresponds to the full 2006 data-set.

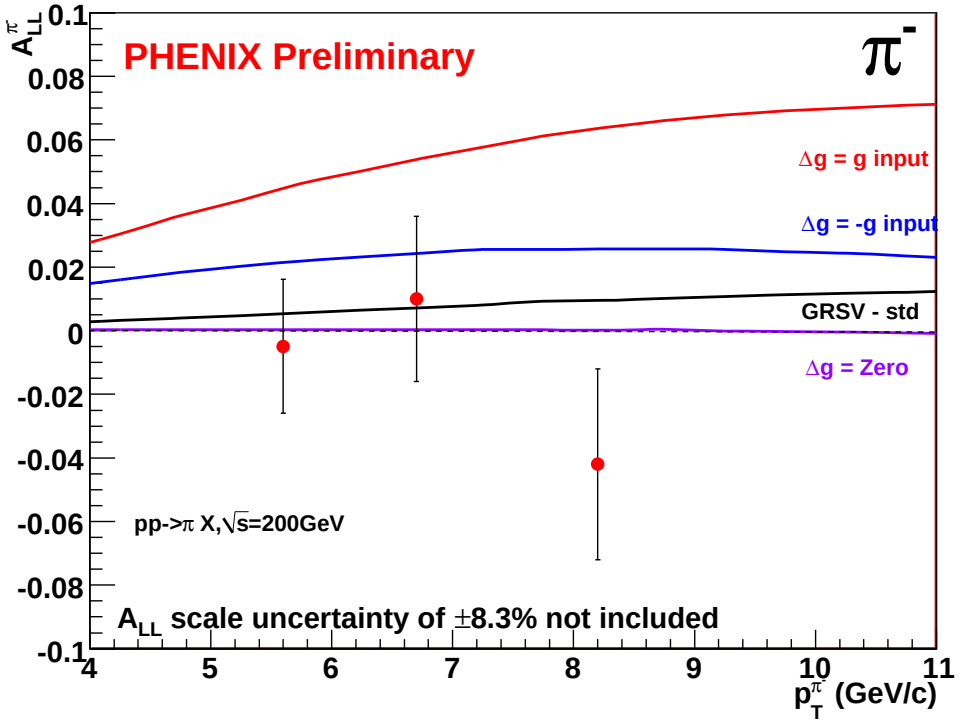

Figure 7.4: Measured A_{LL} compared to GRSV parametrisations for π^-.The red curve represents the size of the asymmetries if ΔG were the maximum value $\Delta G = g$, where g in the value of the unpolarized gluon distribution. The black curve corresponds to ΔG =0.28. The blue curve represents $\Delta G = -g$ while the purple curve represents ΔG =0 (no contribution). Measurements correspond to the 2006 data set.

Determining from where all the contributions to the proton's spin come from is no small endeavor nor can it be determined by a single measurement. Instead, it is a task big enough for an international collaboration. This present work hopes to place a few stones within this monumental task. Different transverse momentum ranges and measurements sample different gluon momentum fractions. Low x constraints to ΔG are currently driven by collider experiments like RHIC and the high x constraints are driven by DIS experiments. For the measurements in the work presented, the corresponding sampled gluon momentum fraction x extracted from a NLO pQCD calculation can be seen in Figure 7.5. Both pion species in the p_T region, applicable to the presented measurements, sample a similar momentum fraction of $\sim$0.02 to 0.1. The benefits of each individual result can illustrate the power of a combined analysis. Figure 7.6 shows an attempt by PHENIX experimental physicists to combine several A_{LL} measurements from the PHENIX detector. One can typically start with several gluon polarization assumptions based on parametrisations of available data. Asymmetries can then be generated similar to the GRSV and DSSV asymmetry models which charged pions have been compared to in the present work. By comparing the values obtained from experiment and the A_{LL} curves from the model, a χ^2 minimization is done until the best value of ΔG which fits the data is obtained. The procedure can be repeated with the inclusion of new emerging experimental results allowing for higher precision. While Figure 7.6 serves to illustrate the benefit of combining different results from the PHENIX detector, it is really through

a more robust method which includes all world data and properly accounts for theoretical and experimental uncertainties that a formal global analysis can be obtained. DSSV is an example of such an effort.

The main contribution of the present work is the constraint of ΔG to the left side of the χ^2 minimization curve in Figure 7.6. In this simple PHENIX combined χ^2 analysis from Figure 7.6, the negative values already seem to be predominantly driven out by the π^+ as it can be seen from the combined bold black curve. With higher statistics, charged pions can provide significant information about the gluon polarization.

The maximal ΔG contribution bounded by *g* -the unpolarized gluon distribution– (Figure 7.4) has been ruled out by the $\pi^{\pm}$ measurements. In addition, the cross sections in Figure 7.1 show that the fragmentation functions[11] used as input to the pQCD cross sections, as well as the unpolarized parton distributions from DIS, describe the data.

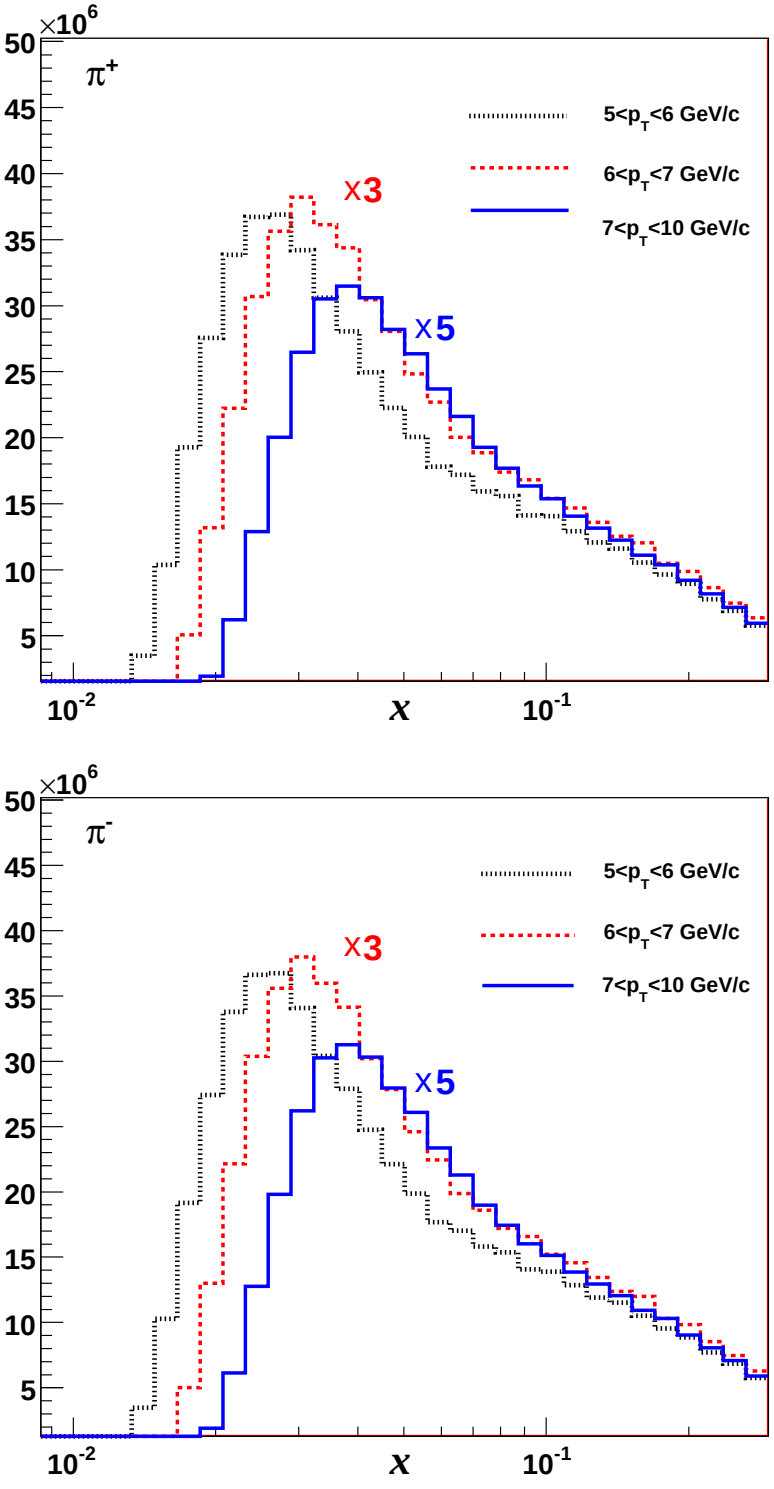

Figure 7.5: Distributions of the gluon's momentum fraction x in the three p_T momentum bins applicable to the measurements presented. The figures were produced from a NLO pQCD simulation developed by Marco Stratmann[32], compiled by K. Boyle[8] and histogrammed by the author.

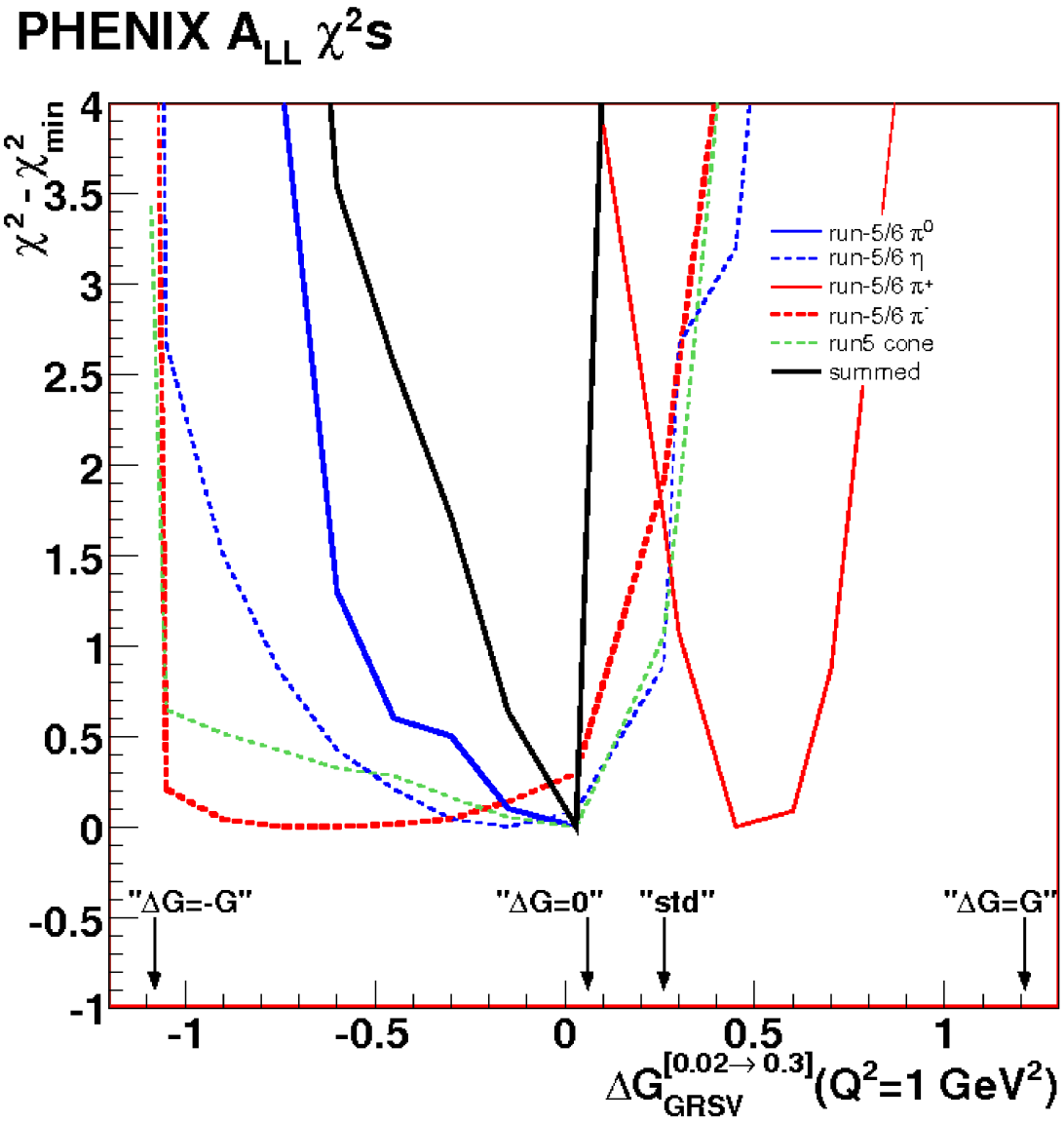

Figure 7.6: $\Delta G\,\chi^2$ minimization performed by Joseph Seele[30]. Different maximal and minimal ΔG scenarios are excluded by the many analyses. The different curves in color represent different processes which are sensitive to ΔG with charged pions in this work represented by the red curves. Blue curves correspond to η (dashed line) and π^0 (solid line). Green curve corresponds to "cone" (part of a jet) measurement. The black curves show all combined results. Data is used as an input to the pQCD model (DSS). Modeling is then repeated until a minimizing value of ΔG is obtained. Charged pion measurements from this work (red curves), correspond to the combined 2006 and 2005 data set.

An important observation to be made about spin structure measurements is that they seek extreme precision. A huge amount of statistics is needed in order to decisively pin down the different contributions to the proton's spin. Charged pion A_{LL} as well as other complementary probes aim at reaching a statistical significance. Precision will help to the constraint of ΔG. Longer RHIC running time at the highest machine design polarization will allow measurements precision. These efforts, in combination with efforts from the DIS community, do paint a better outlook for the next round of pQCD global analyses[10] similar to the way many global analyses fit into the world data. These analyses have now included the π^0[5] from the PHENIX detector and the jet measurements[21] from the STAR detector at RHIC. The current knowledge of the polarized parton distribution functions can be found in Figure 7.7. The incorporation of RHIC measurements into a global analysis has been found to constraint the polarized gluon distribution in a limited x range. While significantly constrained, large uncertainties still remain particularly regarding the sign of ΔG . These uncertainties can only be reduced by incorporating more independent measurements into the global fits. Charged pions can contribute immensely to the disentanglement of the magnitude and the sign of the polarized gluon. Complementary probes will contribute to these measurements by reducing the uncertainty on the fragmentation functions which are used in the pQCD A_{LL} fits. Figure 7.8 illustrates the measurements of A_{LL} presented in this work, using the most current parametrisations obtained from the DSSV[11] fits to RHIC data.

The current DSSV model has small asymmetries, especially for the π^- A_{LL}. The data has not yet reached statistical significance in order to make any statements with this new set of fits.Charged pions have not further constrained ΔG given the small size of the asymmetry parameterizations from DSSV. With larger statistics, however, pions can provide a significant constraint. Charged pions can provide sensitivity to positive and negative scenarios, mapping out the sign of ΔG at the sampled x region. Figures 7.9 and 7.10 show projections of charged pion asymmetries with longer proton beam times at RHIC and machine expected polarizations. The main contributions of the results presented in this work will come from an incorporation of the measured cross-sections and asymmetries into the world's data of polarized spin studies and parton density function parametrisations.

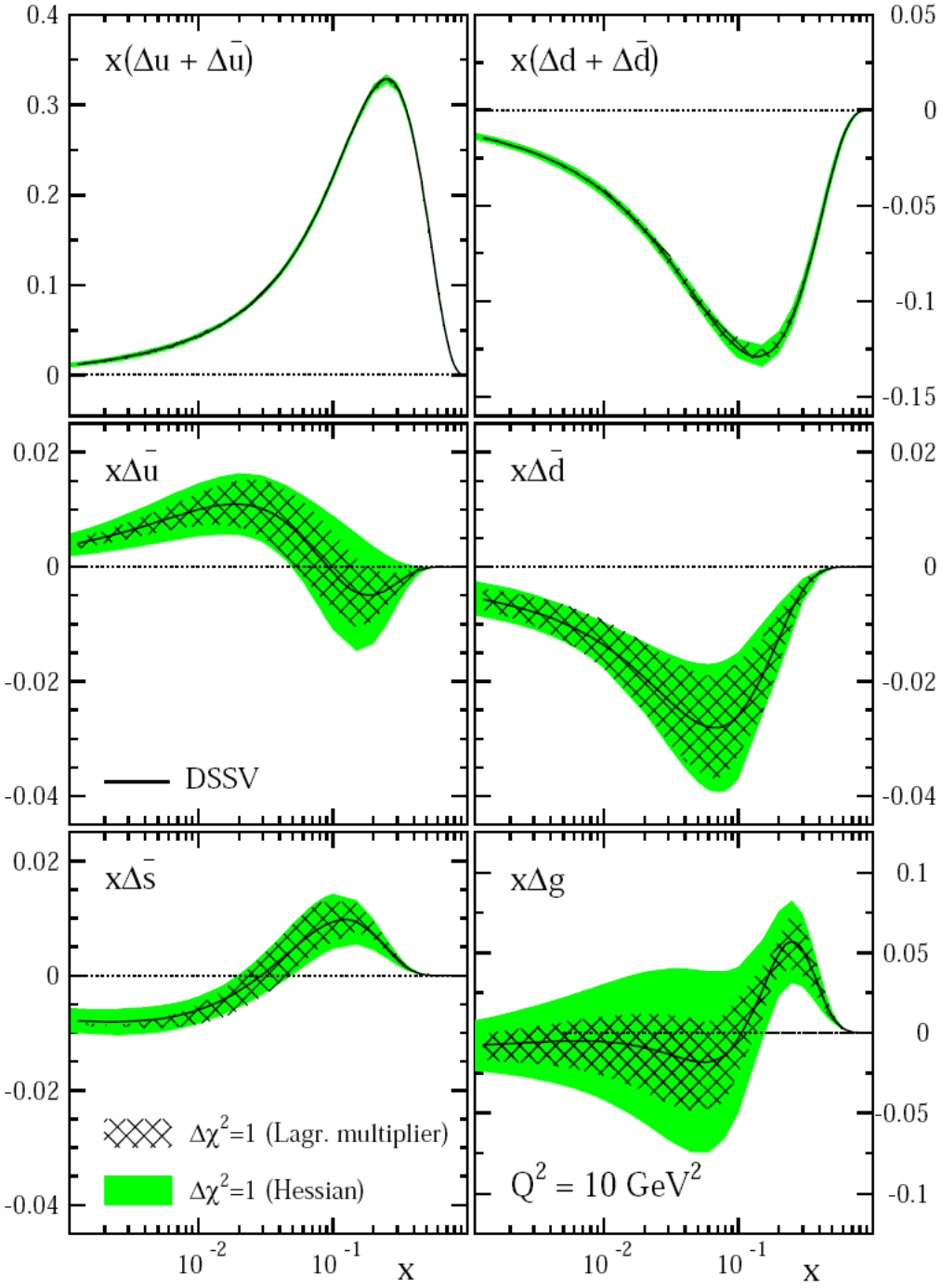

Figure 7.7: DSSV model. Current knowledge of polarized sea and gluon densities (Figure from[11]). Shaded bands represent uncertainties calculated with two different methods. Charged pions from this work sample the x region from $\sim$0.02 to 0.1.

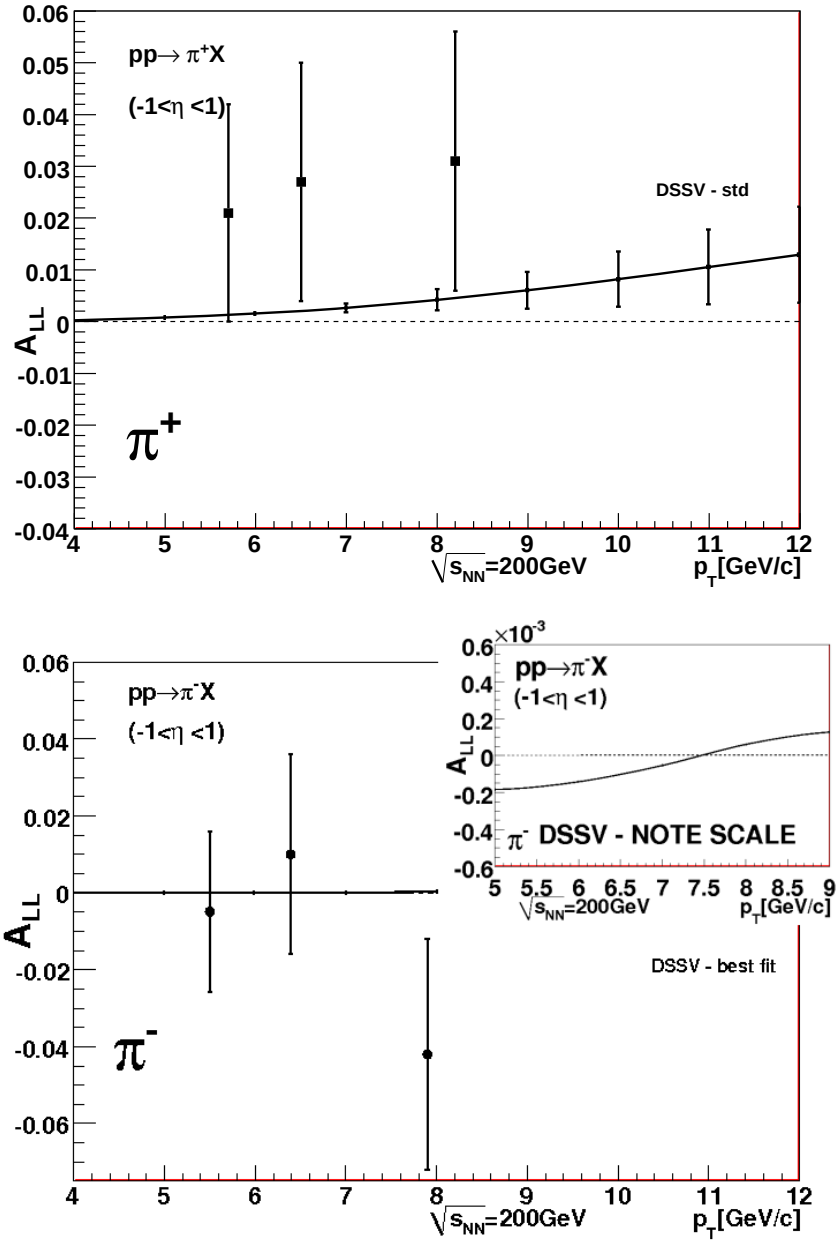

Figure 7.8: Asymmetry measurements compared to latest DSSV best fit parametrisations[11] which incorporate RHIC data. Errors in the model are calculated with a Hessian matrix method. Note that the rapidity is set at $|\eta| < 1$, nevertheless, the value of A_{LL} should be similar for $|\eta| < 0.35$. Note that the inset of the right panel has a different y axis scale to emphasize the size of the expected asymmetries using the DSSV fit.

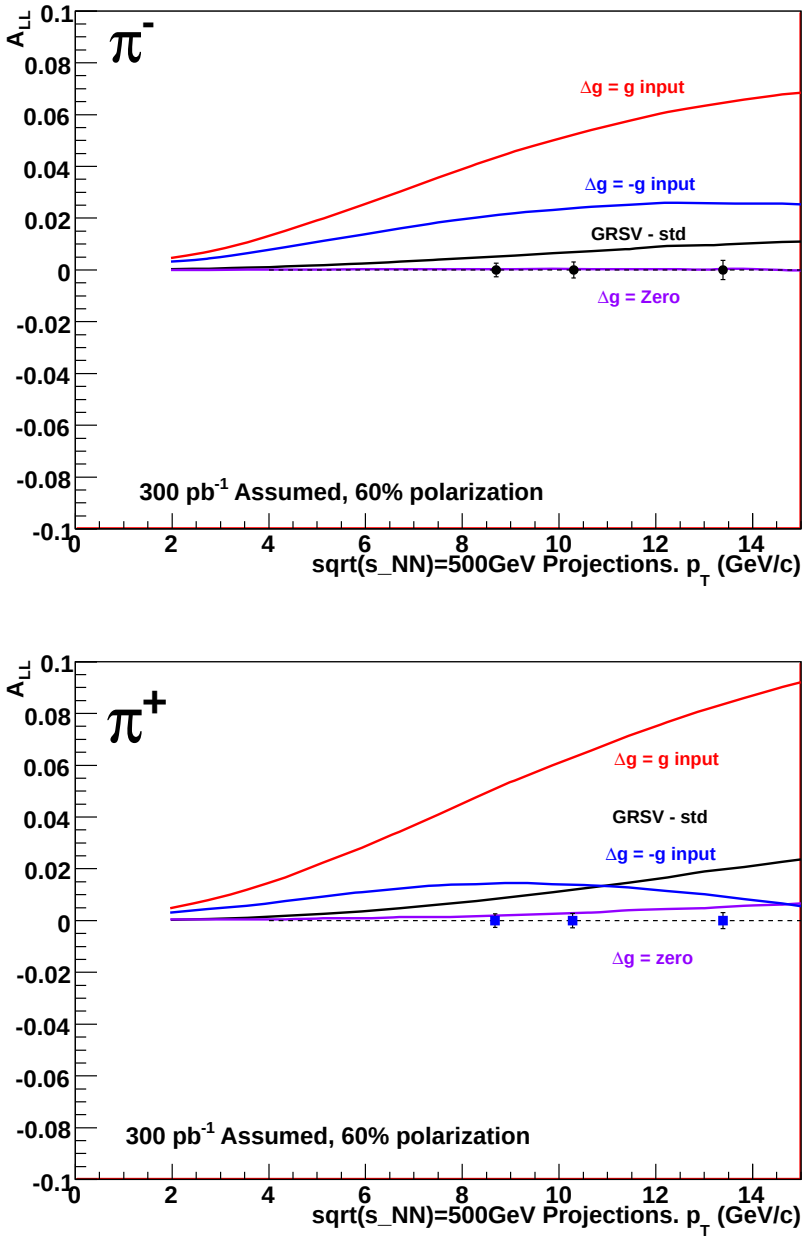

Figure 7.9: Projections of A_{LL} of charged pions with longer proton beam running time at 60% polarization and $\sqrt{s}$ =500 GeV and accumulated integrated luminosity of 300pb^{-1}. Data sensitivities to polarized gluon scenarios begin to have an impact. Charged pions would begin discerning between negative and positive scenarios.

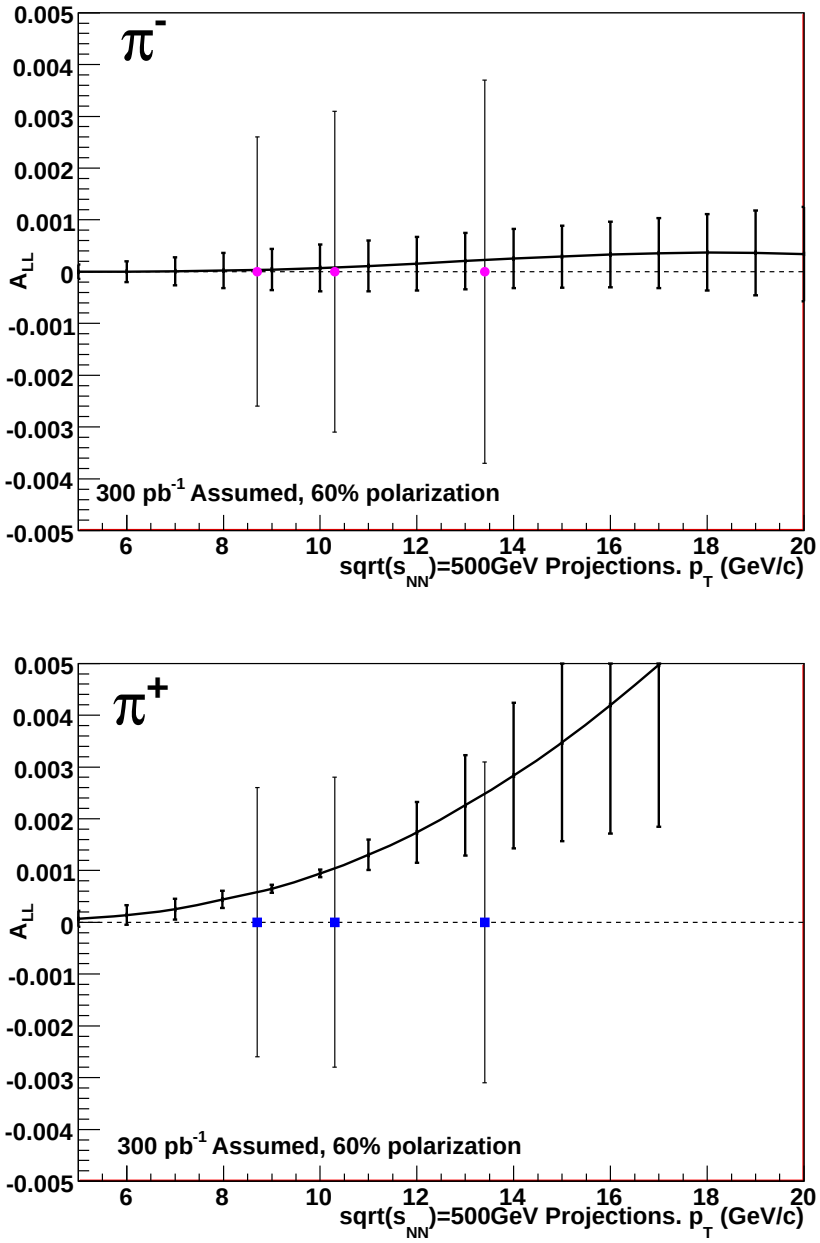

Figure 7.10: Sensitivity projections of A_{LL} of charged pions with longer proton beam running time at RHIC. The plots correspond to expected future RHIC running at $\sqrt{s} =$ 500 GeV with projected beam polarizations of 60% and accumulated integrated luminosity of $300pb^{-1}$. Data sensitivities to the best DSSV fit using jet and π^0 parametrisations are still poorly constrained by charged pions.

Bibliography

[1] A measurement of the spin asymmetry and determination of the structure function g1 in deep inelastic muon-proton scattering. *Physics Letters B*, 206(2):364 – 370, 1988.

[2] A. Adare et al. Inclusive cross section and double helicity asymmetry for π^0 production in p+p collisions at $\sqrt{(s)}$ =200 GeV: Implications for the polarized gluon distribution in the proton. *Phys. Rev.*, D76:051106, 2007.

[3] K. Adcox *et al.* PHENIX Detector Overview. *Nuclear Instruments and Methods in Physics Research Section A*, 499:469, 2003.

[4] Stephen Scott Adler et al. High p_T charged hadron suppression in Au + Au collisions at $\sqrt{s}_{NN} = 200\,GeV$. *Phys. Rev.*, C69:034910, 2004.

[5] S. S. Adler *et al.* Double Helicity Asymmetry in Inclusive Mid-Rapidity π^0 Production for Polarized p + p Collisions at $\sqrt{s} = 200$ GeV. *Physics Review Letters*, 93:202002, 2004.

[6] Guido Altarelli and G. Parisi. Asymptotic Freedom in Parton Language. *Nucl. Phys.*, B126:298, 1977.

[7] M. Bai, T. Roser, L. Ahrens, I. G. Alekseev, J. Alessi, J. Beebe-Wang, M. Blaskiewicz, A. Bravar, J. M. Brennan, D. Bruno, G. Bunce, E. Courant, A. Drees, W. Fischer, C. Gardner, R. Gill, J. Glenn, W. Haeberli, H. Huang, O. Jinnouchi, J. Kewisch, A. Luccio, Y. Luo, I. Nakagawa, H. Okada, F. Pilat, W. W. MacKay, Y. Makdisi, C. Montag, V. Ptitsyn, T. Satogata, E. Stephenson, D. Svirida, S. Tepikian, D. Trbojevic, N. Tsoupas, T. Wise, A. Zelenski, K. Zeno, and S. Y. Zhang. Polarized Proton Collisions at 205 GeV at RHIC. *Physical Review Letters*, 96(17):174801, 2006. `http://link.aps.org/abstract/PRL/v96/e174801`.

[8] Kieran Boyle. Private Communication, kpboyle(AT)gmail.com. *bld. 510C, Upton, NY, 11973*.

[9] RHIC Collaboration. Final 2006 Polarizations for RHIC. 2007. `www4.rcf.bnl.gov/~cnipol/pubdocs/Run06Offline`.

[10] Daniel de Florian, Rodolfo Sassot, Marco Stratmann, and Werner Vogelsang. Global Analysis of Helicity Parton Densities and Their Uncertainties. *Phys. Rev. Lett.*, 101:072001, 2008.

[11] Daniel de Florian, Rodolfo Sassot, Marco Stratmann, and Werner Vogelsang. Extraction of Spin-Dependent Parton Densities and Their Uncertainties, 2009. `http://www.citebase.org/abstract?id=oai:arXiv.org:0904.3821`.

[12] Yuri L. Dokshitzer. Calculation of the Structure Functions for Deep Inelastic Scattering and e+ e- Annihilation by Perturbation Theory in Quantum Chromodynamics. *Sov. Phys. JETP*, 46:641–653, 1977.

[13] C. Amsler et al. Particle Data Group. *Physics Letters B*, 667, 2008.

[14] L. Aphecetche et al. PHENIX calorimeter. *Nuclear Instruments and Methods in Physics Research Section A: Accelerators, Spectrometers, Detectors and Associated Equipment*, 499(2-3):521 – 536, 2003. The Relativistic Heavy Ion Collider Project: RHIC and its Detectors.

[15] Lauret et al. From Geant 3 to Virtual Monte Carlo: Approach and Experience. 2005.

[16] M. Aizawa et al. Phenix central arm particle id detectors. *Nuclear Instruments and Methods in Physics Research Section A: Accelerators, Spectrometers, Detectors and Associated Equipment*, 499(2-3):508 – 520, 2003.

[17] P. D. Acton et al. A study of differences between quark and gluon jets using vertex tagging of quark jets. *Zeitschrift fr Physik C Particles and Fields*, 58, 1993.

[18] Torbjorn S. et al. PYTHIA 6.2 Physics and Manual, 2001. arXiv.org:hep-ph/0108264.

[19] K.Krueger et al. H1 and Zeus Collaboration. Combination and QCD Analysis of H1 and ZEUS Deep Inelastic $e^{\pm}p$ Scattering Cross Section Measurements. 2009. `www-h1.desy.de/h1/www/publications/conf/conflist.html`.

[20] Akiba et al. RIKEN Spin Collaboration. RHIC SPIN Facility overview. 1995. `http://www.rarf.riken.go.jp/rarf/rhic/acc/snake.html`.

[21] Renee Fatemi. Using jet asymmetries to access the gluon helicity distribution of the proton at STAR. *arXiv*, nucl-ex/0606007, 2006. `http://arxiv.org/abs/nucl-ex/0606007`.

[22] M. Gluck, E. Reya, M. Stratmann, and W. Vogelsang. Models for the polarized parton distributions of the nucleon. *Phys. Rev.*, D63:094005, 2001.

[23] V. N. Gribov and L. N. Lipatov. Deep inelastic e p scattering in perturbation theory. *Sov. J. Nucl. Phys.*, 15:438–450, 1972.

[24] David J. Griffiths. *Introduction to Quantun Mechanics*. Prentice Hall, 1994.

[25] Maurice Jacob. *The Quark Structure of Matter*. World Scientific, 1992.

[26] Adam Kocoloski. Recent STAR Results from Charged Pion Production in Polarized pp Collisions at $\sqrt{s} = 200GeV$ at RHIC. *arXiv*, 0905.1033v1, 2009.

[27] S. Kretzer. Fragmentation functions from flavour-inclusive and flavour-tagged e+ e- annihilations. *Phys. Rev.*, D62:054001, 2000.

[28] Elliot Leader. *Spin in Particle Physics*. Cambridge University Press, 2001. `http://www.cambridge.org`.

[29] S.Y. Lee. *Accelerator physics*. World Scientific Publishing Company, 2004.

[30] Joseph Seele. Private communication, seelej(AT)mit.edu. *MIT, 77 Massachusetts Avenue, Cambridge, MA 02139-4307*.

[31] G. Soyez. DGLAP evolution extends the triple pole Pomeron fit. *Phys. Rev. D*, 67(7):076001, Apr 2003.

[32] Marco Stratmann. Private communication, marco.stratmann(AT)physik.uni-regensburg.de. *Wurzburg/Regensburg University*.

[33] Werner Vogelsang. Private Communication, partonic contributions for p+p and central rapidities. *vogelsan(AT)quark.phy.bnl.gov*.

[34] A. Zee. *Quantun Field Theory in a Nutshell*. Princeton University Press, 2003. `http://pupress.princeton.edu`.

Appendix A

Tables of Efficiencies and matching calibrations

Summary of efficiency calculations in table format, as well as calibrations described in Section 5 can be found in this appendix.

Charge	p_T[GeV/c]	Mean	σ
π^+	5-6	-0.26	0.82
	6-7	-0.26	0.81
	7-8	-0.26	0.79
	8-9	-0.26	0.78
	9-10	-0.28	0.79
π^-	5-6	-0.04	0.84
	6-7	-0.04	0.81
	7-8	-0.05	0.82
	8-9	-0.05	0.81
	9-10	-0.05	0.79

Table A.1: Corrections to mean and σ to simulated charged pions in pc3sdϕ,

Charge	p_T[GeV/c]	Mean	σ
π^+	5-6	-0.42	1.10
	6-7	-0.437	1.10
	7-8	-0.37	1.10
	8-9	-0.35	1.10
	9-10	-0.35	1.10
π^-	5-6	-0.20	1.12
	6-7	-0.19	1.11
	7-8	-0.18	1.10
	8-9	-0.17	1.10
	9-10	-0.17	1.10

Table A.2: Corrections to mean and σ to simulated charged pions in emcsdϕ

Charge	p_T[GeV/c]	Mean	σ
π^+	5-6	-0.17	0.84
	6-7	-0.16	0.86
	7-8	-0.17	0.84
	8-9	-0.16	0.84
	9-10	-0.16	0.84
π^-	5-6	-0.16	0.86
	6-7	-0.15	0.87
	7-8	-0.16	0.83
	8-9	-0.16	0.85
	9-10	-0.16	0.84

Table A.3: Corrections to Mean and σ to simulated charged pions in emcsdz

Charge	p_T[GeV/c]	RMS	σ
π^+	5-6	-0.126	0.57
	6-7	-0.12	0.57
	7-8	-0.13	0.57
	8-9	-0.12	0.57
	9-10	-0.128	0.57
π^-	5-6	-0.13	0.57
	6-7	-0.12	0.56
	7-8	-0.12	0.56
	8-9	-0.13	0.57
	9-10	-0.12	0.57

Table A.4: Corrections to Mean and σ to simulated charged pions in dz

Charge	p_T[GeV/c]	$\epsilon_{pc3sd\phi}$	$< 3\sigma$	$< 2.5\sigma$	$< 2\sigma$	$< 1.5\sigma$	$< 1\sigma$.
π^+	5-6	0.70	0.60	0.58	0.56	0.50	0.37
	6-7	0.72	0.63	0.61	0.58	0.51	0.38
	7-8	0.73	0.64	0.62	0.58	0.51	0.39
	8-9	0.73	0.65	0.63	0.60	0.52	0.39
	9-10	0.74	0.67	0.65	0.62	0.54	0.40
π^-	5-6	0.70	0.60	0.58	0.56	0.49	0.38
	6-7	0.73	0.63	0.61	0.58	0.50	0.38
	7-8	0.69	0.59	0.58	0.54	0.49	0.37
	8-9	0.71	0.62	0.61	0.57	0.50	0.38
	9-10	0.74	0.65	0.64	0.60	0.52	0.39

Table A.5: Efficiency extracted from simulation after properly normalizing distributions. $\epsilon_{pc3sd\phi}$ represents the requirement that a charged track from the DC is matched in the pad chamber 3 in sdϕ. The σ efficiencies take $\epsilon_{pc3sd\phi}$ into account as these represent the efficiency of making both a track coincidence requirement, as well as cut on the normalized distributions in σ (See text for details)

Charge	p_T[GeV/c]	ϵ_{pc3sdz}	$< 3\sigma$	$< 2.5\sigma$	$< 2\sigma$	$< 1.5\sigma$	$< 1\sigma$.
π^+	5-6	0.70	0.64	0.64	0.62	0.56	0.44
	6-7	0.72	0.67	0.66	0.64	0.59	0.47
	7-8	0.73	0.68	0.67	0.65	0.59	0.47
	8-9	0.73	0.68	0.67	0.65	0.60	0.48
	9-10	0.74	0.70	0.69	0.67	0.61	0.48
π^-	5-6	0.70	0.64	0.64	0.61	0.56	0.44
	6-7	0.73	0.68	0.67	0.65	0.60	0.48
	7-8	0.69	0.64	0.63	0.61	0.55	0.45
	8-9	0.71	0.66	0.66	0.63	0.57	0.46
	9-10	0.74	0.69	0.68	0.66	0.60	0.48

Table A.6: Efficiency extracted from simulation after properly normalizing distributions ϵ_{pc3sdz} represents the requirement that a charged track from the DC is matched in the pad chamber 3 in sd$z$. The σ efficiencies take ϵ_{pc3sdz} into account as these represent the efficiency of making both a track coincidence requirement, as well as cut on the normalized distributions in σ (See text for details)

Charge	p_T[GeV/c]	$\epsilon_{emcsd\phi}$	$< 3\sigma$	$< 2.5\sigma$	$< 2\sigma$	$< 1.5\sigma$	$< 1\sigma$.
π^+	5-6	0.79	0.74	0.73	0.70	0.62	0.48
	6-7	0.81	0.77	0.75	0.72	0.65	0.51
	7-8	0.82	0.78	0.76	0.73	0.66	0.51
	8-9	0.82	0.79	0.78	0.75	0.68	0.54
	9-10	0.83	0.80	0.79	0.76	0.69	0.55
π^-	5-6	0.80	0.75	0.74	0.71	0.65	0.51
	6-7	0.83	0.79	0.78	0.75	0.68	0.54
	7-8	0.78	0.74	0.73	0.70	0.64	0.52
	8-9	0.80	0.77	0.75	0.72	0.66	0.53
	9-10	0.84	0.81	0.80	0.77	0.70	0.56

Table A.7: Efficiency extracted from simulation after properly normalizing distributions $\epsilon_{emcsd\phi}$ represents the requirement that a charged track from the DC is matched in the EMCal in ϕ. The σ efficiencies take $\epsilon_{emcsd\phi}$ into account as these represent the efficiency of making both a track coincidence requirement, as well as cut on the normalized distributions in σ (See text for details)

Charge	p_T[GeV/c]	ϵ_{emcsdz}	$< 3\sigma$	$< 2.5\sigma$	$< 2\sigma$	$< 1.5\sigma$	$< 1\sigma$.
π^+	5-6	0.79	0.72	0.70	0.66	0.61	0.48
	6-7	0.81	0.74	0.72	0.69	0.63	0.5
	7-8	0.82	0.76	0.74	0.70	0.64	0.51
	8-9	0.82	0.76	0.74	0.70	0.63	0.5
	9-10	0.83	0.78	0.76	0.73	0.66	0.53
π^-	5-6	0.80	0.73	0.71	0.67	0.61	0.49
	6-7	0.83	0.77	0.75	0.71	0.65	0.53
	7-8	0.96	0.73	0.71	0.67	0.60	0.48
	8-9	0.80	0.74	0.72	0.69	0.62	0.51
	9-10	0.84	0.78	0.76	0.72	0.66	0.52

Table A.8: Efficiency extracted from simulation after properly normalizing distributions ϵ_{emcsdz} represents the requirement that a charged track from the DC is matched in the EMCal in z. The σ efficiencies take ϵ_{emcsdz} into account as these represent the efficiency of making both a track coincidence requirement, as well as cut on the normalized distributions in σ (See text for details)

Charge	Matching	p_TGeV/c]	Mean	σ
-1	emcsdϕ	5-6	-1.85	1.80
		6-7	-1.70	1.50
		7-8	-1.50	1.30
		8-9	-1.30	1.40
		9-10	-1.10	1.20
+1		5-6	1.78	2.03
		6-7	1.49	1.77
		7-8	1.47	1.43
		8-9	1.44	1.43
		9-10	1.20	1.44
-1	pc3sdϕ	5-6	-5.78	5.30
		6-7	-5.27	4.90
		7-8	-4.77	4.27
		8-9	-4.20	4.40
		9-10	-4.05	3.90
+1		5-6	5.70	6.00
		6-7	4.40	4.30
		7-8	4.50	4.40
		8-9	4.40	3.40
		9-10	4.20	9.80
-1	pc2sdϕ	5-6	-5.01	4.15
		6-7	-5.41	4.01
		7-8	-5.34	4.55
		8-9	-4.71	3.83
		9-10	-4.65	6.55
+1		5-6	4.76	5.48
		6-7	4.24	4.69
		7-8	4.23	4.31
		8-9	3.82	3.61
		9-10	3.37	4.03

Table A.9: Summary of matching mean and sigma corrections(ϕ)to 2006 minimum bias data, for positive (+1) and negative (-1) tracks

Charge	Matching	p_T[GeV/c]	Mean	σ
-1	emcsd$z$	5-6	0.09	1.50.
		6-7	0.14	1.68.
		7-8	0.11	1.42.
		8-9	0.08	1.42.
		9-10	0.19	1.61.
+1		5-6	0.18	1.56.
		6-7	0.13	1.51.
		7-8	0.02	1.38.
		8-9	-0.08	1.57.
		9-10	0.21	1.59.
-1	pc3sd$z$	5-6	0.02	2.05.
		6-7	0.10	2.05.
		7-8	0.01	1.90.
		8-9	0.09	1.82.
		9-10	-0.03	3.15.
+1		5-6	0.01	1.92.
		6-7	0.00	2.02.
		7-8	-0.07	1.95.
		8-9	-0.12	1.84.
		9-10	0.02	-1.55.
-1	pc2sd$z$	5-6	0.03	1.75.
		6-7	0.01	2.16.
		7-8	-0.05	1.98.
		8-9	-0.16	1.32.
		9-10	-0.09	1.80.
+1		5-6	0.00	2.17.
		6-7	-0.19	2.06.
		7-8	-0.22	1.93.
		8-9	-0.26	1.69.
		9-10	-0.18	1.73.

Table A.10: Summary of matching Mean and σ corrections (z) to 2006 minimum bias data for positive (+1) and negative (-1) tracks

Charge	Matching	p_T[GeV/c]	mean	σ
+1	emcsdϕ	5-6	-0.15	1.09
		6-7	-0.13	1.06
		7-8	-0.15	1.08
		8-9	-0.18	1.10
		9-10	-0.22	1.11
		7-10	-0.17	1.10
-1		5-6	0.08	1.08
		6-7	0.05	1.07
		7-8	0.088	1.10
		8-9	0.15	1.12
		9-10	0.29	0.02
		7-10	0.13	1.12
-1	pc3sdϕ	5-6	0.00	1.00
		6-7	-0.06	1.00
		7-8	-0.13	1.04
		8-9	-0.14	1.05
		9-10	-0.14	1.01
		7-10	-0.13	1.04
+1		5-6	-0.22	1.04
		6-7	-0.08	1.01
		7-8	-0.05	1.00
		8-9	-0.02	1.00
		9-10	-0.00	1.02
		7-10	-0.039	1.00

Table A.11: Summary of matching mean and σ corrections(ϕ) to ERT sample (2006) data, for positive (+1) and negative (-1) tracks.

Charge	Matching	p_T	Mean	sigma
-1	emcsd$z$	5-6	0.08	1.36.
		6-7	0.079	1.33
		7-8	0.096	1.32
		8-9	0.067	1.29
		9-10	0.064	1.30
		7-10	0.080	1.31
+1	emcsd$z$	5-6	0.07	1.37
		6-7	0.08	1.34
		7-8	0.08	1.33
		8-9	0.10	1.29
		9-10	0.08	1.30
		7-10	0.08	1.32
+1	pc3sd$z$	5-6	-0.04	0.99
		6-7	-0.05	0.97
		7-8	-0.08	0.97
		8-9	-0.08	0.99
		9-10	-0.06	0.96
		7-10	-0.08	0.98
-1	pc3sd$z$	5-6	-0.05	0.95
		6-7	-0.04	0.96
		7-8	-0.06	0.95
		8-9	-0.02	0.90
		9-10	-0.09	0.91
		7-10	-0.04	-0.94

Table A.12: Summary of matching mean and σ Corrections (z) to ERT sample (2006) data for positive (+1) and negative (-1) tracks. For ERT 2005 sample see A.12

p_T[GeV/c]	-70 to -60	-60 to -50	-50 to -40	-40 to -30	-30 to -20	-20 to -10	-10 to 0.
9-10	-0.2	0.62	2.86	3.16	3.91	4.65	5.44
8-9	-0.42	0.59	2.03	3.63	4.21	5.61	6.30
7-8	0.05	1.2	2.06	3.4	4.01	4.83	5.44
6-7	-0.23	0.72	2.05	3.06	4.13	4.36	4.81
5-6	-0.29	0.16	-0.1	2.54	2.81	4.32	1.70
p_T[GeV/c]	60 to 70	50 to 60	40 to 50	30 to 40	20 to 30	10 to 20	0 to 10.
9-10	0.27	0.93	1.97	3.67	5.33	4.56	4.44
8-9	0.31	0.97	2.01	3.62	4.65	5.05	5.37
7-8	0.05	0.61	2.0	3.72	5.01	5.0	5.37
6-7	0.08	0.88	1.42	3.05	4.04	5.32	4.85
5-6	-0.42	0.23	1.77	1.91	3.41	4.24	3.22

Table A.13: Mean of narrow Gaussian fit of π^+ in 10 cm *zed* increments

p_T[GeV/c]	-70 to -60	-60 to -50	-50 to -40	-40 to -30	-30 to -20	-20 to -10	-10 to 0.
9-10	2.19	2.19	2.61	1.84	2.73	2.954	2.29
8-9	1.85	2.84	4.27	3.04	2.31	3.42	2.58
7-8	2.32	3.47	3.49	3.12	2.50	2.99	2.99
6-7	2.53	2.663	2.95	3.67	3.82	2.56	3.98
5-6	1.77	2.17	2.09	2.63	2.59	3.44	1.7
p_T[GeV/c]	60 to 70	50 to 60	40 to 50	30 to 40	20 to 30	10 to 20	0 to 10.
9-10	1.92	2.49	4.62	3.05	3.18	6.38	2.13
8-9	2.13	3.43	3.6	3.08	3.41	2.57	2.08
7-8	2.92	2.83	3.19	3.88	3.03	2.9	2.52
6-7	2.22	3.08	3.44	4.07	3.46	3.81	3.61
5-6	2.00	1.69	2.88	1.61	3.09	3.99	2.82

Table A.14: σ of narrow Gaussian fit of π^+ in 10 cm *zed* increments. From an inspection of these widths, it already appears that the highest p_T bin (9 GeV/c) shows higher deviations than the other bins. In the final calculation of backgrounds in this data sample, it will be shown that this momentum range is contaminated beyond a physics consideration for a cross section p_T bin candidate (Section 5.15)

p_T[GeV/c]	-70 to -60	-60 to -50	-50 to -40	-40 to -30	-30 to -20	-20 to -10	-10 to 0.
9-10	-0.04	0.67	0.12	1.85	1.37	1.69	1.92
8-9	-0.25	1.1	2.41	2.13	3.01	2.54	3.87
7-8	-0.56	0.66	1.91	3.4	3.08	3.21	3.76
6-7	-0.23	2.71	2.46	3.15	4.37	4.49	5.14
5-6	-0.15	2.34	1.31	3.06	4.41	4.48	4.46
p_T[GeV/c]	60 to 70	50 to 60	40 to 50	30 to 40	20 to 30	10 to 20	0 to 10.
9-10	-0.5	1.89	3.03	2.9	-0.84	14.39	3.68
8-9	-0.61	2.3	4.4	2.87	4.45	4.1	3.61
7-8	0.79	2.11	3.63	3.23	3.76	3.56	4.89
6-7	-1	2.49	5.15	5.96	3.82	4.14	5.62
5-6	-0.11	2.05	3.57	3.08	4.67	4.12	5.09

Table A.15: mean of wide Gaussian fit of π^+ in 10 cm *zed* increments

p_T[GeV/c]	-70 to -60	-60 to -50	-50 to -40	-40 to -30	-30 to -20	-20 to -10	-10 to 0.
9-10	7.39	7.12	10.32	10.52	13.41	13.46	9.24
8-9	7.71	10.53	21.01	11.08	9.51	13.58	11.7
7-8	9.71	13.02	14.69	11.43	10.55	12.32	12.57
6-7	9.87	9.04	10.2	12.69	14.72	11.33	13.33
5-6	5.52	7.01	7.2	9.86	11.89	13.49	11.39
p_T	60 to 70	50 to 60	40 to 50	30 to 40	20 to 30	10 to 20	0 to 10.
9-10GeV/c	6.84	8.72	17.42	11.43	12.61	27.94	12.82
8-9GeV/c	6.33	15.3	13.2	12.35	12.39	12.26	14.58
7-8Gev/c	13.7	9.31	12.13	12.98	12.26	14.45	13.35
6-7GeV/c	9.61	10.9	13.6	17.24	14.93	13.88	16.42
5-6GeV/c	6.29	5.99	10.15	8.33	10.95	12.31	12.51

Table A.16: σ of wide Gaussian fit of π^+ in 10 cm *zed* increments

p_T[GeV/c]	-70 to -60	-60 to -50	-50 to -40	-40 to -30	-30 to -20	-20 to -10	-10 to 0.
9-10	0.51	-3.22	-4.32	-4.33	-5.51	-5.67	-6.69
8-9	-0.20	-2.71	-5.3	-5.59	-6.25	-12.63	-6.44
7-8	-0.96	-4.11	-2.92	-6.16	-4.98	-7.01	-7.44
6-7	-1.24	-3.54	-5.67	-6.31	-2.63	-7.13	-7.51
5-6	-1.36	-2.5	-4.9	-7.28	-9.01	-5.60	-9.94
p_T	60 to 70	50 to 60	40 to 50	30 to 40	20 to 30	10 to 20	0 to 10.
9-10GeV/c	0.19	-2.63	-3.60	-5.12	-5.69	-4.84	-3.93
8-9GeV/c	0.56	-2.17	-3.65	-4.1	-4.3	-5.21	-5.16
7-8Gev/c	-1.32	-2.38	-4.66	-5.13	-5.91	-6.48	-7.27
6-7GeV/c	-0.12	-3.38	-4.68	-6.27	-6.12	-10.15	-7.45
5-6GeV/c	-1.41	-3.58	-4.68	-7.33	-7.10	-8.54	-8.48

Table A.17: mean of narrow Gaussian fit of π^- in 10 cm *zed* increments

p_T[GeV/c]	-70 to -60	-60 to -50	-50 to -40	-40 to -30	-30 to -20	-20 to -10	-10 to 0.
9-10	3.8	3.76	4.2	0.95	2.02	2.41	2.94
8-9	3.04	3.69	3.68	3.63	2.42	2.58	3.37
7-8	2.38	3.94	1.24	3.35	2.27	2.21	3.13
6-7	3.27	4.4	4.34	3.87	2.5	5.34	4.4
5-6G	2.86	3.01	4.06	4.53	6.11	3.82	5.67
p_T[GeV/c]	60 to 70	50 to 60	40 to 50	30 to 40	20 to 30	10 to 20	0 to 10.
9-10	2.43	3.08	3.03	2.97	1.87	1.43	1.1
8-9	4.01	3.63	3.59	1.00	2.18	2.93	2.11
7-8	2.63	5.16	3.67	1.95	3.15	3.81	2.03
6-7	3.58	3.83	2.54	3.05	3.82	2.24	3.14
5-6	3.20	4.32	3.35	5.84	3.50	1.20	2.37

Table A.18: σ of narrow Gaussian fit of π^- in 10 cm *zed* increments

p_T[GeV/c]	-70 to -60	-60 to -50	-50 to -40	-40 to -30	-30 to -20	-20 to -10	-10 to 0.
9-10	2.19	2.61	-6.56	-7.66	-10.06	-10.99	-10.99.
8-9G	2.02	18.83	-2.74	-15.42	-10.78	-5.78	-0.32
7-8	0.39	3.33	-6.62	-14.79	-8.31	-10.29	-10.59
6-7	0.97	-0.02	-17.58	-10.55	-9.52	-18.27	-14.23
5-6	-1.69	-5.16	-7.94	-14.98	-26.1	-10.42	-5.53
p_T	60 to 70	50 to 60	40 to 50	30 to 40	20 to 30	10 to 20	0 to 10.
9-10GeV/c	1.67	3.33	-3.22	-11.24	-7.1	-7.45	-7.86
8-9GeV/c	5.32	-1.32	-7.71	-6.42	-8.26	-7.91	-8.65
7-8Gev/c	0.84	6.91	-6.05	-8.76	-9.08	-10.48	-11.41
6-7GeV/c	1.83	-1.48	-6.41	-11.43	-11.09	-8.16	-11.52
5-6GeV/c	2.374	0.94	-7.21	-8.81	-10.01	-10.56	-10.46

Table A.19: Mean of wide Gaussian fit of π^- in 10 cm *zed* increments

p_T[GeV/c]	-70 to -60	-60 to -50	-50 to -40	-40 to -30	-30 to -20	-20 to -10	-10 to 0.
9-10	16.15	15.39	25.56	5.55	5.71	8.77	11.94
8-9	9.08	36.62	11.43	10.85	8.27	3.25	24.15
7-8	6.82	16.54	4.52	11.92	5.71	5.97	8.73
6-7	9.74	21.24	24.19	9.58	4.86	7.6	8.34
5-6	9.16	6.65	9.89	12.07	6.78	6.53	12.92
p_T[GeV/c]	60 to 70	50 to 60	40 to 50	30 to 40	20 to 30	10 to 20	0 to 10.
9-10	9.15	13.42	17.59	12.48	4.94	4.37	11.73
8-9	18.3	17.63	4.55	4.86	5.09	5.04	7.22
7-8	8.22	15.92	17.7	6.42	6.86	7.64	6.53
6-7	8.11	11.65	6.26	8.98	7.29	6.01	14.97
5-6	9.65	18.08	8.49	10.14	7.63	6.85	7.63

Table A.20: σ of wide Gaussian fit of π^- in 10 cm *zed* increments

	p_T[GeV/c]	<70cm	<65cm	<60cm	<55cm	<50cm	<45cm	<40cm	<35cm.
e^+	0-10	0.72	0.65	0.54	0.47	0.44	0.37	0.32	0.26
	p_T[GeV/c]	<70cm	<65cm	<60cm	<55cm	<50cm	<45cm	<40cm	<35cm.
e^-	0-10	0.72	0.83	0.70	0.6	0.55	0.47	0.35	0.29

Table A.21: Efficiency of *zed* extracted from simulated $\gamma \longrightarrow e^{\pm}$

	p_T[GeV/c]	<70	<65	<60	<55	<50	<45	<40	<35.
$e^-_{Primary}$	5-6	0.9	0.84	0.78	0.72	0.66	0.6	0.55	0.48
	6-7	0.89	0.82	0.76	0.68	0.61	0.55	0.5	0.44
	7-8	0.89	0.81	0.76	0.71	0.63	0.57	0.5	0.44
	8-9	0.89	0.83	0.77	0.71	0.65	0.59	0.53	0.47
	9-10	0.88	0.81	0.76	0.69	0.63	0.57	0.51	0.44
	p_T[GeV/c]	<70	<65	<60	<55	<50	<45	<40	<35.
$e^+_{Background}$	0-10	0.76	0.68	0.61	0.54	0.46	0.41	0.36	0.32
	p_T[GeV/c]	<70	<65	<60	<55	<50	<45	<40	<35.
$e^+_{Primary}$	5-6	0.9	0.82	0.76	0.71	0.64	0.57	0.52	0.46
	6-7	0.88	0.83	0.77	0.72	0.66	0.59	0.52	0.45
	7-8	0.88	0.83	0.76	0.71	0.65	0.58	0.51	0.43
	8-9	0.89	0.83	0.76	0.7	0.64	0.57	0.51	0.44
	9-10	0.88	0.82	0.76	0.68	0.62	0.57	0.5	0.43
	p_T[GeV/c]	<70	<65	<60	<55	<50	<45	<40	<35.
$e^-_{Background}$	0-10	0.73	0.64	0.56	0.49	0.43	0.38	0.34	0.29

Table A.22: Efficiency of *zed* extracted from simulated primary $e^{\pm}$

Appendix B

Fiducial Cuts and Drift Chamber Dead Map studies

Complete studies of the fiducial cuts on the DC acceptance as mentioned in Section 5.2.1 can be found in this appendix. The following figures show DC's gaps which are insensitive to particle detection due to dead areas and/or channels. The plots found here are separated by charge and by PHENIX tracking arm (Figure **??**. These compare both data and simulation for accurate description of the gaps. As a refresher of the fidual cuts functional form, where *BBCVtx* is collision vertex which is located at the (0,0) (Figure **??**) in a two-dimensional coordinate system. Refer to 4.3:

- $(cos(\theta) > -0.002 * BBCVtx + 0.016)$

- $(cos(\theta) < -0.0019 * BBCVtx - 0.007)$
- $(cos(\theta) > -0.0046 * BBCVtx + 0.016)$
- $(cos(\theta) < -0.00467 * BBCVtx - 0.014)$
- $|(cos(\theta))| < 0.4$
- $(cos(\theta) < -0.0044 * BBCVtx + 0.302)$
- $(cos(\theta) > -0.0042 * BBCVtx - 0.302)$

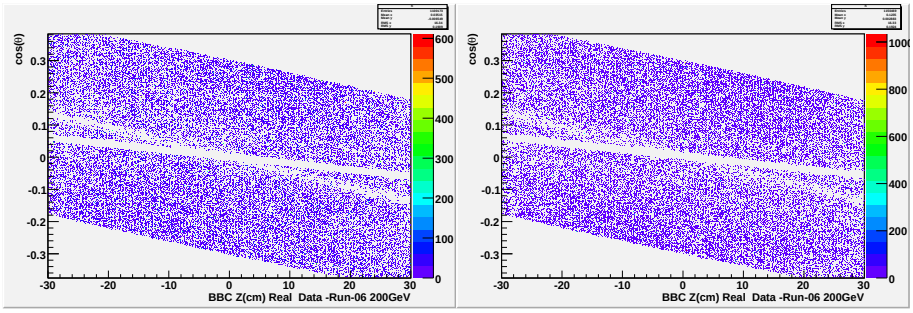

Figure B.1: Real fiducial gaps found in the DC and RICH's West(Left) and East(right)Arms, Momentum range is as described in Section 5.2.1

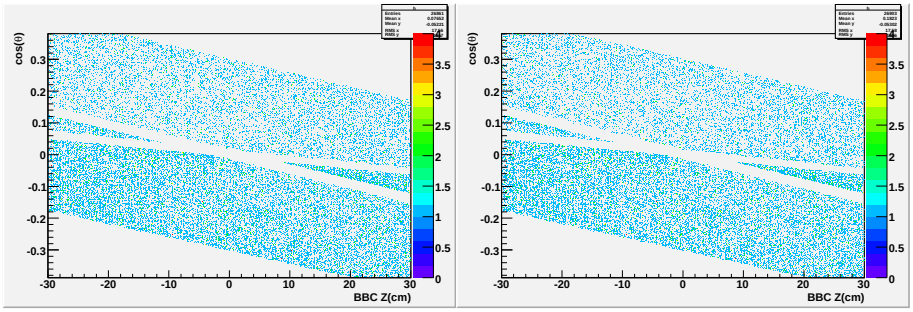

Figure B.2: Fiducial distributions DC and RICH gaps in SIMULATION West (Left) and East (right) Arms

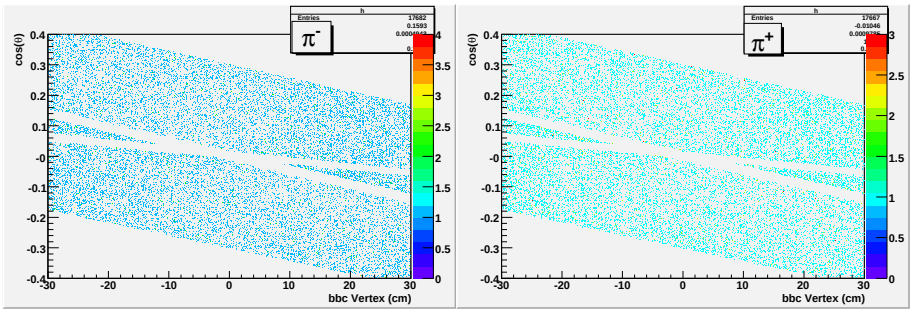

Figure B.3: Simulated drift chamber Distributions by charge, Only West Arm is shown

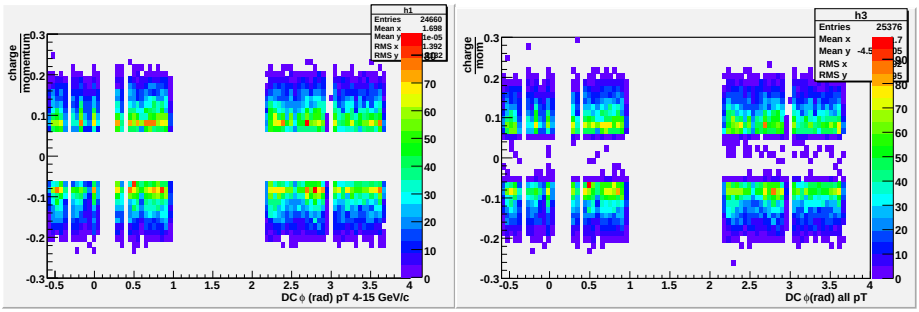

Figure B.4: Geometrical acceptance of Pions after accounting dead maps and Fiducial corrections. Left figure is simulated data from 4GeV/c $< \mathrm{p}_T <$ 15GeV/c. The figure on the right is the whole reconstructed p_T spectrum

Appendix C

Un-reconstructed Tracks

The figures found in this appendix illustrate the number of charged tracks that typically fail to create a match hit between two or more detectors (DC and PC for example, or DC, PC and EMCal). Summary of these figures can be found in Table 5.1 which show the number of charged tracks that failed reconstruction.

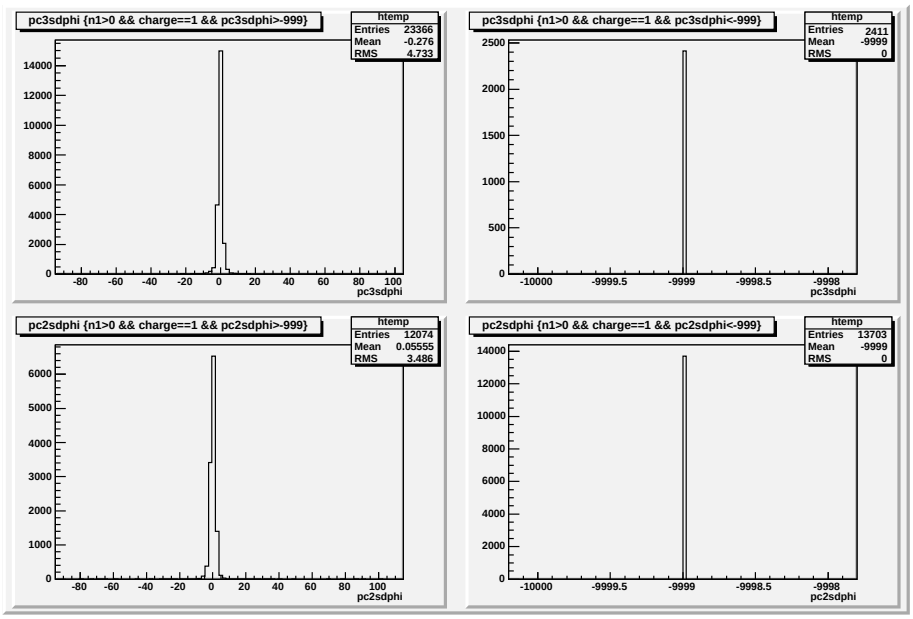

Figure C.1: Match in the ϕ coordinate of the PC3 (top) and PC2 (bottom) to the DC track. The right histograms represent tracks that failed reconstruction recognition in the PC2 and PC3 detectors

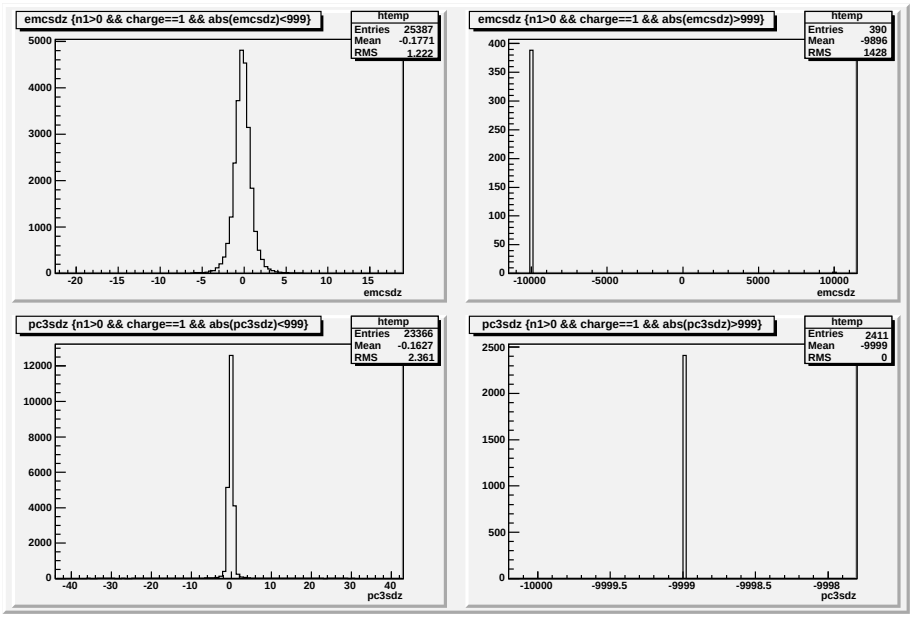

Figure C.2: Match in the z coordinate of the EMCal (top) and PC3 (bottom) to the DC track. The right histograms represent tracks that failed reconstruction recognition in the EMCal and PC3 detectors

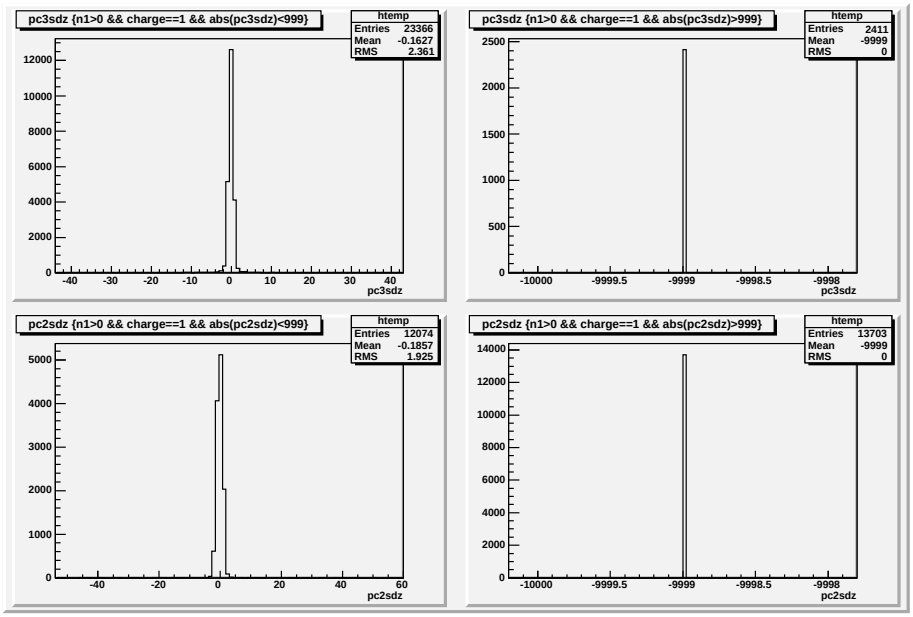

Figure C.3: Match in the z coordinate of the PC3 (top) and PC2 (bottom) to the DC track. The right histograms represent tracks that failed reconstruction recognition in the PC3 and PC2 detectors

Appendix D

Detector Acceptance Corrections of $\pi^{\pm}$

The figures found in this appendix, show the PHENIX detector acceptance to charge pions as outlined in 5.2.3 and 5.2. The geometrical acceptance trends are organized in 1 GeV/c p_T bins and by pion charge. Details of the input momentum spectra can be found in Section 5.2.1.

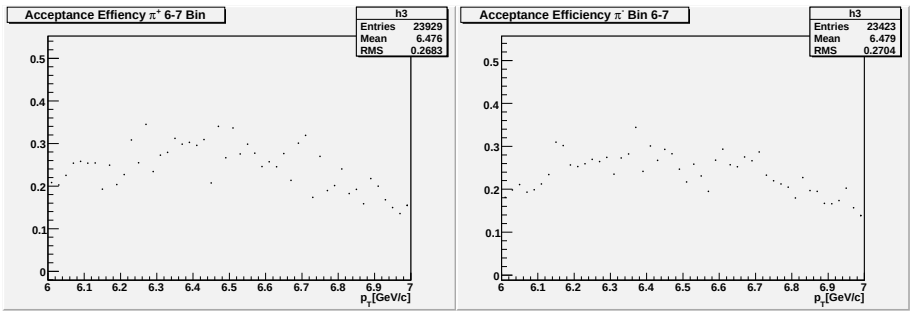

Figure D.1: Detector acceptance within a p_T window of 6 GeV/c $< p_T <$ 7 GeV/c. π^+ left and π^- right

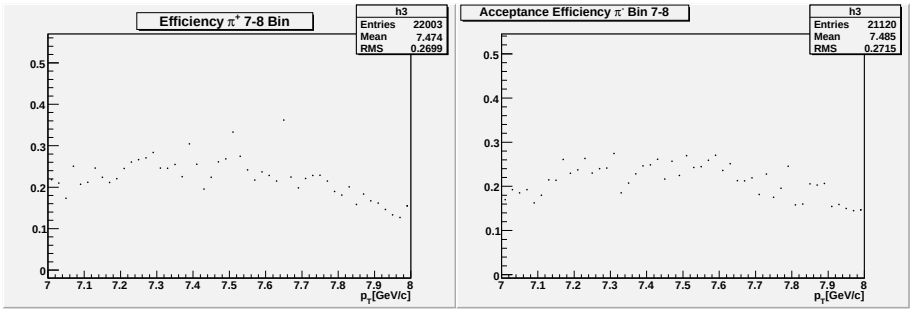

Figure D.2: Detector acceptance within a p_T window of 7 GeV/c $< p_T <$ 8 GeV/c. π^+ left and π^- right

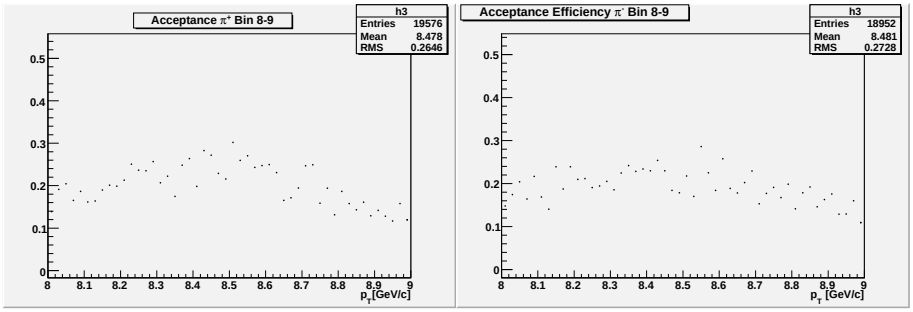

Figure D.3: Detector acceptance within a p_T window of 8 GeV/c $< p_T <$ 9 GeV/c. π^+ left and π^- right

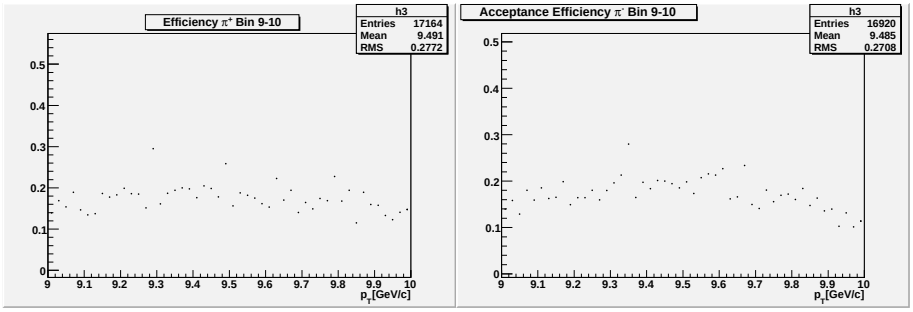

Figure D.4: Detector acceptance within a p_T window of 9 GeV/c $< p_T <$ 10 GeV/c. π^+ left and π^- right

Appendix E

Matching Distributions of ERT

Triggered Data Set

The plots which are found in this section are the fits of the matching distributions as outlined in section 5.4. The data inspected, fitted and corrected consists of ERT Triggered data collected with the PHENIX detector, from RHIC years 2005 (Section E.0.2) and 2006 (Section E.0.3) proton proton collisions.

E.0.2 2006 dataset

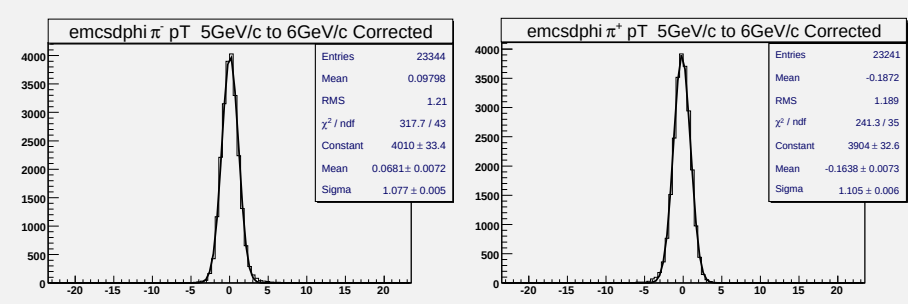

Figure E.1: Emcsdphi π^- (left) and π^+ (right) at 5 GeV/c $< p_T <$ 6GeV/c Bin

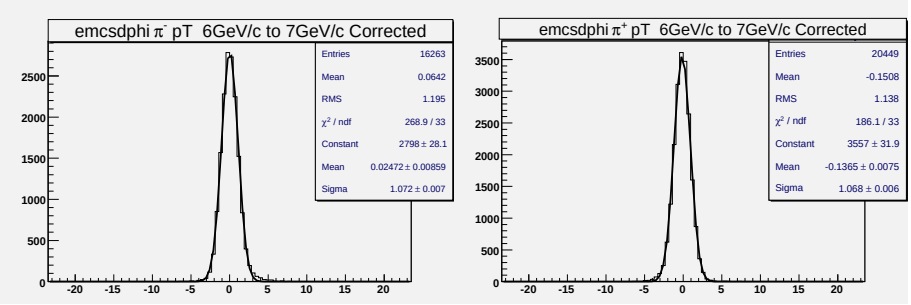

Figure E.2: Emcsdphi π^- (left) and π^+ (right) at 6 GeV/c $< p_T <$ 7 GeV/c Bin

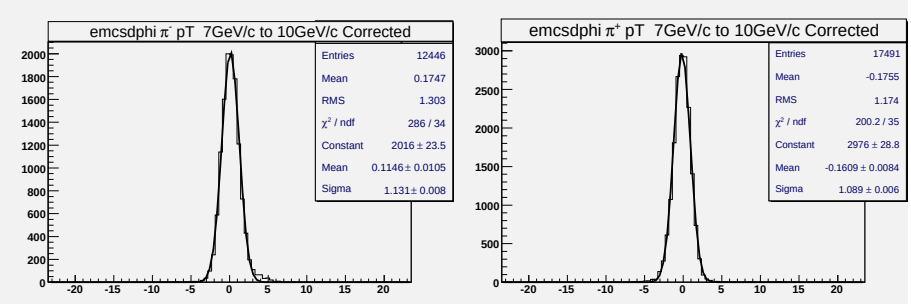

Figure E.3: Emcsdphi π^- (left) and π^+ (right) at 7 GeV/c $< p_T <$ 10 GeV/c Bin

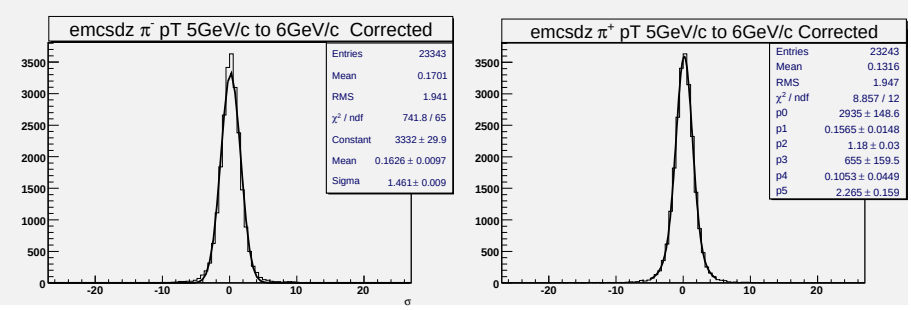

Figure E.4: Emcsdz π^- (left) and π^+ (right) at 5 GeV/c $< p_T <$ 6 GeV/c Bin

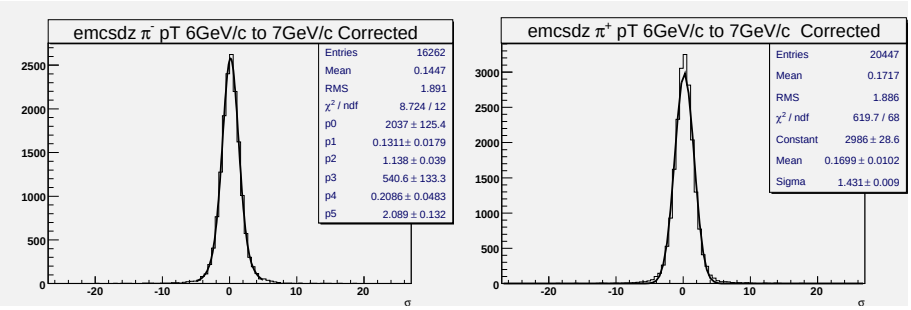

Figure E.5: Emcsdz π^- (left) and π^+ (right) at 6 GeV/c $< p_T <$ 7 GeV/c Bin

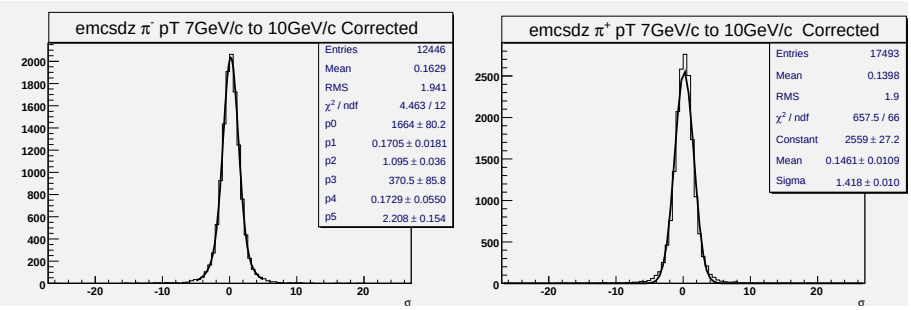

Figure E.6: Emcsdz π^- (left) and π^+ (right) at 7 GeV/c $< p_T <$ 10 GeV/c Bin

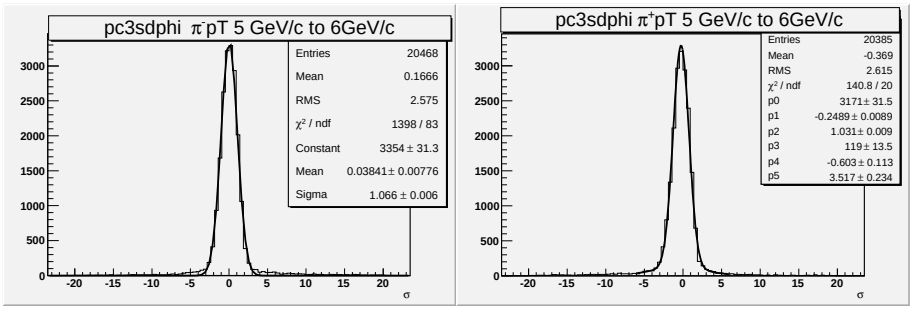

Figure E.7: pc3sdph π^- (left) and π^+ (right) at 5 GeV/c $< p_T <$ 6 GeV/c Bin

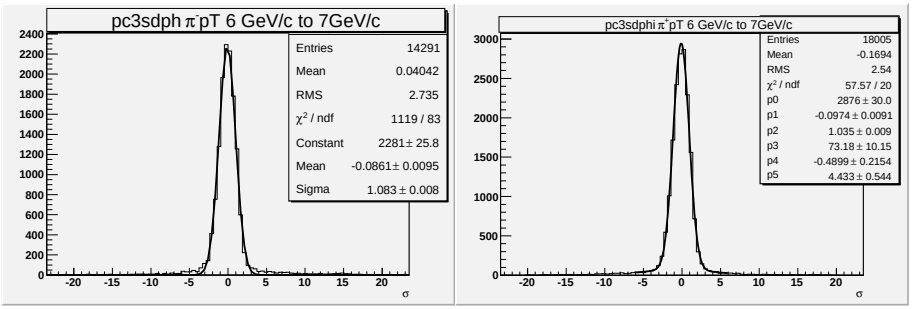

Figure E.8: pc3sdphi π^- (left) and π^+ (right) at 6 GeV/c $< p_T <$ 7 GeV/c Bin

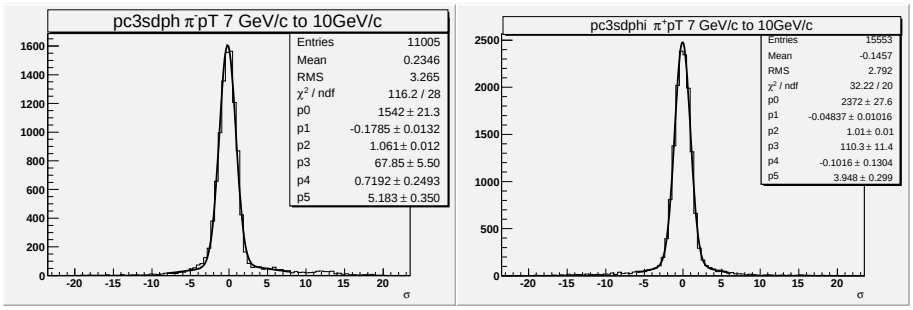

Figure E.9: pc3sdphi π^- (left) and π^+ (right) at 7 GeV/c $< p_T <$ 10 GeV/c Bin

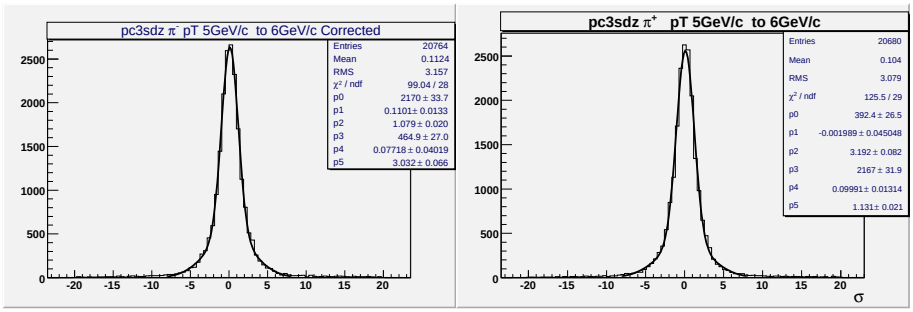

Figure E.10: pc3sdz π^- (left) and π^+ (right) at 5 GeV/c $< p_T <$ 6 GeV/c Bin

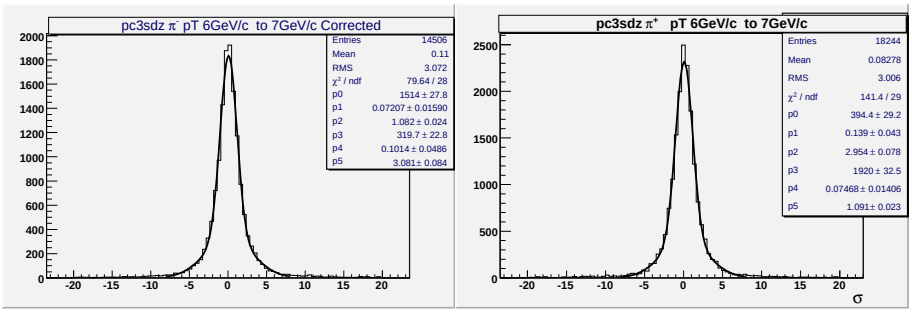

Figure E.11: pc3sdz π^- (left) and π^+ (right) at 6 GeV/c $< p_T <$ 7 GeV/c Bin

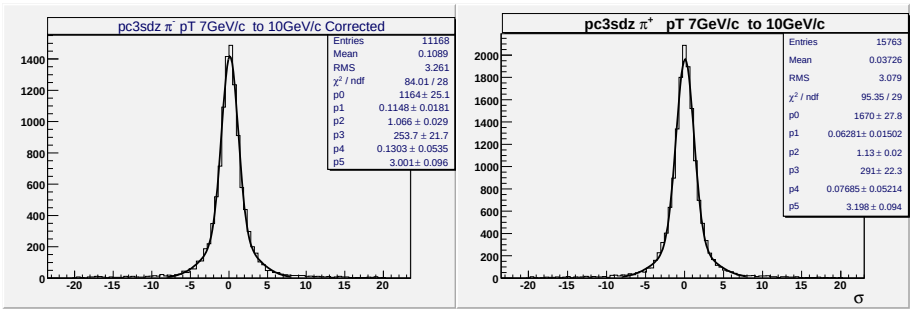

Figure E.12: pc3sdz π^- (left) and π^+ (right) at 7 GeV/c $< p_T <$ 10 GeV/c Bin

Charge π^+	p_T[GeV/c]	mean	σ π^-	p_T	mean	σ
pc3sdϕ						
	5-6	2.5	6.2	5-6	-2.6	6.5
	6-7	1.2	6.3	6-7	-2.6	6.3
	7-10	1.4	5.0	7-10	-1.8	5.2
pc3sdz						
	5-6	0.4	4.8	5-6	0.2	1.9
	6-7	0.4	4.6	6-7	0.2	4.3
	7-10	0.4	4.9	7-10	0.3	4.6
emcsdϕ						
	5-6	0.0	1.0	5-6	-0.2	1.1
	6-7	0.0	1.0	6-7	-0.2	1.0
	7-10	0.0	1.0	7-10	-0.2	1.1
emcsdz						
	5-6	0.2	1.2	5-6	0.2	1.2
	6-7	0.2	1.2	6-7	0.1	1.2
	7-10	0.2	1.2	7-10	0.1	1.2

Table E.1: Corrections to mean and σ to 2005 charged pions data

E.0.3 2005 Dataset

2005 data set was also calibrated, and a table with the Gaussian and mean values found by p_T bin and charge is given.

Appendix F

Matching Distributions of Minimum Bias Data Set

Matching distributions from data colected in the year 2006 with the minimum biased trigger were inspected in several formats as described in Section 5.4. The figures to follow illustrate the fits performed on the distributions. The organization of the distributions and their corresponding fits are done by charge, transverse momentum bin (1 GeV/c Intervals), type of detector and coordinate matched (ϕ and z).

F.0.4 Distributions in emcsdϕ

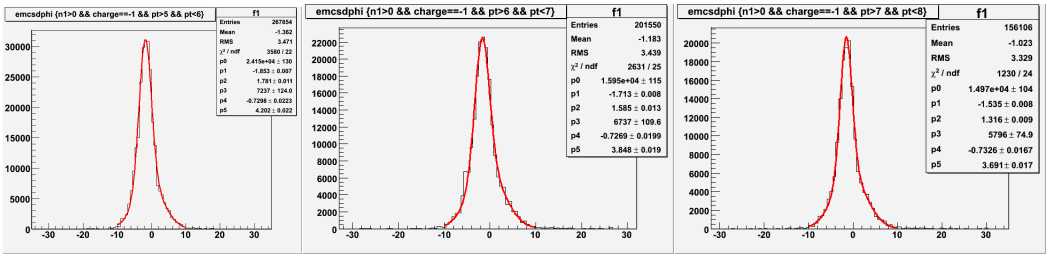

Figure F.1: Residual distributions in emcsdϕ of negatively charged tracks. These are fitted with double Gaussians. p_T intervals (in GeV/c) from left to right are $5< p_T <6$, $6< p_T <7$ and $7< p_T <8$

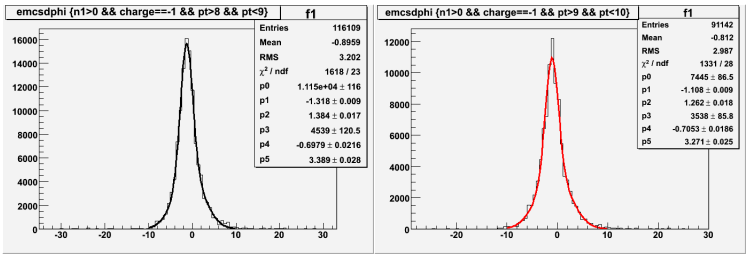

Figure F.2: Residual distributions in emcsdϕ of negatively charged tracks. These are fitted with double Gaussians. p_T intervals (in GeV/c) from left to right are 8< p_T <9 and 9< p_T <10

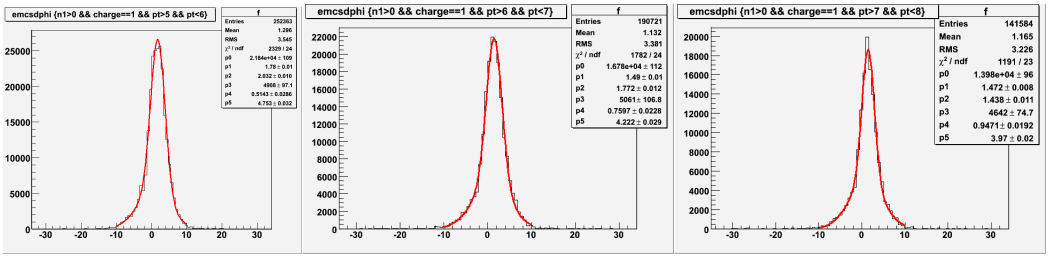

Figure F.3: Residual distributions in emcsdϕ of positively charged tracks. These are fitted with double Gaussians. p_T intervals (in GeV/c) from left to right are 5< p_T <6, 6< p_T <7 and 7< p_T <8

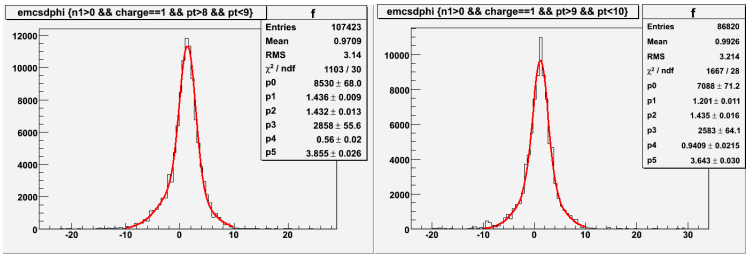

Figure F.4: Residual distributions in emcsdϕ of positively charged tracks. These are fitted with double Gaussians. p_T intervals (in GeV/c) from left to right are 8< p_T <9 and 9< p_T <10

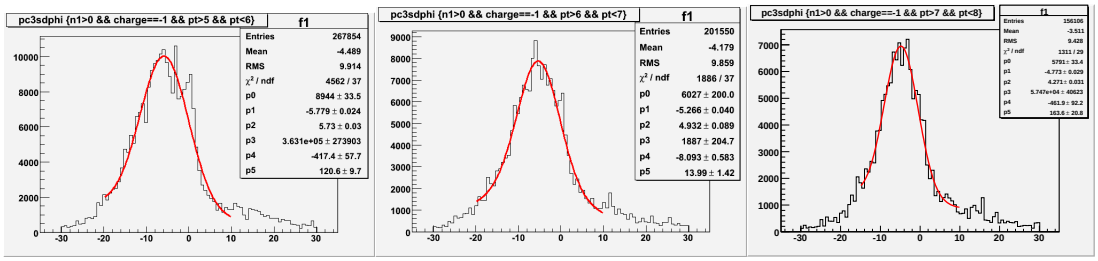

Figure F.5: Residual distributions in pc3sdϕ of negatively charged tracks. These are fitted with double Gaussians. p_T intervals (in GeV/c) from left to right are 5< p_T <6, 6< p_T <7 and 7< p_T <8

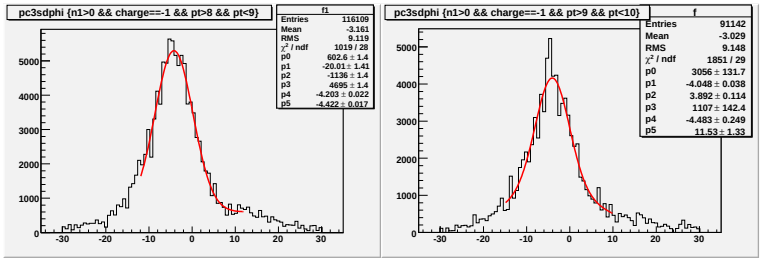

Figure F.6: Residual distributions in pc3sdϕ of negatively charged tracks.These are fitted with double Gaussians. p_T intervals (in GeV/c) from left to right are 8$<$ p_T $<$9 and 9$<$ p_T $<$10

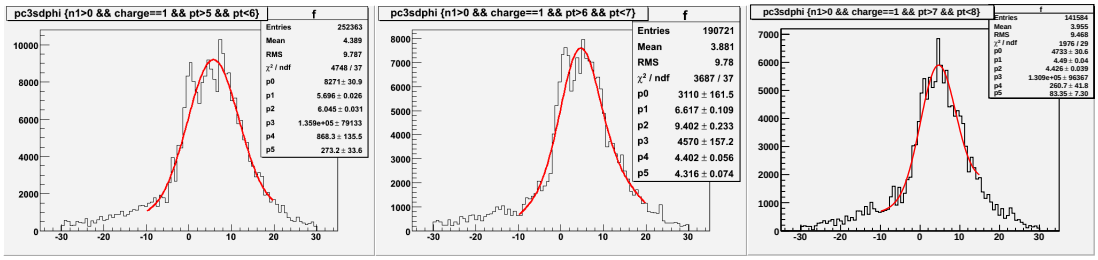

Figure F.7: Residual distributions in pc3sdϕ of positively charged tracks. These are fitted with double Gaussians. p_T intervals (in GeV/c) from left to right are 5$<$ p_T $<$6, 6$<$ p_T $<$7 and 7$<$ p_T $<$8

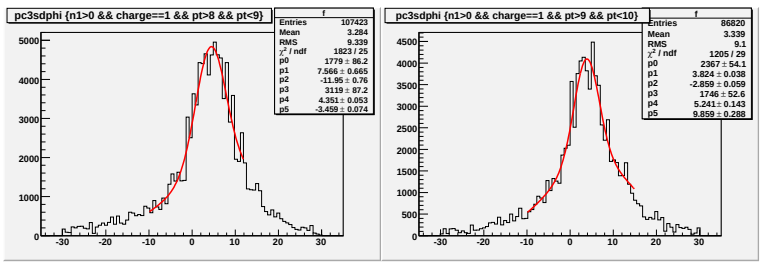

Figure F.8: Residual distributions in pc3sdϕ of positively charged tracks.These are fitted with double Gaussians. p_T intervals (in GeV/c) from left to right are 8$<$ p_T $<$9 and 9$<$ p_T $<$10

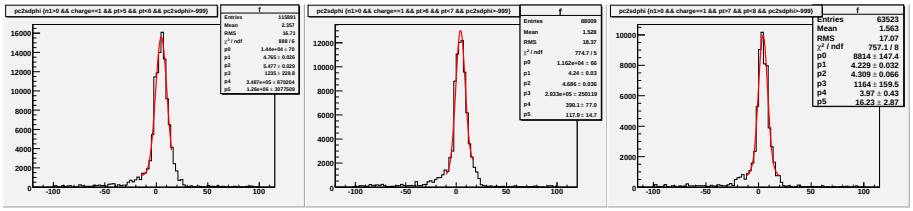

Figure F.9: Residual distributions in pc2sdϕ of positively charged tracks. These are fitted with double Gaussians. p_T intervals (in GeV/c) from left to right are 5$< p_T <$6, 6$< p_T <$7 and 7$< p_T <$8

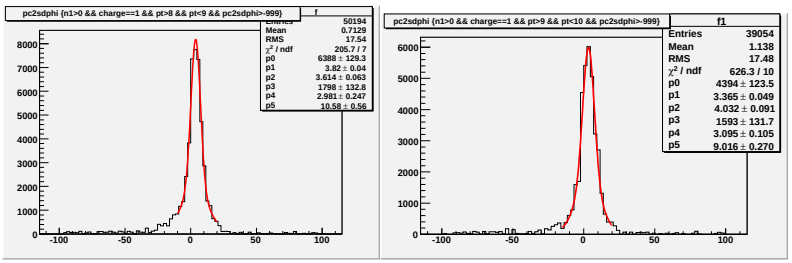

Figure F.10: Residual distributions in pc2sdϕ of positively charged tracks.These are fitted with double Gaussians. p_T intervals (in GeV/c) from left to right are 8$< p_T <$9 and 9$< p_T <$10

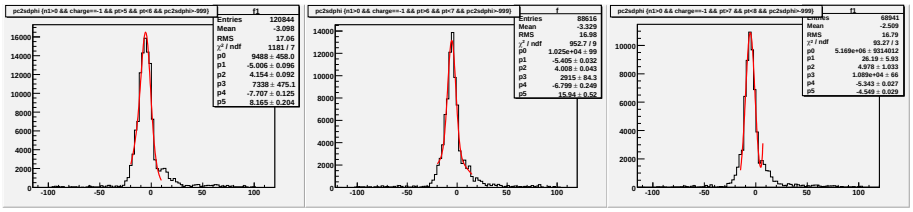

Figure F.11: Residual distributions in pc2sdϕ of negatively charged tracks.These are fitted with double Gaussians. p_T intervals (in GeV/c) from left to right are 5$< p_T <$6, 6$< p_T <$7 and 7$< p_T <$8

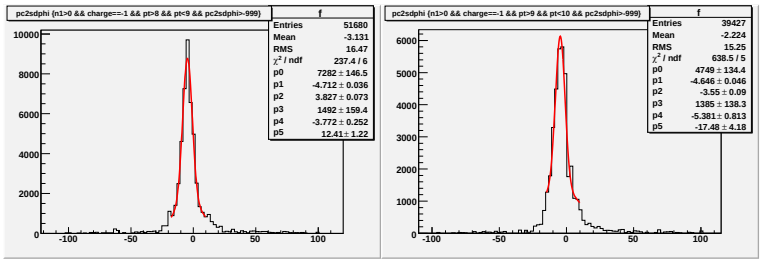

Figure F.12: Residual distributions in pc2sdϕ of negatively charged tracks.These are fitted with double Gaussians. p_T intervals (in GeV/c) from left to right are 8$< p_T <$9 and 9$< p_T <$10

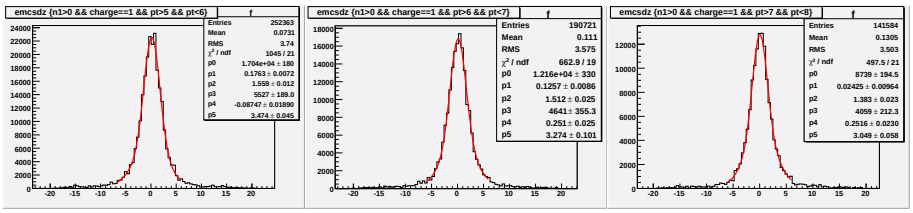

Figure F.13: Residual distributions in emcsdz of positively charged tracks.These are fitted with double Gaussians. p_T intervals (in GeV/c) from left to right are 5$< p_T <$6, 6$< p_T <$7 and 7$< p_T <$8

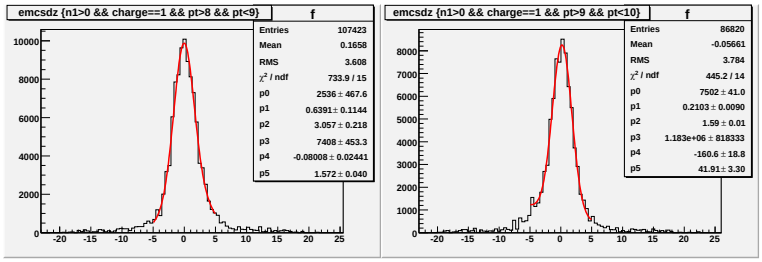

Figure F.14: Residual distributions in emcsdz of positively charged tracks.These are fitted with double Gaussians. p_T intervals (in GeV/c) from left to right are 8$< p_T <$9 and 9$< p_T <$10

F.0.5 Distributions in emcsdz

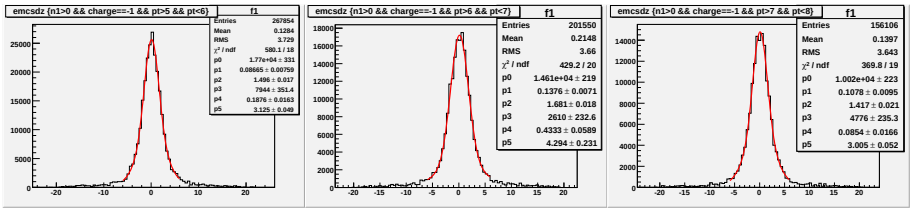

Figure F.15: Negative charge tracks I, emcsdz
Residual distributions in emcsdz of negatively charged tracks.These are fitted with double Gaussians. p_T intervals (in GeV/c) from left to right are 5$< p_T <$6, 6$< p_T <$7 and 7$< p_T <$8

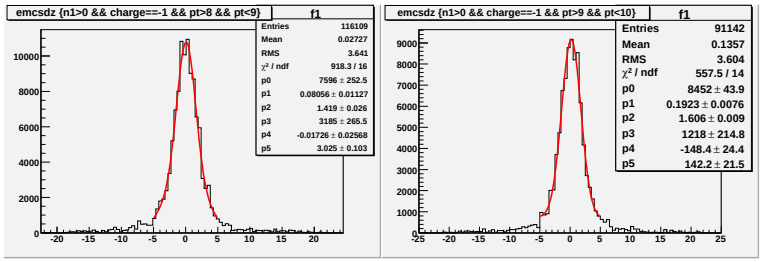

Figure F.16: Negativecharge tracks II, emcsdz
Residual distributions in emcsdz of negatively charged tracks.These are fitted with double Gaussians. p_T intervals (in GeV/c) from left to right are 8$< p_T <$9 and 9$< p_T <$10

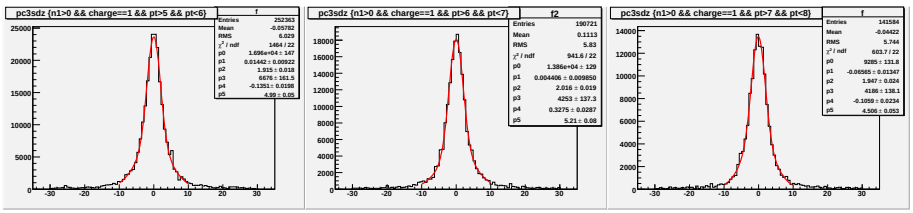

Figure F.17: Positive charge tracks I, pc3sdz
Residual distributions in pc3sdz of positively charged tracks.These are fitted with double Gaussians. p_T intervals (in GeV/c) from left to right are 5$< p_T <$6, 6$< p_T <$7 and 7$< p_T <$8

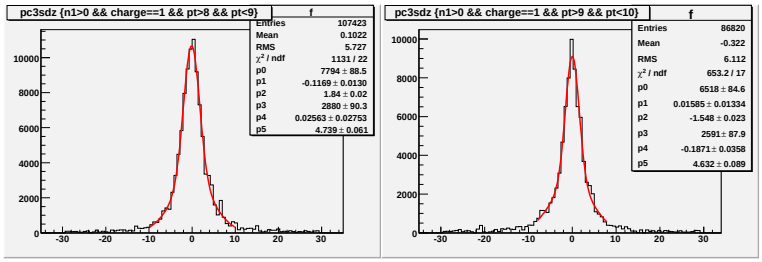

Figure F.18: Positive charge tracks II, pc3sdz
Residual distributions in pc3sdz of positively charged tracks.These are fitted with double Gaussians. p_T intervals (in GeV/c) from left to right are 8$< p_T <$9 and 9$< p_T <$10

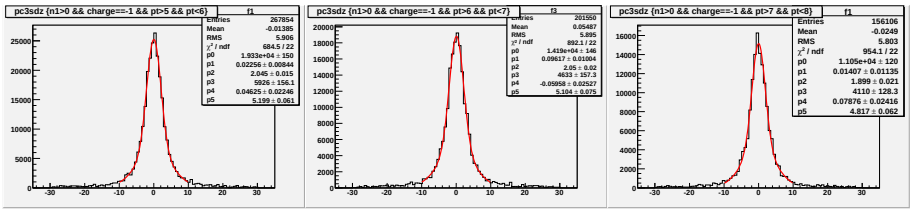

Figure F.19: Negative charge tracks I, pc3sdz
Residual distributions in pc3sdz of negatively charged tracks.These are fitted with double Gaussians. p_T intervals (in GeV/c) from left to right are 5$< p_T <$6, 6$< p_T <$7 and 7$< p_T <$8

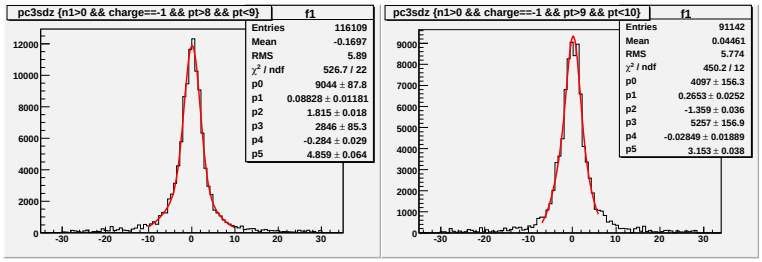

Figure F.20: Negative charge tracks II, pc3sdz
Residual distributions in pc3sdz of negatively charged tracks. These are fitted with double Gaussians. p_T intervals (in GeV/c) from left to right are 8$< p_T <$9 and 9$< p_T <$10

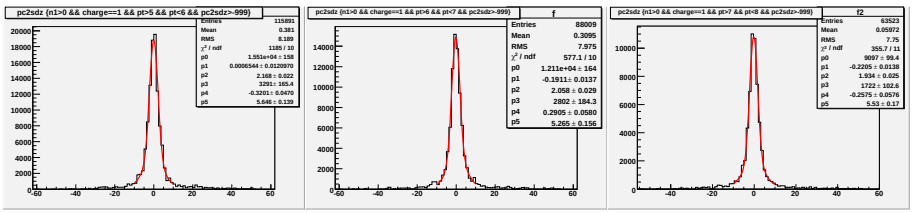

Figure F.21: Positive charge tracks I, pc2sdz
Residual distributions in pc2sdz of positively charged tracks.These are fitted with double Gaussians. p_T intervals (in GeV/c) from left to right are 5$< p_T <$6, 6$< p_T <$7 and 7$< p_T <$8

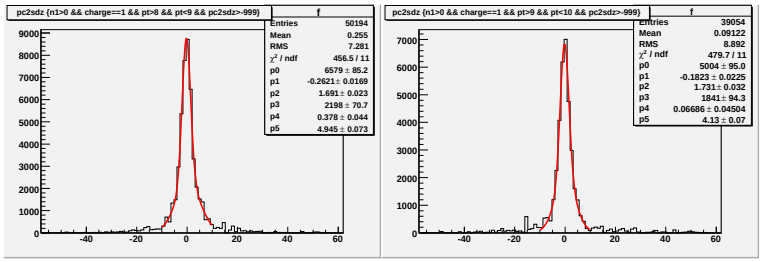

Figure F.22: Positive charge tracks II, pc2sdz
Residual distributions in pc2sdz of positively charged tracks.These are fitted with double Gaussians. p_T intervals (in GeV/c) from left to right are 8$< p_T <$9 and 9$< p_T <$10

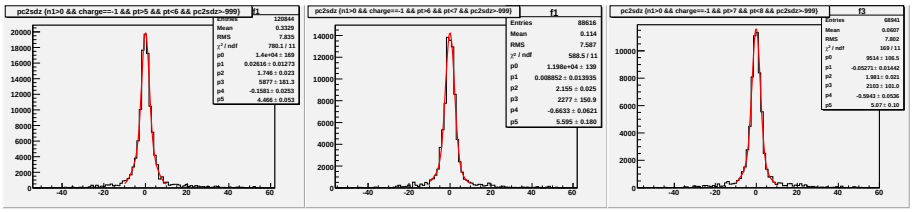

Figure F.23: Negative charge tracks I, pc2sdz
Residual distributions in pc2sdz of negatively charged tracks.These are fitted with double Gaussians. p_T intervals (in GeV/c) from left to right are 5$< p_T <$6, 6$< p_T <$7 and 7$< p_T <$8

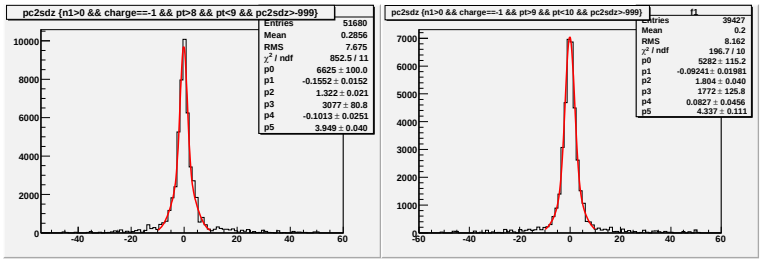

Figure F.24: Negative charge tracks II, pc2sdz
Residual distributions in pc2sdz of negatively charged tracks. These are fitted with double Gaussians. p_T intervals (in GeV/c) from left to right are 8< p_T <9 and 9< p_T <10

Appendix G

Zed and Matching Distribution Studies

To try to understand the background in the minimum bias sample used for the differential cross section measuremt, several bins of zed were inspected. The context of these studies as well as summary tables, were discussed in Section **??**. In this appendix, results of the inspections and fits to the matching distributions in full *zed* and 10 cm *zed* intervals, are presented in this appendix.

G.0.6 Zed versus pc3sdϕ distributions

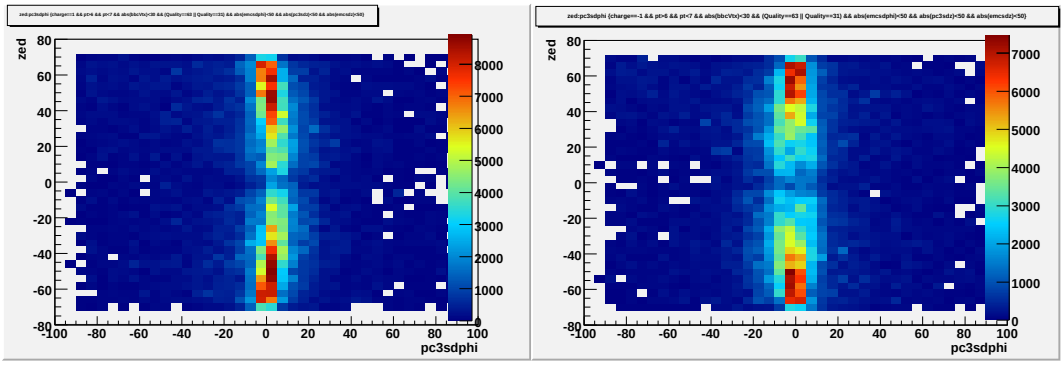

Figure G.1: Zed versus pc3s$d\phi$. Left figure are positive tracks, while right figure corresponds to negative tracks. p_T range is 6GeV/c $< p_T <$ 7 GeV/c

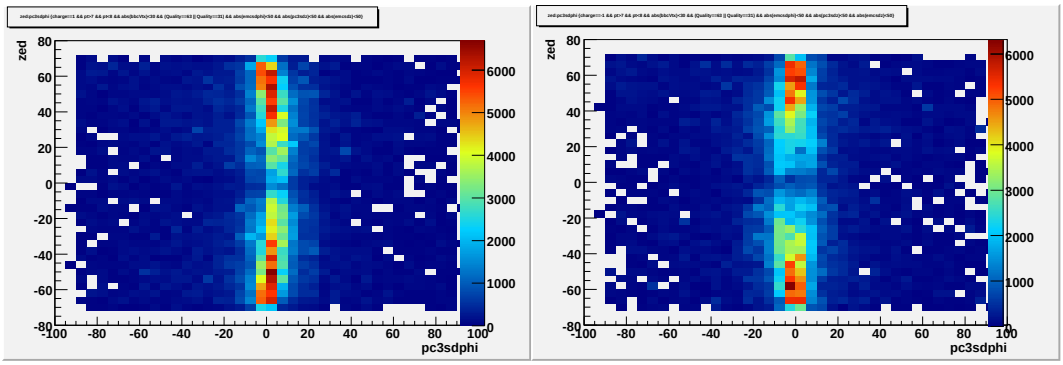

Figure G.2: Zed versus pc3s$d\phi$. Left figure are positive tracks, while right figure corresponds to negative tracks. p_T range is 7GeV/c $< p_T <$ 8 GeV/c

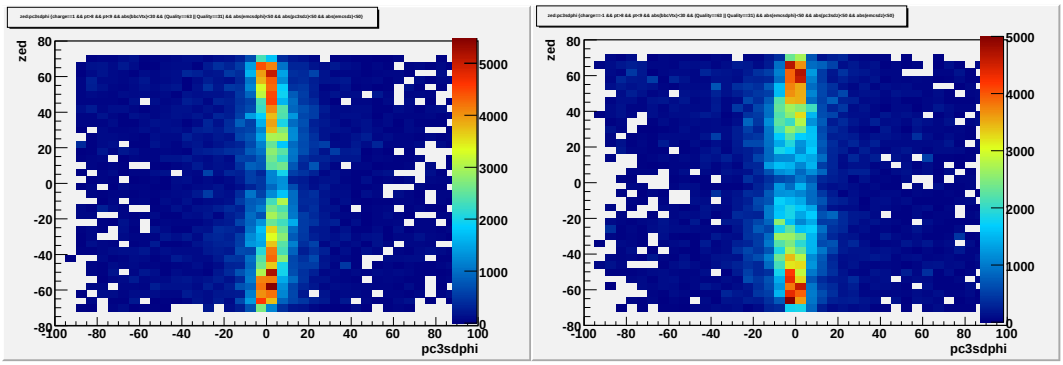

Figure G.3: Zed versus pc3s$d\phi$. Left figure are positive tracks, while right figure corresponds to negative tracks. p_T range is 8GeV/c $< p_T <$ 9 GeV/c

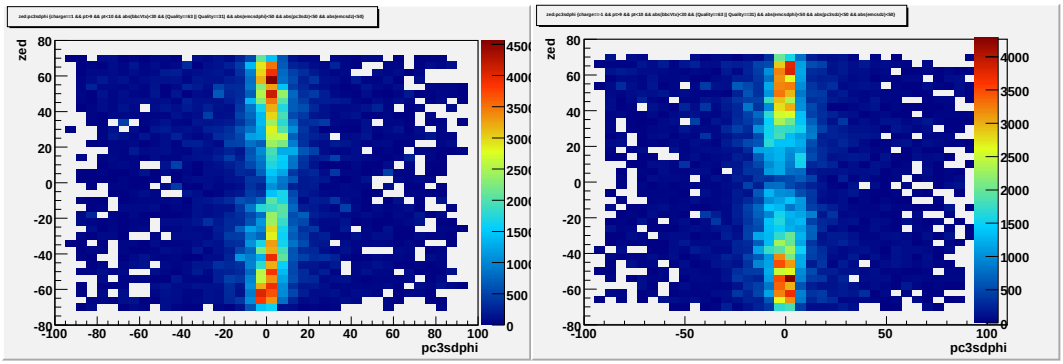

Figure G.4: Zed versus pc3s$d\phi$. Left figure are positive tracks, while right figure corresponds to negative tracks. p_T range is 9GeV/c $< p_T <$ 10 GeV/c

G.0.7 Distributions in pc3sdz

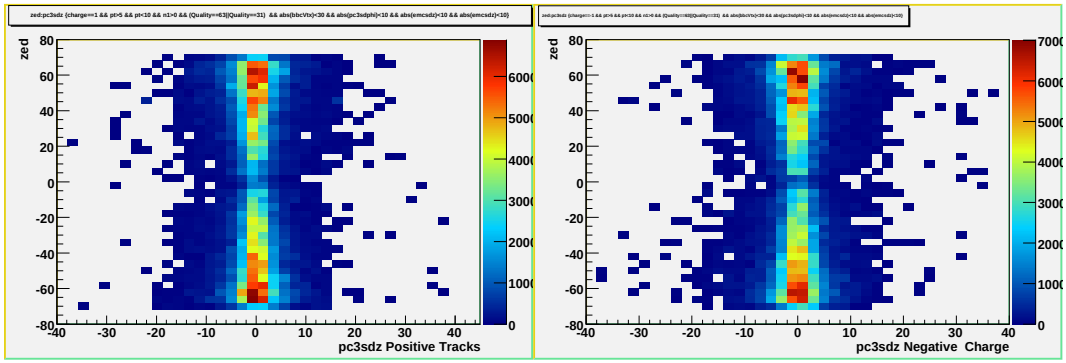

Figure G.5: pc3sdz versus *zed*, p_T is 5-10 GeV/c. Left panel are positive tracks, while right panel are negative tracks

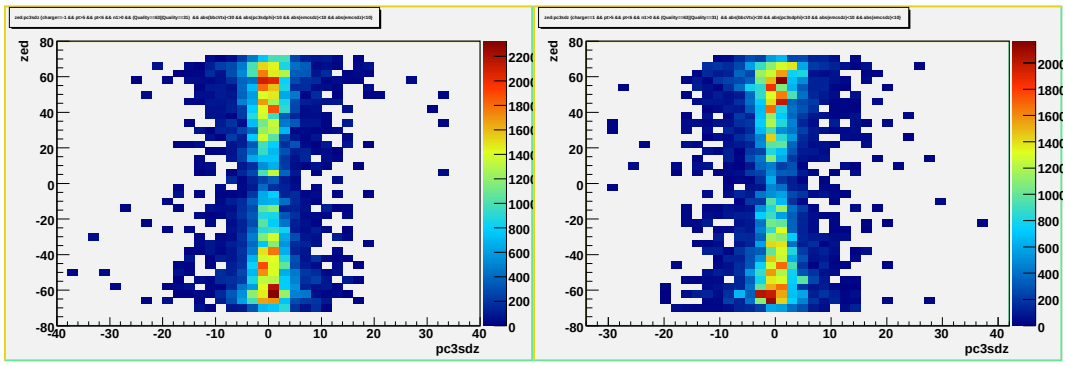

Figure G.6: pc3sdz versus *zed*, p_T is 5-6 GeV/c. Left panel are positive tracks, while right panel are negative tracks

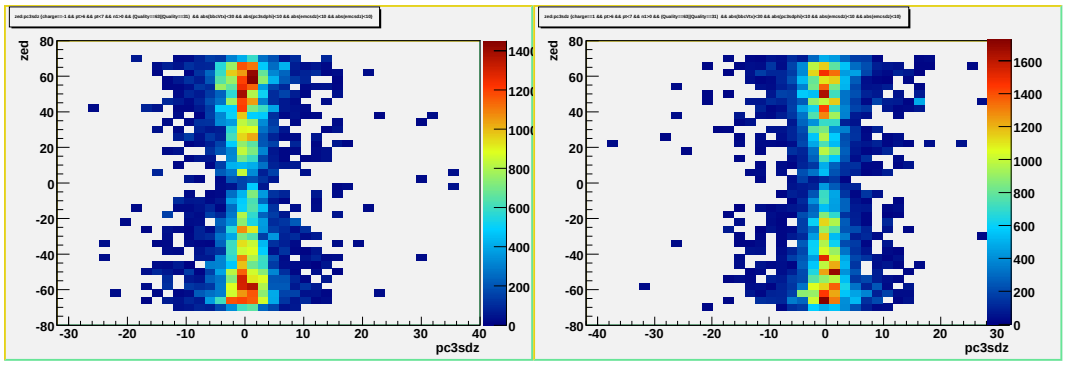

Figure G.7: pc3dz versus *zed*, p_T is 6-7 GeV/c. Left panel are positive tracks, while right panel are negative tracks

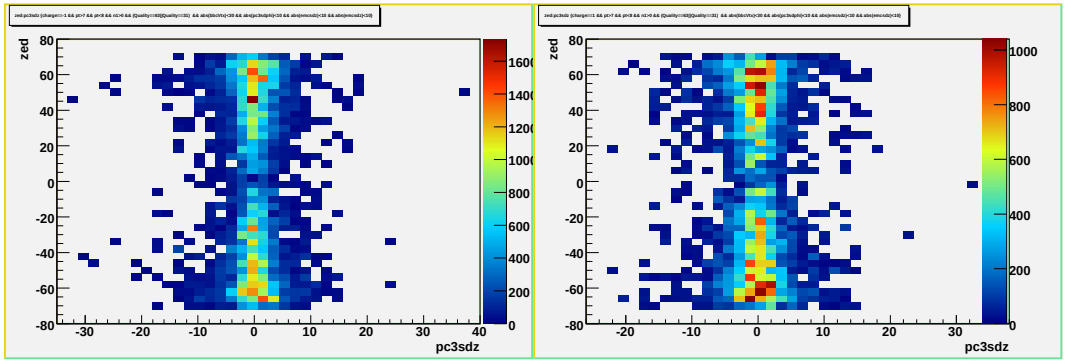

Figure G.8: pc3dz versus *zed*, p_T is 7-8 GeV/c. Left panel are positive tracks, while right panel are negative tracks

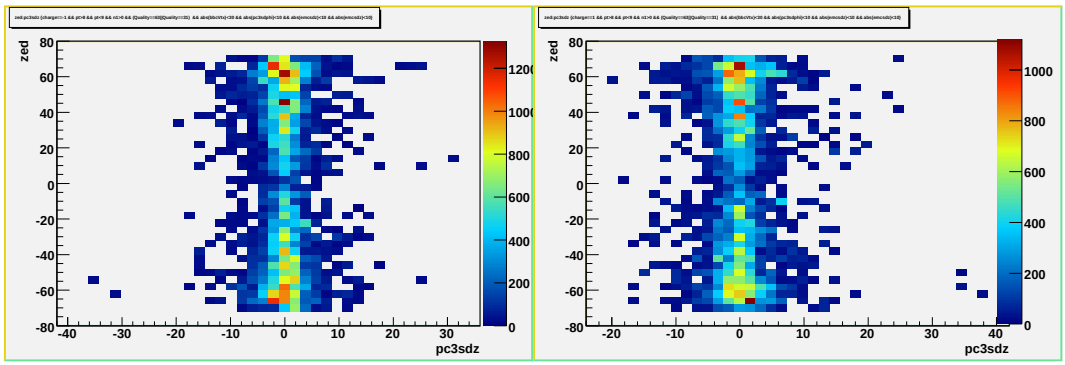

Figure G.9: pc3dz versus *zed*, p_T is 8-9 GeV/c. Left panel are positive tracks, while right panel are negative tracks

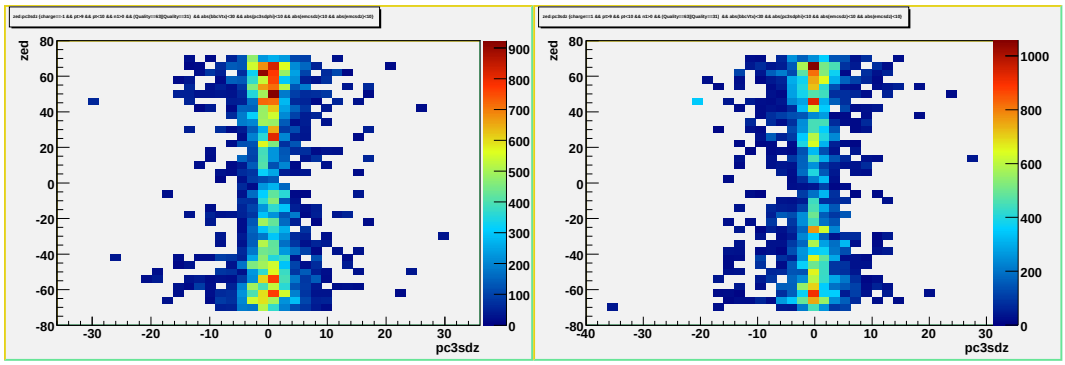

Figure G.10: pc3sdz versus *zed*, p_T is 9-10 GeV/c. Left panel are positive tracks, while right panel are negative tracks

G.0.8 Positive distributions of zed versus emcsdϕ

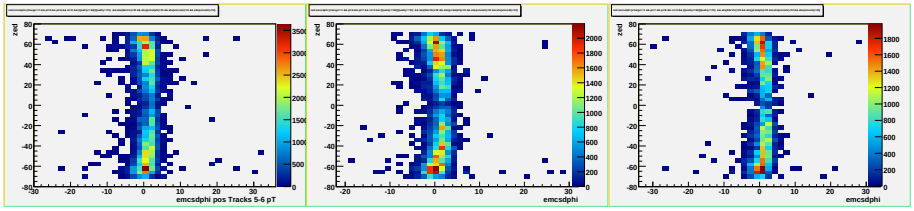

Figure G.11: emcsdϕ distributions of matching versus zed of positive tracks. p_T ranges from left to right are 5> p_T >6, 6> p_T >7 and 7> p_T >8

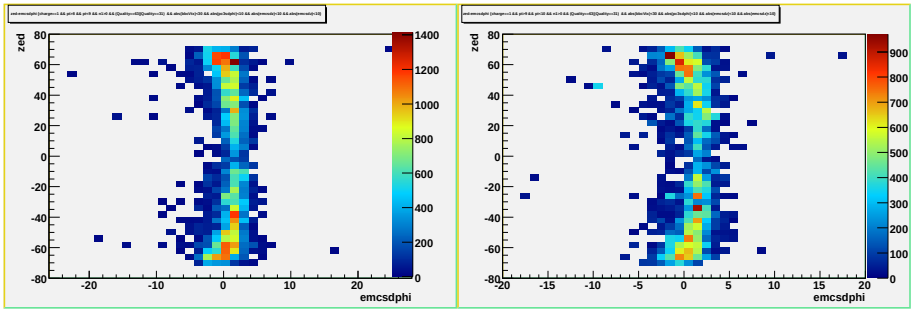

Figure G.12: emcsdϕ distributions of matching versus zed of positive tracks. p_T range from left to right are 8> p_T >9 and 9> p_T >10

G.0.9 Positive Distributions fitted to double Gaussians

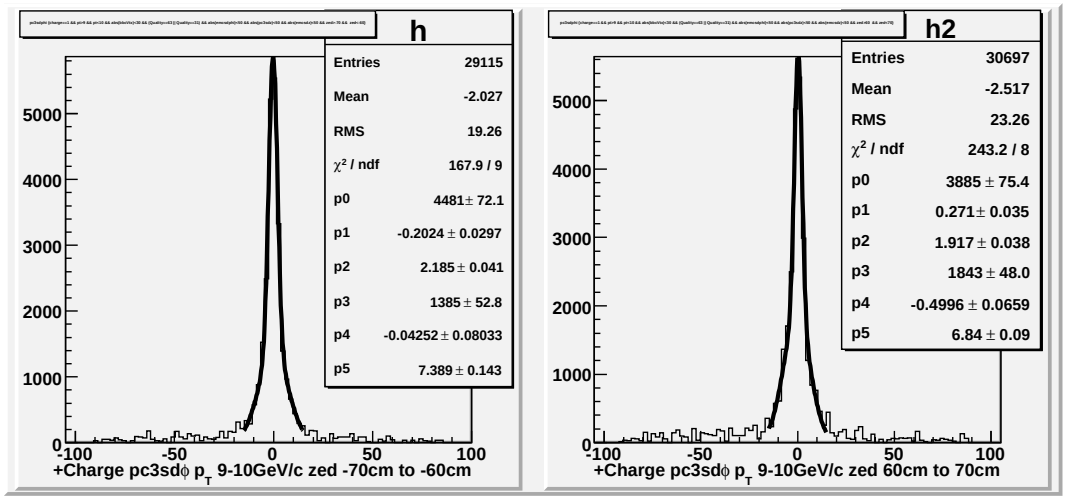

Figure G.13: pc3s$d\phi$ p_T 9-10 GeV/c *zed* 60-70 cm

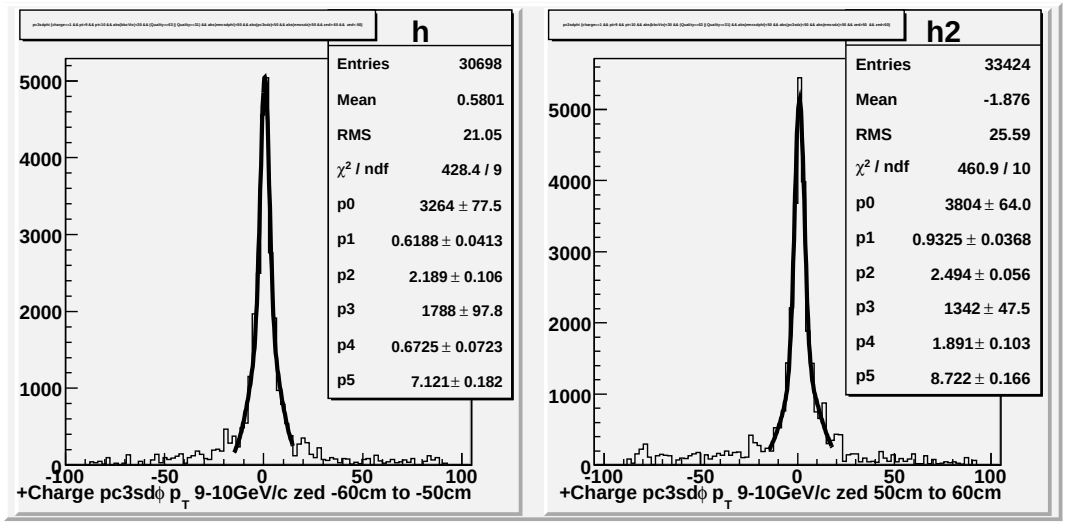

Figure G.14: pc3s$d\phi$ p_T 9-10 GeV/c *zed* 50-60 cm

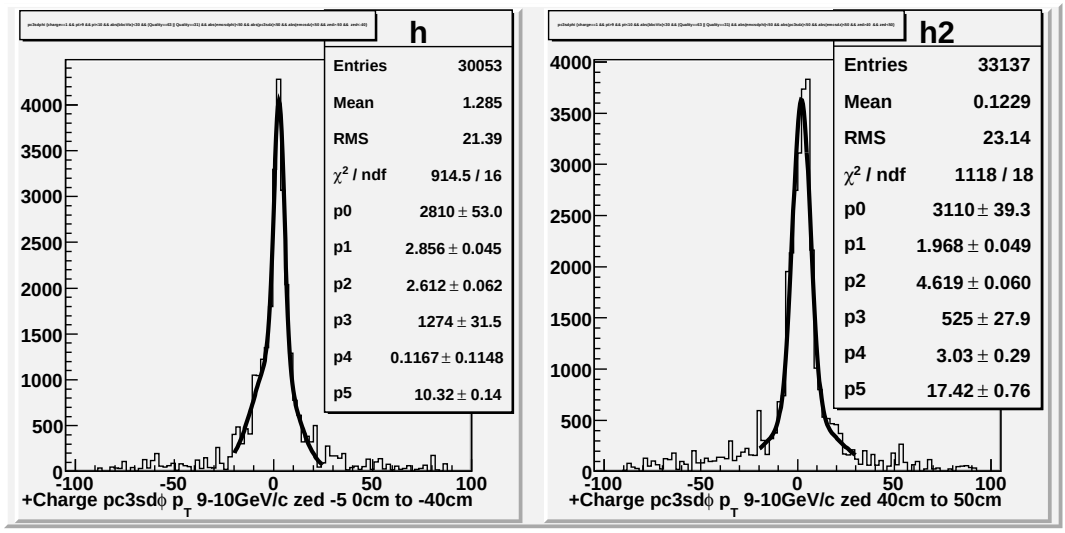

Figure G.15: pc3s$d\phi$ p_T 9-10 GeV/c *zed* 40-50 cm

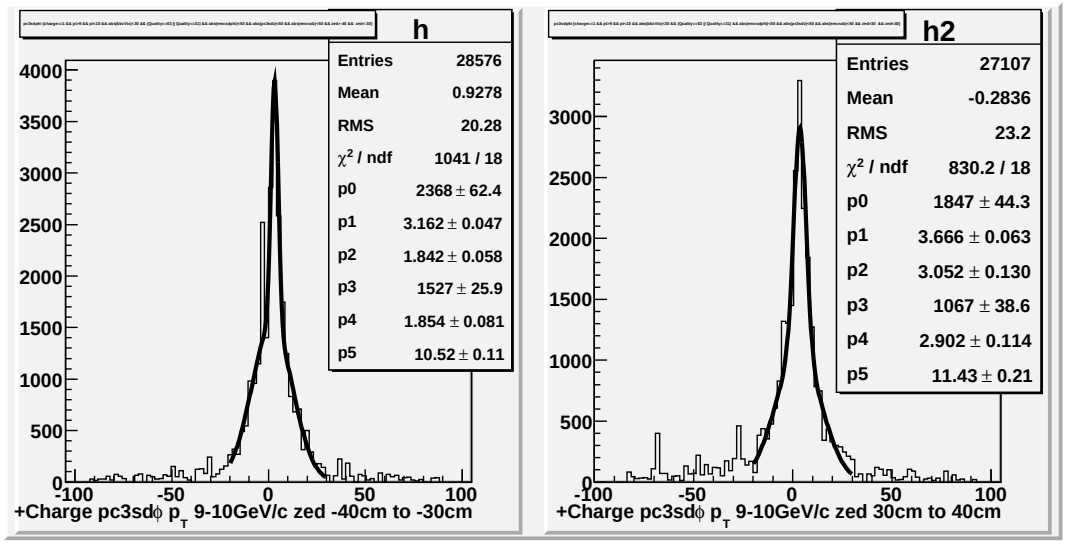

Figure G.16: pc3s$d\phi$ p_T 9-10 GeV/c *zed* 30-40 cm

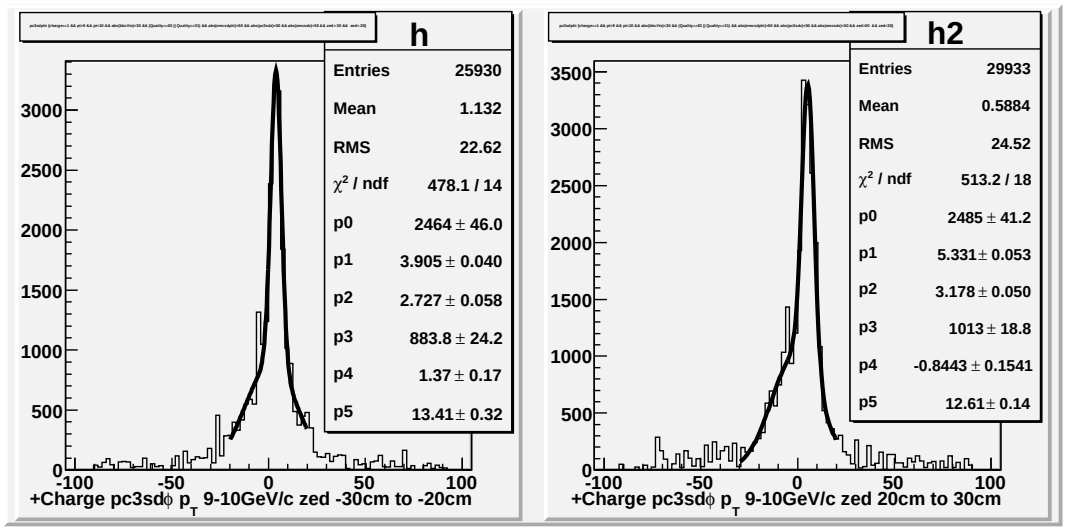

Figure G.17: pc3s$d\phi$ p_T 9-10 GeV/c *zed* 20-30 cm

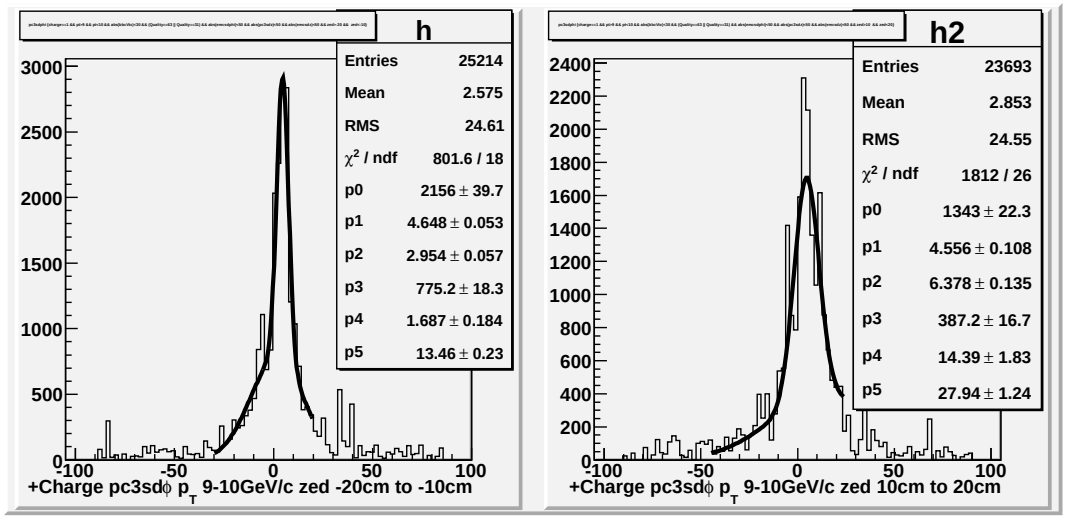

Figure G.18: pc3s$d\phi$ p_T 9-10 GeV/c *zed* 10-20 cm

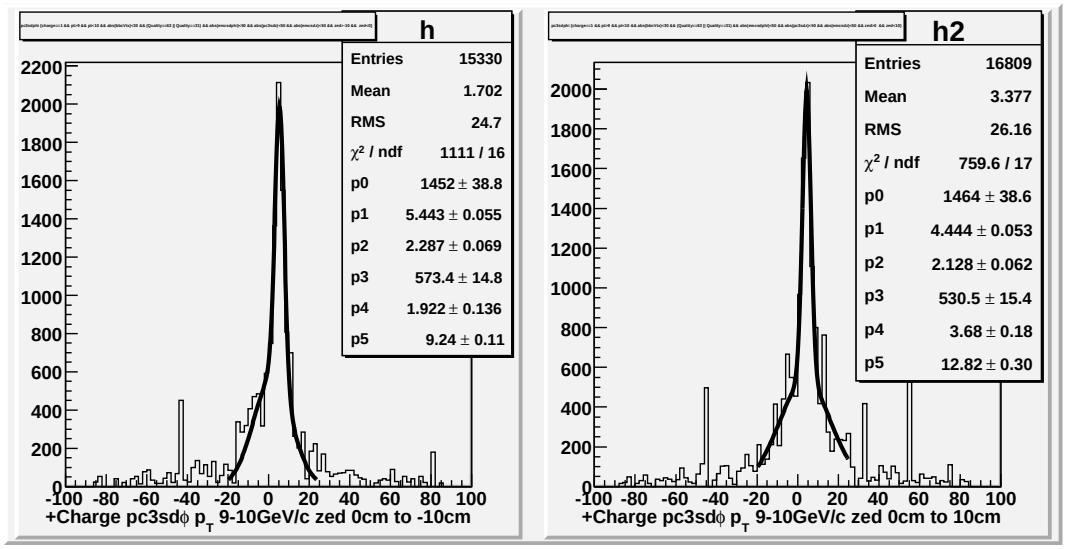

Figure G.19: pc3s$d\phi$ p_T 9-10 GeV/c *zed* 0-10 cm

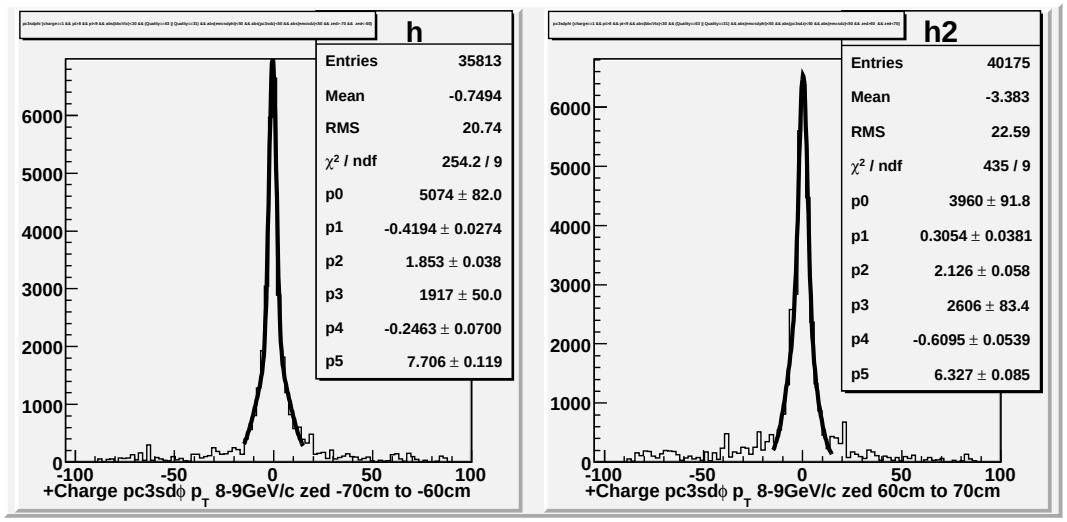

Figure G.20: pc3s$d\phi$ p_T 8-9 GeV/c *zed* 60-70 cm

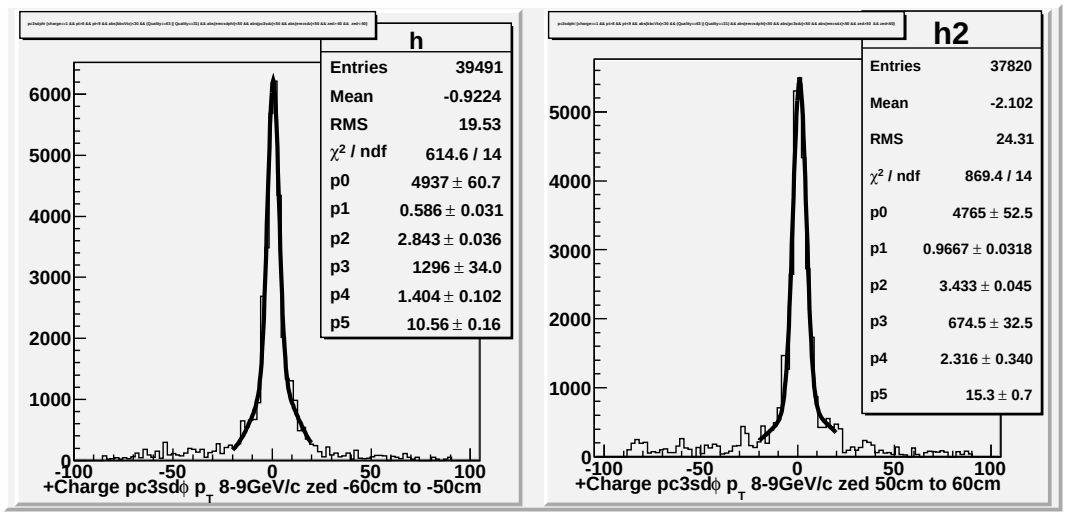

Figure G.21: pc3s$d\phi$ p_T 8-9 GeV/c *zed* 50-60 cm

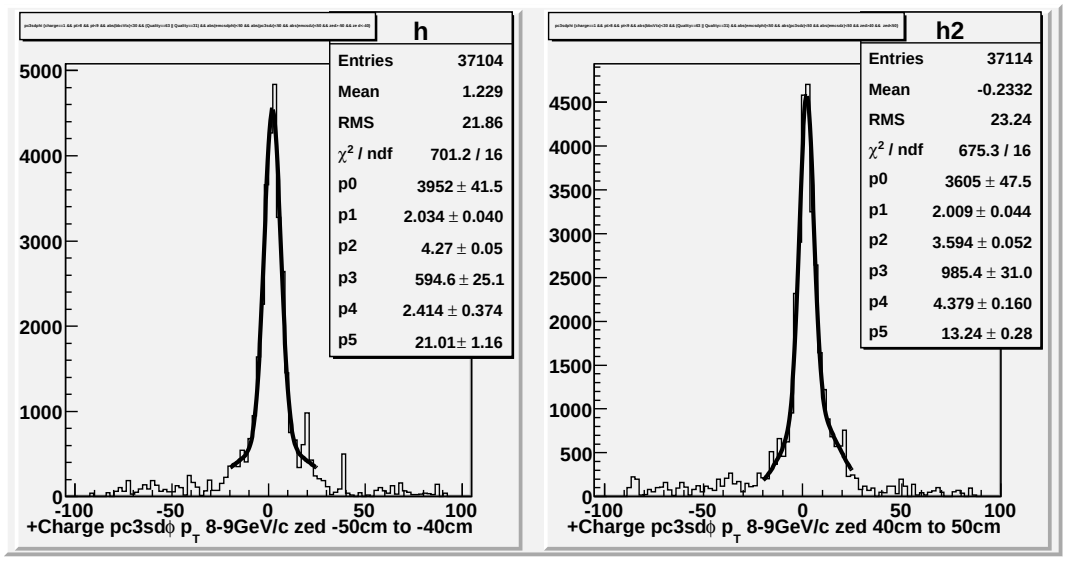

Figure G.22: pc3s$d\phi$ p_T 8-9 GeV/c *zed* 40-50 cm

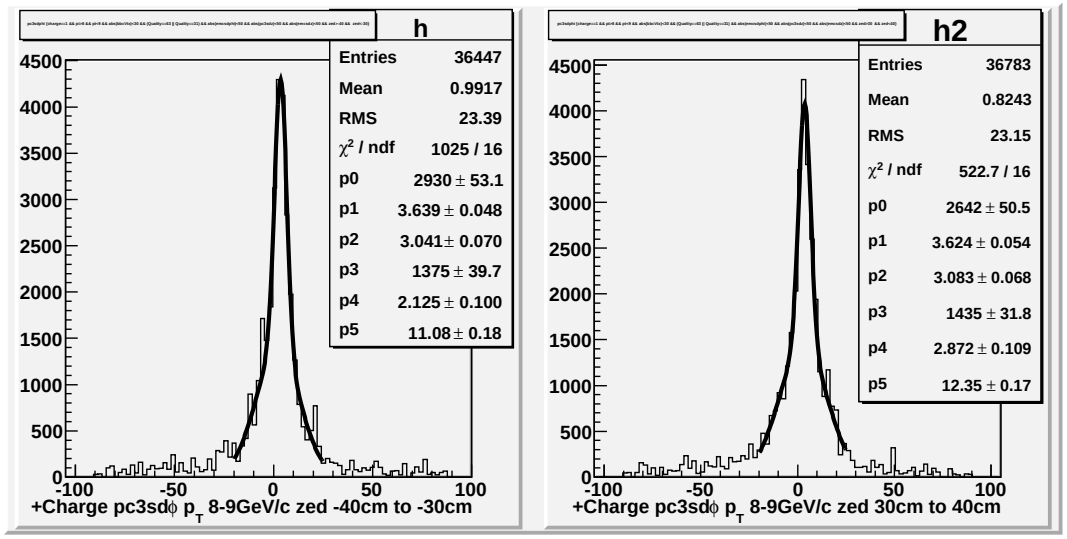

Figure G.23: pc3s$d\phi$ p_T 8-9 GeV/c *zed* 30-40 cm

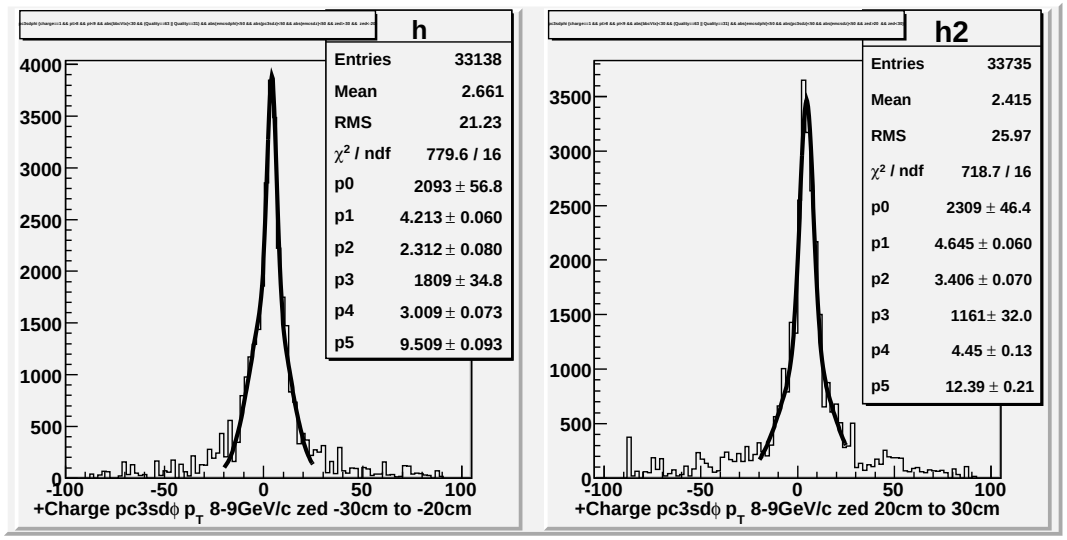

Figure G.24: pc3s$d\phi$ p_T 8-9 GeV/c *zed* 20-30 cm

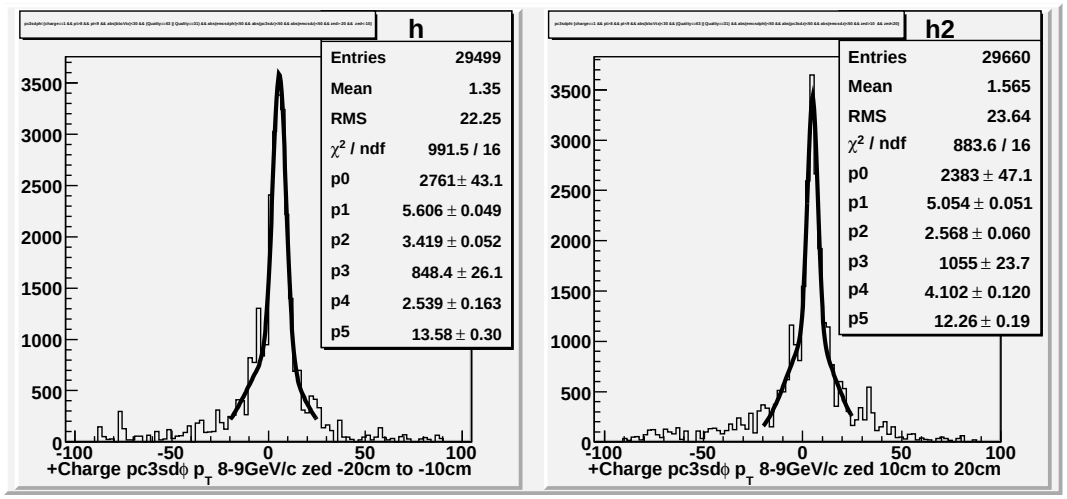

Figure G.25: pc3s$d\phi$ p_T 8-9 GeV/c *zed* 10-20 cm

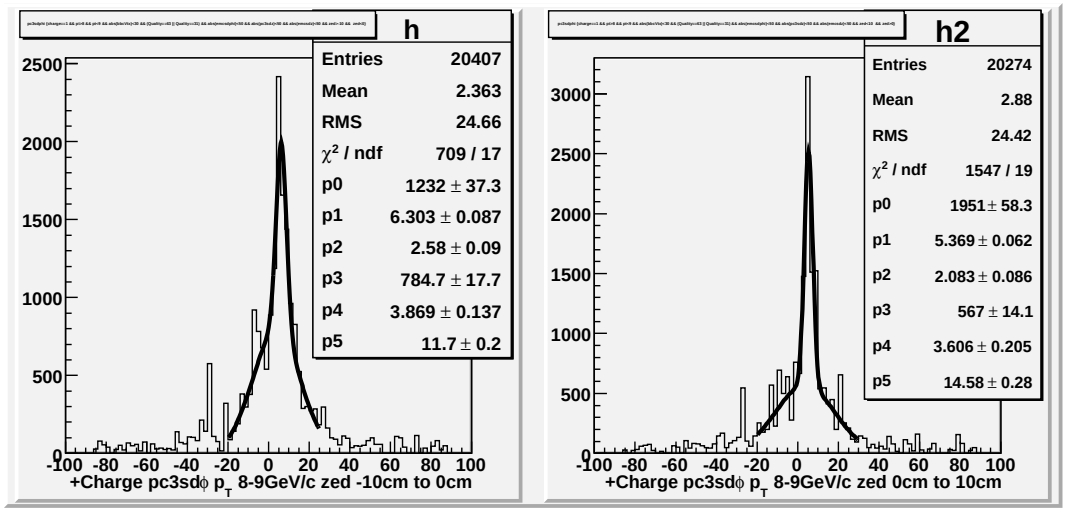

Figure G.26: pc3s$d\phi$ p_T 8-9 GeV/c *zed* 0-10 cm

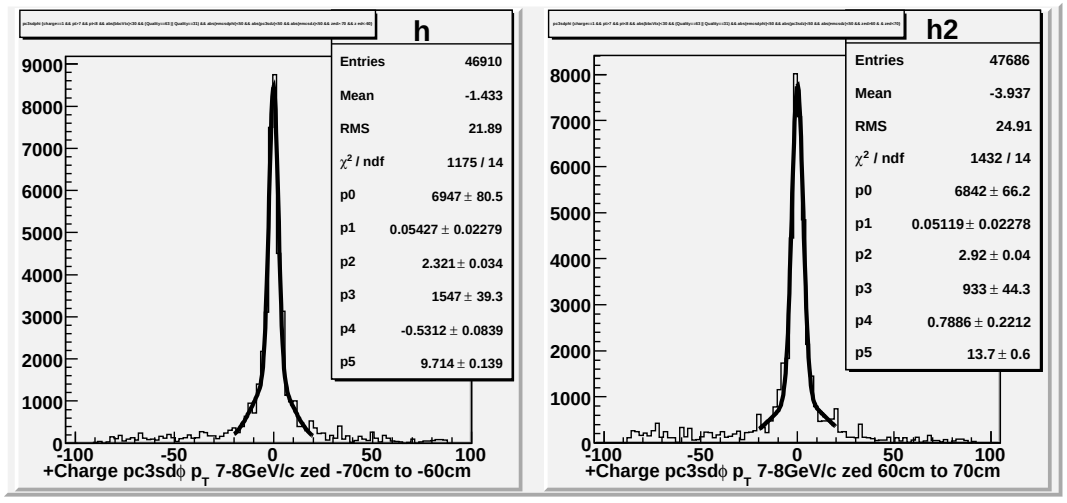

Figure G.27: pc3s$d\phi$ p_T 7-8 GeV/c *zed* 60-70 cm

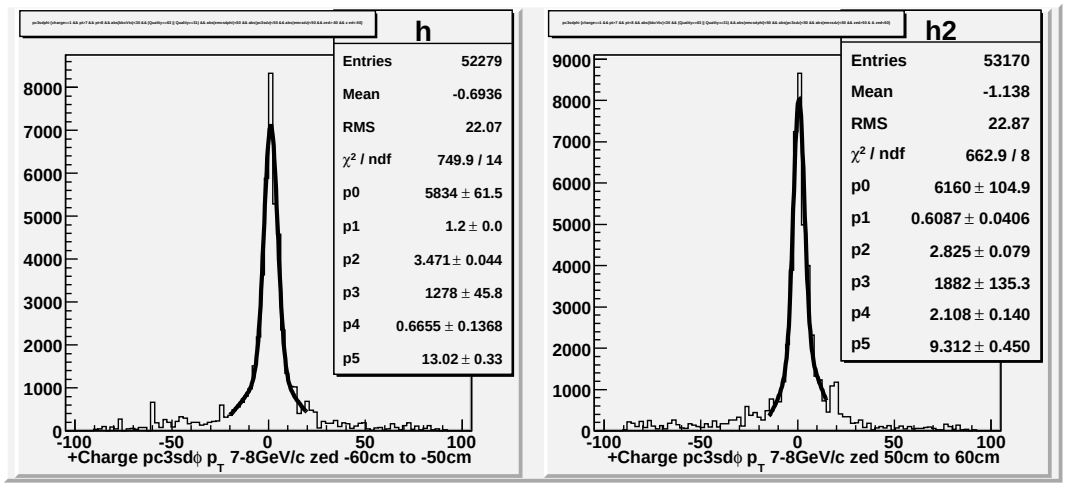

Figure G.28: pc3s$d\phi$ p$_T$ 7-8 GeV/c *zed* 50-60 cm

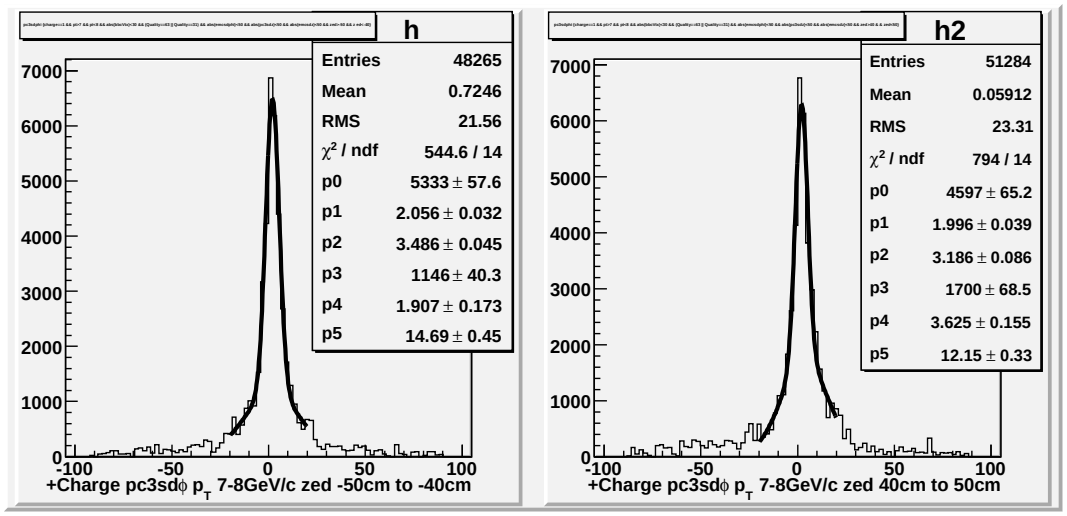

Figure G.29: pc3s$d\phi$ p_T 7-8 GeV/c *zed* 40-50 cm

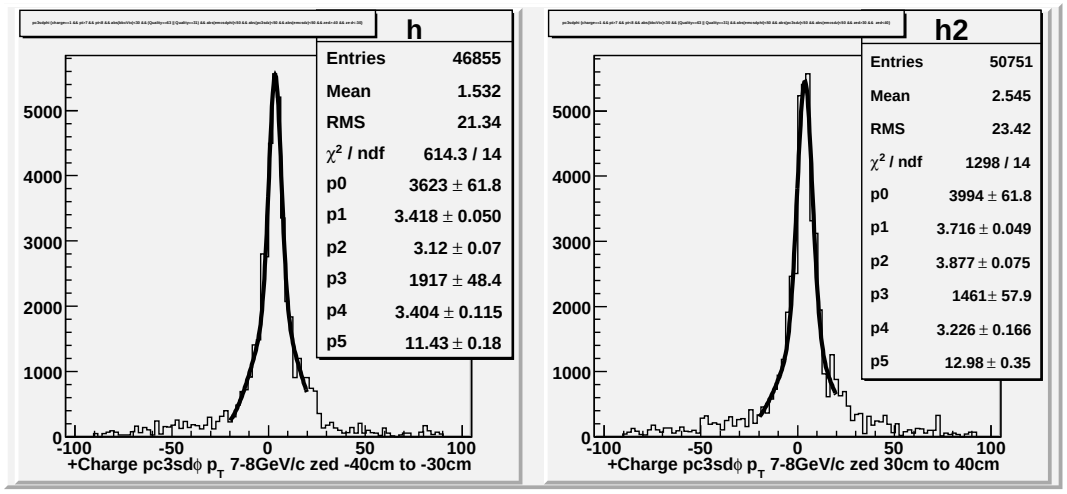

Figure G.30: pc3s$d\phi$ p_T 7-8 GeV/c *zed* 30-40 cm

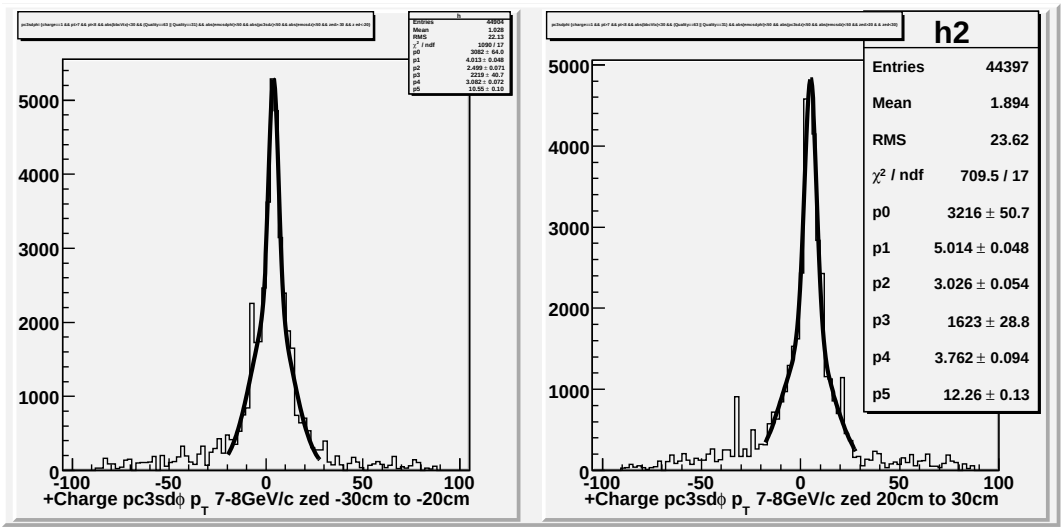

Figure G.31: pc3s$d\phi$ p_T 7-8 GeV/c *zed* 20-30 cm

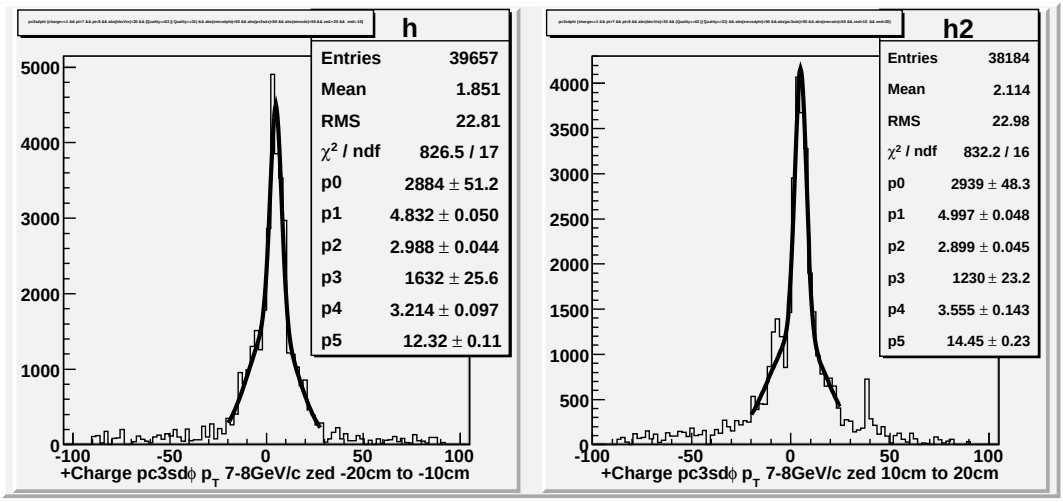

Figure G.32: pc3s$d\phi$ p_T 7-8 GeV/c *zed* 10-20 cm

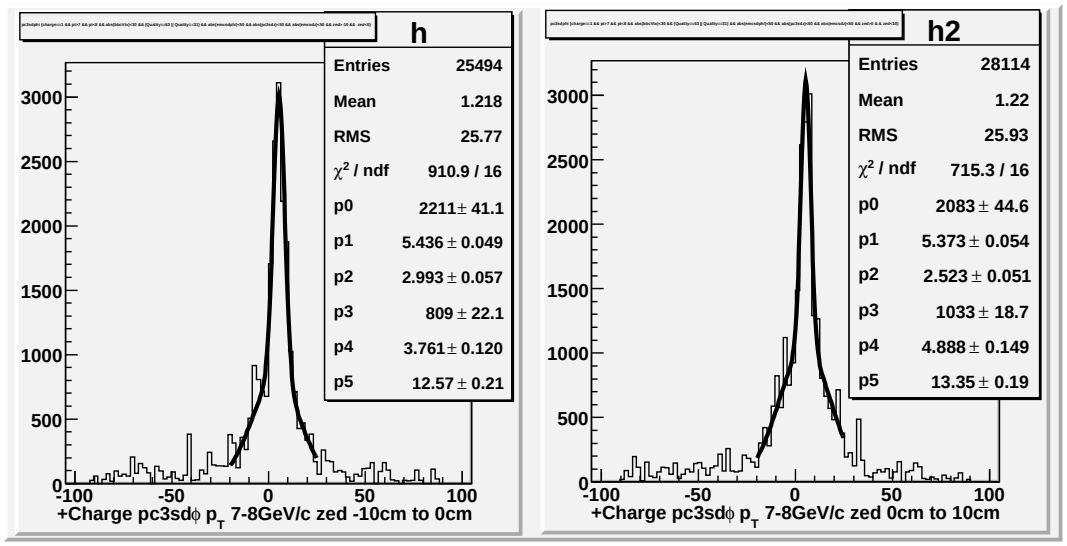

Figure G.33: pc3s$d\phi$ p$_T$ 7-8 GeV/c *zed* 0-10 cm

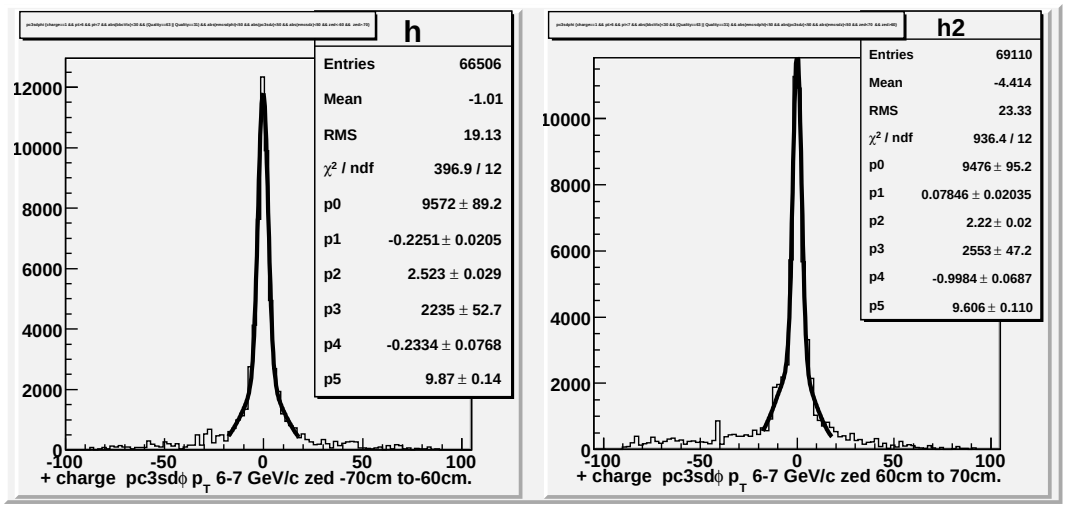

Figure G.34: pc3s$d\phi$ p_T 6-7 GeV/c *zed* 60-70 cm

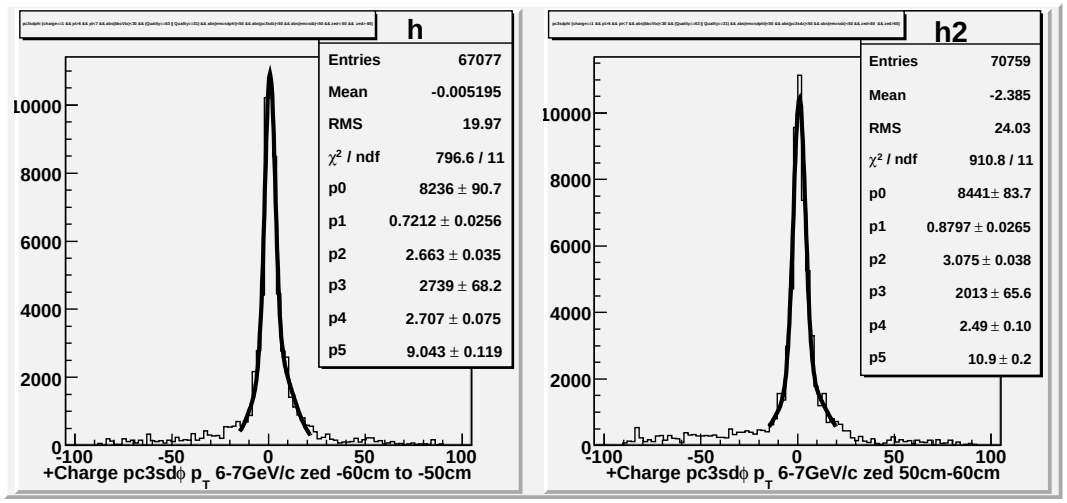

Figure G.35: pc3s$d\phi$ p_T 5-6 GeV/c *zed* 50-60 cm

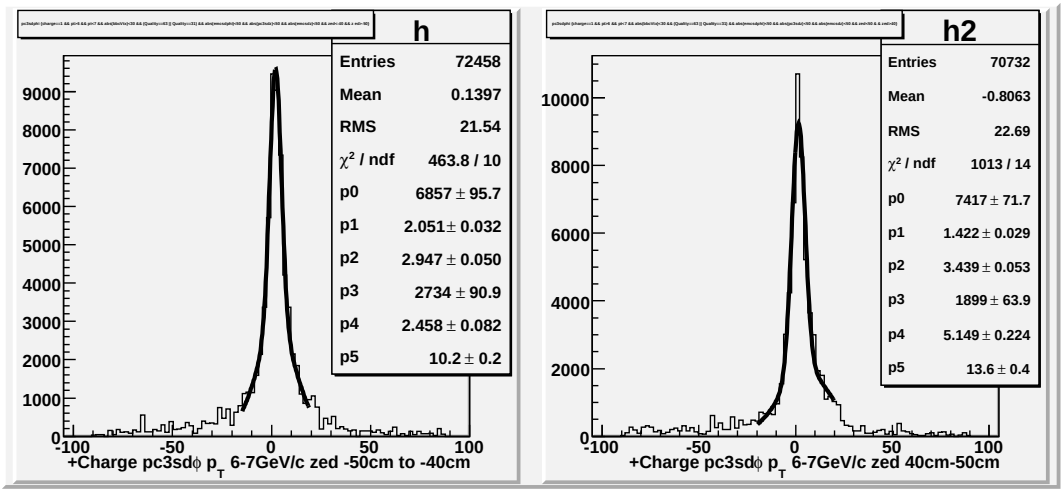

Figure G.36: pc3s$d\phi$ p_T 6-7 GeV/c *zed* 40-50 cm

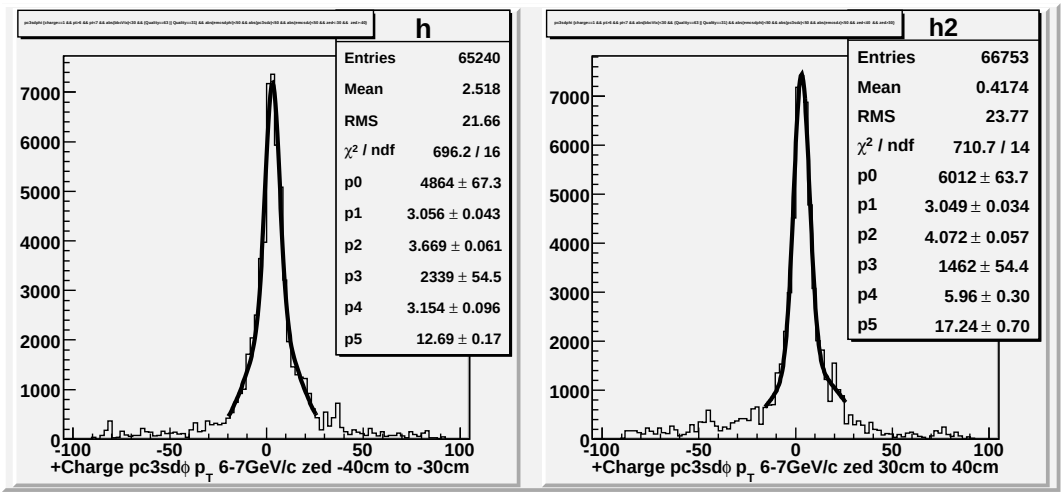

Figure G.37: pc3s$d\phi$ p_T 6-7 GeV/c *zed* 30-40 cm

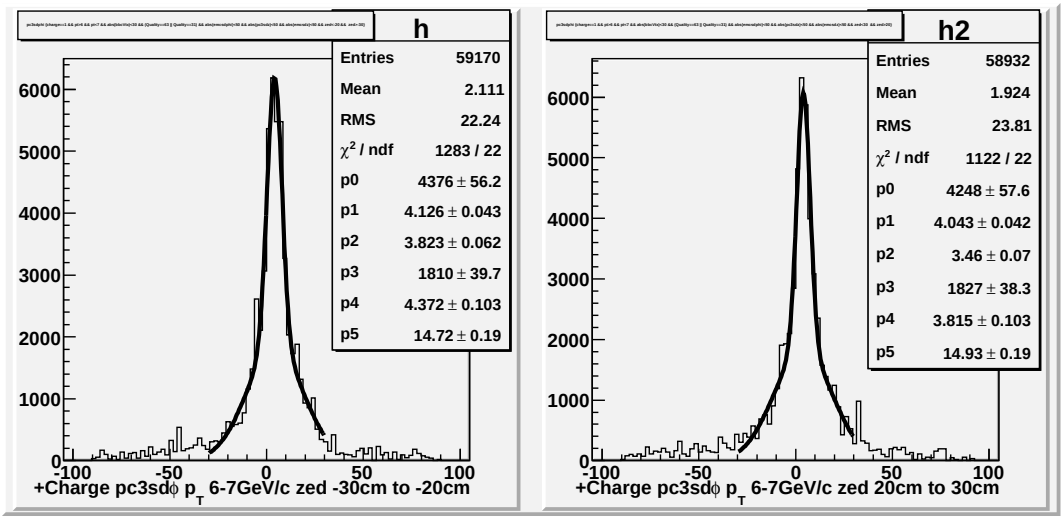

Figure G.38: pc3s$d\phi$ p_T 6-7 GeV/c *zed* 20-30 cm

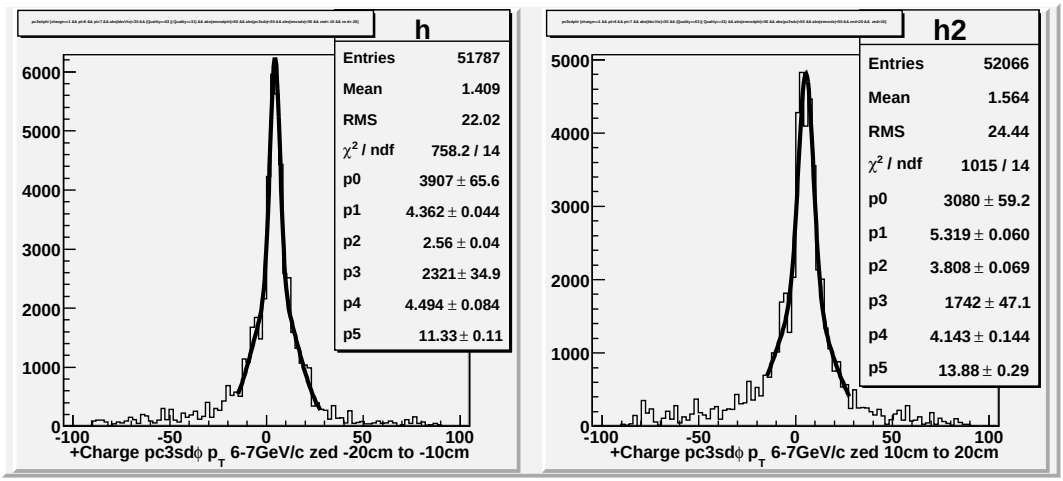

Figure G.39: pc3s$d\phi$ p_T 6-7 GeV/c *zed* 10-20 cm

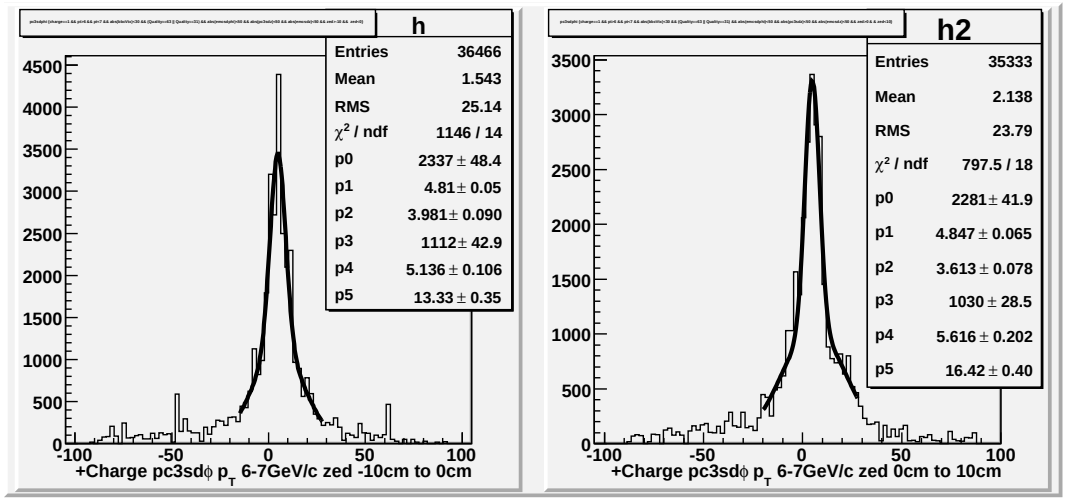

Figure G.40: pc3s$d\phi$ p_T 6-7 GeV/c *zed* 0-10 cm

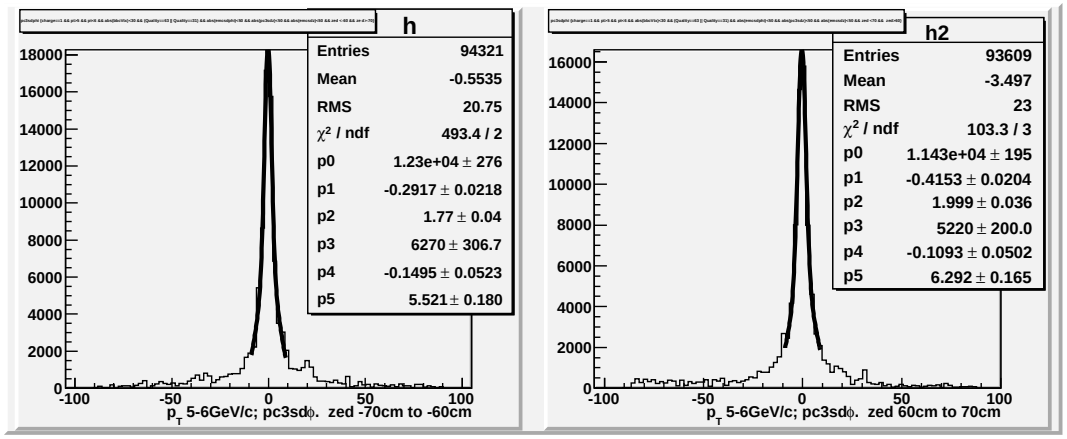

Figure G.41: pc3s$d\phi$ p_T 5-6 GeV/c *zed* 60-70 cm

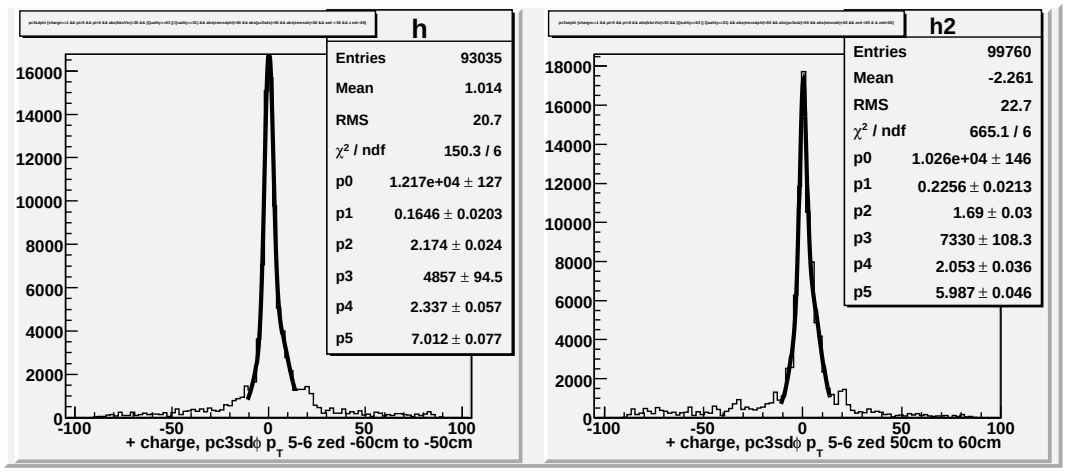

Figure G.42: pc3s$d\phi$ p_T 5-6 GeV/c *zed* 50-60 cm

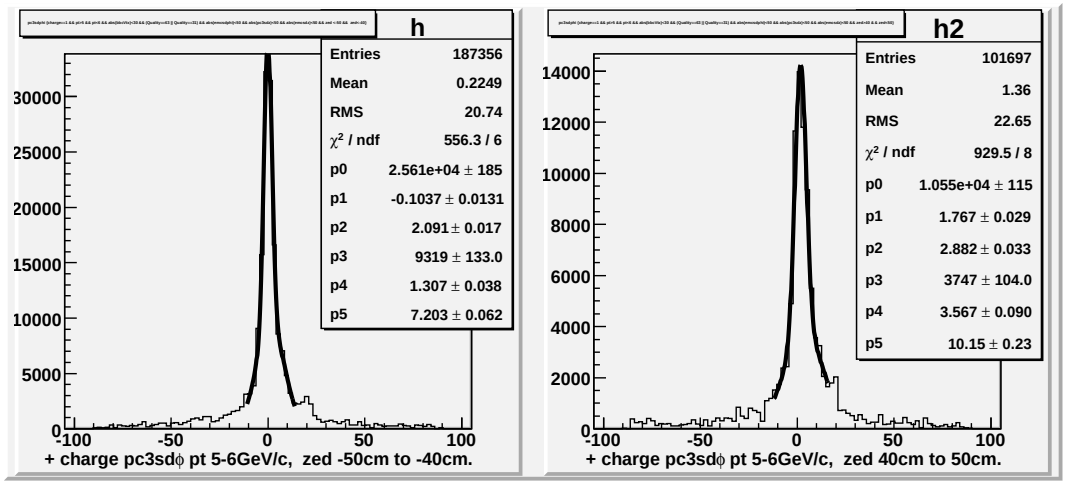

Figure G.43: pc3s$d\phi$ p_T 5-6 GeV/c *zed* 40-50 cm

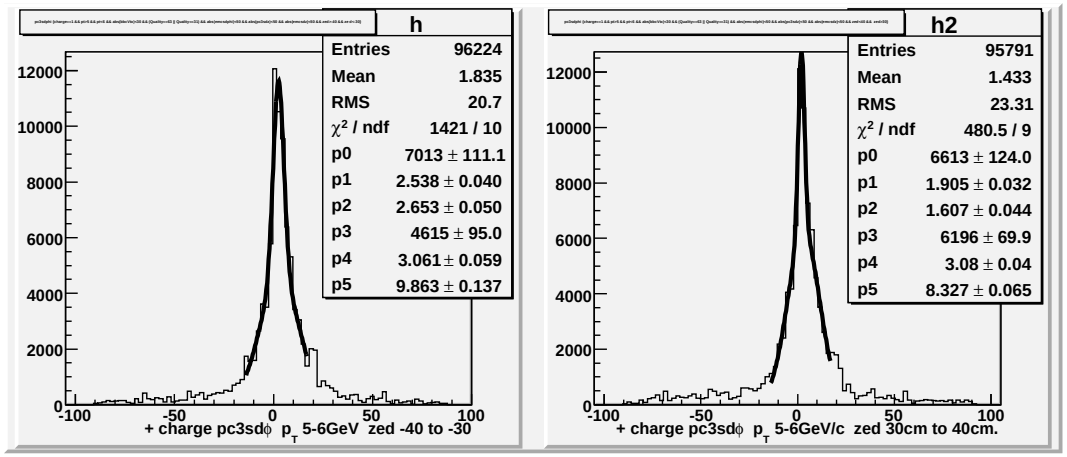

Figure G.44: pc3s$d\phi$ p_T 5-6 GeV/c *zed* 30-40 cm

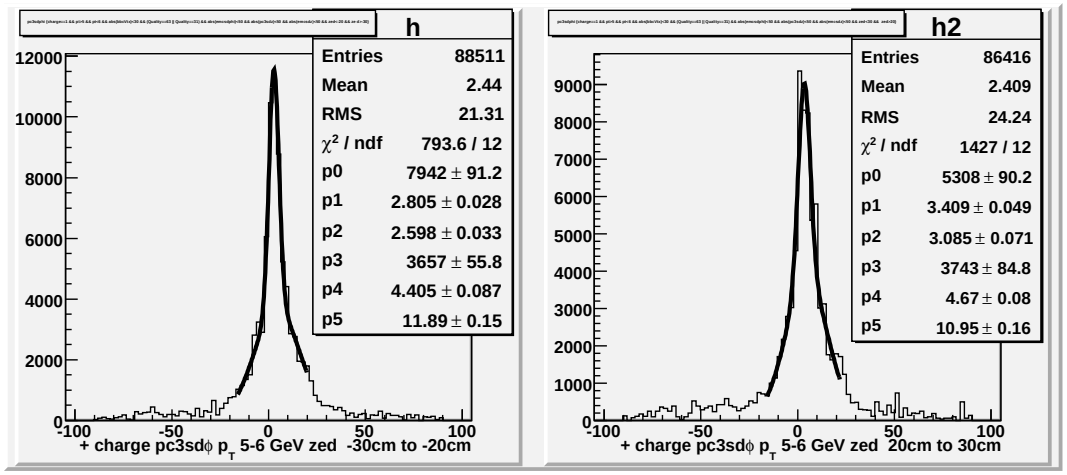

Figure G.45: pc3s$d\phi$ p_T 5-6 GeV/c *zed* 20-30 cm

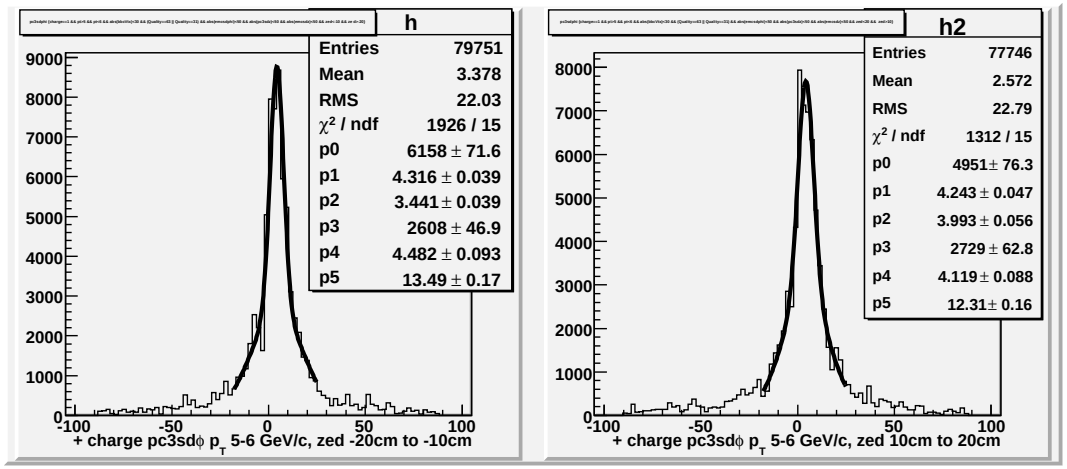

Figure G.46: pc3s$d\phi$ p_T 5-6 GeV/c *zed* 10-20 cm

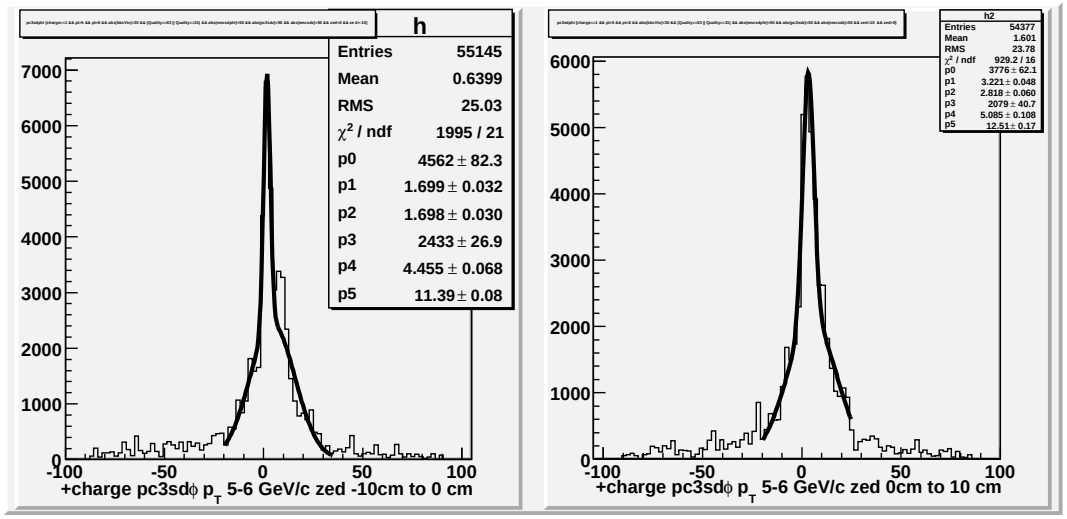

Figure G.47: pc3s$d\phi$ p_T 5-6 GeV/c *zed* 0-10 cm

G.0.10 Negative Distributions fitted to double Gaussians

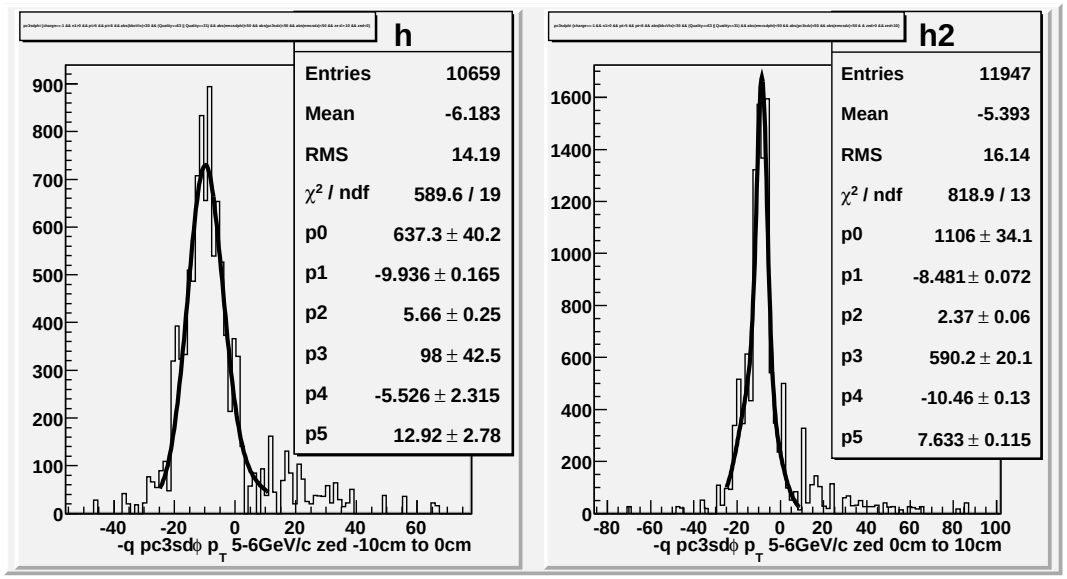

Figure G.48: π^- pc3s$d\phi$ p_T 5-6 GeV/c *zed* 0-10 cm

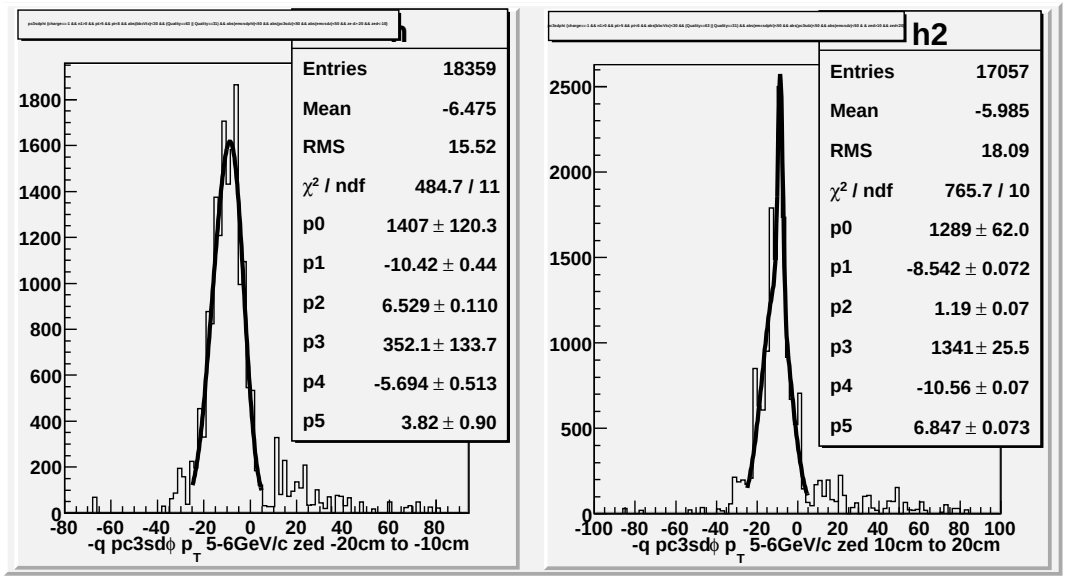

Figure G.49: π^- pc3s$d\phi$ p_T 5-6 GeV/c *zed* 10-20 cm

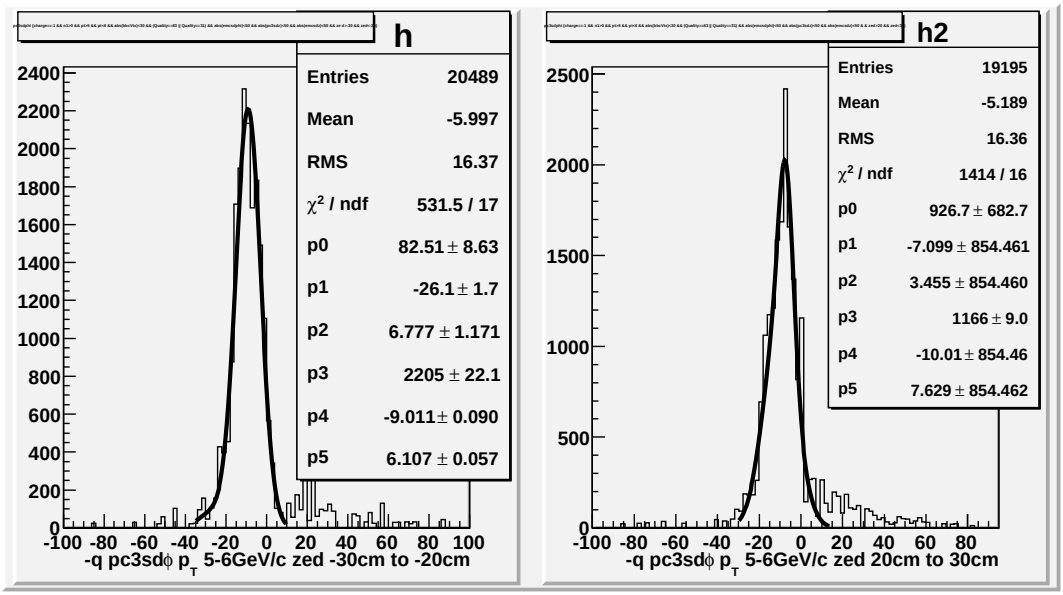

Figure G.50: π^- pc3s$d\phi$ p_T 5-6 GeV/c *zed* 20-30 cm

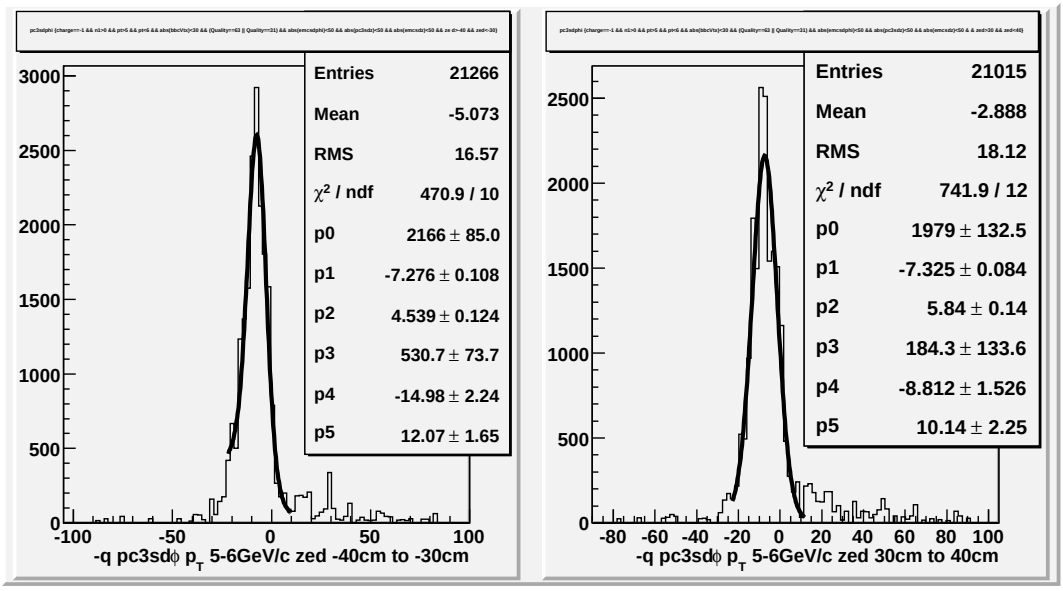

Figure G.51: π^- pc3s$d\phi$ p_T 5-6 GeV/c *zed* 30-40 cm

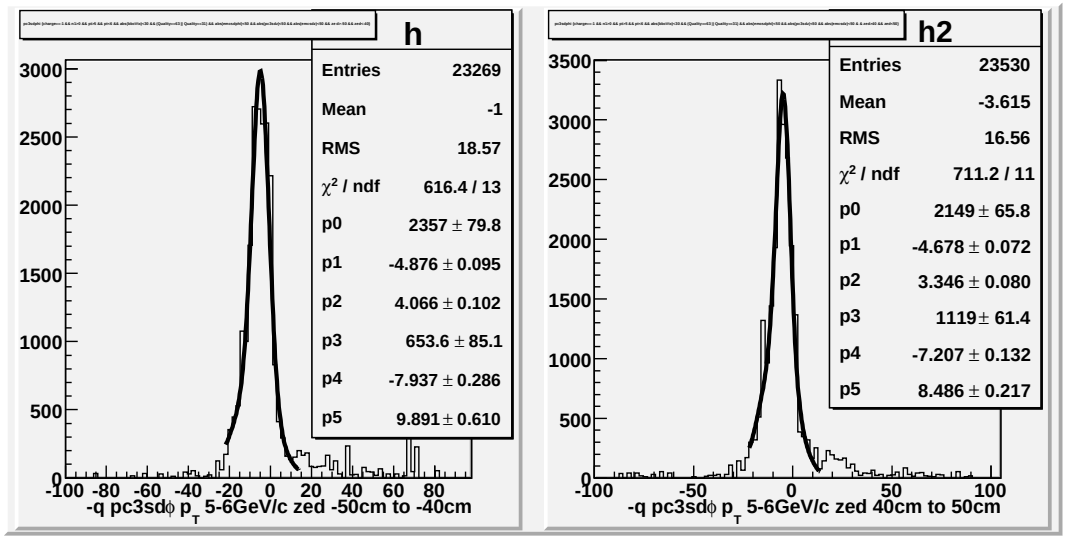

Figure G.52: π^- pc3s$d\phi$ p_T 5-6 GeV/c *zed* 40-50 cm

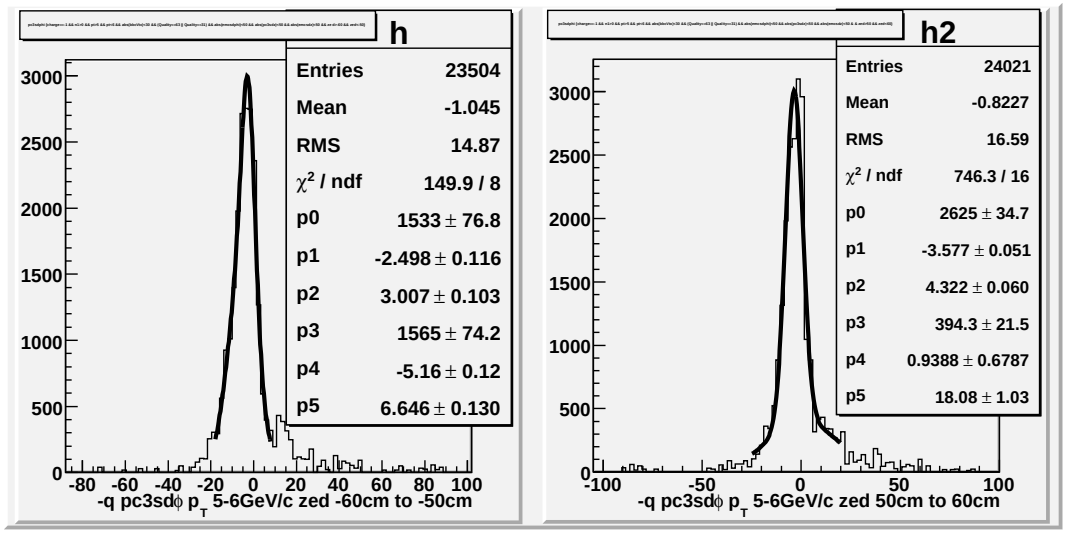

Figure G.53: π^- pc3s$d\phi$ p_T 5-6 GeV/c *zed* 50-60 cm

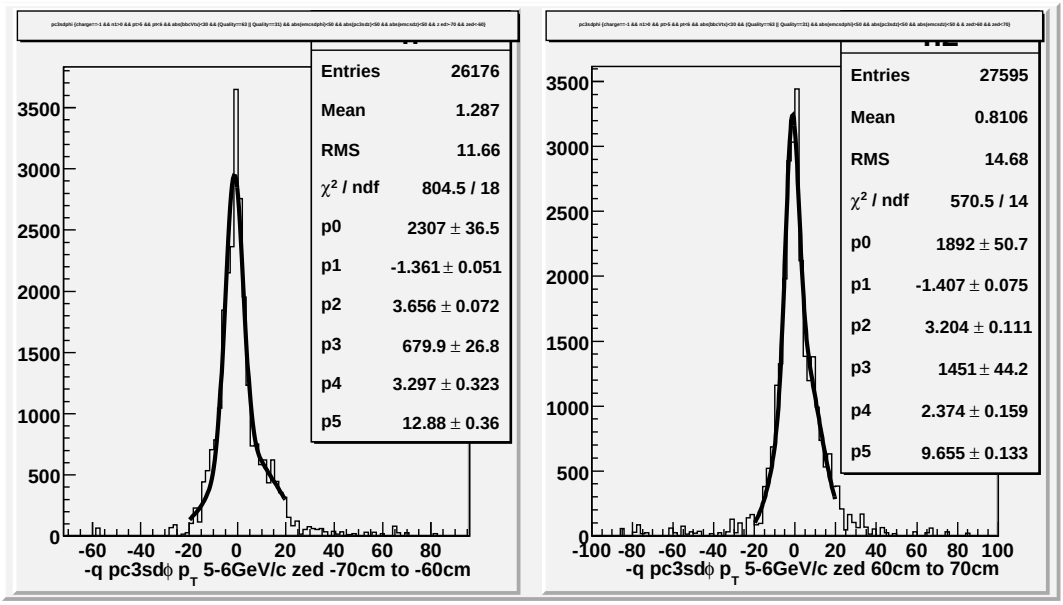

Figure G.54: π^- pc3s$d\phi$ p_T 5-6 GeV/c *zed* 60-70 cm

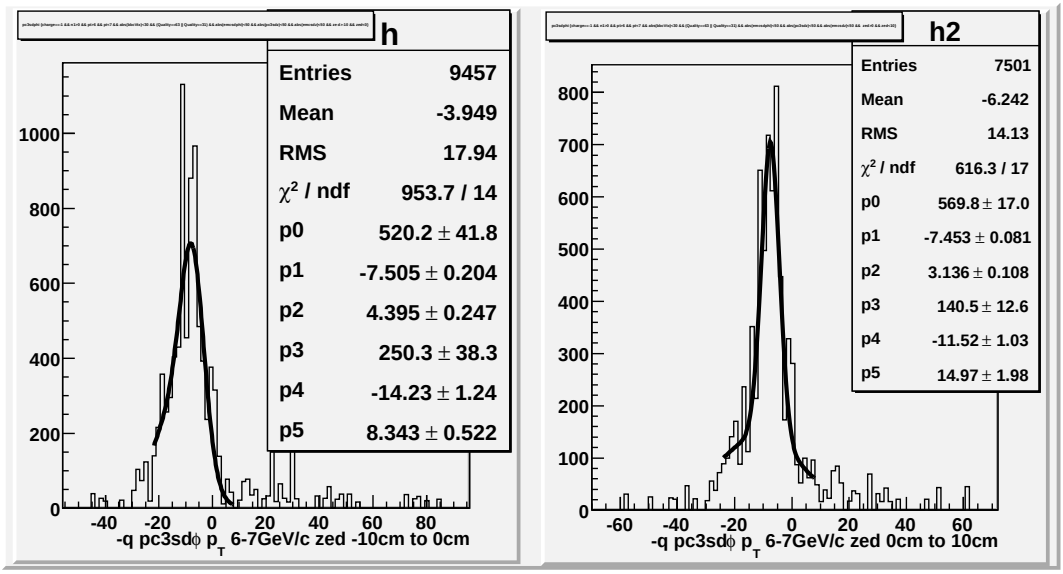

Figure G.55: π^- pc3s$d\phi$ p_T 6-7 GeV/c *zed* 0-10 cm

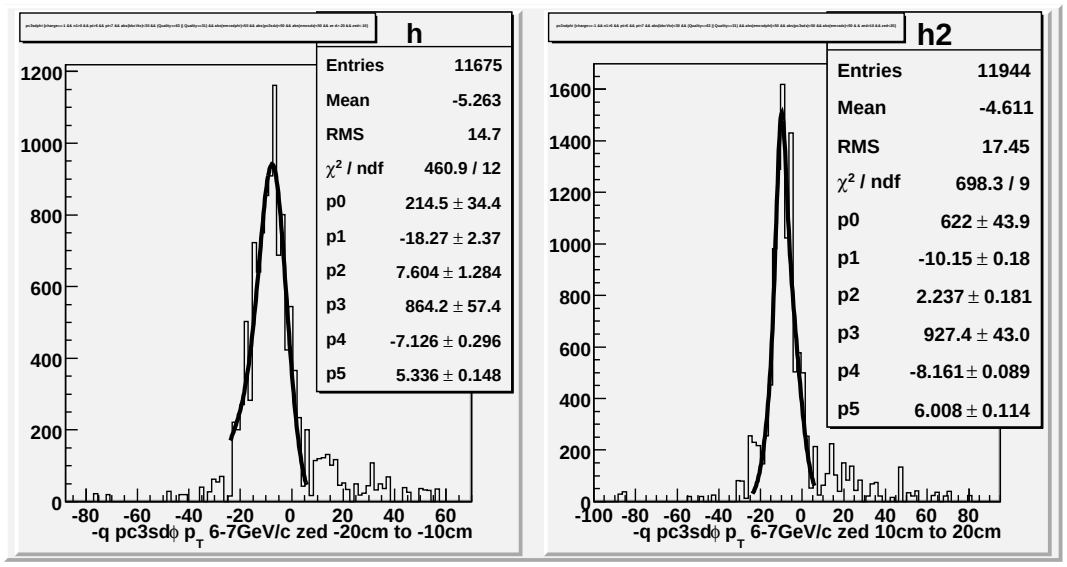

Figure G.56: π^- pc3s$d\phi$ p$_T$ 6-7 GeV/c *zed* 10-20 cm

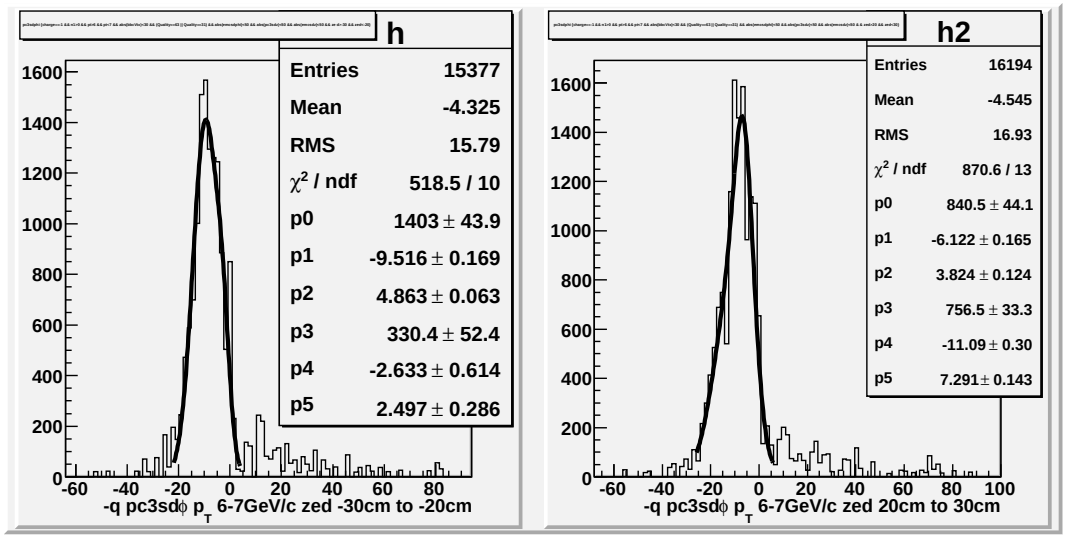

Figure G.57: π^- pc3s$d\phi$ p$_T$ 6-7 GeV/c *zed* 10-20 cm

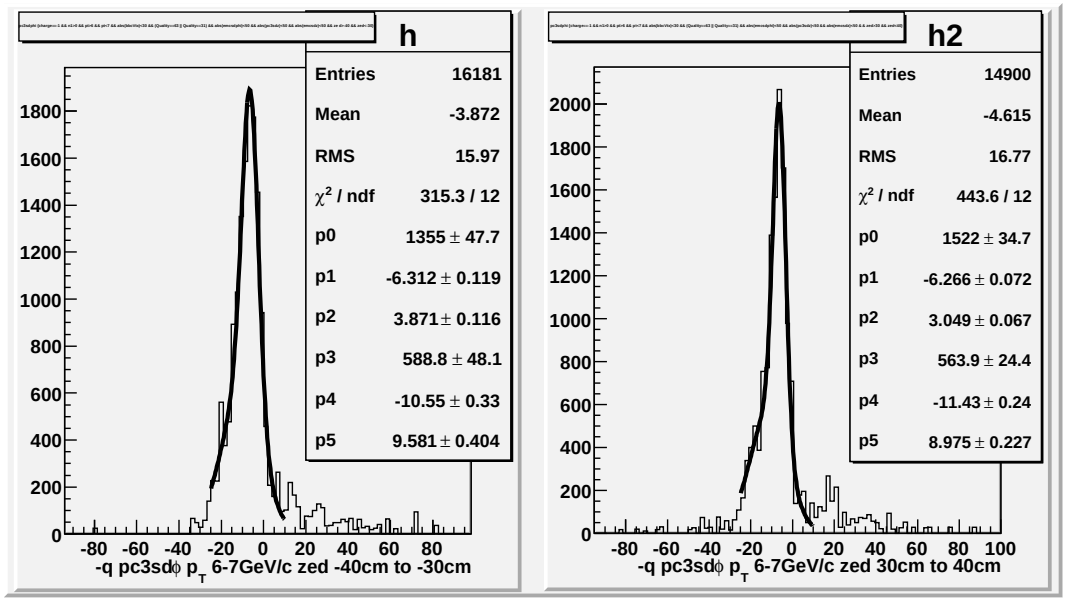

Figure G.58: π^- pc3s$d\phi$ p_T 6-7 GeV/c *zed* 30-40 cm

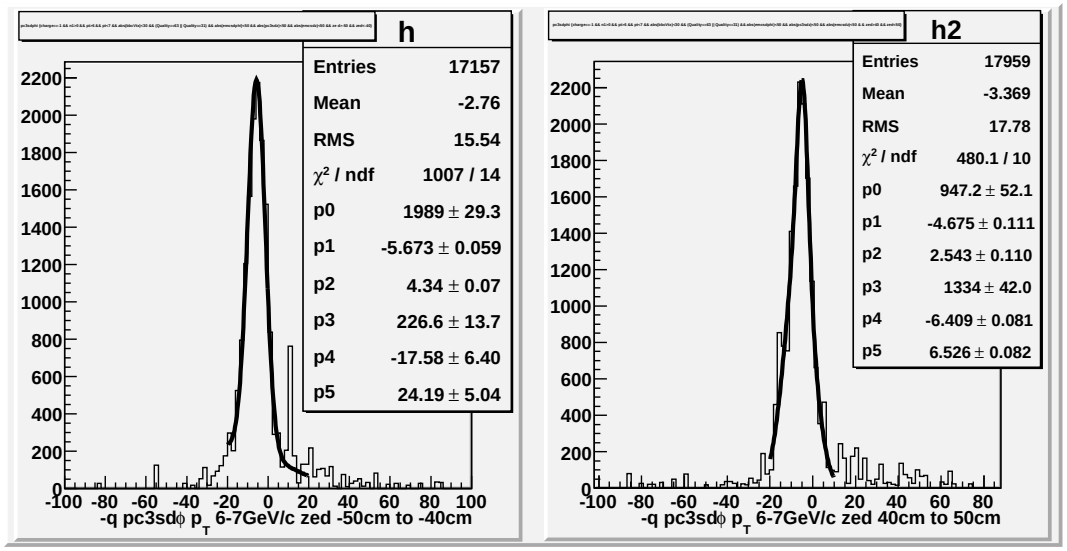

Figure G.59: π^- pc3s$d\phi$ p_T 6-7 GeV/c *zed* 40-50 cm

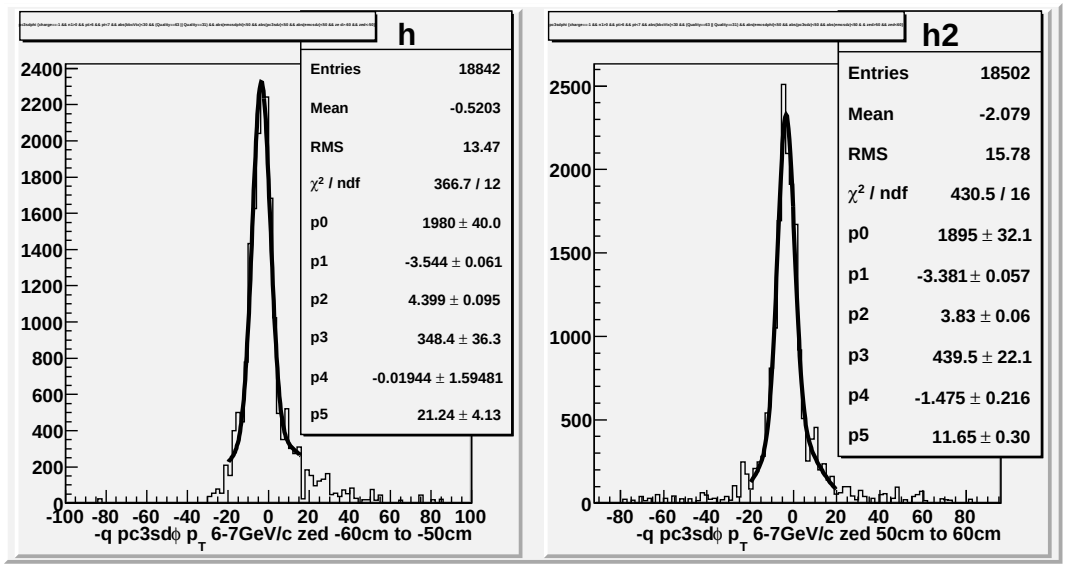

Figure G.60: π^- pc3s$d\phi$ p$_T$ 6-7 GeV/c *zed* 50-60 cm

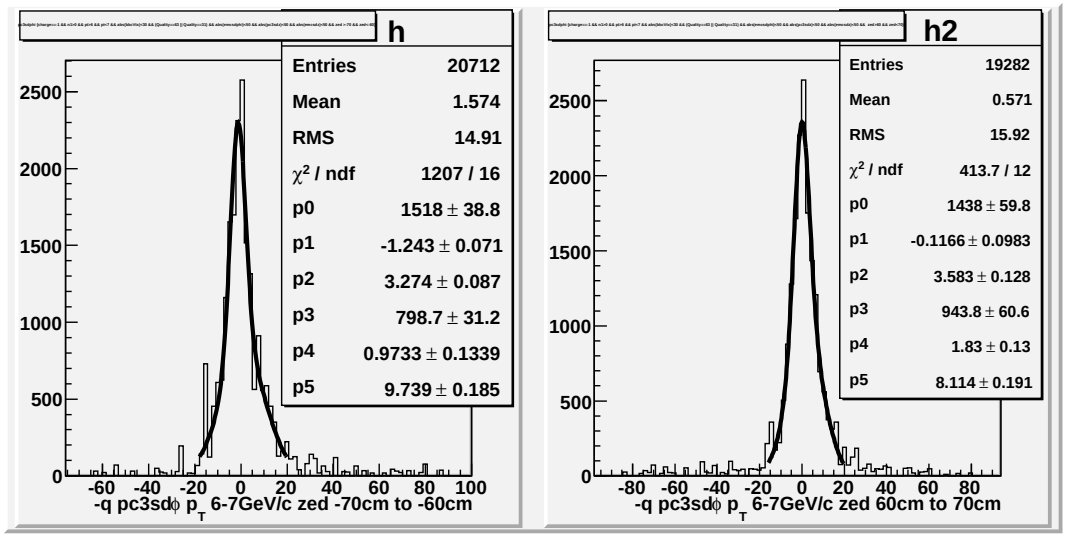

Figure G.61: π^- pc3s$d\phi$ p$_T$ 6-7 GeV/c *zed* 60-70 cm

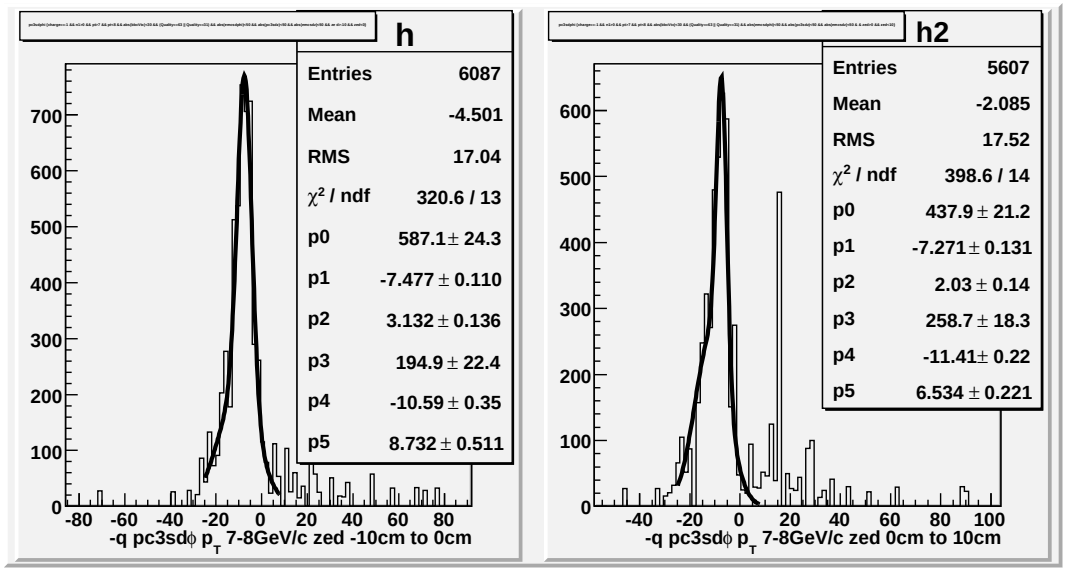

Figure G.62: π^- pc3s$d\phi$ p$_T$ 7-8 GeV/c *zed* 0-10 cm

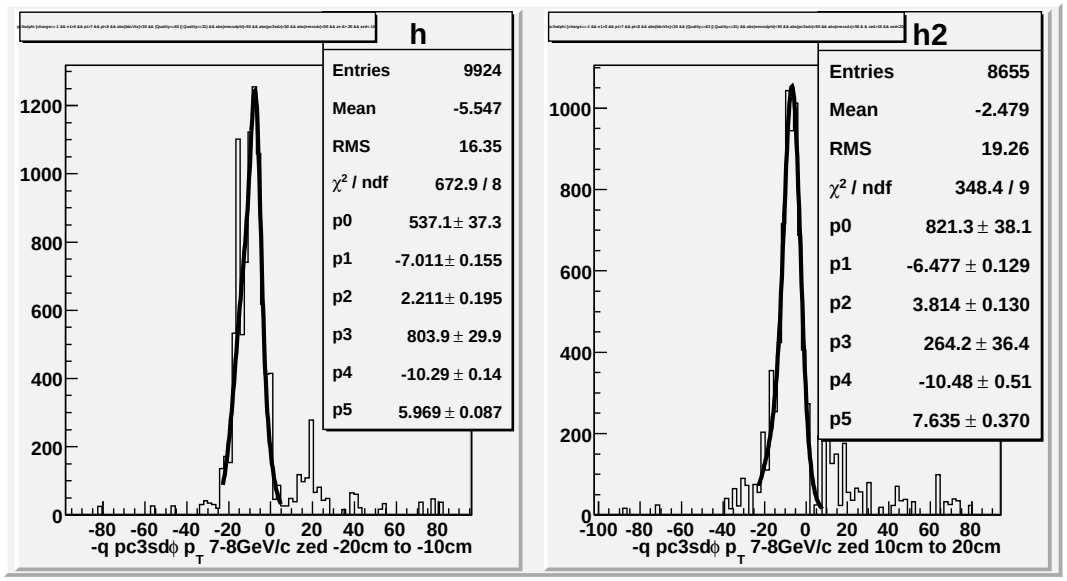

Figure G.63: π^- pc3s$d\phi$ p$_T$ 7-8 GeV/c *zed* 10-20 cm

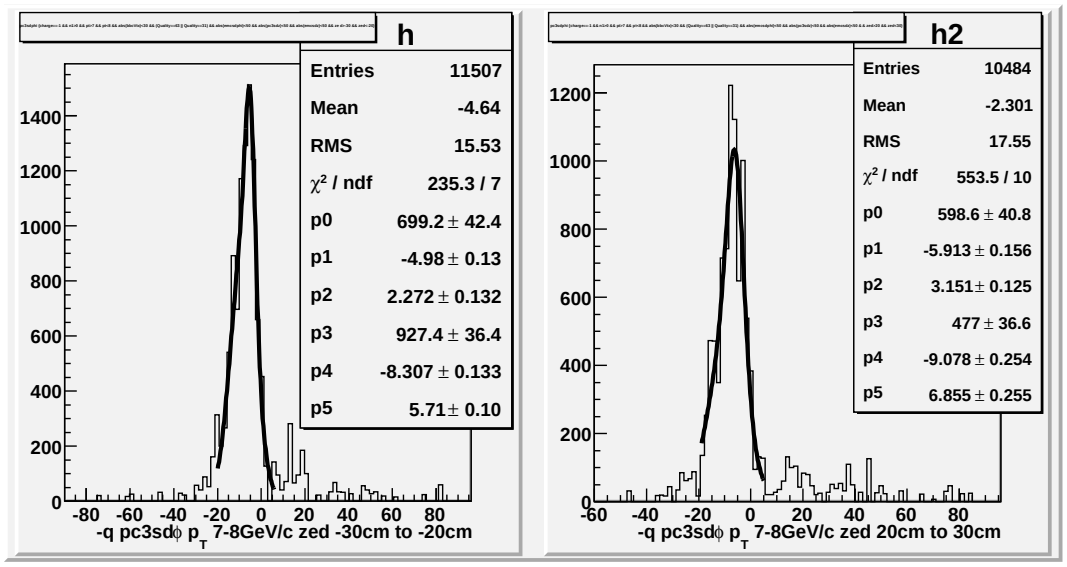

Figure G.64: π^- pc3s$d\phi$ p$_T$ 7-8 GeV/c *zed* 20-30 cm

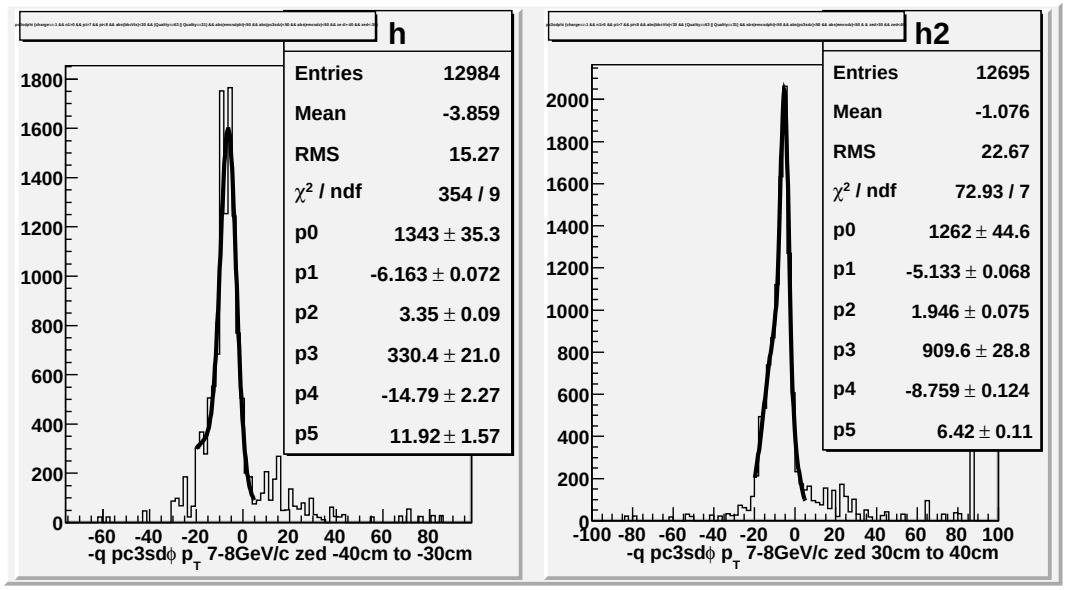

Figure G.65: π^- pc3s$d\phi$ p$_T$ 7-8 GeV/c *zed* 30-40 cm

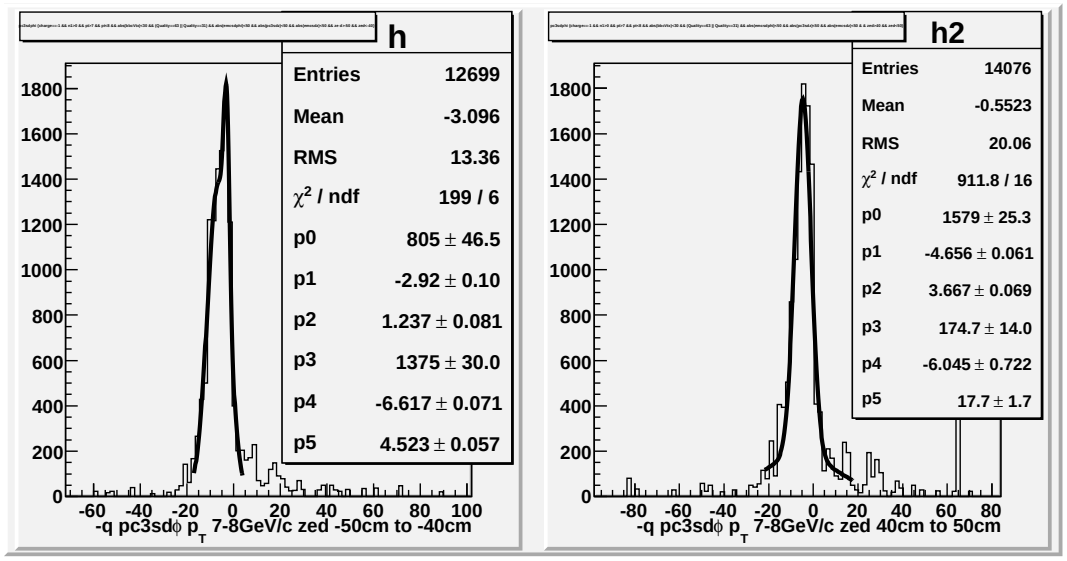

Figure G.66: π^- pc3s$d\phi$ p_T 7-8 GeV/c *zed* 40-50 cm

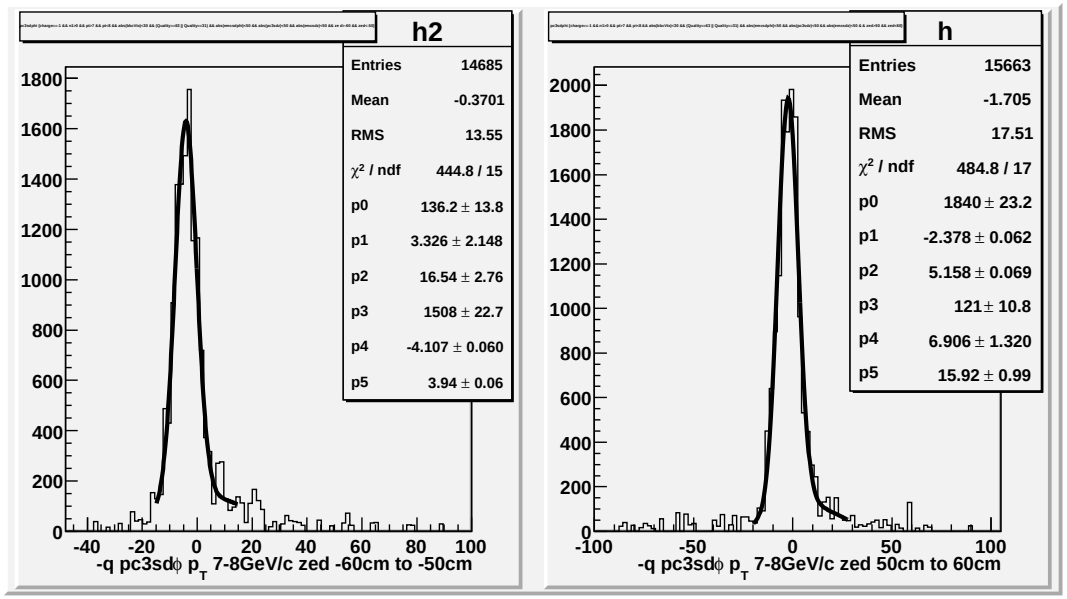

Figure G.67: π^- pc3s$d\phi$ p_T 7-8 GeV/c *zed* 50-60 cm

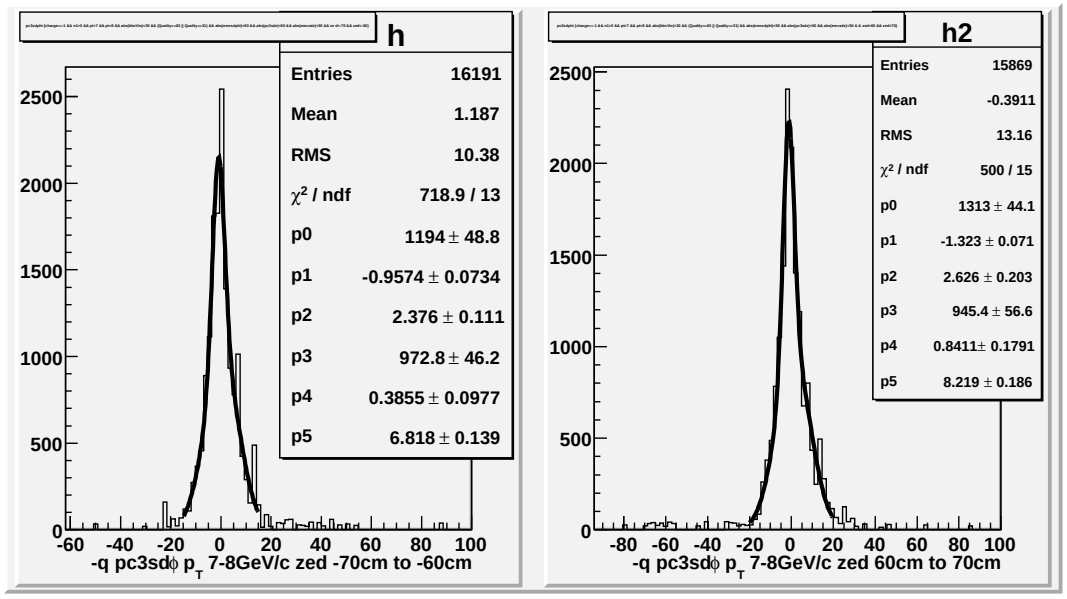

Figure G.68: π^- pc3s$d\phi$ p_T 7-8 GeV/c *zed* 60-70 cm

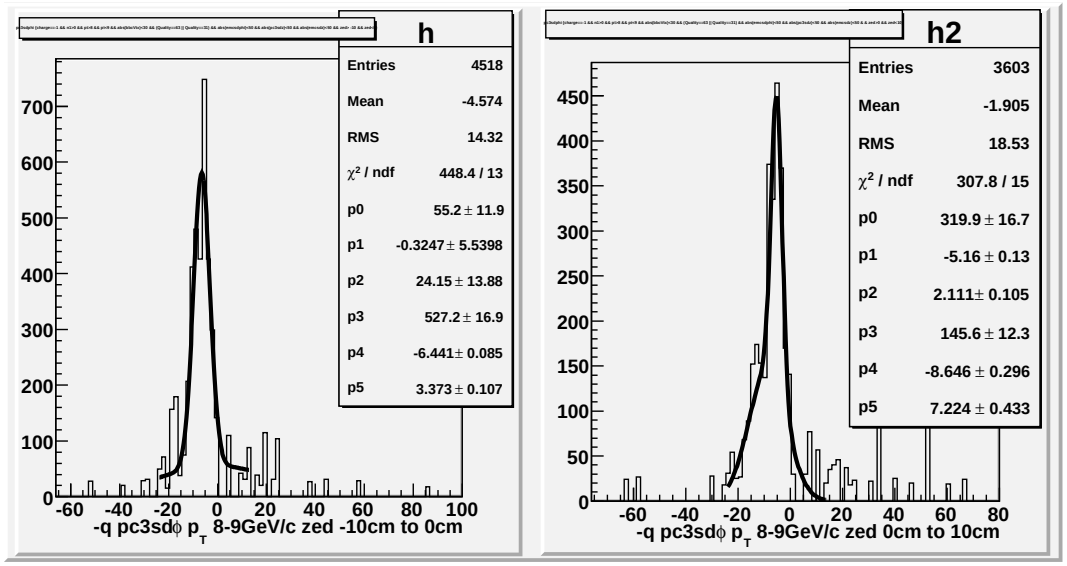

Figure G.69: π^- pc3s$d\phi$ p_T 8-9 GeV/c *zed* 0-10 cm

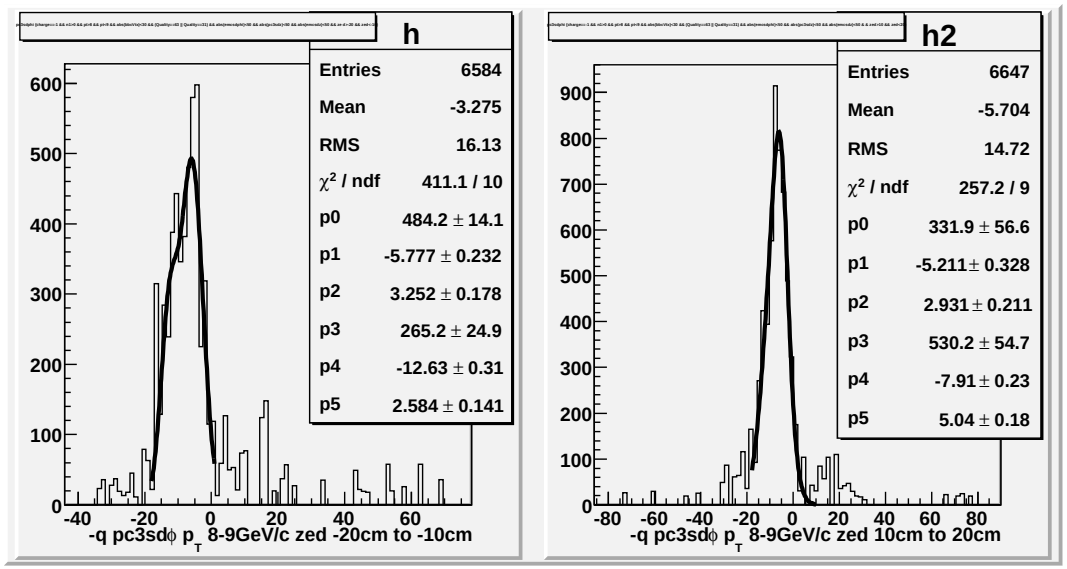

Figure G.70: π^- pc3s$d\phi$ p_T 8-9 GeV/c *zed* 10-20 cm

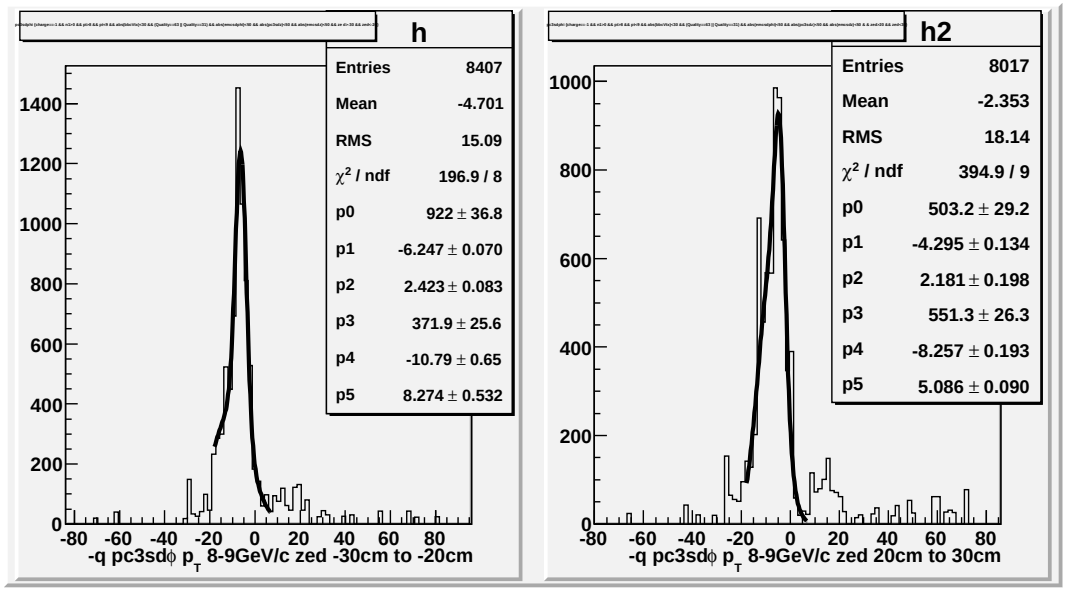

Figure G.71: π^- pc3s$d\phi$ p_T 8-9 GeV/c *zed* 20-30 cm

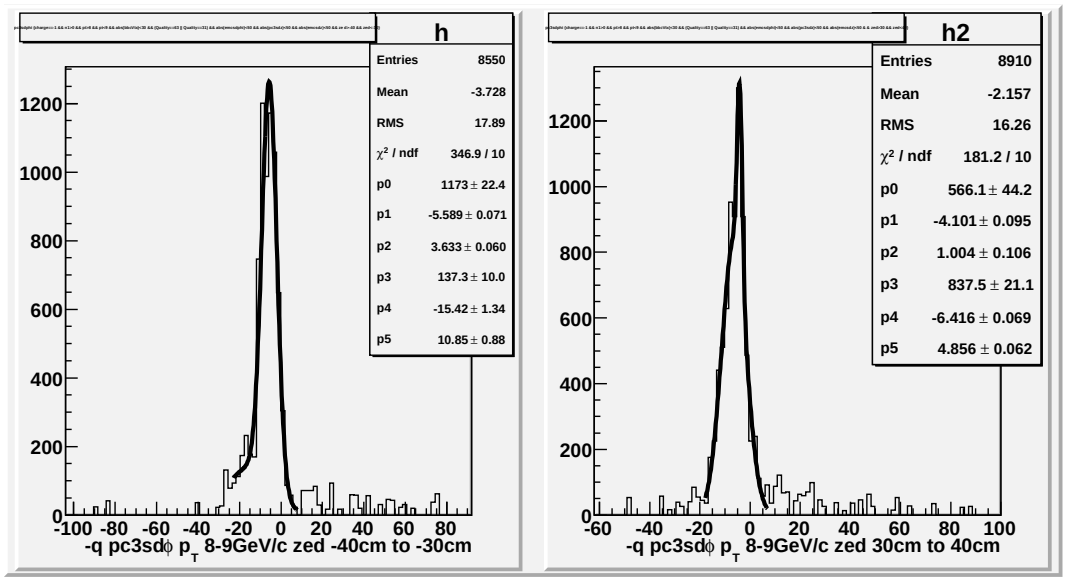

Figure G.72: π^- pc3s$d\phi$ p_T 8-9 GeV/c *zed* 30-40 cm

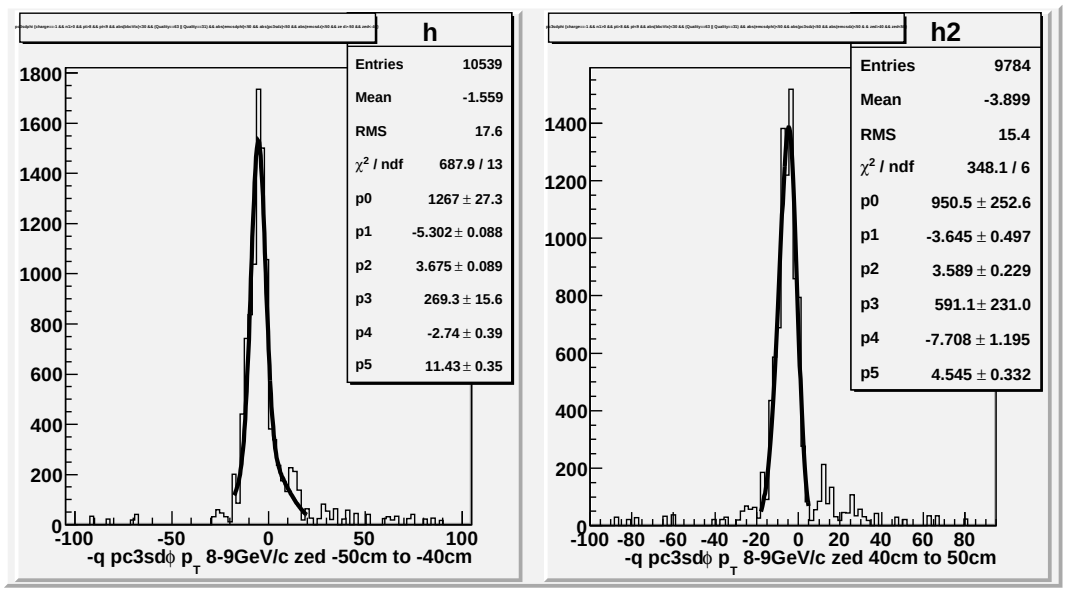

Figure G.73: π^- pc3s$d\phi$ p_T 8-9 GeV/c *zed* 40-50 cm

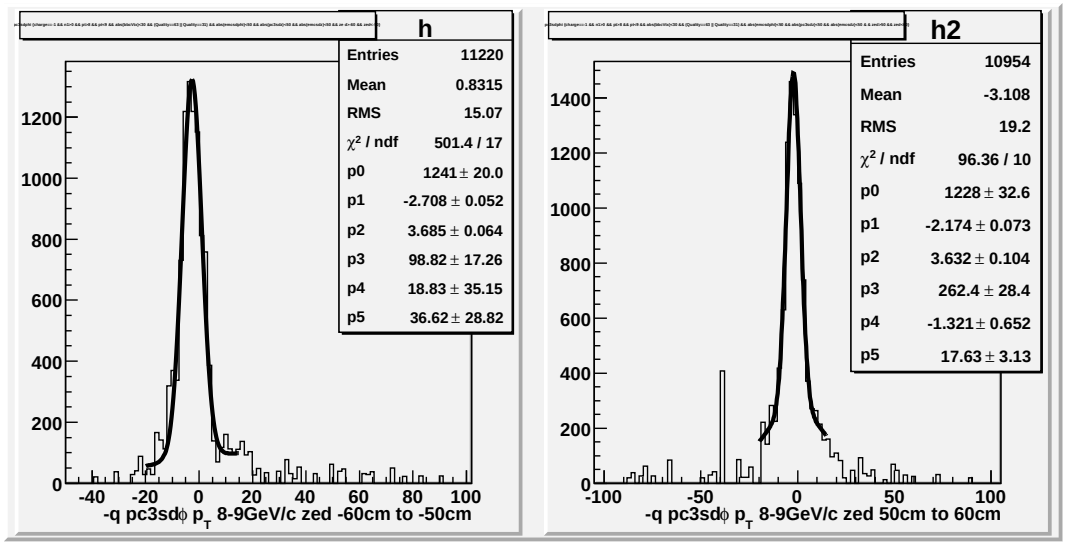

Figure G.74: π^- pc3s$d\phi$ p_T 8-9 GeV/c *zed* 50-60 cm

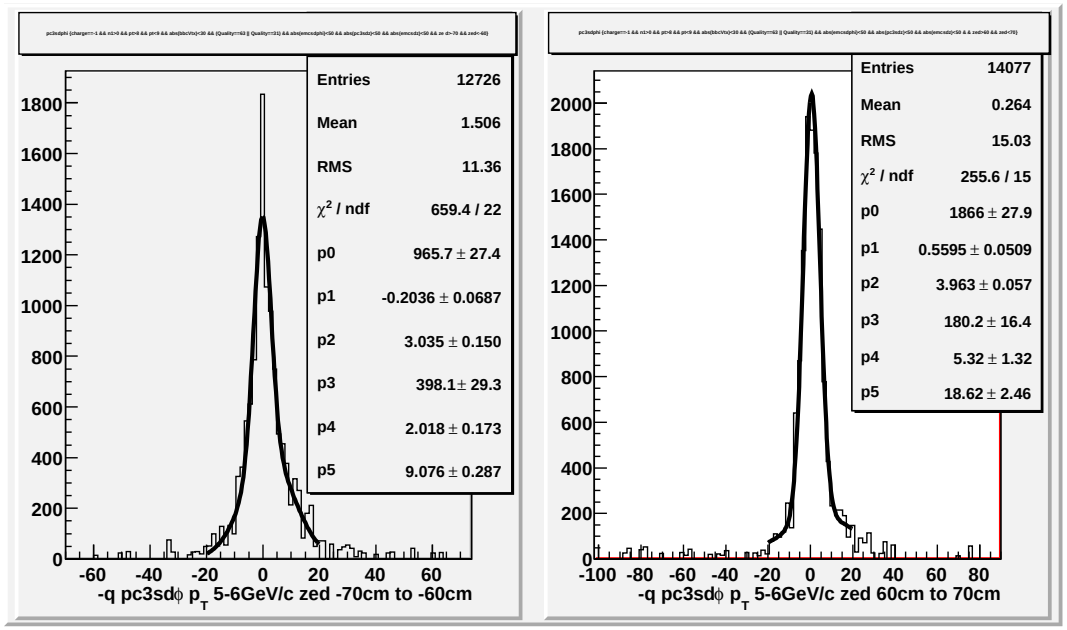

Figure G.75: π^- pc3s$d\phi$ p_T 8-9 GeV/c *zed* 60-70 cm

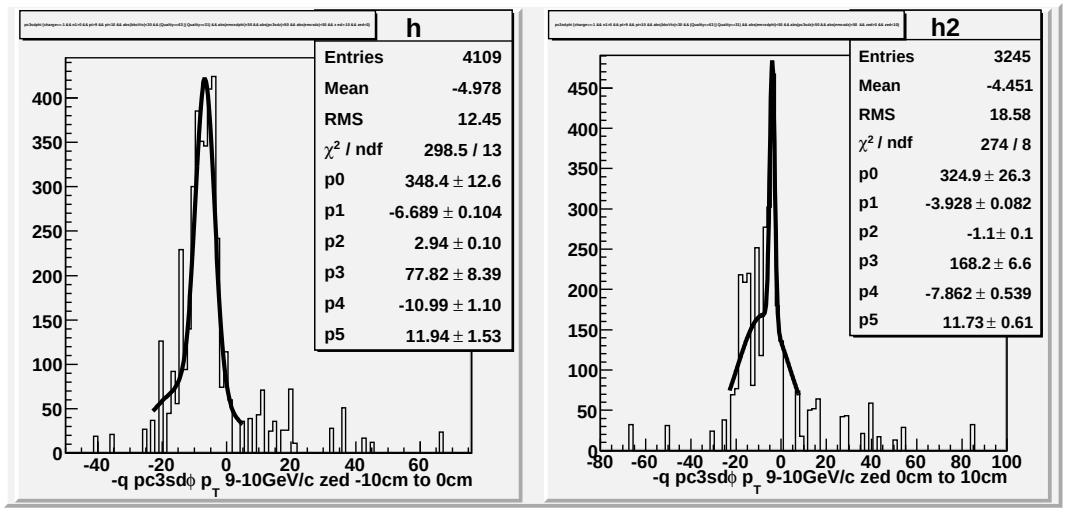

Figure G.76: π^- pc3s$d\phi$ p_T 9-10 GeV/c *zed* 0-10 cm

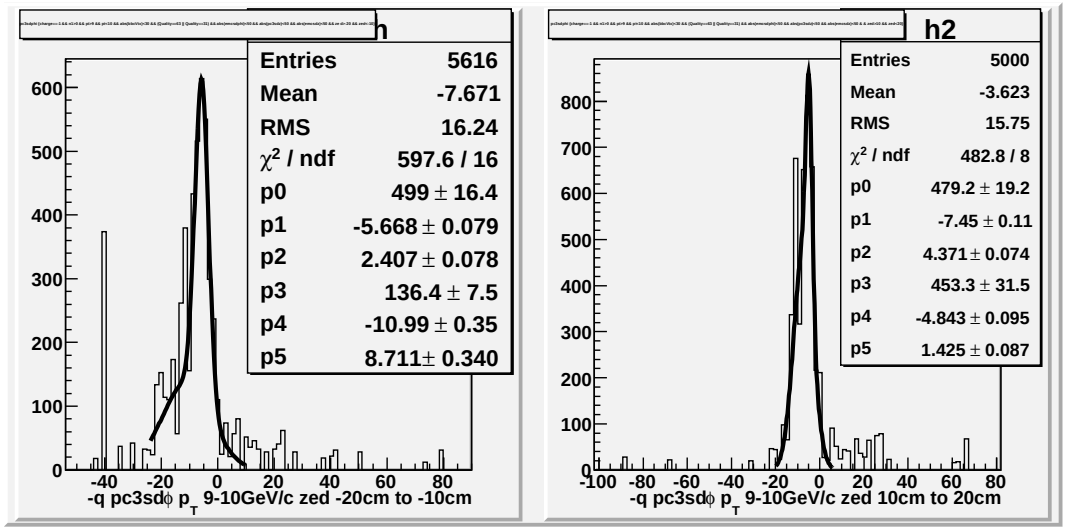

Figure G.77: π^- pc3s$d\phi$ p_T 9-10 GeV/c *zed* 10-20 cm

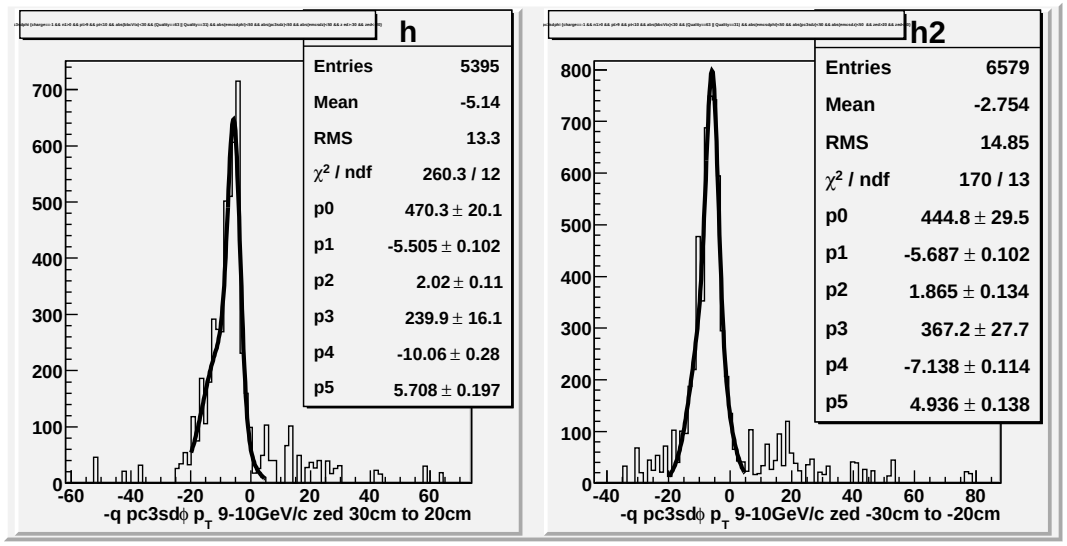

Figure G.78: π^- pc3s$d\phi$ p_T 9-10 GeV/c *zed* 10-20 cm

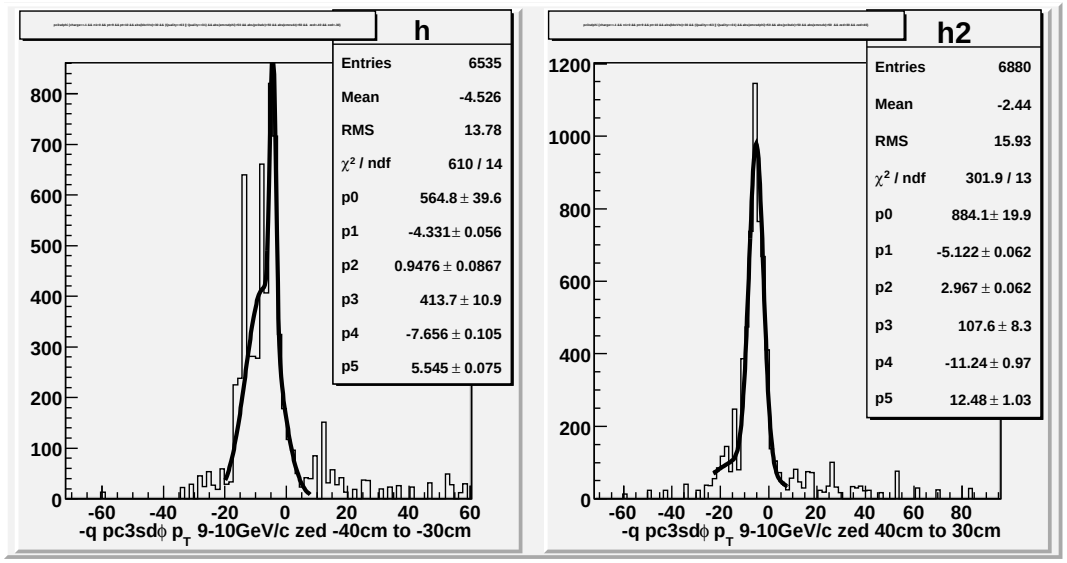

Figure G.79: π^- pc3s$d\phi$ p_T 9-10 GeV/c *zed* 30-40 cm

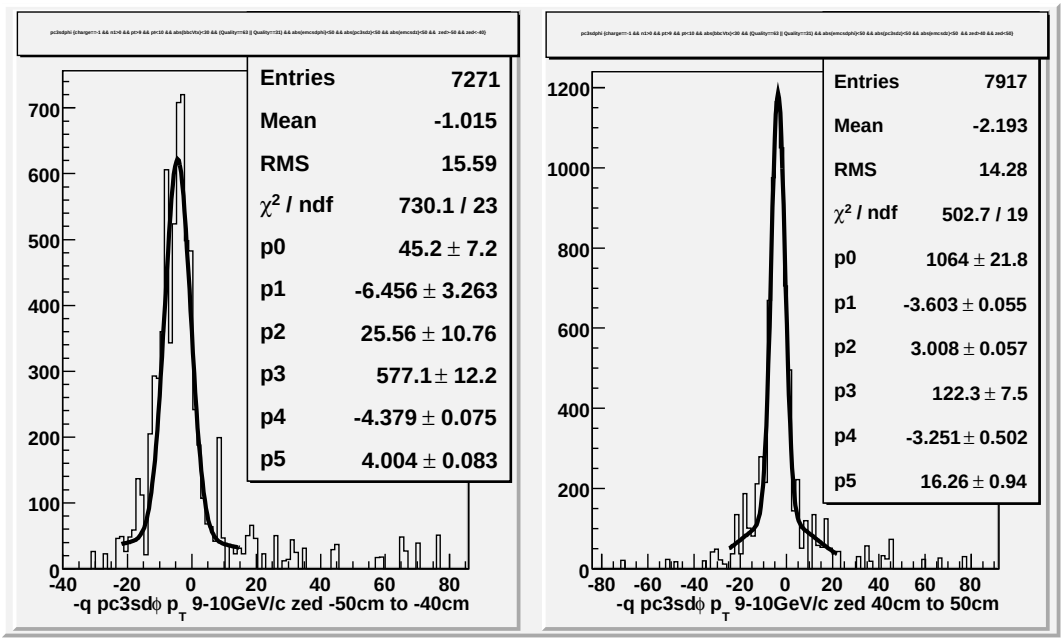

Figure G.80: π^- pc3s$d\phi$ p_T 9-10 GeV/c *zed* 40-50 cm

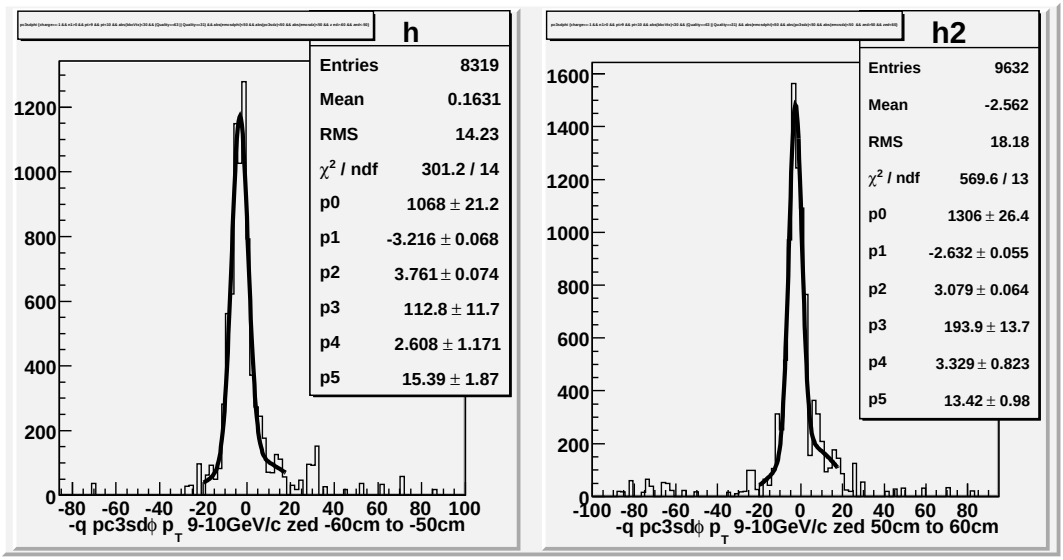

Figure G.81: π^- pc3s$d\phi$ p_T 9-10 GeV/c *zed* 50-60 cm

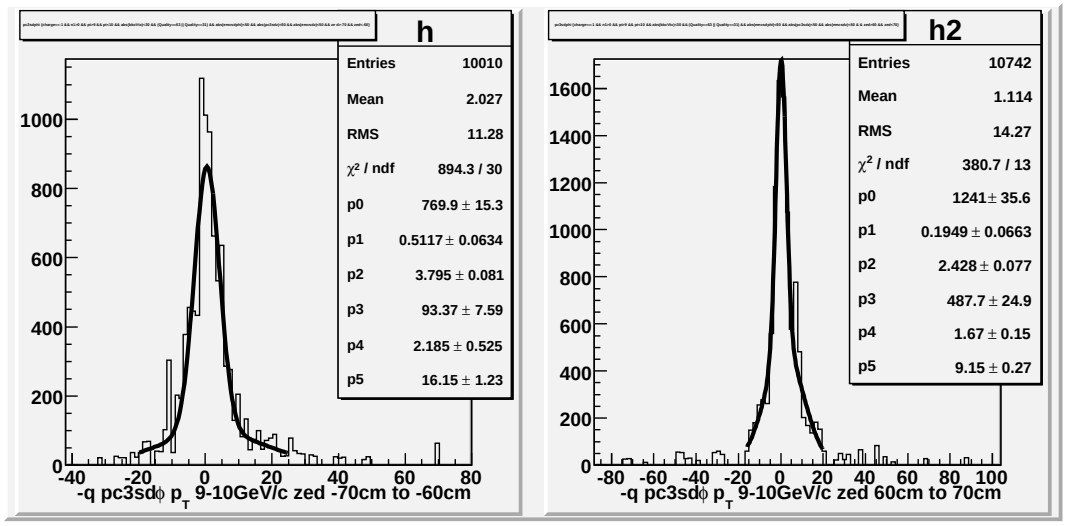

Figure G.82: π^- pc3s$d\phi$ p$_T$ 9-10 GeV/c *zed* 60-70 cm

Appendix H

Spin Asymmetries Studies

Refer to text in Section 6 for a detailed explanation of the context of these figures.

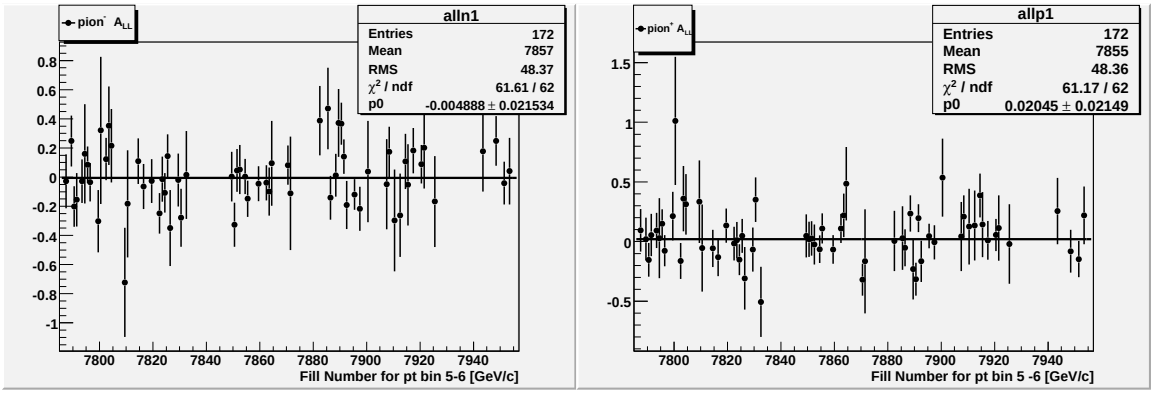

Figure H.1: Fill by fill spin Asymmetries for π^- (left) and π^+ (right). $5 < p_T < 6$ GeV/c. The error bars are the statistical precision (ΔA_{LL}), in the measurement

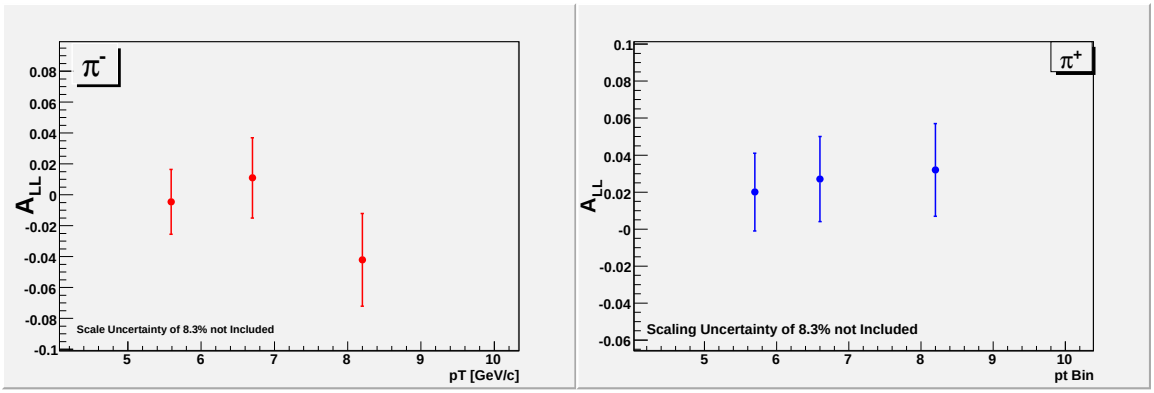

Figure H.2: Fill combined double spin asymmetries (A_{LL}) using χ^2 method for π^-(left) and π^+(right)The error bars are the statistical precision (ΔA_{LL}), in the measurement, Units on the x axis are GeV/c

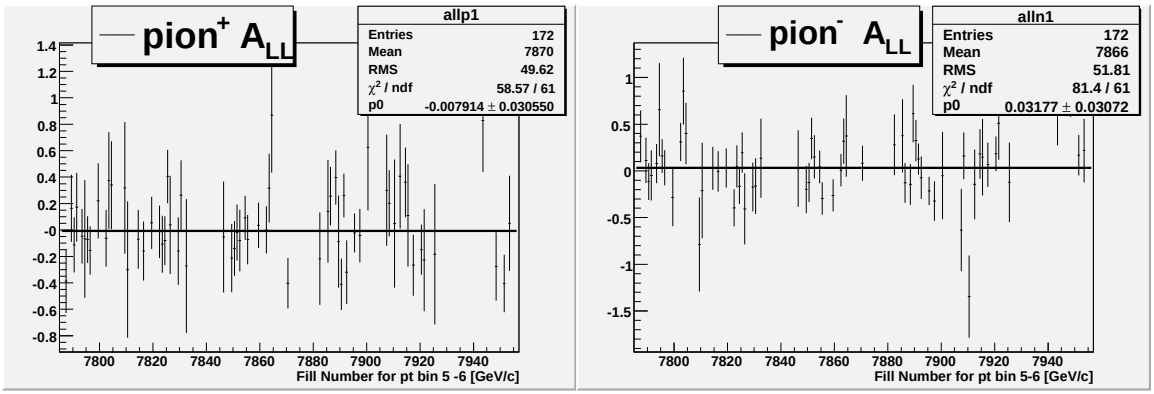

Figure H.3: Odd separated asymmetries using the χ^2 method for π^+ left panel and π^- right panel. Data Corresponds to 5 Gev/c $< p_T <$ 6 GeV/c

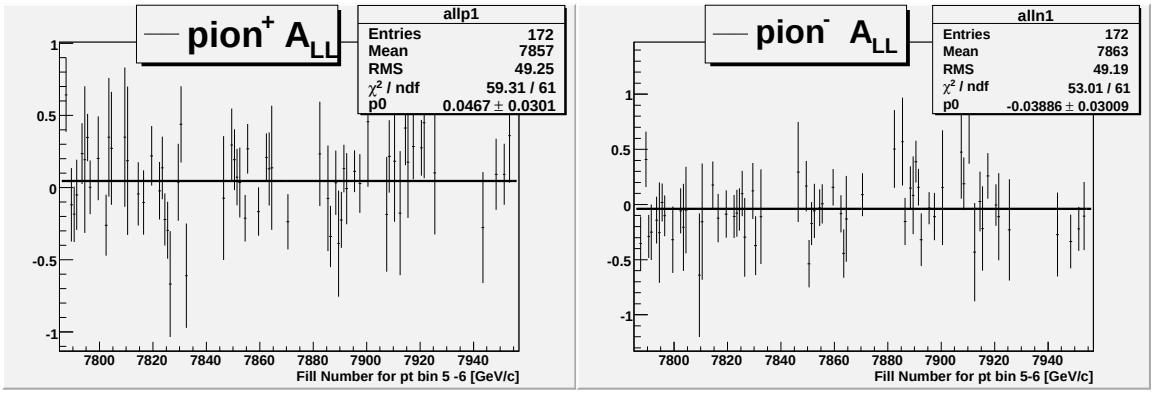

Figure H.4: Even separated asymmetries using the χ^2 method for π^+ left panel and π^- right panel. Data Corresponds to 5 Gev/c $< p_T <$ 6 GeV/c

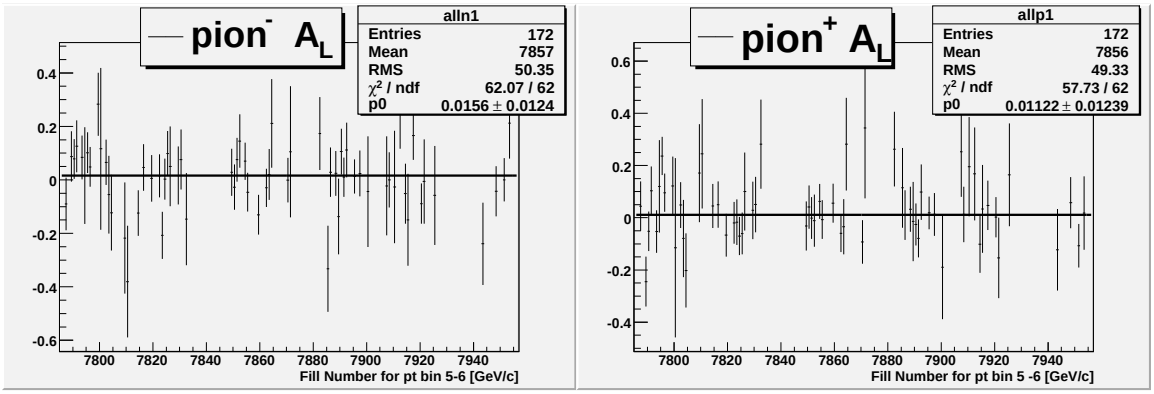

Figure H.5: A_L by fill yellow beam for π^- (left) and π^+ (right). Data corresponds to 5 Gev/$c < p_T <$ 6 GeV/c

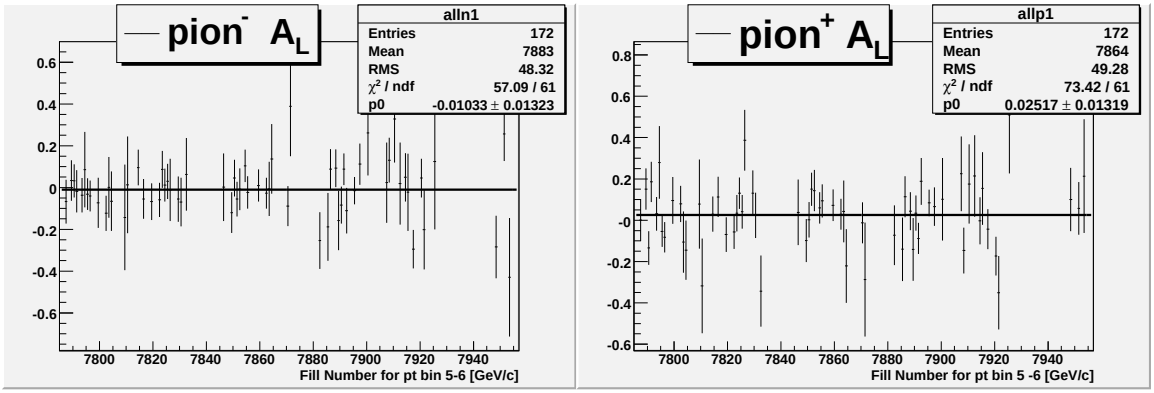

Figure H.6: A_L by fill blue beam for π^- (left) and π^+ (right). Data corresponds to 5 Gev/$c < p_T <$ 6 GeV/c

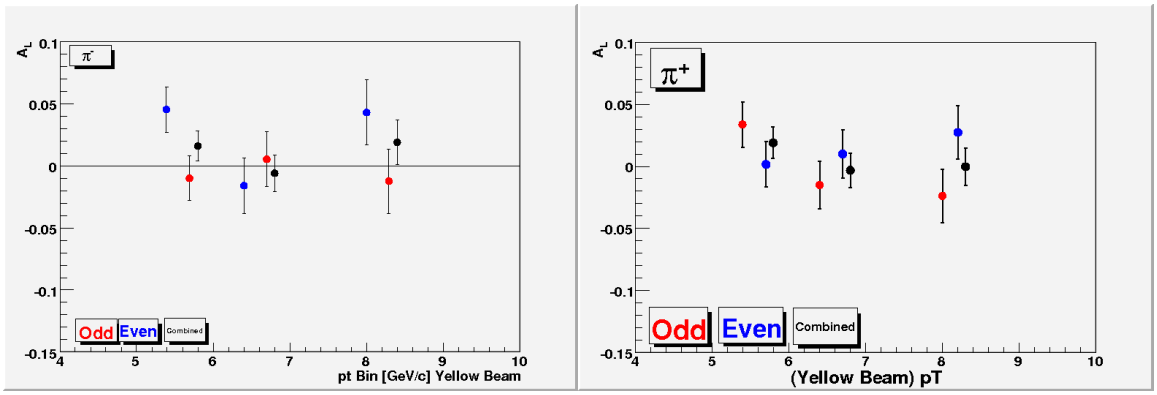

Figure H.7: Crossing separated single asymmetries yellow Beam

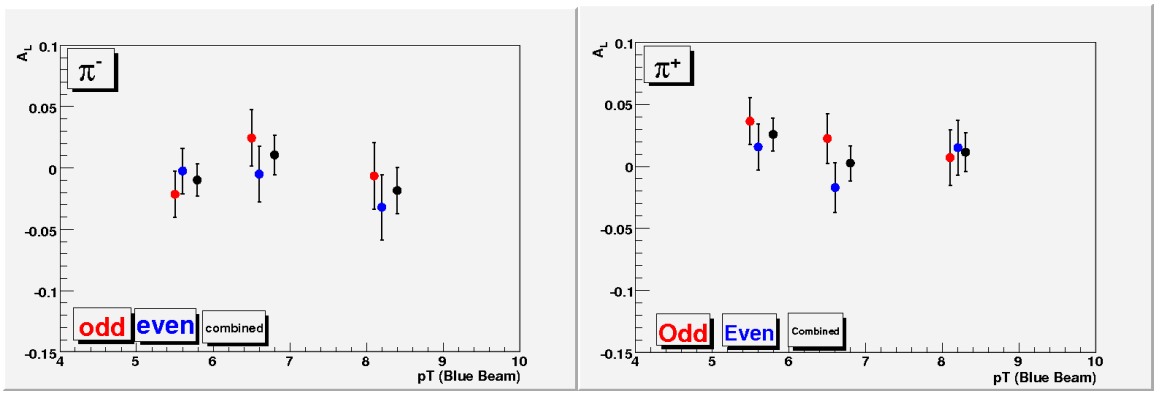

Figure H.8: Crossing separated single asymmetries blue beam

Appendix I

Further Figures and Studies for A_{LL}

I.0.11 ratio of different shower probabilities prob cut

Refer to section 6.5.2

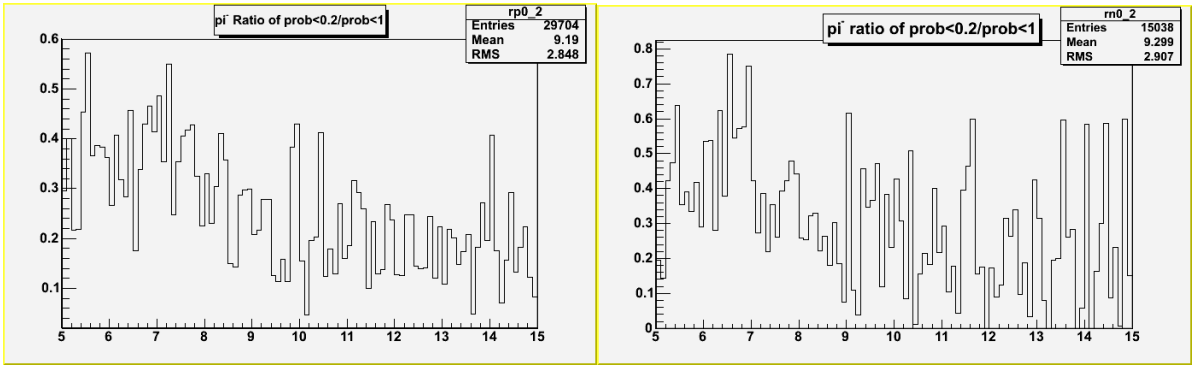

Figure I.1: ratio of data with a probability of electromagnetic shower $\frac{prob<20\%}{prob<100\%}$ for positive (left) and negative (right tracks)

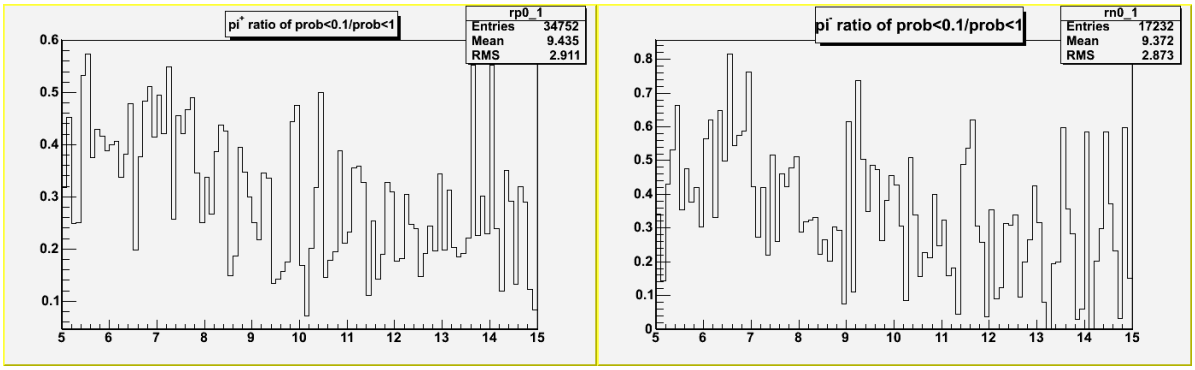

Figure I.2: ratio of data with a probability of electromagnetic shower $\frac{prob<10\%}{prob<100\%}$ for positive (left) and negative (right tracks)

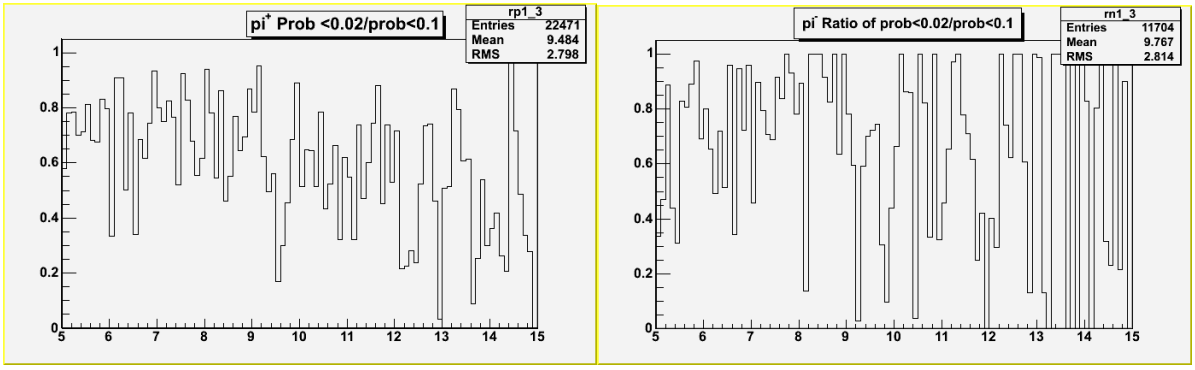

Figure I.3: ratio of data with a probability of electromagnetic shower $\frac{prob<2\%}{prob<10\%}$ for positive (left) and negative (right tracks)

I.0.12 Fill by fill A_{LL}

refer to section 6.9.1

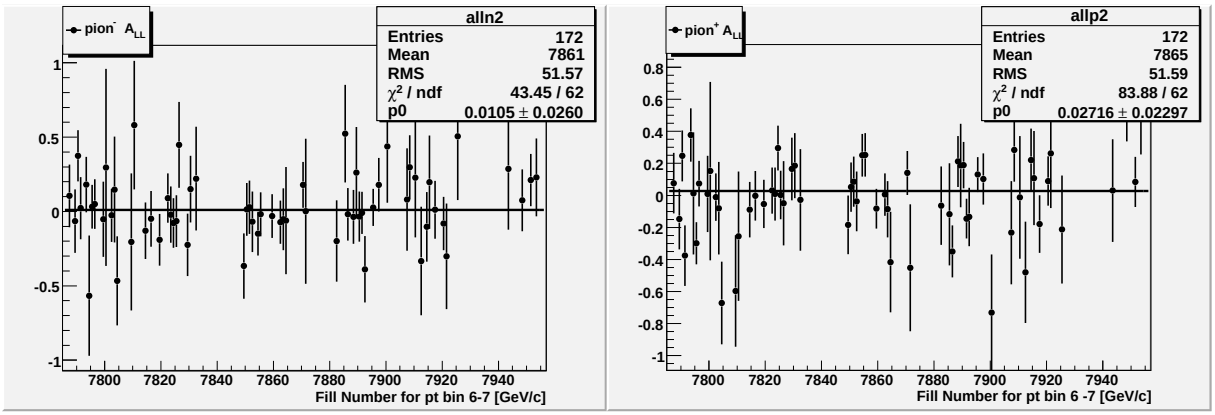

Figure I.4: Fill by fill spin Asymmetries for π^- (left) and π^+ (right). 6$<$ p$_T$ $<$ 7 GeV/c

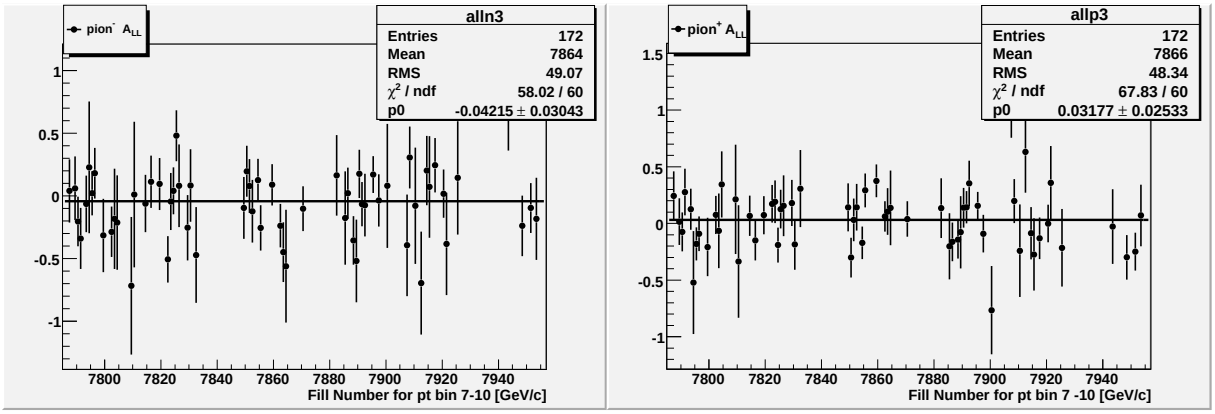

Figure I.5: Fill by fill spin Asymmetries for π^- (left) and π^+ (right). 7$<$ p$_T$ $<$ 10 GeV/c

I.0.13 Bunch Shuffled asymmetries

Refer to section 6.10

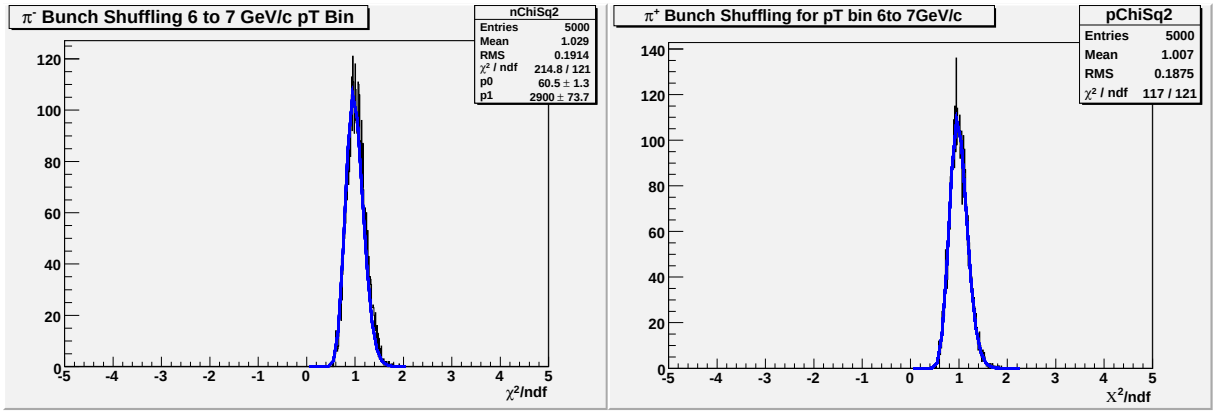

I.0.14 Spin Asymmetries by beam

Refer to section **??**

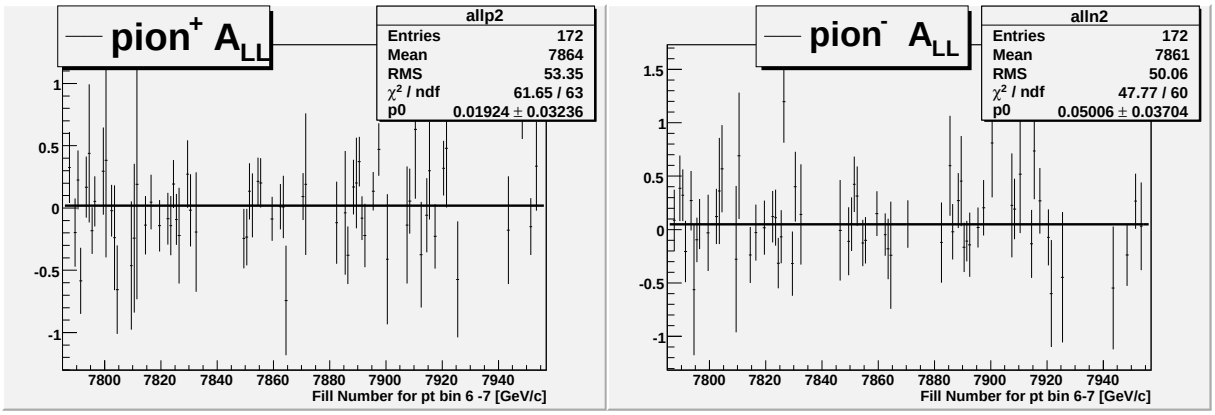

Figure I.8: Odd separated asymmetries using the χ^2 method for π^+ (left panel) and π^- (right) panel is 6-7 GeV/c

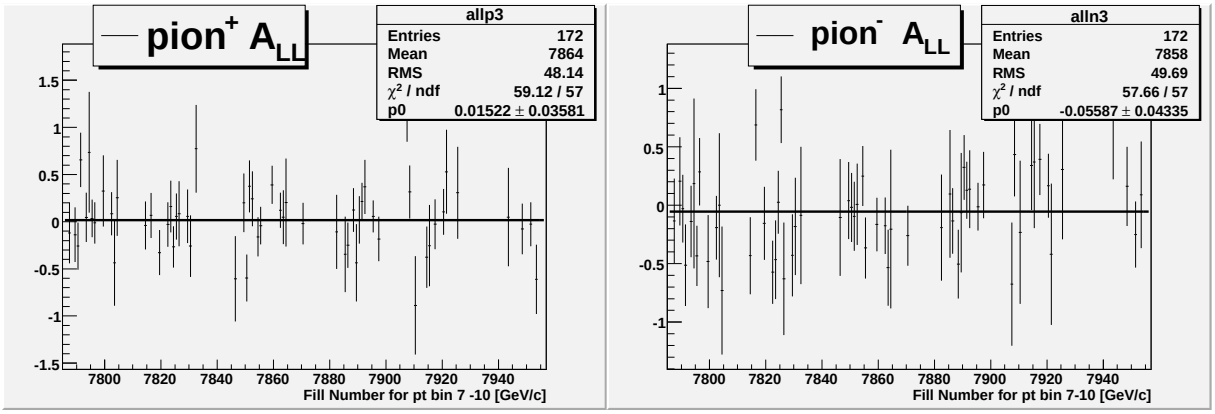

Figure I.9: Odd separated asymmetries using the χ^2 method for π^+ (left panel) and π^- (right panel) is 7-10 GeV/c

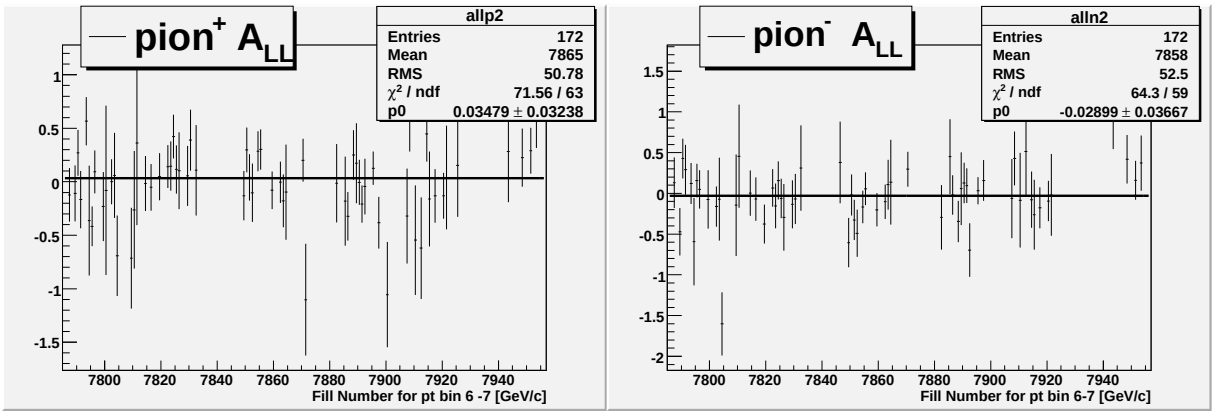

Figure I.10: Even separated asymmetries using the χ^2 method for π^+ (left panel) and π^- (right panel) p_T is 6-7 GeV/c

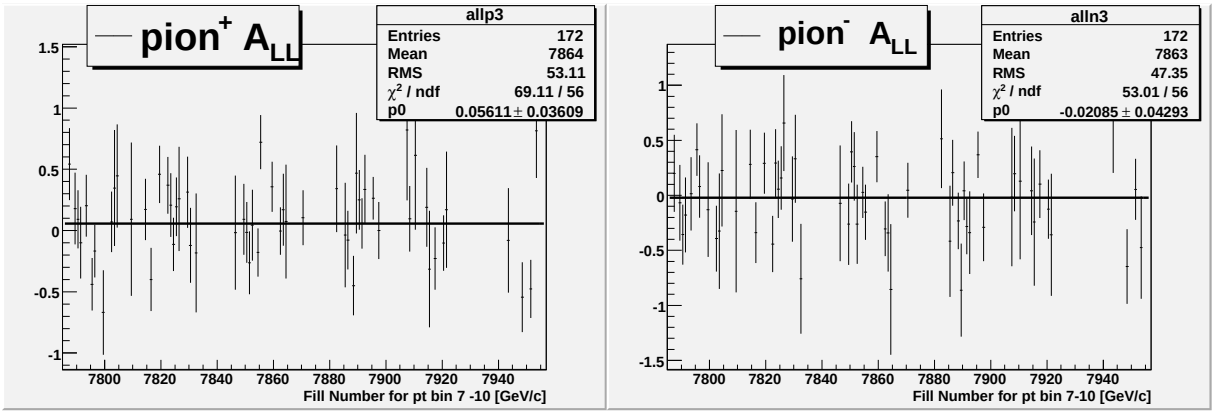

Figure I.11: Odd separated asymmetries using the χ^2 method for π^+ (left panel) and π^- (right panel) p_T is 7-10 GeV/c

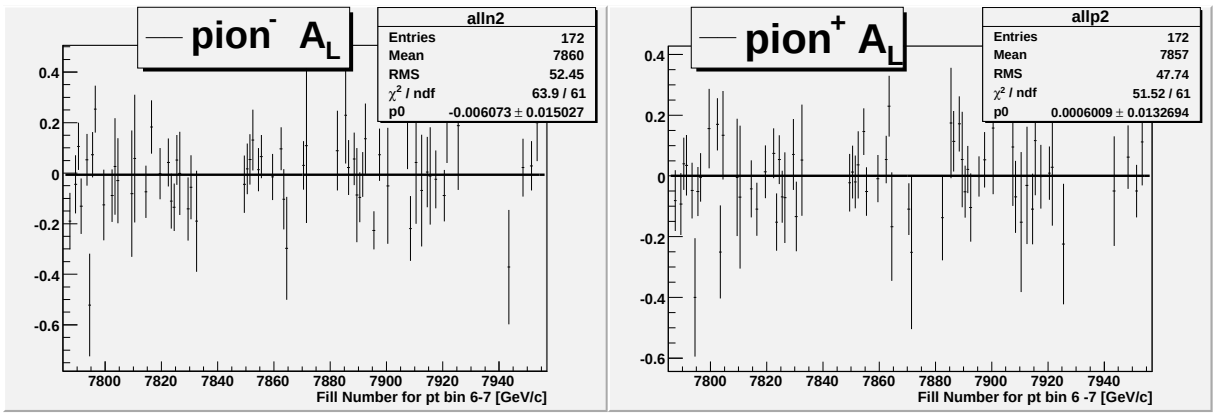

Figure I.12: A_L by fill Yellow Beam for π^- (left) and π^+ (right), p_T is 6-7 GeV/c

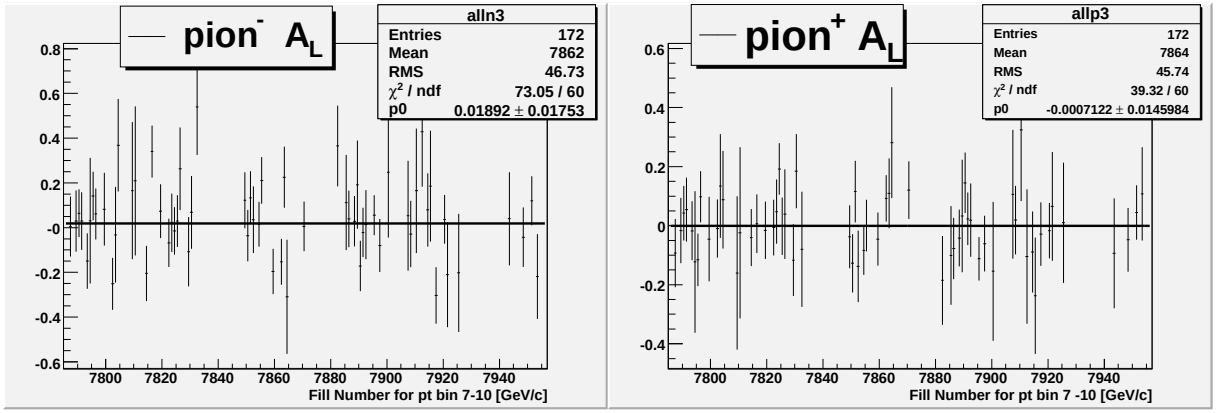

Figure I.13: A_L by fill Yellow Beam for π^- (left) and π^+ (right), p_T is 7-10 GeV/c

A_L by Blue and yellow Beam

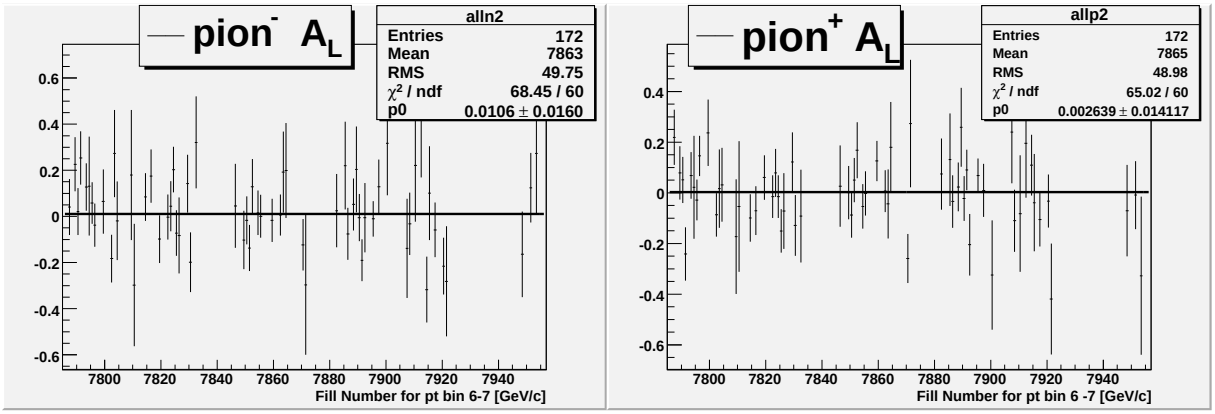

Figure I.14: A_L by fill Blue Beam for π^- (left) and π^+ (right), p_T is 6-7 GeV/c

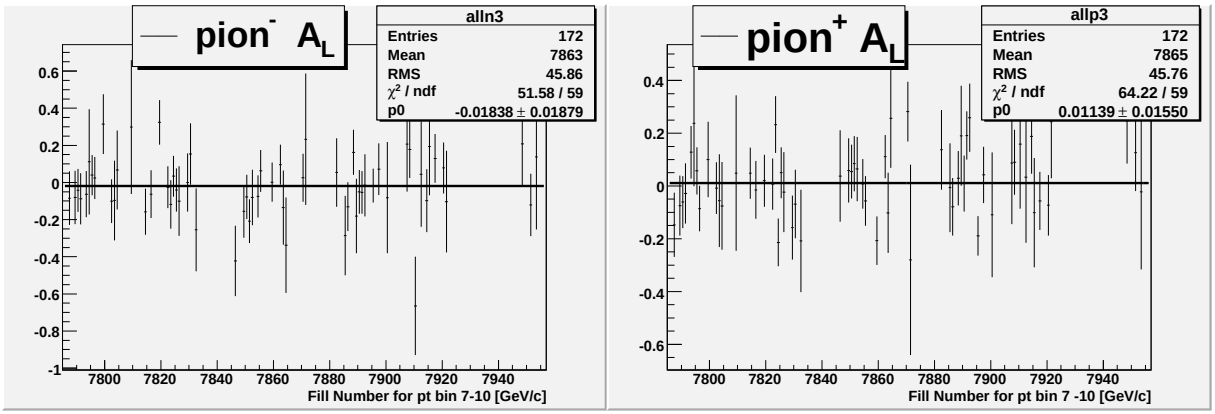

Figure I.15: A_L by fill Blue Beam for π^- (left) and π^+ (right), p_T is 7-10 GeV/c

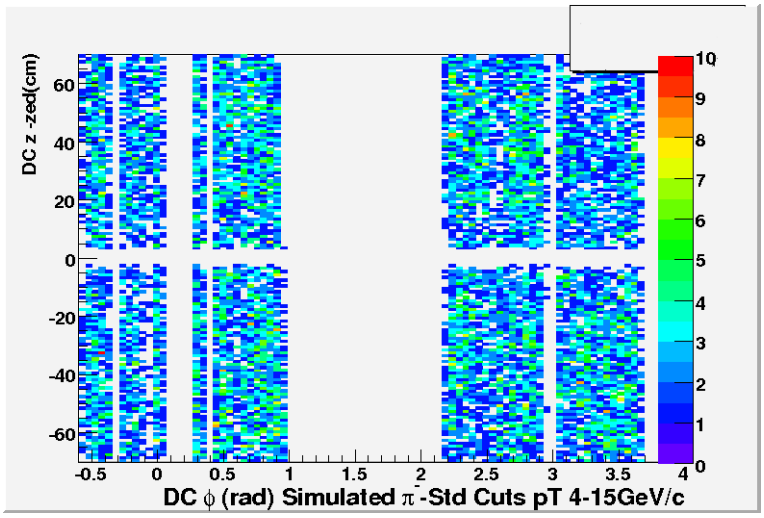

Figure I.16: Simulated drift chamber's ϕ vs *zed* π^-. The white gaps found in the Figures combine physical gaps in the detector as described above (Section 5.2.1), as well as dead maps caused by broken wires within the sub-detectors, and dead electronic channels. Additional studies can be found in Appendix B

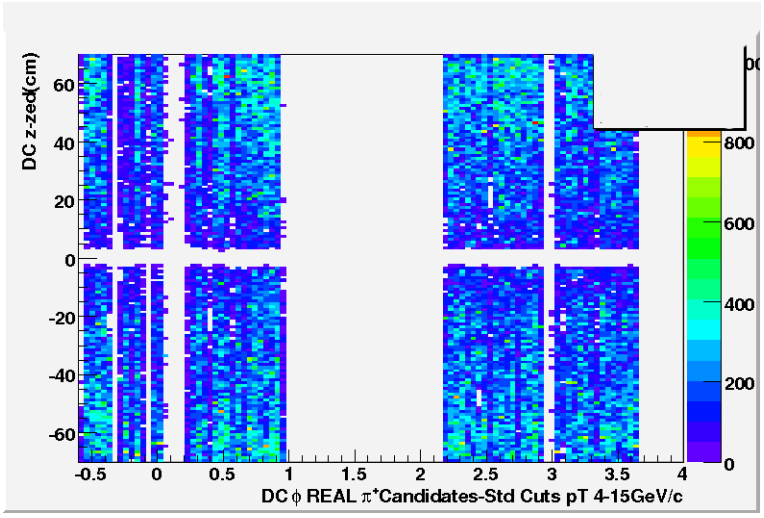

Figure I.17: Real drift chamber data's ϕ vs *zed* π^+ left, and π^- right. These Figures demonstrate the reproducibility of the implemented dead maps from real data onto simulation. Additional studies can be found in Appendix B

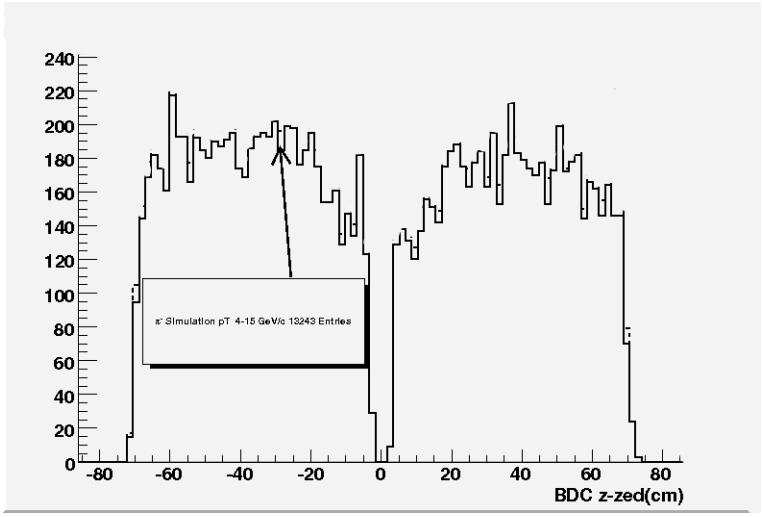

Figure I.18: Simulated drift chambers *zed* distributions for π^+ (left), and π^- (right panel). The simulation found in these Figures contain minimal cuts, as the goal was to inspect the shape of the *zed* distributions. As it is shown above, the distributions are relatively flat

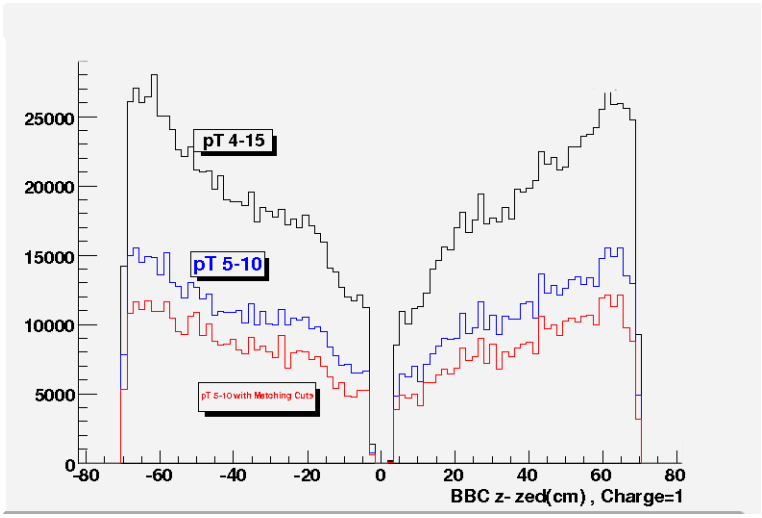

Figure I.19: *zed* distributions of data in different bins of p_T, which displays the high tails at high and low *zed* (See also Figure 5.15), indicating the presence of secondary electron/positron background. The data used for this study was minimum bias with standard identification cuts, including a loose matching (Section 5.4) cut of 3σ (red lines)

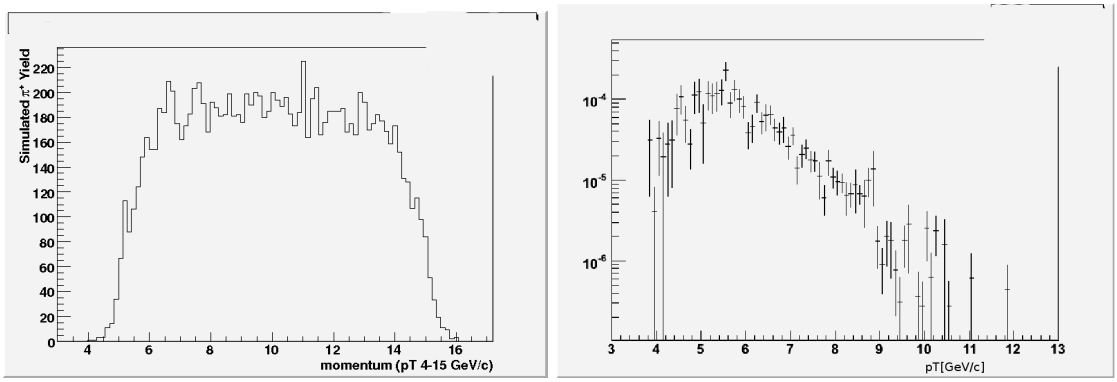

Figure I.20: π^+ simulated momentum distributions within 4 GeV/c <p_T <15 GeV/c. Top Figure shows the spectra after a flat momentum distribution is used as input. The bottom Figure has momentum weighted distributions by the function 14.43/$p_T^{8.1}$[5] to simulate a realistic decaying particle spectra in the detector. Errors on bottom Figure, are histogram bin entries. Abscissa is p_T in units of GeV/c

Appendix J

Further QCD Related Figures and Studies

J.1 Extra Studies Performed

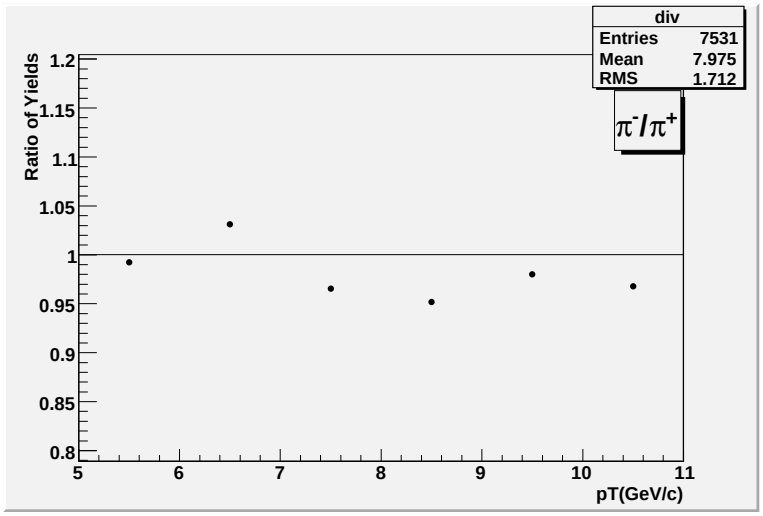

Figure J.1: Ratio of equal number of simulated pions after being put through the PHENIX central Arms.

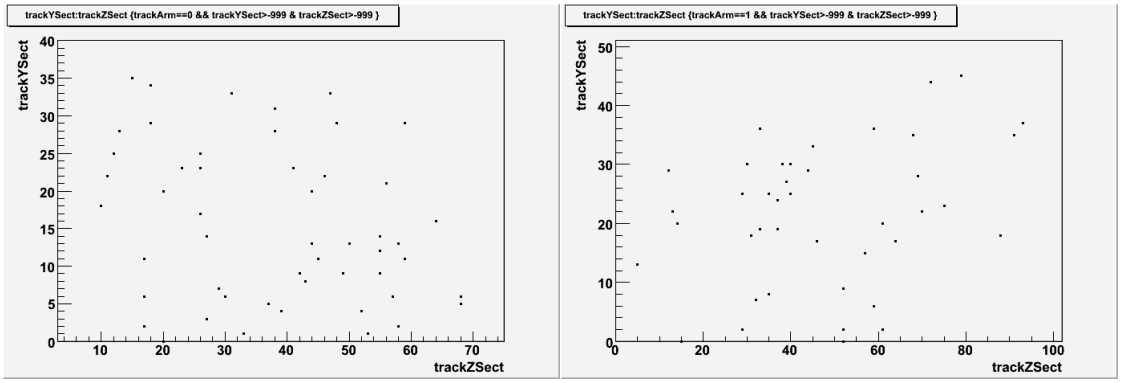

Figure J.2: Simulated quark-gluon scattering events. The scattered plot distributions show the energy deposition of the particles in the EMCal in the *x* and z plane. EMCal Arm west(east), left (right). Number of particles detected are 51(41) for west (east) arms

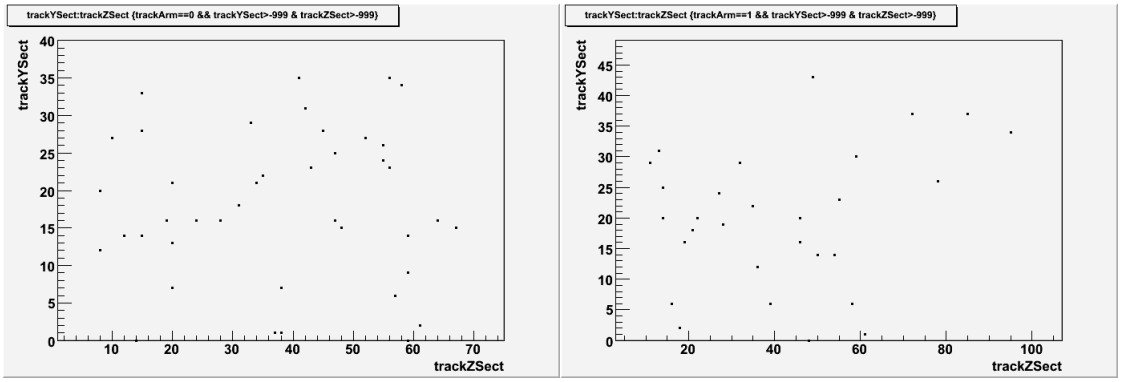

Figure J.3: Simulated quark-quark scattering events. The scattered plot distributions show the energy deposition of the particles in the EMCal in the *x* and z plane. EMCal Arm west(east), left (right). Number of particles detected are 42(30) for west(east) arm